Kent Academic Repository

Falsaperna, Mario (2022) *Influence of Structure and Doping on Frustration in Low-Dimensional Coordination Polymers.* Doctor of Philosophy (PhD) thesis, University of Kent,.

Versions of research works

Versions of Record

Author Accepted Manuscripts

Enquiries

Influence of Structure and Doping on Frustration in Low-Dimensional Coordination Polymers

Mario Falsaperna

Division of Natural Sciences,

University of Kent

Canterbury

U.K

This thesis is submitted for the title of

Doctor of Philosophy

July 2022

Declaration

I hereby declare that the work which is being presented in this thesis, in partial fulfilment of the requirement for the award of the degree of Doctor of Philosophy in Chemistry, constitutes original research carried out under the supervision of Dr Paul J. Saines, University of Kent, except where specific references are made to the work and contribution of others. The content of this thesis has not been submitted either in whole or in part for consideration for any other degree or qualification, or to any other University.

Mario Falsaperna

July 2022

Acknowledgments

I would like to thank my supervisor, Paul Saines, without whom the realisation of this project would have not been possible. His experience, patience and invaluable mentoring have allowed me to learn a lot on how to conduct research and how to be kind and collaborative in a team. I will never forget his teachings and his kindness, and I will carry his example with me throughout my career and my life.

I would like to thank past and current academics in the School of Physical Sciences at the University of Kent: Donna Arnold, Emma McCabe, Nicholas Bristowe, Anna Corrias and Gavin Mountjoy. Thank you all for the helpful discussions, training, collaboration, help, and your immense kindness. I would also like to thank all the former and current members of my group, for their friendship and the fantastic discussions. Special thanks to Patrick Doheny for helping with the proofreading of this thesis, for all his help and for often sharing his knowledge with me in rich scientific discussions. To all of them and my friends in room 104, I wish the best, I pray they will all achieve their dreams, and I am grateful for their kindness and affection.

My gratefulness also goes to all the collaborators that played a vital role in measurements in central facilities, namely Andrew Studer at ANSTO; Gavin Stenning, Pascal Manuel and Ivan da Silva at the ISIS Neutron and Muon Source. I would also like to thank our collaborators at the University of Oxford, Andrew Goodwin and Johnathan Bulled, for their help in carrying out part of this project. To professor Goodwin, special thanks for being such an inspiration, and for his infectious enthusiasm for science.

Many thanks to the Leverhulme Trust for their financial support for this research, for the necessary training and for the attendance to conferences during the years.

To my parents, Salvatore and Adriana, thank you for your enormous sacrifices, love and support throughout the years, which have made this achievement possible, and to my brother and my sister, Corrado and Eleonora, whose love and support is priceless. Words cannot begin to picture how much I love you all.

Finally, I would like to thank my girlfriend, Alexandra Rosie Paul, for all her love and support, as well as for the inspiration she has given me through her creativity, and her perseverance and love for science and all the things she does. I am grateful you are in my life.

Mario Falsaperna

Abstract

Low-dimensional and frustrated magnets have long attracted interest. The interrelation between structure, composition and magnetic properties of such materials is vital to understand their exotic states, such as the Triangular Ising Antiferromagnet (TIA), and to optimise them for technological applications, such as magnetic refrigeration, a greener alternative to conventional gas compression refrigeration. Metal-organic frameworks (MOFs) offer a multitude of structures, and are good candidates for magnetic cooling. In particular, dense coordination frameworks, such as $Tb(HCO_2)_3$, exhibit magnetocaloric properties enhanced for use with magnetic fields close or below 2 T, resulting from a combination of lanthanide cations with magnetocrystalline anisotropy, strong local magnetic interactions and magnetic frustration.

In this thesis, an introduction to magnetism and magnetic materials of interest is provided in Chapter 1. To set context for the work completed, the known promising magnetocaloric coordination polymers are reviewed in Chapter 2. Chapter 3 describes the experimental and analytical methods used. Chapter 4 focuses on the $Ln(HCO_2)(C_2O_4)$ ($Ln = Sm^{3+}–Er^{3+}$) family of coordination frameworks, which resemble the related $Ln(HCO_2)_3$ frameworks. The magnetocaloric effect of $Gd(HCO_2)(C_2O_4)$ is amongst the highest found in coordination frameworks for high magnetic field changes. Lanthanides with magnetocrystalline anisotropy did not improve the magnetocaloric properties of these materials at lower fields, in contrast with similar materials. Neutron diffraction suggested that the Tb and Ho members lack significant local magnetic correlations, which might be essential for optimising magnetocaloric materials.

Chapter 5 describes the magnetic properties of the $Ln(HCO_2)_3$ frameworks containing earlier lanthanides — specifically Ce^{3+}, Pr^{3+} and Nd^{3+}. We confirmed these frameworks lack magnetic order and any noticeable local correlations. The novel $Ho_{1-x}Er_x(HCO_2)_3$ series of solid solutions was then explored as these should contain a mixture of ferromagnetic and antiferromagnetic 1D interactions. Their composition affects their magnetic properties and $Ho_{0.5}Er_{0.5}(HCO_2)_3$, a potential spin-chain paramagnet, was shown to be paramagnetic down to 400 mK, with this further confirmed by neutron diffraction. Finally, the $Tb_{1-x}Y_x(HCO_2)_3$ series was studied. Diamagnetic dopants, *i.e.* Y, are expected to disrupt the TIA state found in $Tb(HCO_2)_3$ and alter its magnetocaloric properties. The TIA state proved to be robust to doping, which was also found responsible for low-temperature contributions to the heat capacity. The magnetocaloric properties decrease across the series, but the magnetocaloric entropy per Tb increases at higher x. These observed properties are ascribed to be arising from entropic effects resulting from the fragmentation of quasi-1D spin chains by the dopant.
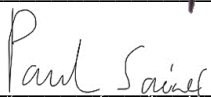
Chapter 6 investigates the magnetic structure of a complex 2D-antiferromagnet, $[Li(C_2O_4)]_2[Co_5(OH)_8]$, where Co sites are arranged in a triangular fashion within the layers, potentially causing geometric frustration. This material has an antiferromagnetic transition at ~55 K. Neutron diffraction down to 8 K has shown additional Bragg-like reflections emerge at 55.6 K, confirming the magnetic transition temperature. The magnetic structure is $P\bar{1}$ triclinic and Rietveld refinements have shown this material constitutes an example of a 2D-canted antiferromagnet. DFT has confirmed our experimental model and has allowed for the estimation of values of magnetic coupling constants, J, which confirmed this material indeed behaves as a 2D magnet. The nature and strength of the coupling within a layer provides further indication that geometric frustration might be present in this system.

Covid-19 Impact Statement

In accordance with the [Kent Covid Impact Information](#) issued by the University of Kent in March 2021 and in force since April 2021, it is hereby declared that the Covid-19 pandemic has hindered part of the research work presented in this dissertation. With lockdowns enforced following the decision of the UK government in March 2020, access to the laboratories in the School of Physical Sciences, Ingram building, University of Kent, was forbidden in 2020 for a period of about four months. With the lifting of some lockdown restrictions in July 2020, work in the laboratories gradually restarted, albeit on a rota system which has severely limited access to them. Overall, this resulted in restricted access to research laboratories for ~9 months, delaying key aspects of experimental work. In addition to this, access to facilities central to the work carried out, such as the ISIS Neutron and Muon source and ANSTO, was significantly restricted. This was followed by long maintenance shutdowns in the facilities, scheduled long before the start of the Covid-19 pandemic, and prolonged due to the latter. These factors have both contributed to the increased difficulty in being awarded beamtime at the facilities and have restricted planned aspects of this work, *e.g.* inelastic neutron scattering for $Tb(HCO_2)_3$ and $Ho(HCO_2)_3$.

Steps to mitigate the impact of lockdowns were taken. The candidate wrote a review on magnetocaloric coordination polymers, which resulted in a publication and is presented herein in Chapter 2. In addition to this, neutron diffraction data on a material synthesised by collaborators in the group of Dr Keene (University College Dublin, Ireland) were provided to the candidate and were analysed for the determination of its magnetic structure. This now constitutes a significant part of the work presented in Chapter 6 and similarly constitutes material for a future publication. An overall extension

Student signature_____ Date 05/07/2022

Supervisor signature_____ Date 05/07/2022

List of publications

This is a list of journal articles published during the duration of the work presented in this dissertation. Publication 2 and 3 have directly contributed to Chapter 3 and 4 of this dissertation, respectively. The submitted manuscript at 1 has contributed to Chapter 5.

1. "Anomalous evolution of the magnetocaloric effect in dilute triangular Ising antiferromagnets $Tb_{1-x}Y_x(HCO_2)_3$", manuscript submitted to Physical Materials Review

2. "Development of magnetocaloric coordination polymers for low temperature cooling" M. Falsaperna and P. J. Saines, *Dalton Trans.*, 2022, **51**, 3394-3410

3. "Magnetocaloric $Ln(HCO_2)(C_2O_4)$ frameworks: synthesis, structure and magnetic properties" M.Falsaperna, G. B. G. Stenning, I. da Silva and P. J. Saines, *J. Mater. Chem. C.*, 2021, **9**, 13209-13217

Table of Contents

List of Figures

List of Tables

Nomenclature and Abbreviations

K	Kelvin
χ^2	Goodness of fit squared
π	~3.14159
λ	Wavelength
θ	Bragg angle
θ_{CW}	Curie-Weiss temperature
Å	Angstrom (1×10^{-10} m)
AFM	Antiferromagnetic
ANSTO	Australian Nuclear Science and Technology Organisation
CW	Constant Wavelength
T_C	Curie Temperature
DSC	Differential Scanning Calorimetry
ECO	Emergent Charge Order
FM	Ferromagnetic
FC	Field Cooled
FTIR	Fourier Transform Infrared (Spectroscopy)
GGG	Gadolinium Gallium Garnet
GEM	General Materials (Diffractometer)

Ln	Lanthanide
MPMS	Magnetic Properties Measurement system
MCE	Magnetocaloric Effect
MOF	Metal-Organic Framework
meV	Millielectron Volt
MC	Monte Carlo
T_N	Néel Temperature
PPMS	Physical Properties Measurement System
PXRD	Powder X-ray Diffraction
RMC	Reverse Monte Carlo
SQUID	Superconducting Quantum Interference Device
TGA	Thermogravimetric Analysis
TOF	Time of Flight
TIA	Triangular Ising Antiferromagnet
WISH	Wide-angle in Single Histogram
ZFC	Zero-field Cooled

1 Introduction

1.1 Background Context

The phenomenon of magnetism was known to the ancient Greeks — at least since the 6th century BC, as writings from the philosopher Thales of Miletus report —[1] who observed it in lodestone, a rock containing the ferromagnetic mineral Fe_3O_4, also known as magnetite, due to its natural attraction to iron and other lodestones. It is speculated that the term *magnet* comes from the region of Magnesia, Anatolia, where lodestones could be found.

In modern times, magnetic materials have been studied not only for their fundamental properties,[2] but also for their potential applications, including data storage and transfer,[3,4] magnetic cooling,[5,6] quantum computing,[7] and medical applications, such as magnetic imaging techniques.[8,9]

The origin of the ferromagnetic behaviour of materials such as magnetite was explained in 1907 by Pierre-Ernest Weiss, where the idea of molecular field, a precursor to the mean-field theory, was introduced.[10] In 1933, another type of magnetic behaviour antiferromagnetism, was proposed by Lev Landau,[11] and further explained by Louis Néel in 1948.[12] The discovery of another type of magnetic behaviour and the possibility of materials exhibiting mixed behaviour, *i.e.* ferrimagnetism, drew significant attention to the field of magnetism.

As in the case of magnetite, a great number of magnetic materials studied in the last century are close-packed materials such as oxides, halides and alloys, due to these typically featuring strong magnetic interactions between their magnetic centres, with

many of these materials being successfully used in technological applications. As an example, the reader will be familiar with traditional hard drives for data storage on personal computers, which initially made use of iron(III) oxide, γ-Fe_2O_3, and, in more recent times, of cobalt-based alloys.[13]

More recently, hybrid materials, combining both organic and inorganic components, have attracted considerable interest due possibility of synergy between the two components.[14] More specifically, coordination polymers containing polyatomic ligands, including MOFs, have drawn significant attention due to the surprising flexibility they offer in the design of structures and properties. These include gas absorption,[15–17] gas storage, gas sensing,[18–20] catalysis,[21–25] and drug-delivery,[26] applications for which MOFs tend to be good-candidates due to the considerably high surface areas and pore sizes that can be achieved when organic ligands of appropriate dimensions are chosen to build the structure.[27]

More recently, magnetic coordination polymers have become increasingly important due to the possibility of synthesising structures that differ from the close-packed ones typically adopted by purely inorganic materials. This enables the realisation of materials with a wider range of structures, and the achievement of targeted topologies and low-dimensional motifs, such as two-dimensional magnetic sheets and one-dimensional magnetic chains, incorporated in the three-dimensional crystalline structure. These features make these materials interesting both from a fundamental perspective, particularly within these low dimensional units, as well as their potential applications.

A particularly relevant application of magnetic coordination polymers is that of magnetic cooling. This is achieved thanks to the magnetocaloric effect (MCE), an

entropy-driven phenomenon where a temperature change of the material is observed upon the ordering and subsequent disordering of the magnetic moments when an external magnetic field is applied. Magnetocaloric materials have drawn considerable interest in recent years due to the necessity to substitute traditional gas compression/expansion technologies for refrigeration,[28] particularly at low temperatures where liquid helium is increasingly scarce and expensive.[29]

An interesting property that is found in some magnetic materials, including coordination polymers, is geometric frustration, where competitions between the magnetic moments arise due to the structure of the material itself, leading to a suppression of magnetic order. The presence of low-dimensional motifs, such as one-dimensional chains or two-dimensional sheets, and frustration has been shown to improve the performance of magnetocaloric materials, particularly in lower applied fields.[5] Coordination polymers have therefore proved to be excellent candidates for magnetic cooling because it is easier to fabricate materials featuring low-dimensional magnetism and geometric frustration.[30][31,32] The research in this thesis focuses on magnetic coordination polymers with the potential feature geometric frustration, some of which are useful magnetocalorics. Before discussing these results, it is first necessary to explain some of the fundamental aspects of magnetism along with introducing some related coordination polymers that promising magnetocaloric properties as a result of their magnetic frustration, which is the focus of this chapter.

1.2 The Origin of Magnetism

Magnetism arises in nature due to electrons. The electron is a fermion possessing spin s = ½, with electric charge (-1.602×10^{-19} C) and a mass of 9.109×10^{-31} kg. Electrons are found in the orbitals of individual atoms and their interaction is responsible

for the formation of larger molecules and condensed matter. In the context of condensed matter, and magnetism in particular, it is of paramount importance to understand how magnetic behaviour arises from the presence of unpaired electrons in materials.

The motion of the electron is the result of two contributions: the spin, which can classically be thought of as the rotation about its own axis, and its motion in space, such as the orbiting around the nucleus of an atom. As a charged particle in motion, electrons are responsible for the generation of a magnetic field, as the French mathematician and physicist André-Marie Ampère, considered the father of electromagnetism, discovered.

A way of describing electrons in orbit around the nucleus of an atom is by means of the quantum numbers n, l, m_l, m_s. n is the **principal quantum number**, describing the energy of the electron as well as the size of the orbital, which increases with n; l is the **orbital angular momentum quantum number**, which describes the magnitude of the angular momentum; m_l is the **magnetic quantum number,** which represents the orientation of the angular momentum; the fourth parameter, m_s, the **spin quantum number**, which specifies the intrinsic angular momentum of the electron. In the case of the electron which, as stated, is a spin ½ fermion, m_s can only have values of $\pm 1/2$. As fermions, multiple electrons cannot occupy the same quantum state at the same time. For this reason, only two electrons can occupy the same orbital and only on the condition that they differ by their spin quantum number m_s, in which case the two electrons are said to be "paired".

When considering one single electron and its motion, its magnetic moment is given by:

$$\mu_B = \frac{e\hbar}{2m_e} L = 9.274 \times 10^{-24} \text{J T}^{-1}, \tag{1.1}$$

with e the electron charge, $\hbar$ the reduced Planck constant, m_e the mass of the electron and L its angular momentum. The magnetic moment of a single electron, μ_B, is defined as the Bohr magneton.

For an atom possessing a partially filled orbital, it is possible to describe many different configurations, but only one has the lowest energy. The German physicist Friedrich Hund devised a set of three rules that would help identify this lowest-energy configuration:

1. The electrons maximize their total spin S, therefore implying that they will arrange in such a way that one electron per orbital is present and that these are parallel to one another, *i.e.* with the same spin, "pairing" up only when all of the orbitals are first filled with at least one electron. This also implies that the lowest-energy level maximises the spin multiplicity, represented by the term $(2S+1)$.

2. For a given spin arrangement, the configuration possessing the largest total atomic orbital angular momentum, L, possesses the lowest energy.

3. For atoms with less than half-filled orbitals, the lowest-energy configuration is the one with $J = |L - S|$. In contrast, when the orbitals are more than half-filled, the lowest-energy configuration is the one given by $J = |L + S|$. This has to do with the spin-orbit coupling, expressed by J, the **total angular momentum quantum number**.

The spin-orbit coupling can be thought of as the interaction of the two magnetic moments generated by the spin contribution S and the orbital momentum contribution L, an interaction that becomes particularly relevant for heavier atoms. For lanthanides, where the splitting of the energy of the $4f$ orbitals, responsible for their magnetism, via

interactions with their ligands is very small, this interaction can be quantified using the Russell-Saunders coupling scheme (also known as the *LS* coupling scheme), with the quantum number *J* representing its magnitude, as mentioned. This is in contrast with the 3*d* transition metals, where spin-orbit coupling is typically quenched, *i.e.* $L = 0$, due to the splitting of the energy levels caused by the crystal field, an effect due to the *d*-orbitals interacting much more with the surrounding ligands than is the case for the core-like 4*f* orbitals of the lanthanides. The implication of this **orbital quenching** is that the Russell-Saunders coupling scheme does not accurately predict the effective magnetic moments, which are not in agreement with the experimental values and are better estimated by considering the spin-only contribution.

As an example, let's consider a gadolinium atom, which has a configuration [Xe] $5d^1\,4f^7\,6s^2$. In condensed matter, gadolinium is typically found as the Gd^{3+} cation, possessing the configuration [Xe] $4f^7$. Since there are seven possible *f* orbitals, the electrons in this orbital can have seven different m_l orientations. Figure 1.1 shows a representation of the lowest-energy configuration for the Gd^{3+} ion according to Hund's rules. According to Hund's first rule, electrons will occupy the orbitals one at a time before pairing up. With only seven electrons present, no pairing will occur. This leads to a total spin quantum number of $S = 7/2$ and multiplicity $(2S+1) = 8$. Continuing with the second rule, the largest value of *L* needs to be found. In this case $L = 0$, meaning that Gd^{3+} possesses no total orbital momentum, which has significant implications as will be discussed later on. Finally, because the 4*f* orbitals are exactly half-filled, $J = |L + S|$ needs to be considered, with $J = 7/2$ in this case. Conventionally, the so-called Hund's **terms** are represented with the symbol $^{(2S+1)}L_J$, with the value of L replaced by a letter (S, L, P, F, etc.), in analogy with those used for the atomic orbitals (*i.e. s, l, p, f,* etc.*)*. The lowest-energy configuration for Gd^{3+} is therefore $^8S_{7/2}$.

$$m_l$$

| -3 | -2 | -1 | 0 | 1 | 2 | 3 |
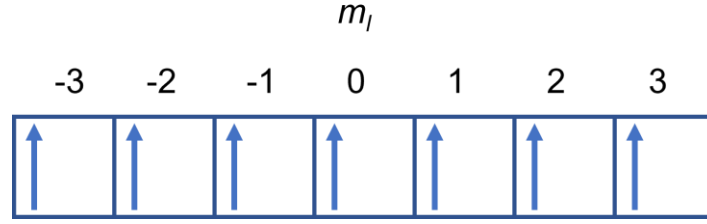
Figure 1.1: Diagram of the lowest-energy configuration for the Gd^{3+} $4f$ orbitals according to Hund's rules.

For a partially filled atom or cation like Gd^{3+}, it is possible to calculate an effective magnetic moment μ_{eff}, arising from the contribution of all the unpaired electrons present in the outer orbital, their spin and orbital motion and the coupling between the two. This is given by:

$$\mu_{eff} = g_j \sqrt{J(J+1)}, \qquad (1.2)$$

where g_j is the Landé g-factor for a lanthanide ion, named after the German-American physicist Alfred Landé:

$$g_j = \frac{3}{2} + \frac{S(S+1) - L(L+1)}{2J(J+1)}, \qquad (1.3)$$

A table of the ground-state configuration S, L and J values along with the corresponding term symbol and calculated effective moment, μ_{eff}, for each lanthanide cation is provided in Table 1.1.[33]

Table 1.1: List of the *S*, *L*, *J* values for the ground-states of the *Ln³⁺* cations, corresponding Hund's ground state term symbol and effective magnetic moment μ_B.

Ln³⁺	**Electron configuration**	*S*	*L*	*J*	μ_{eff} (μ_B)	μ_{obs} (μ_B)
Ce	$4f^1$	1/2	3	5/2	2.5	2.3–2.5
Pr	$4f^2$	1	5	4	3.58	3.4–3.6
Nd	$4f^3$	3/2	6	9/2	3.62	3.5–3.6
Pm	$4f^4$	2	6	4	2.68	-
Sm	$4f^5$	5/2	5	5/2	0.85	1.4–1.7
Eu	$4f^6$	3	3	0	0.0	3.3–3.5
Gd	$4f^7$	7/2	0	7/2	7.94	7.9–8.0
Tb	$4f^8$	3	3	6	9.72	9.5–9.8
Dy	$4f^9$	5/2	5	15/2	10.63	10.4–10.6
Ho	$4f^{10}$	2	6	8	10.60	10.4–10.7
Er	$4f^{11}$	3/2	6	15/2	9.59	9.4–9.6
Tm	$4f^{12}$	1	5	6	7.57	7.1–7.6
Yb	$4f^{13}$	1/2	3	7/2	4.53	4.3–4.9

1.3 Magnetic Interactions

Before magnetic order in condensed matter is discussed, it is beneficial to first explore the most relevant interactions that can occur between the magnetic moments in the materials that are the subject of this research.

1.3.1 The Dipolar Interaction

The most straightforward interaction is the dipolar interaction, illustrated in Figure 1.2.
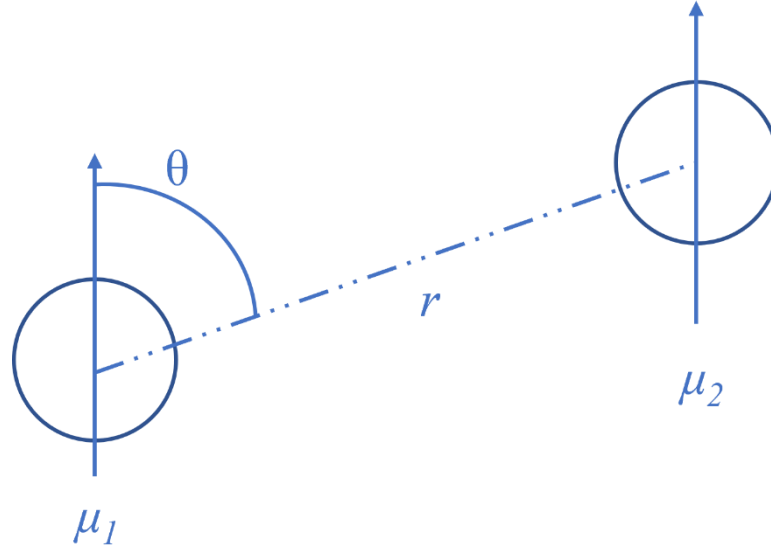
Figure 1.2: Two magnetic dipoles, μ_1 and μ_2 at a distance r interacting with one another.

Spins can be thought of as magnets, and a system constructed of two spins can be thought of as containing two magnetic dipoles, μ_1 and μ_2, separated by a distance r and having an energy E given by:

$$E = \frac{\mu_0}{4\pi r^3}\left[\mu_1 \cdot \mu_2 - \frac{3}{r^2}(\mu_1 \cdot r)(\mu_2 \cdot r)\right], \qquad (1.4)$$

with μ_0 the vacuum permeability. It can be noted that the energy is inversely proportional to the cube of the distance r, the size of the magnetic moments and their relative alignment. For $\mu_1 \sim \mu_2 \sim 1\ \mu_B$, and for $r \sim 1$ Å, the energy is approximately 1 K in

temperature. Therefore, the magnetic interactions are too weak to account for magnetic ordering observed in most magnetic materials.[34] The magnetic dipolar interaction, however, becomes important for materials that order at sub-Kelvin temperatures.[34] The dipolar interaction D can be approximated by:

$$D = \frac{\mu_0 \mu_{\text{eff}}^2}{4\pi R_{\text{nn}}^3}, \tag{1.5}$$

with μ_{eff} the effective magnetic moment and R_{nn} the distance between two near-neighbouring magnetic moments.

1.3.2 Exchange Interactions

Long range magnetic order is most commonly caused by the so-called exchange interactions. Consider a system constructed of two electrons and possessing spatial coordinates r_1 and r_2, where the electron states can be represented by two wave functions, $\varphi_a(r_1)$ and $\varphi_b(r_2)$. The different types of interactions discussed here are **direct exchange** and **superexchange** interactions. Other types of interactions are possible, but these are not relevant in coordination polymers since these are typically insulating materials, with all the structures explored here containing cations with the same oxidation state.

1.3.2.1 Direct Exchange

Direct exchange occurs when electrons on neighbouring magnetic atoms interact with one another, without any intermediary needed. This interaction therefore occurs because of the overlap between two orbitals allowing for the direct coupling of their electrons. This interaction thus requires short distances between magnetic centres and it is very unlikely to happen for rare-earth *Ln* elements because of the strongly localised nature of the 4*f* orbitals, whose electron density does not extend far enough from the nucleus to allow for direct exchange interactions. Similarly, it is less likely to be

significant for $3d$ metals, particularly where these are well separated in coordination polymers, than the larger $4d$ and $5d$ metals whose orbitals are more diffuse.

1.3.2.2 Superexchange

Materials where there is no direct overlap of the orbitals of the magnetic cations, such as many functional ionic solids, can still exhibit magnetic order at sufficiently low temperatures. This is because the metallic species can indirectly interact with one another. For example, MnO, and MnF_2 show antiferromagnetic order, although there is no direct overlap between the orbitals of the Mn^{2+} cations. In this case, it is possible to observe **superexchange interactions**, where this is mediated by a non-magnetic ion placed between the two magnetic ions, as shown in Figure 1.3 for NiO. This mechanism can be easily understood by assuming that the metallic cation M^+ possesses one single unpaired electron, and this populates the same molecular orbital as the electron of the anionic species, e.g. O^{2-}, the molecular orbital arising from the overlap of the atomic orbitals of the two ions.[34] This is usually the dominant magnetic interaction in coordination polymers, where molecular anions are present leading to more complex polyatomic bridges,[35] including those discussed in this thesis.
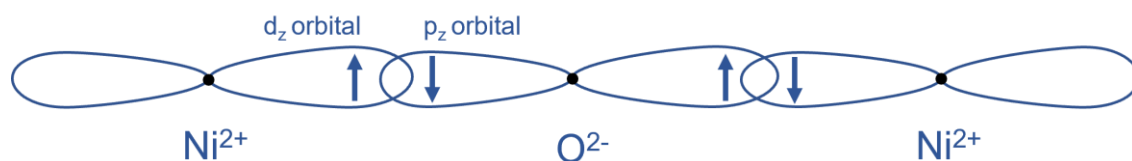
Figure 1.3: Depiction of superexchange interaction in NiO.

1.3.3 Antisymmetric Interactions

Coupling between magnetic species is also possible due to their spin-orbit interaction, which plays the role of an intermediary, similarly to oxygen in the superexchange interaction.[34] An ion with an excited state can be produced by the spin-orbit interactions and it can interact with the ground state of another ion, resulting

in the **anisotropic exchange interaction**, also known as **Dzyaloshinksy-Moriya interaction**. The Hamiltonian for the two interacting spins, S_1 and S_2 is given by:

$$\widehat{H}_{DM} = D \cdot S_1 \times S_2, \tag{1.7}$$

where D is a vector representing the direction and magnitude of the anisotropic interaction. The direction of D depends largely on the symmetry of the structure and the interaction tries to force the two spins to lie perpendicular to one another on a plane perpendicular to D itself. Therefore, the resulting effect of the anisotropic interaction is such that a slight rotation of the spins, *i.e.* **spin canting**, can be observed. Materials showing such an interaction are a great many, with typical examples being magnetite Fe_3O_4, manganese carbonate $MnCO_3$ and cobalt carbonate $CoCO_3$.[34]

1.4 Spins degrees of freedom: Heisenberg, XY and Ising models

When considering the magnetic interactions described above, the simplest approach is to assume that the spins can be oriented in any direction in space. In such a Heisenberg model, the spins have the greatest numbers of degrees of freedom, with a dimensionality $D = 3$, *i.e.* the spins are three-dimensional vectors. The Heisenberg model can be represented by the Hamiltonian:

$$\widehat{H} = -\sum_{<ij>} J\vec{S_i} \cdot \vec{S_j}, \tag{1.8}$$

where J is a constant, and i and j are nearest-neighbours.

Spins can also have smaller dimensionality, hence have fewer degrees of freedom. In the Ising model, spins can only point up or down. As a consequence, it is

only possible to consider one direction for these spins, conventionally the z direction. Therefore, eqn. 1.8 becomes:

$$\hat{H} = -\sum_{<ij>} J\overrightarrow{S_i^z} \cdot \overrightarrow{S_j^z}, \tag{1.9}$$

Finally, spins can be described according to the XY model, having a dimensionality $D = 2$, therefore being able to move on an easy plane.

The lattice on which these spins sit has a dimensionality d itself. An interesting situation can be observed when an isolated system consists of Ising spins ($D = 1$) sitting on a one-dimensional lattice ($d = 1$), such as in the case of one-dimensional magnetic chains. In such a system, it can be demonstrated that long-range magnetic order cannot exist for temperatures higher than 0 K, as the presence of even a single defect above this temperature leads to an infinite entropy gain. The entropy of the system can be described by $S = k_B \ln N$, where N is the number of positions available for the defect to occupy along the chain. For a very large chain, $N \rightarrow \infty$ and, given the free energy of the system is $F = H - TS$ (H denoting the enthalpy of the system and S its entropy), for any $T \neq 0$, this tends to $-\infty$.[34]

1.5 Ferromagnetism and Antiferromagnetism

Having discussed how the magnetic moments interact with one another and the models used to describe systems of spins, it is possible now to describe the different types of magnetic order than can be observed in a magnetic system. Magnetic order can be achieved below some critical temperature, where the thermal fluctuations are sufficiently low that the exchange interactions, J, between the spins overcome the thermal barrier and it is energetically favourable for the system to orient the spins in such a way that a specific low-energy configuration emerges from the paramagnetic state. This usually results in

some sort of alignment of the spins, as is the case for the two most common forms of magnetic order, ferromagnetism and antiferromagnetism.

1.5.1 Paramagnetism and the Curie-Weiss law

When materials experience an applied magnetic field H, a magnetic flux is induced in the sample, as given by

$$B = \mu_0 H + \mu_0 M, \tag{1.10}$$

where μ_0 is the permeability in free space and M is the internal magnetisation of the sample. The magnetisation of a material depends on how strongly it responds to an external field or how much it is "susceptible" to it. It is possible to define the magnetic susceptibility as:

$$\chi = \frac{\partial M}{\partial H}, \tag{1.11}$$

which describes the response of a material to the applied field and depends strongly on its temperature, as the thermal energy, $k_B T$, affects the interactions between the magnetic moments in a system. Based on χ, it is possible to classify materials into four common groups, as shown in Table 1.2.

Table 1.2: Magnetic susceptibilities for different magnetic behaviours.

Magnetic behaviour	χ (cm^3 mol^{-1})	χ trend with decreasing temperature
Diamagnetism	-8×10^{-6}	No trend
Paramagnetism	10^{-1}–10^{-3}	Increase
Ferromagnetism	5×10^3	Increase
Antiferromagnetism	0–10^{-2}	Decrease

Paramagnets are materials containing unpaired electrons, whose spins can be aligned parallel to an external magnetic field and a magnetisation can be induced.

Without an external magnetic field, the spins point in random directions because the thermal energy of the system is high enough to overcome any magnetic interactions between atoms. When a magnetic field is applied and the spins align, a positive magnetic susceptibility occurs. At sufficiently low temperatures in most systems, magnetic order can emerge, and the ordering temperature is known as the Curie temperature (T_C) or the Néel temperature (T_N), depending on whether the material exhibits ferromagnetic or antiferromagnetic order.

A system with perfectly isolated paramagnetic cations obeys the Curie Law, which states that the magnetic susceptibility is inversely proportional to the temperature, and is given by:

$$\chi = \frac{C}{T},$$
(1.12)

where C is the Curie constant and T is the temperature. However, because magnetic centres interact in paramagnets, a modified Curie law, the Curie-Weiss law, is instead obeyed:

$$\chi = \frac{C}{T - \theta_{CW}},$$
(1.13)

where θ_{CW} is known as the Curie-Weiss temperature and a measure of the strength of the interactions. This law is useful for the identification of ferromagnets and antiferromagnets. A positive θ_{CW} indicates that the dominant correlations within a material are ferromagnetic, whereas a negative value indicates those correlations are antiferromagnetic. For simple systems, θ_{CW} is close to T_C or T_N. When susceptibility measurements are carried out, as it will be explained in Section 3.5.1, it is possible to fit the inverse magnetic susceptibility $1/\chi$ and extract the values of C and θ_{CW}, as shown in equation 1.14:

$$\frac{1}{\chi} = \frac{C}{T - \theta_{\text{CW}}}. \tag{1.14}$$

It is possible to determine the observed effective magnetic moment from the Curie constant using the equation:

$$\mu_{\text{eff}} = \sqrt{\frac{3k_{\text{B}} \cdot C}{N_{\text{A}} \cdot \mu_{\text{B}}^2}}, \tag{1.15}$$

with k_{B} the Boltzmann constant, N_{A} is Avogadro's constant and μ_{B} the Bohr magneton.

The magnetic susceptibility of a material can also depend on the single-ion anisotropy of the magnetic cations, which arises from the interaction between the orbitals of a magnetic ion and the surrounding crystalline field, and that results from the quenching of the orbital moment due to this interaction. This includes lanthanides with orbital angular momentum since the small crystal field splitting of the generally well shielded $4f$ orbitals become significant at low temperatures were these effects become more relevant due to the stronger interactions with the $4f$ orbitals, partially quenching the orbital moment and therefore changing the magnetic behaviour of the metallic centres. This is an important point as it implies that the crystal field might strongly affect the susceptibility of a rare-earth-containing material while the interactions between magnetic centres might remain unaltered and also highlights the fact that data on the magnetic properties measured at lower temperatures are a better reflection of the behaviour of the magnetic centres and of the material. Single ion-anisotropy also leads to anisotropy of the magnetic susceptibility due to the fact that magnetic moments, in this case possessing a preferred orientation axis, will better respond to an external field when this is applied in certain directions rather than others, *i.e.* parallel or otherwise perpendicular to an easy axis of magnetisation which results from the single-ion anisotropy.

Some antiferromagnetic materials show significantly different values of transition temperature T_N and Curie-Weiss temperature. A dimensionless parameter known as the **frustration index** f_i, defined as the ratio between the two:

$$f_i = \frac{T_N}{\theta_{CW}}, \qquad (1.16)$$

provides an indication of magnetic frustration in a material, with those having $f > 10$ considered to be highly frustrated. In those cases where the extent of orbital angular momentum changes with temperature, the information provided by the frustration index must be considered tentatively due to the above considerations.

1.5.2 The Landau Model for Ferromagnetism

A ferromagnetic material exhibits spontaneous magnetisation in the absence of an applied magnetic field, with the magnetic moments aligned along the same unique direction and being parallel to each other, as shown in Figure 1.4. The first explanation of this phenomenon was provided by Weiss in 1907, with the introduction of a molecular field that explained the magnetic order.[10]

However, a more recent model for ferromagnetic materials was proposed by the Soviet physicist Lev Landau 1936, in which the concept of mean-field is introduced.[36] In his theory, Landau also describes the nature of the phase transition to a ferromagnetic ordered state, by first expressing the free energy F of the system with magnetisation M as a power series of M, hence:

$$F(M) = F_0 + a(T)M^2 + bM^4, \qquad (1.18)$$

where F_0 and b are positive constants and $a(T)$ is a temperature-dependent constant. A phase transition can occur when $a(T)$ changes sign at the transition temperature T_C, with $a(T)$ near the transition being:

$$a(T) = a_0(T - Tc), \tag{1.19}$$

with a_0 a positive constant.

By considering $\frac{\delta F}{\delta M} = 0$, it can be shown that the magnetisation M of the magnetic system can only be:

$$M = 0 \text{ or } M = \pm \left[\frac{a_0(T_C - T)}{2b} \right]^{\frac{1}{2}}, \tag{1.20}$$

with the second condition possible only for $T < T_C$, whereas the first condition is possible when $T > T_C$. The idea of "mean-field" proposed by Landau assumes all the spins are subject to the same average exchange field produced by all the neighbours, very similar to what Weiss had proposed almost 30 years before.
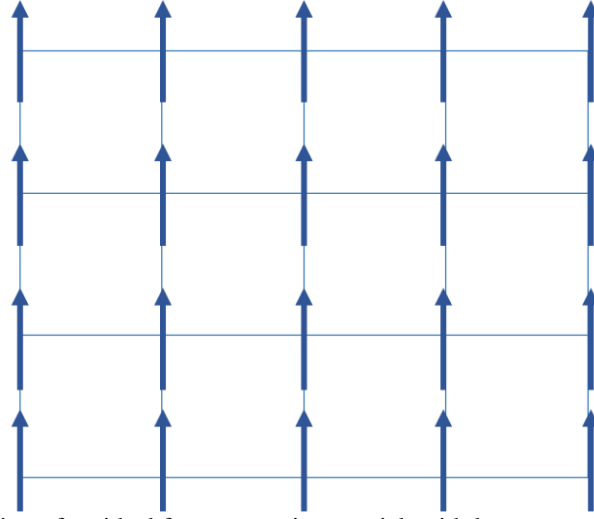
Figure 1.4: Representation of an ideal ferromagnetic material, with long-range order characterised by all the spins parallel and pointing towards the same direction.

1.5.3 Theory of Antiferromagnetism

When the exchange interaction J among the spins is negative, antiferromagnetic order is observed, with the spins oriented along the same direction, but being antiparallel to one another. It is possible to describe such a system by identifying two distinct sublattices possessing ferromagnetic order, one sublattice possessing all the spins

pointing up (the + sublattice) whilst the other contains all the spins pointing down (the − sublattice), and yielding an antiferromagnetic ordered state when these are combined, as shown in Figure 1.5.

$$M_+ \qquad\qquad M_- \qquad\qquad M = 0$$
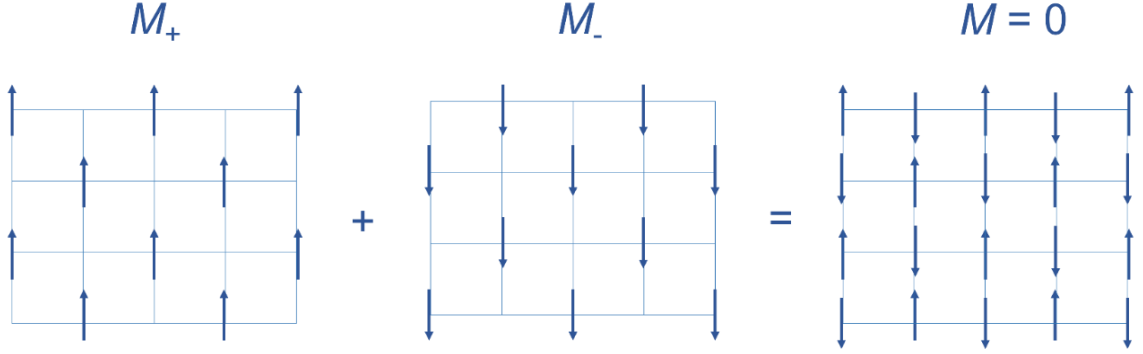
Figure 1.5: Representation of an ideal antiferromagnetic material, with long-range order characterised by all the spins anti-parallel to each other, while lying on the same direction. An antiferromagnetic lattice can be described as the combination of two sublattices possessing magnetisation M_+ and M_-.

Each individual sublattice can be described in terms of a molecular field dependent on the molecular field, as follows:

$$B_- = -|F_{\mathrm{mf}}|M_-,$$

$$B_+ = -|F_{\mathrm{mf}}|M_+, \tag{1.21}$$

where F_{mf} is the strength of the molecular field and $M_\pm$ the magnetisation of each sublattice. In a perfect antiferromagnet, these differ only in direction, hence:

$$|M_+| = |M_-| = M. \tag{1.22}$$

Therefore, the combination of the two sublattices will result in a zero net magnetisation.

The transition temperature for an antiferromagnet, known as the Néel temperature T_N can be expressed as:

$$T_N = \frac{g_j \mu_B (J+1)|F_{\mathrm{mf}}|M_s}{3k_B} = \frac{n|F_{\mathrm{mf}}|\mu_{\mathrm{eff}}^2}{2k_B}, \tag{1.23}$$

with μ_{eff} the effective magnetic moment of the system, M_s the saturation magnetisation — that is the maximum magnetisation exhibited by the system in high applied fields, and n is the number of magnetic atoms per unit volume.

Because the sum $M_+ + M_- = 0$ in a perfect antiferromagnet, it is often possible to use the difference $M_+ - M_-$, known as **staggered magnetisation**, which is non-zero for temperatures below T_N, as a parameter to describe an antiferromagnet.[34]

It is possible to find materials where the two lattices possess different number of cations or the cations possess different moments, which results in a **ferrimagnet**. In such a material, the spins of the two lattice, M_+ and M_- do not cancel out as in an ideal antiferromagnet, with the net result being that bulk properties resemble to that of a ferromagnet.

1.6 Competing interactions and frustrated magnetism

Let us now consider a system where spins are correlated antiferromagnetically, that is the exchange interaction among the sites, J_{ij}, is negative. While this interaction is easily satisfied when the spins sit on a square lattice, the opposite is true when some other geometries are considered. In such a situation, competitions arise among the spins, with the result that the interactions cannot all be satisfied simultaneously, leading to systems known as **frustrated magnets**.

The simplest example of such a system is the triangular Ising antiferromagnet, where spins sit on a triangular lattice, as shown in Figure 1.6.
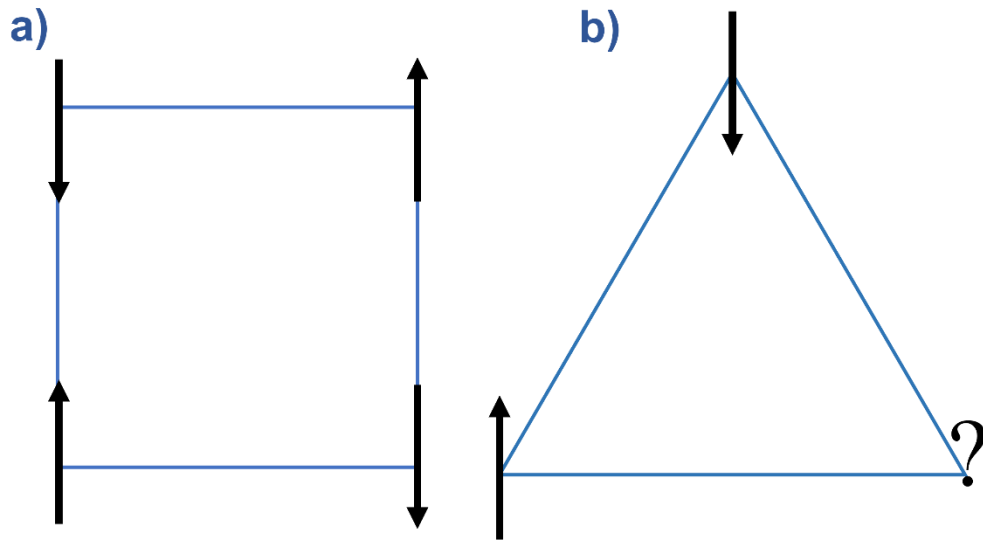
Figure 1.6: Antiferromagnetically coupled Ising spins sitting on a) a square lattice and b) a triangular lattice. In the latter case, it is not possible for all the spins to satisfy all the interactions simultaneously.

In this system, the energetically favourable correlation between the spins is an antiferromagnetic one, but the geometry of the system is such that two nearest neighbours compete for the same interaction to be satisfied and achieve the antiparallel alignment. This results in a frustrated ground state which is an average of many degenerate states. It is easy to understand that the competing interactions are somewhat dependant on the degrees of freedom possessed by the spins, with Ising spins possessing the lowest number of degrees of freedom. Indeed, if spins adopting a Heisenberg-like behaviour are populating the very same lattice, the frustration can be somewhat relieved, as shown in Figure 1.7. It should be noted that the triangle here is equilateral. When this is not the case, e.g. isosceles triangles constitute the lattice geometry, interactions are inequivalent and frustration can be relieved as well. When frustration arises purely due to the geometry of the lattice, the system is said to feature **geometric frustration**.
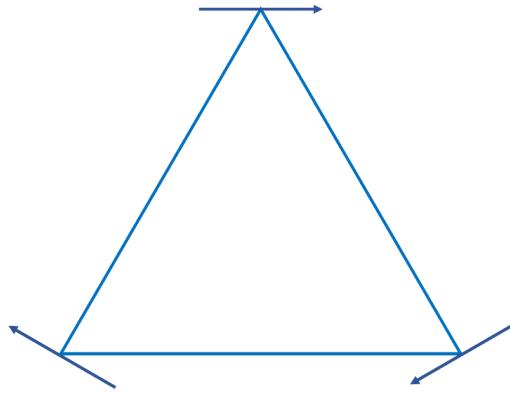
Figure 1.7: Antiferromagnetically coupled Heisenberg-like spins sitting on a triangular lattice. While it is not possible for all the spins to satisfy all the interactions simultaneously, the higher degrees of freedom allow for their orientation to change in such a way that frustration is relieved.

While this simple triangular lattice effectively conveys the idea of geometric frustration, it is possible for the triangles to be arranged in different ways according to the structure of the crystal. Indeed, when extending the discussion to the infinite structure of a material, the triangles might be arranged in an edge-sharing or vertex-sharing fashion in two dimensions, or even adopt three-dimensional arrangements. In an array of two-dimensional edge-sharing triangles each site belongs to six triangles, whereas for a two-dimensional corner-sharing lattice, each site belongs to two triangles at a time. In the last case, the lattice takes the name of **kagome** lattice, a reference to popular Japanese bamboo baskets (*kago*) with a woven pattern (*me*), shown in Figure 1.8 (b).[37]
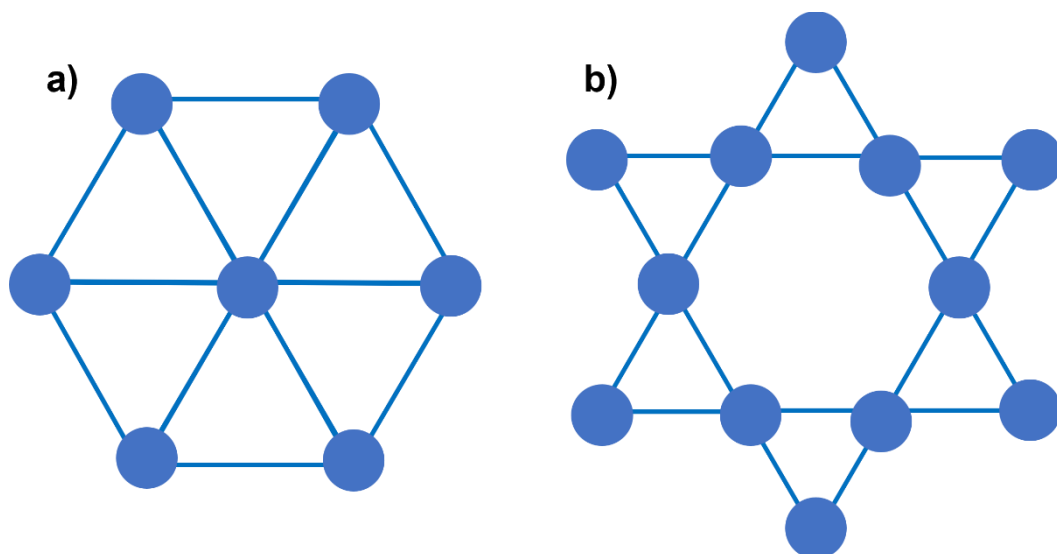
Figure 1.8: (a) Edge-sharing triangular lattice and (b) the Kagome lattice, consisting of vertex-sharing triangles.

The **pyrochlore** lattice is arguably the most well-studied example of a frustrated three-dimensional lattice, consisting of a network of vertex-sharing polyhedra, shown in Figure 1.9. $Dy_2Ti_2O_7$ and $Ho_2Ti_2O_7$ are some of the most studied pyrochlores, with their polyhedra of lanthanide magnetic cations acting as four ferromagnetically coupled Ising spins.[38] In these materials, the spins tend to adopt a specific orientation on the tetrahedral vertices following what is known as the "two-in, two-out" rule, with two of the spins pointing towards the center of the invididual tetrahedra and the remainder pointing outwards.[2] This is refered to as spin-ice behaviour since this is analogous to the behaviour of water ice phases, which exhibit two short (covalent) O-H bonds and two long (hydrogen-bonding) interactions. It should be noted that in the case of $Dy_2Ti_2O_7$ and $Ho_2Ti_2O_7$, the spins are actually ferromagnetically coupled. The frustration in this case is not caused by the coupling of the spins but rather by the strong local magnetic anisotropy due to the crystal field that forces the spins into their "two-in, two-out" orientation, rendering the interactions frustrated. This also leads to interesting properties, such as the existence of magnetic monopoles, which cannot exist in isolation.[39]
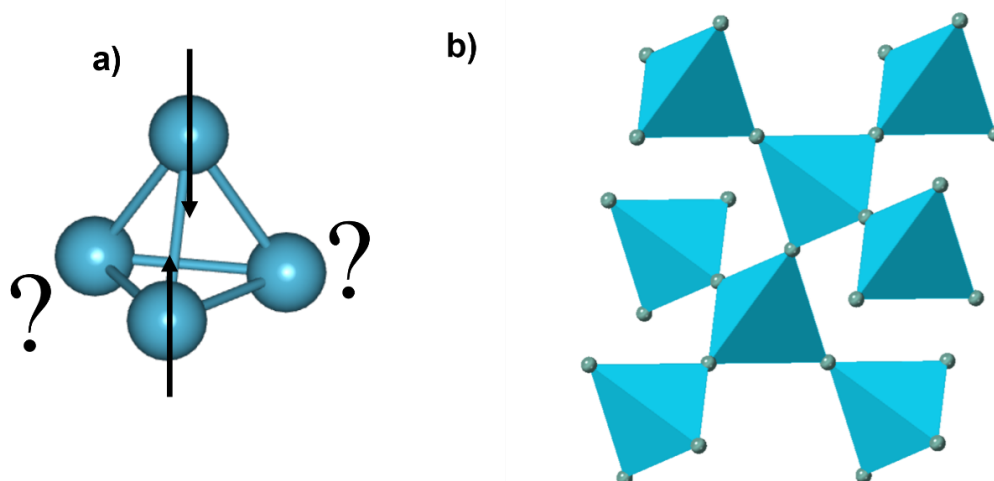
Figure 1.9: (a) Pyrochlore lattice, with magnetic ions sitting on the vertices of tetrahedra and (b) extending in three-dimensions in a corner-sharing fashion.

The spin-ice behaviour is one of the many possible in frustrated magnets, with others being that of spin-liquids and spin-glasses observable both in pyrochlore lattices as well as others. In a spin-glass, it is possible to cool the system down to a temperature where the material ceases to be paramagnetic with the spins freezing into random orientations resulting in a disordered structure. Spin-glasses are characterised by this "freezing" temperature, akin to the glass transition temperature. These systems have therefore a large number of equilibrium states, in analogy with glass, while not possessing a unique ordered structure. In contrast to spin-glasses, spin-liquids never freeze: it is possible to observe fluctuations of spins leading to disordered magnetic states down to temperatures close to absolute zero, implying they always present a dynamic disorder, despite strong magnetic interactions between their cations.

1.7 Low-dimensional magnetism

The exchange interactions between magnetic ions can be restricted to one or two dimensions, where magnetism is confined to low dimensional motifs, such as chains or sheets. Low-dimensional systems, particularly 1D systems, have attracted significant interest for the discovery of new phases of matter. Achieving them constitutes a challenge for materials such as oxides and salts because obtaining isolated low-dimensional motifs is required to prevent three-dimensional order from emerging, and these are usually incompatible with their typical close-packed structures. Some examples of one-dimensional magnets include perovskite ABX_3 materials, namely $CsNiF_3$ and $CsCuCl_3$, which show quasi-1D magnetic structures, where ferromagnetic interactions are strong along the direction of the chains, but with weaker antiferromagnetic coupling between the chains.[40,41] Another important example of 1D magnetism is found in Sr_3CuIrO_6 and Sr_3CuPtO_6, presenting 1D Heisenberg ferromagnetic and

antiferromagnetic magnetic structures, respectively.[42] It has been shown it is possible to tune the properties of the systems by altering the ratios of Ir and Pt, hence obtaining $Sr_3CuIr_{1-x}Pt_xO_6$ solid solutions, with an example of quantum spin-chain paramagnet reported for $Sr_3CuIr_{0.5}Pt_{0.5}O_6$.[42]

1.8 Magnetic coordination polymers

More recently, interest in coordination polymers, and dense MOFs , which feature polyatomic ligands linking their magnetic cations into extended frameworks, has grown significantly. The varied architectures of these materials allow for the design of structures that contain low-dimensional motifs, thanks to the ligands being able to impart strong structural anisotropy.[30,31,43] Thus, these materials depart from close-packed structures and host well isolated magnetic chains and sheets. Furthermore, it is possible to design structures featuring competing magnetic geometric frustration to further suppress the onset of long-range magnetic order. Examples of coordination polymers exhibiting 2D magnetism are metal malonates $Na_2M(mal)_2 \cdot 2H_2O$ (M = Mn, Fe, Co, Ni or Cu; mal = malonate) which feature 2D inorganic layers connected by the carboxylate groups of the malonate ligand,[44] and $Gd_2O(OH)_4(H_2O_2)$, also featuring a 2D structure, represented in Figure 1.10.[45] It is possible to find an example of one-dimensional magnetic coordination framework in copper hydroxide p-pyridinecarboxylate $Cu(OH)(C_5H_4NCO_2) \cdot H_2O$, shown in Figure 1.11, where edge-sharing CuO_4N chains propagate through its monoclinic $P2_1/n$ structure, and one-dimensional antiferromagnetic order is observed at $T_N \sim 51$ K.[46]
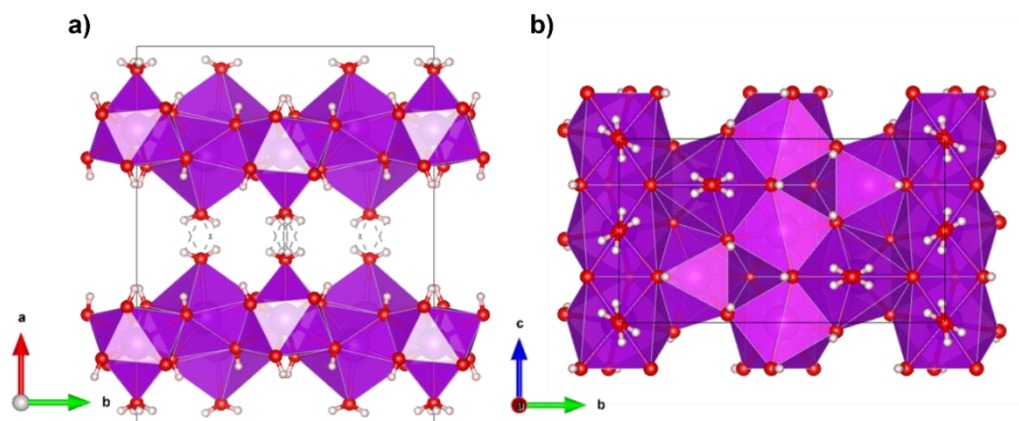
Figure 1.10: Crystal structure of $Gd_2O(OH)_4(H_2O)_2$ with (a) 2D layers stacking along the *a*-axis and (b) extending on two dimensions on the *cb*-plane.
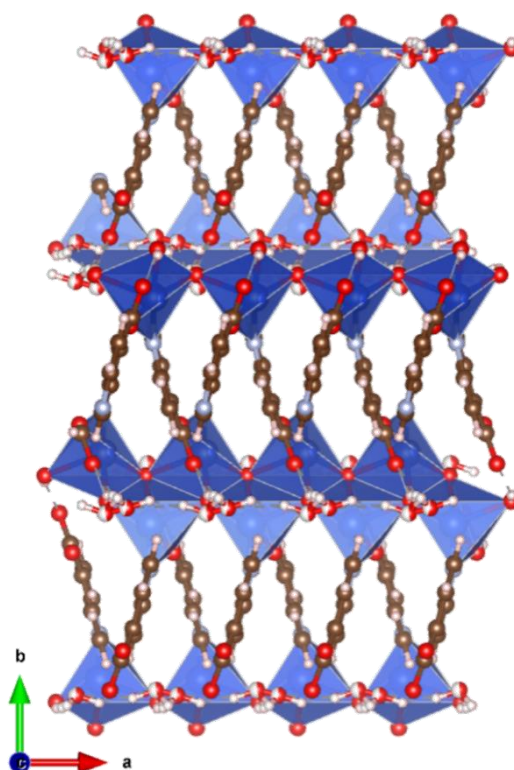
Figure 1.11: Crystal structure of $Cu(OH)(C_5H_4NCO_2)\cdot H_2O$ with zig-zag chains propagating along the *b*-axis.

An example of coordination polymers featuring geometric frustration is $Mn_2(OH)_2(sq)$ (sq = squarate), which features edge-sharing chains of MnO_6 octahedra and constitutes an example of a partially frustrated spin-ladder, where competing interactions are present, although the presence of inequivalent interactions allows for stronger interactions to prevail at sufficiently low temperature and reach a stable ground state.[47] $Co_3(OH)_2(sq)_2\cdot3H_2O$ is another example of a coordination polymer exhibiting

magnetic frustration, specifically in its CoO_6 ribbons.[48] Due to the Co cations forming isosceles triangles, the potential frustration is lowered, and the material does in fact order at sufficiently low temperatures.[48] $M(tca)_2$ (tca = tricyanamide) is a family of materials, based on stacked rows of triangles and featuring magnetic chains along the *a*-axis, that shows frustration, although 3D ordering is reached at sufficiently low temperatures.[49,50] Going from Mn to Fe to Cr as the metal incorporated in the structure, it was observed that intrachain interactions increase, reducing frustration. The examples shown above are far from exhaustive and the reader is referred to reviews on the topic for further details.[31,43,51,52]

1.9 The $Ln(HCO_2)_3$ family of coordination polymers

Of particular interest in the context of this work is the $Ln(HCO_2)_3$ family of dense coordination polymers. These materials adopt a rhombohedral *R*3*m* structure and feature LnO_9 face-sharing polyhedra forming infinite 1D-chains propagating along the *c*-axis. These chains are then linked together along the *ab*-plane via the formate ligands and leads to the formation of a triangular lattice structure.[53] $Gd(HCO_2)_3$ has been shown to be a very promising magnetocaloric material,[53] while $Tb(HCO_2)_3$ and $Ho(HCO_2)_3$ outperform the Gd analogue in lower field conditions above 4 K (a more widely used cryogenic temperature).[5] More will be discussed about the magnetocaloric properties of this material in the following chapter. For the time being, it is important to mention the exotic magnetic states found in this family, in particular $Tb(HCO_2)_3$ which constitutes an experimental realisation of a triangular ising ferromagnet (TIA), an exotic magnetic state, as first reported by Harcombe *et al.*[54] and that perfectly exemplifies the effect of the combination of magnetic frustration and one-dimensional magnetism.[54]

1.9.1 Tb(HCO₂)₃: magnetic properties and structure

In Tb(HCO$_2$)$_3$, strong diffuse features are observed between ~20 and 1.6 K in neutron diffraction patterns, with these indicating the presence of strong local interactions emerging from the intrachain and interchain correlations with Ising-like spins oriented along the chains.[51] At about 1.6 K, additional Bragg-like features are observed; these have been suggested to be caused by partial 1D long-range ferromagnetic order being achieved along the chains, while only short-range order is observed between the chains along the other dimensions due to frustrated antiferromagnetic interchain interactions, resulting in the TIA state.[51] A second transition is observed at 0.5 K, indicating a more complete order antiferromagnetic order is achieved.[51] Below this temperature, an emergent-charge ordered state (ECO) has been identified, which is an antiferromagnet in which the chains have different ordered magnetic moments that sum to the same value, found to be ±0.75 μ_B, around each triangle.[51]

The combination of 1D and frustrated magnetism in Tb(HCO$_2$)$_3$ have been identified as being the potential causes of the enhancement of its magnetocaloric properties at low temperatures;[5] with magnetic frustration suppressing long-range ordering down to low temperatures and the partial-long range order at 1.6 K, allowing for a prompt alignment of the spins along the direction of the magnetic field, enhancing the resulting magnetocaloric effect. Indeed, the evolution of the structure of Tb(HCO$_2$)$_3$ has been followed at 1.5 K in neutron diffraction experiments under applied fields from 0–3 T.[55] For an applied field of 0.1 T, the TIA state could be observed, with Bragg-like features having a full-width at half-maximum (FWHM) sharper than in previous zero-field elastic neutron scattering,[51] therefore suggesting the application of an external field contributes to more ordered chains in the lattice.[55] Increasing the field to 0.2 T causes the emergence of additional magnetic reflections, indicating a second simple

ferromagnetic state forms.[55] As the field increases further, the ferromagnetic phase becomes increasingly dominant while the TIA phase gradually decreases, until at 0.8 T, only the ferromagnetic phase exists.[55] The evolution of the magnetic structure of $Tb(HCO_2)_3$ under magnetic applied fields could therefore further constitute proof that the ferromagnetic chain align when small fields are applied and this could be a key factor in its optimised magnetocaloric performance for small field changes in comparison to $Gd(HCO_2)_3$.[55]
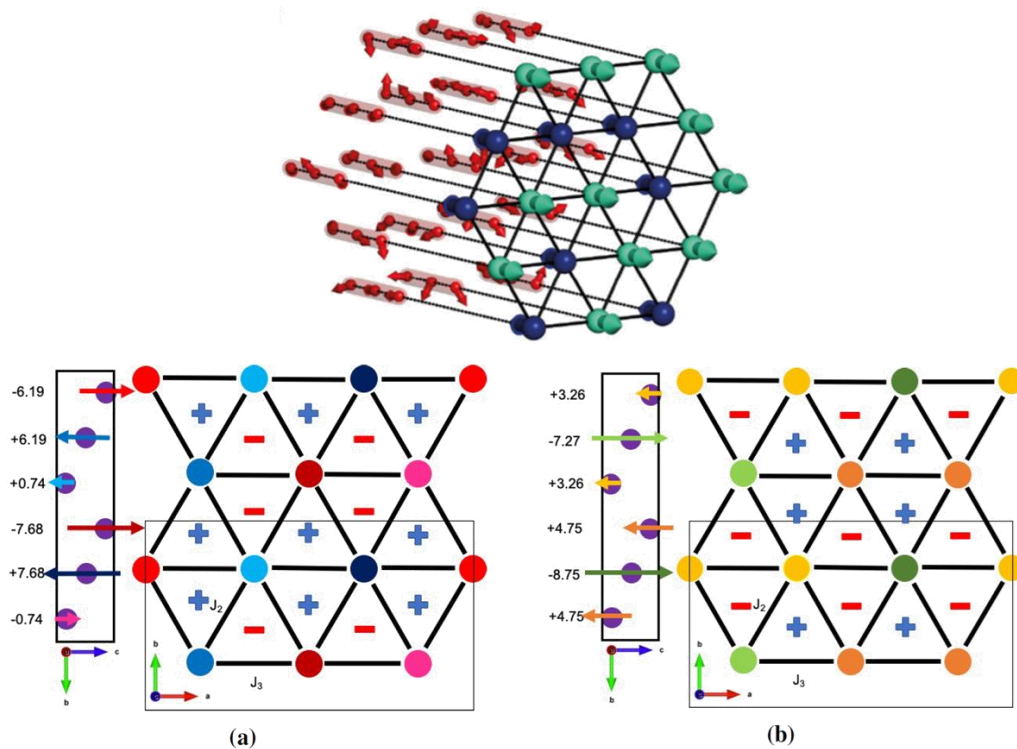
Figure 1.12: Fragment of the magnetic structure of $Tb(HCO_2)_3$ at 1.5 K when the TIA state is reached (top) and two possible average structure solutions of $Tb(HCO_2)_3$ at 0.28 K. Top: reprinted figure with permission from Daniel R. Harcombe *at al.*, Physical Review B, 94, 174429, 2016. Copyright 2016 by the American Physical Society.

1.9.2 Other *Ln*(HCO₂)₃ phases

Ln(HCO₂)₃ phases with a broader range of lanthanides have also been investigated. Members of this series with Ce to Er, at least, also adopt a rhombohedral *R*3*m* structure.[51] Magnetic property measurements down to 1.8 K indicate these materials remain paramagnetic and lack interesting magnetocaloric properties. Neutron diffraction studies of the Ce, Pr, Dy, Ho and Er members of this series all lacked any magnetic Bragg peaks

down to 1.5 K. Of these $Ln(HCO_2)_3$ phases, only $Ho(HCO_2)_3$ shows strong diffuse scattering below 10 K, which is similar in character to that observed for $Tb(HCO_2)_3$.[51] Analysis of the diffuse scattering via Reverse Monte-Carlo (RMC) fitting indicated that the spins are preferentially aligned along the directions of the chains and ferromagnetically coupled, with a strong Ising character.[51] Similar to $Tb(HCO_2)_3$, the intrachain and interchain correlations are ferromagnetic and antiferromagnetic respectively, although those in the Ho phase are significantly weaker.[51] $Ho(HCO_2)_3$ does not show an intermediate TIA state but transitions directly into an ECO state at ~0.7 K.[56] The weaker magnetic interactions in $Ho(HCO_2)_3$ might explain both why it shows diffuse scattering only below 10 K and why it is a worse magnetocaloric material than $Tb(HCO_2)_3$.[51]

As opposed to the Tb and Ho analogues, the isostructural $Er(HCO_2)_3$ does not show any indication of long- or short-range magnetic order down to 0.4 K from magnetic susceptibility and magnetisation measurements, the latter indicating the spins in this system have Ising-like behaviour.[56] However, upon cooling down to 50 mK, the emergence of additional weak reflections has been observed, and these were attributed to the onset of long-range order.[56] The observed
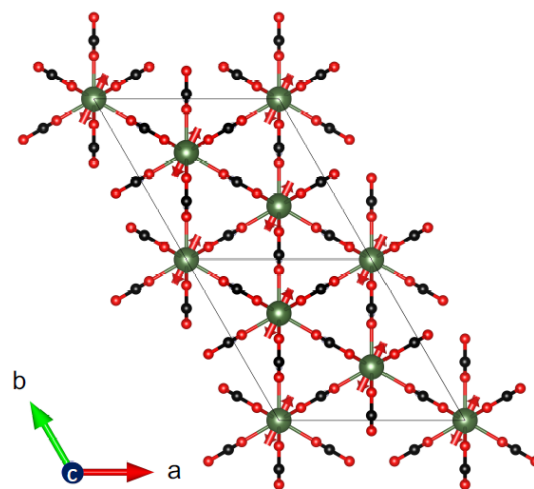
Figure 1.13: Antiferromagnetic structure of $Er(DCO_2)_3$ at 50 mK. Erbium shown in green, oxygen in red and carbon shown in black. Reproduced from R.J.C Dixey Doctoral Thesis.[51]

magnetic structure, shown in Figure 1.13 for $Er(DCO_2)_3$, indicates $Er(HCO_2)_3$ features intrachain antiferromagnetic coupling in direct contrast with $Tb(HCO_2)_3$ and

Ho(HCO$_2$)$_3$.[56] In the Er(HCO$_2$)$_3$ chains, the magnetic moment lies along the [0.720,−0.217,0.00] vector, close to the [1, 0, 0] axis.[56]

2. Overview of Magnetocaloric Coordination Polymers for Low-temperature Cooling

2.1 Introduction

2.1.1 Conventional Refrigeration and the Alternative of Solid-State Caloric Materials

In the past three decades, combating climate change has become a major challenge, which requires a decrease in energy consumption and a reduction of environmentally harmful greenhouse gas emissions. The International Institute of Refrigeration (IIR) estimates that, as of 2019, there are approximately 5 billion refrigeration, air conditioning and heat pump units worldwide that contribute to climate change, with 63% of this contribution being indirect due to the energy consumption required to power these and around 37% being directly caused by leakage of refrigerant gases e.g. fluorinated molecules.[57] With refrigeration becoming increasingly important both in our daily lives, as well as for more specific applications such as in the food industry and transportation,[58] medicine and science,[59,60] it is vital to find alternatives to traditional gas compression\expansion refrigeration technologies,[29] for which, in general, energy efficiencies are typically limited to a maximum of 40–50% of the theoretical

Carnot efficiency;[61] This limitation is often determined by mechanical inefficiences of the components for the refrigerating device, such as the compressor. [61]

Solid-state caloric materials are an alternative for gas-based refrigeration technologies with the advantage of avoiding emissions of environmentally harmful and/or non-renewable refrigerant gases. Furthermore, the predicted cooling efficiency for some of these materials is higher than that of traditional gas cooling devices, with above 60% of Carnot efficiency attained by some prototypes.[62] It is possible to identify four main classes of caloric materials for refrigeration applications, as shown in Figure 2.1, which differ from one another depending on the stimuli that drive their caloric effects, *i.e.* their heating and cooling processes. These are namely barocalorics, elastocalorics, electrocalorics and, finally, magnetocalorics, on which this dissertation focuses (see Figure 2.1). In all cases, the cooling step typically occurs *via* an entropically driven process when the applied stimulus is removed. Electrocaloric materials are solids exhibiting the electrocaloric effect (ECE), where adiabatic depolarization upon the application and subsequent removal of an external electric field results in a temperature change of the material.[63] Polymeric materials such as the copolymer polyvinylidene fluoride-tetrafluoroethylene (PVDF-TFE) have shown to be promising candidates for electrocaloric applications,[64] along with Rochelle salt ($KNaC_4H_4O_6 \cdot 4H_2O$),[65] $KTaO_3$,[66] $BaTiO_3$ and $SrTiO_3$,[67,68] and NH_4HSO_4.[69] It is also possible to achieve cooling with the application of mechanical stress or pressure when elastocaloric or barocaloric (BCE) materials are used. In materials exhibiting the elastocaloric effect (eCE), the change in temperature is caused by the uniaxial stress-induced Martensitic phase transformation process, which is a displacive transformation occurring due to shifts of atoms without long-range diffusion in the structure. Application of mechanical stress decreases the

entropy of the material and releases latent heat, with this reversed when the mechanical

stress is removed, therefore enabling the material to absorb heat from its surroundings.[70]
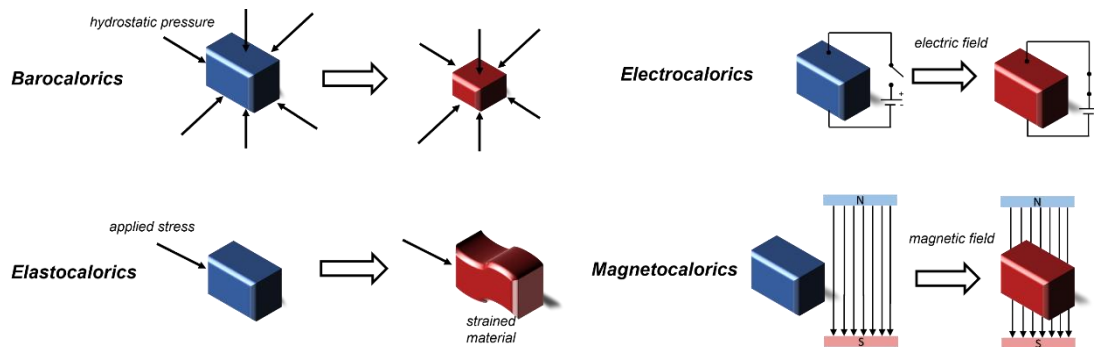
Figure 2.1: Different types of caloric materials and the stimuli responsible for their caloric effects.

Elastocaloric materials include phases such as alloys, including Ni-Ti and Cu-Zn-Al,[71]

alongside Cu-, Fe- and Ni-Ti-based superelastic alloys, which completely recover their

original shape after an applied stress is removed without any need for treatment, e.g.

annealing.[72] Barocalorics materials exhibit a thermal response due to isotropic

compression from hydrostatic pressure, typically associated with a concurrent first-order

phase transition.[73] The BCE has been identified in many materials,[74–76] including

elastomeric polymers,[77,78] including natural rubber,[79,80] plastic crystals[81] and magnetic

memory shape alloys,[82] and coordination polymers, particularly inorganic-organic

perovskites that have shown the so-called giant barocaloric effect, including

$[TPrA][Mn(dca)_3]$,[83,84] $[(CH_3CH_2CH_2)_4N]Cd[N(CN)_2]_3$ $([TPrA]Cd[dca]_3)$[85]   and

$[(CH_3)_4N]Mn[N_3]_3$.[86]

The final category of caloric solids are magnetocalorics, which were first

discovered by Weiss and Picard in 1917.[87,88] The magnetocaloric effect (MCE) is driven

by the application and removal of an externally applied magnetic field. Many

magnetocalorics show promising magnetocaloric properties, with some prototype

devices developed for applications such as domestic refrigeration and air-conditioning,[89]

and as established candidates for subkelvin cooling with predicted energy efficiencies

higher than 60% of the Carnot cycle.[90,91] The so-called giant MCE (GMCE) is associated with first-order magneto-structural transitions that enable significantly higher magnetocaloric effects than conventional MCE materials near ambient temperatures and modest applied magnetic fields, enabling their use in near ambient temperature applications. This term was first coined for $Gd_5Si_2Ge_2$ which showed a magnetic entropy change of nearly 15 J kg^{-1} K^{-1} for a 2-0 T field change, double that of the best near ambient temperature magnetocalorics then known.[92] Conversely magnetocalorics for low temperature cooling rely on gradual field-induced magnetic ordering of paramagnetic spins. [91,92]

Amongst caloric materials, magnetocalorics are particularly promising and thermodynamically efficient candidates for low temperature cooling applications. Cryogenic cooling has become increasingly relevant recently for technologies that are dependent on cooling to low- and ultra-low temperatures such as hydrogen liquefaction,[93] quantum computing,[7] spintronics[4], medical imaging,[59] and high-performance infrared sensing.[94] Liquid cryogenics are conventionally used for this purpose, with liquid helium vital for reaching temperatures below the boiling point of liquid nitrogen (77 K), including the millikelvin regime. In particular, ^{4}He can reach 2 K, while mixtures of ^{4}He with ^{3}He can be used in dilution refrigerators to reach temperatures below 0.1 K. With liquid helium becoming an increasingly scarce and expensive resource, it is essential to find alternatives suitable for low-temperature cryogenic cooling.[95] In magnetocalorics used at low temperatures, application of an externally applied magnetic field induces a transition from a disordered paramagnetic state to an ordered magnetic state; the orientation of the magnetic moments along the direction of the field in magnetocaloric materials leads to a temperature change, ΔT_{ad}, in an adiabatic process. Heat can then be removed from the system whilst keeping the spins aligned with the magnetic field under

isothermal conditions. In a subsequent step, removing the magnetic field under adiabatic conditions will result in the material cooling down due to the disordering of the spins, *i.e.* an increase in entropy occurs. Due to this final temperature change, which results in the material having a lower temperature than its initial state, the material can then be used as a heat sink for cooling utilising the magnetic refrigeration process (see Figure 2.2). The biggest accomplishment of magnetic refrigeration lies in the fact that the cooling process does not rely on the use of gases, therefore no refrigerant leakage or CO_2 emission is possible, resulting in a renewable and much more environmentally sustainable process.
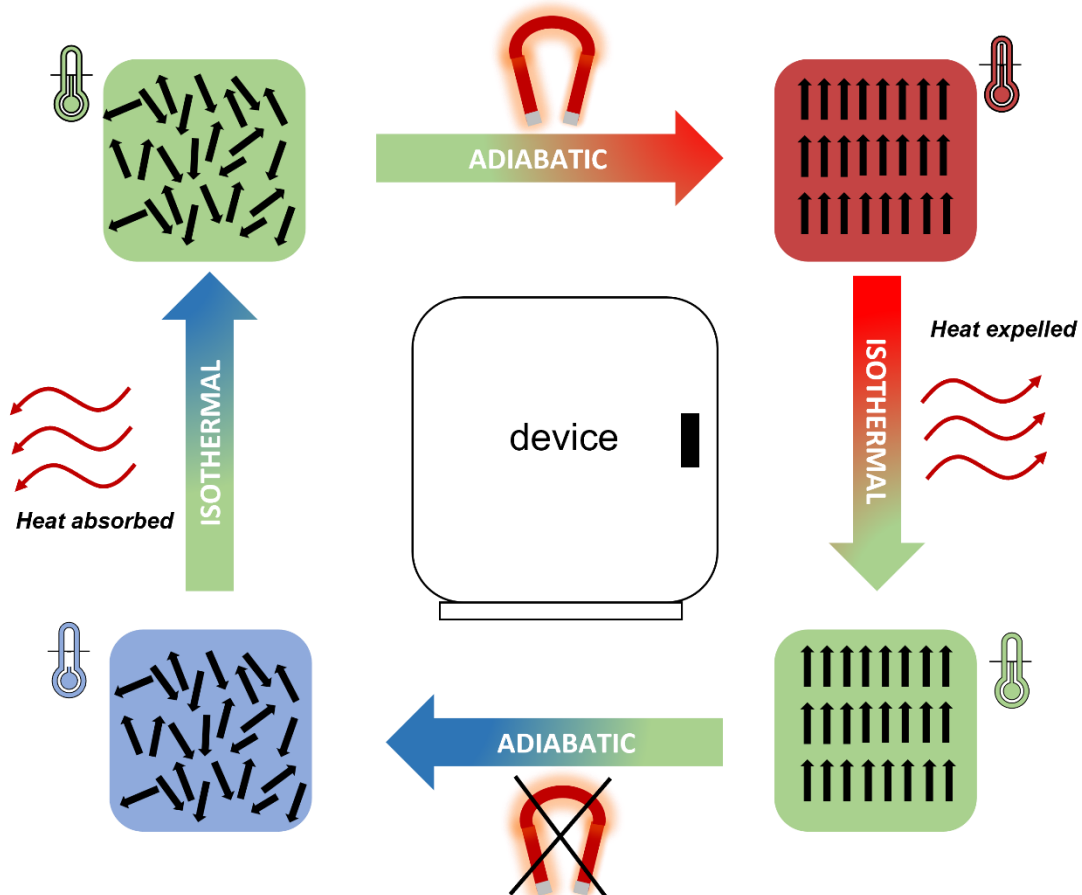
Figure 2.2: Scheme of the magnetic refrigeration cycle of a magnetocaloric material.

2.1.2 Theory and Measurement of the Magnetocaloric Effect

The MCE is an intrinsic property of all magnetic materials,[96] and parameters are necessary to classify them.[97] More will be said in Section 3.5.2 about how to measure the magnetocaloric properties of MCE materials and how the methods were used in this work, but it is necessary to provide a brief introduction to these here.

The most commonly reported parameter in literature is the maximum magnetic entropy change, $-\Delta S_m^{max}$ (where the negative sign stems from the entropy conventionally decreasing when the field is applied) for a given applied magnetic field change, typically reported with respect to the mass of the material in J kg^{-1} K^{-1}. A second parameter, the volumetric entropy change, is easily obtained by considering the product between the former and the density of the material ($-\Delta S_m^{max} \times \rho$) and is reported in mJ cm^{-3} K^{-1}. The magnetic entropy change can be determined from either direct or indirect measurements. In the former case, the total heat capacity C_T of the material is measured, with this being the result of electronic C_e, lattice C_l and magnetic C_m contributions. Therefore, it is necessary to isolate the magnetic contribution, C_m to determine the magnetic entropy change ΔS_m, the relationship between the two given by $\Delta S_m = \int (C_m/T)\mathrm{d}T$. Indirect measurement of ΔS_m requires determining the isothermal magnetisation of a material and applying the Maxwell relation, $\Delta S_m(T,\Delta H) = \int [\delta M(T,H)/\delta T]_H \mathrm{d}H$, therefore requiring measurements to be carried out as a function of temperature for a variety of magnetic fields.

It is also possible to utilise the Clausius-Clapeyron method as an indirect method for calculating ΔS_m for magnetocalorics that rely on first order transitions, as is the case for "giant" magnetocalorics, such as Gd$_5$Si$_2$Ge$_2$.[98] However, this is generally not relevant for magnetocalorics for low temperature applications, due to these relying more on

gradual changes in applied field.[99] A third parameter, the aforementioned adiabatic temperature change, ΔT_{ad}, is a more direct measure of the MCE. Nevertheless, this parameter is less well characterised for most new magnetocalorics as determining ΔT_{ad} requires a detailed understanding of how the heat capacity changes as a function of temperature and applied field and this is also free from detrimental kinetic effects that might occur during the removal of the applied magnetic fields.[99] The need for this additional information often limits the calculation of ΔT_{ad} for new materials, whose magnetocaloric effect parameters are instead assessed by indirect measurements.

The maximum entropy change $-\Delta S_m^{max}$ that can be theoretically extracted from a material is given by nRln(2J+1), where R is the universal gas constant, n the number of unpaired spins and J the total angular momentum.[100] Increasing the magnetic moment is thus essential to increase the maximum realisable $-\Delta S_m^{max}$, as well as minimising the diamagnetic components of the material, such as non-magnetic cations and coordinating ligands, which negatively affect the entropy change with respect to its weight and volume. As a non-zero orbital angular momentum might result in zero-field splitting (ZFS) effects, which are responsible for splitting the ground state energy level which lowers the magnetic entropy change, most magnetocaloric materials studied have negligible orbital momentum. Thus, their maximum expected entropy corresponds to nRln(2S+1), and it is therefore entirely dependent on the magnetic degrees of freedom, as expressed by the term (2S+1), the spin multiplicity. Therefore, when choosing an appropriate metal for the fabrication of magnetocaloric materials, gadolinium is considered the best candidate, as the 4f orbitals of the Gd^{3+} cation are exactly half-filled, resulting in a total spin quantum number of $S = 7/2$, and due to it being strongly isotropic, *i.e.* it possesses zero orbital angular momentum and its magnetism is determined only by its spins, eliminating any ZFS effects. As a result, considerable effort has been put into

the design and characterization of gadolinium-based materials with oxides such as gadolinium gallium garnet $Gd_3Ga_5O_{12}$ (GGG) and the iron-substituted derivatives $Gd_3(Ga_{1-x}Fe_x)_5O_{12}$ (GGIG) well established as candidates for low-temperature cooling, superseding traditional metal salts due to the higher $-\Delta S_m^{max}$, which stems from the higher density of magnetic cations in these oxides.[30]

More recently, molecule-based magnetic materials have been proposed for low- and ultra-low temperature cooling applications.[30] Molecule-based materials can adopt a wide variety of structures that are not easily obtained with traditional oxides due to the tendency of these to adopt close-packed structures. This, combined with their lack of significant intermolecular magnetic interactions, enables these molecule-based magnetocalorics to be used at lower temperatures. However, research on these materials has recently lost traction as their $-\Delta S_m^{max}$ with respect to their weight and, particularly, volume, is limited due to the need to use large ligands for the fabrication of their structures.[30,101]

2.1.3 Beyond Conventional Materials: Coordination Polymers

In contrast to discrete complexes and metal oxides, there has recently been significant interest in dense coordination polymers, including Metal-Organic Frameworks (MOFs), as potential magnetocaloric materials.[30,102–104] IUPAC provisionally defines coordination polymers as a coordination compound continuously extending in 1, 2 or 3 dimensions through coordination bonds.[105] While according to IUPAC the definition of coordination bond is a covalent bond where two of the electrons taking part to the bond come from the same chemical entity, as the IUPAC definition itself acknowledges, the term "coordination" is also used with a wider connotation, generally to define the ligands surrounding a metal centre regardless of whether the

character of the bond is covalent or ionic. With this in mind, and with the balance of covalent and ionic bonds being difficult to clearly discern for many materials, in this context the term coordination polymers is used to describe any extended structure in which metals are linked by polyatomic ligands. The focus on polyatomic ligands is to avoid considering those more well-known compounds with monodentate ligands that would be generally considered salts, e.g. oxides or halides. In doing so we acknowledge this restriction is somewhat arbitrary and some of the materials reviewed here will likely possess predominantly ionic bonds and that some of the materials included may be considered by others to simply be salts. The varied structural topologies of coordination polymers offer more freedom in the tuning of their magnetic properties than is commonly found in oxides due to the structure-directing effect of their polyatomic ligands leading to a variety of structures rather than the close packed arrays typically adopted by simple salts.[43]

The variety of structures accessible with coordination polymers makes it possible to design three-dimensional structures containing low-dimensional motifs, such as one-vdimensional magnetic chains or two-dimensional magnetic sheets, *via* the structure-directing effect of the ligand.[30,43] When these structural motifs are well isolated from one another structures with a higher density of magnetic cations with long-range order occurring at very low temperatures can be realised due to the resulting weak interactions between these units. In addition to this, it is possible to design structures featuring competing magnetic interactions due to the arrangement of the cations in the crystal lattice, called geometric frustration,[106] to further suppress the onset of long-range magnetic order to much lower temperatures and, therefore, allow for an even higher density of magnetic cations in the structure. Typically, this occurs in structures containing triangular motifs, such as those discussed in Chapter 1, responsible for the competition

of antiferromagnetic interactions, such as the two-dimensional triangular or Kagome lattices,[106,107] as well as pyrochlore structures,[106] such as that of $Gd_2Ti_2O_7$.[108] While conventional materials can exhibit geometric frustration, GGG being a classic example,[109] coordination polymers expand the scope for this through the plethora of topologies they can adopt. Coordination polymers showing low dimensional units and/or magnetic frustration have been suggested to be excellent candidates for low-temperature cooling, highlighting that attention to the structural characteristics of materials plays a key role in the optimisation of their MCE. The combination of lower ordering temperatures in coordination polymers compared to metal oxides, which enables them to remain useful magnetocalorics at lower temperatures, and higher density of magnetic cations than is possible in molecular complexes, greatly enhances their $-\Delta S_m^{max}$ as a function of weight and volume, making them very promising candidates as magnetocalorics materials.[30] Furthermore, many coordination polymers have already been reported to have greater $-\Delta S_m^{max}$ than the benchmark oxide materials, such as GGG.[30]

The coordination polymers and dense MOFs with the highest $-\Delta S_m^{max}$, approximately 40 J kg^{-1} K^{-1} or higher for large field changes, tend to be found amongst materials with either purely inorganic (in which there are no C-H bonds) or carboxylate ligands. The majority of the magnetocaloric coordination polymers studied to date incorporate only lanthanides, primarily Gd^{3+}, as their magnetic centres, although there has been recent interest in a handful of systems that feature both $3d$ and $4f$ metals as a future potential route to enhancing their magnetocaloric properties. This was seen previously in molecular magnetocalorics where the combination of the high number of unpaired spins in lanthanide cations and the stronger interactions in $3d$ would ideally improve the correlations among the metal-centres.[30] In this chapter, we will discuss the

most promising magnetocalorics coordination polymers and dense MOFs known to date across these categories.

2.2 Coordination Polymers Containing Inorganic Ligands

Coordination polymers with inorganic ligands are attractive as their smaller polyatomic anions typically allow denser packing of their magnetic cations than systems with larger organic ligands, thus increasing the magnetocaloric entropy change as a function of volume. Among inorganic coordination polymers, $GdPO_4$ has attracted significant interest for having a higher $-\Delta S_m^{max}$ than the GGG benchmark material.[110] At room temperature, this material adopts a monoclinic $P2_1/n$ structure in which the nine-coordinate Gd^{3+} node is bound to four oxygens from the distorted tetrahedral phosphate groups (see Figure 2.3), with an average Gd-O distance of 2.47 Å, and linked together in a chain-like fashion.[111] The reported magnetic entropy change, $-\Delta S_m^{max}$, for this material is 62.0 J kg^{-1} K^{-1} (376 mJ cm^{-3} K^{-1}) at 2.1 K and an applied field change of 7 T, higher than that of the benchmark material, GGG, under the same conditions.[30,110] The magnetic properties, including the MCE, of this material are largely attributed to the high density of Gd^{3+} cations in the structure, coupled with the presence of weak magnetic interactions and the low magnetocrystalline anisotropy, allowing for magnetic order to appear only below 60 mK as a dipolar antiferromagnet. [110]
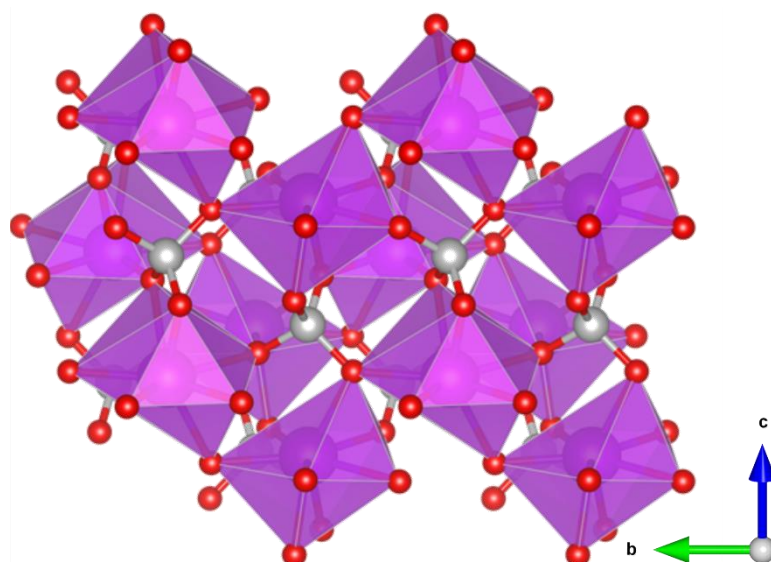
Figure 2.3: Crystal structure of $GdPO_4$. The GdO_9 polyhedra are bridged by the tetrahedral phosphate groups. Colour codes: Gd: purple, P: grey, O: red.

More recently, a $Gd(OH)SO_4$ coordination polymer has been synthesised and has been shown to exhibit a $-\Delta S_m^{max}$ comparable to that of GGG.[112] This material crystallises in a monoclinic $P2_1/n$ structure with the asymmetric unit consisting of one Gd^{3+} cation, one sulfate ion and a single hydroxide anion. The Gd cations are nine-coordinate and form a capped square antiprism coordination geometry, with six oxygens from the SO_4^{2-} ligands, with two of the sulfate oxygens being μ_2-bridging, and three oxygens from three OH^- anions, this being μ_3-bridging.[113] The Gd^{3+} cations are connected to form 1D-chains along the *a*-axis, and these further extend *via* hydroxy oxygens the *bc* direction to form a three-dimensional framework (see Figure 2.4).[113]

The magnetic coupling is negligible in this material with a Curie-Weiss temperature, θ_{CW}, of about -0.2 K which indicates the presence of weak antiferromagnetic interactions. The magnetic entropy change, $-\Delta S_m$, of this material was extracted from magnetisation data using the Maxwell relation, with a $-\Delta S_m^{max}$ value of 53.5 J kg^{-1} K^{-1} (276 mJ cm^{-3} K^{-1}) obtained at 2 K and for a 7 T field change, demonstrating a higher gravimetric $-\Delta S_m^{max}$ than GGG, but a comparable volumetric $-\Delta S_m^{max}$ to the benchmark material.[30,114]
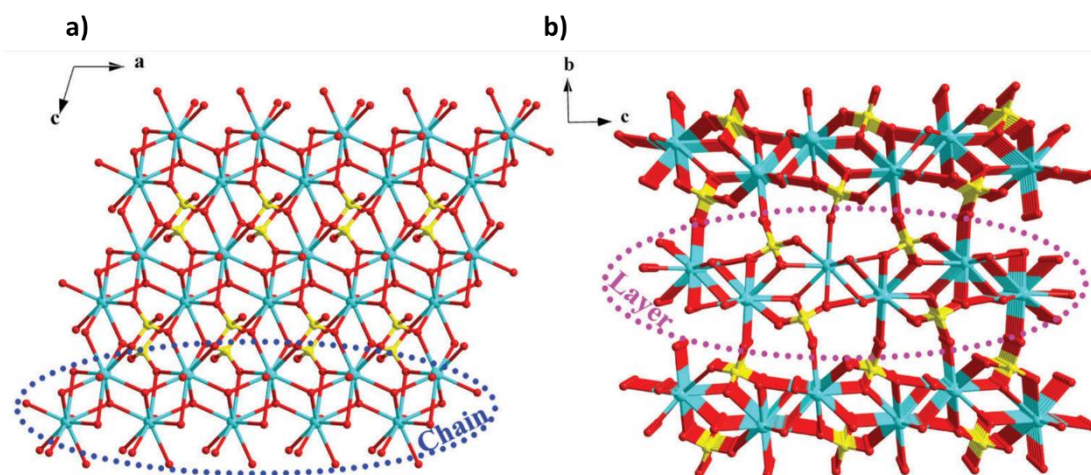
Figure 2.4: a) Crystal structure of Gd(OH)SO$_4$, with one-dimensional chains propagating along the *a*-axis and forming layers along the *ac*-plane, (b) with the latter stacking along the *b*-axis. Colour codes: Gd: cyan, O: red, S: yellow. The hydrogen atoms have omitted for clarity. Reproduced from *Mater. Chem. Front.*, 2018, 2, 2327–2332. with permission from the Chinese Chemical Society (CCS), Institute of Chemistry of Chinese Academy of Sciences (IC) and Royal Society of Chemistry.

Another family of coordination polymers, the lanthanide orthoborates *Ln*BO$_3$ (Ln= Gd, Tb, Dy, Ho, Er, Yb), have proven to be viable magnetocalorics for liquid helium temperature regimes at both high and low applied magnetic fields.[115] These materials adopt a monoclinic *C*2/*c* structure with triangular layers of *Ln*$^{3+}$ cations separated by sheets of three-membered rings of corner sharing BO$_4$$^{5-}$ tetrahedra that form isolated B$_3$O$_9$$^{9-}$ units.[115] While the existence of antiferromagnetic interactions within triangular layers suggest the possibility of geometric frustration, the monoclinic symmetry results in the triangles being scalene and the difference in *Ln-Ln* distances within different triangles make this less likely than in higher symmetry systems.[116,117] Consistent with this, it was found that GdBO$_3$ has a low frustration index $f = 3.1$ and, although the Er and Dy analogues possess $f > 10$, consistent with highly frustrated systems, it cannot be ruled out that this difference is partly due to effects such as lattice distortions on θ_{CW}.[115] In GdBO$_3$, the average in-plane Gd-Gd distance is 3.84 Å, while the average interplanar distance is 4.52 Å. The maximum magnetic entropy change, $-\Delta S_m^{max}$, for this material is found to be 57.8 J kg^{-1} K^{-1} (366 mJ cm^{-3} K^{-1}) for a field change of 9 T at 2 K.[115] While this value is higher than the benchmark material, GGG,

under the same conditions, the high magnetic field strength would limit its application to where superconducting magnets are employed. For a 2 T field change, $-\Delta S_m^{max}$ drops significantly, reaching values below 10 J kg^{-1} K^{-1} (about 60 mJ cm^{-3} K^{-1}) at 2 K. Amongst other members of the LnBO$_3$ series, it is worth noting that DyBO$_3$ has been shown to outperform the Gd analogue at lower applied fields, with a $-\Delta S_m^{max}$ of 13.9 J kg^{-1} K^{-1} (92.5 mJ cm^{-3} K^{-1}) for a field change of 2 T at 2 K.

Among inorganic coordination polymers, the LnOHCO$_3$ frameworks (Ln = Gd^{3+}, Tb^{3+}, Dy^{3+}, Ho^{3+}, and Er^{3+}) have the highest $-\Delta S_m^{max}$ as a function of weight. Work on these compounds started with GdOHCO$_3$,[118,119] which adopts an orthorhombic $P2_12_12_1$ structure in which the Gd^{3+} cation is 10-coordinate, binding to five carbonate anions, three in a chelating fashion, and two hydroxide groups. These polyhedra connect in a face-sharing fashion to form zig-zag chains with short 3.82 Å Gd-Gd contacts that are packed in a dense and distorted triangular lattice with edge-sharing connectivity. (see Figure 2.5).
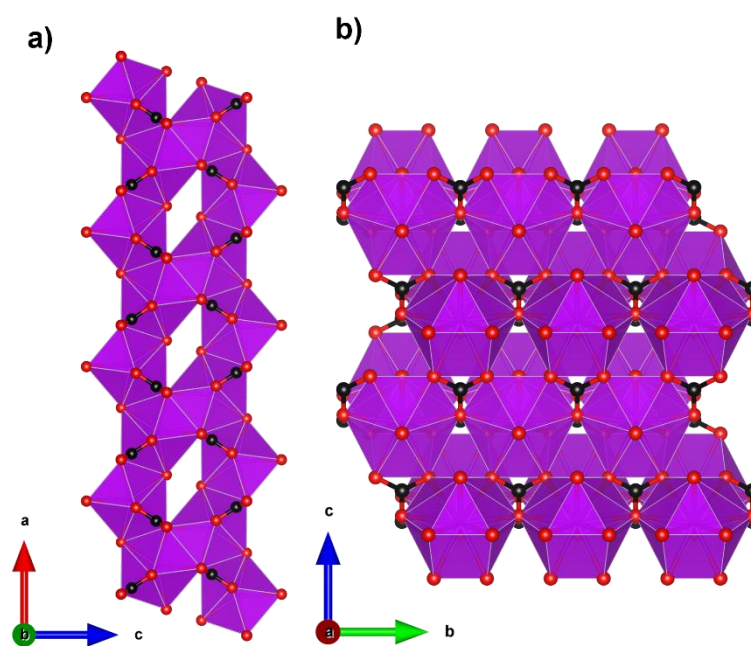
Figure 2.5: a) Crystal structure of GdOHCO$_3$ with face-sharing GdO$_{10}$ polyhedra forming zig-zag chains along the a-axis and b) packing of the distorted triangular lattice along the bc-plane. Colour codes: Gd: purple, C: black, O: red. The hydrogen atoms have been omitted for clarity.

The MCE effect was determined *via* the Maxwell equation from the magnetisation data to give a $-\Delta S_m^{max}$ of 66.4 J kg^{-1} K^{-1} (355 mJ cm^{-3} K^{-1}) at 1.8 K for a field change of 7 T, which is very similar to that determined from heat capacity measurements, 67.1 J kg^{-1} K^{-1} (359 mJ cm^{-3} K^{-1}). An impressive ΔT_{ad} of 24 K was also determined for a field change of 9 T from heat capacity measurements.

Interest in the magnetocaloric properties of GdOHCO$_3$ led Dixey *et al.*[120] to an investigation of heavier lanthanides from Tb–Er, which were confirmed to adopt orthorhombic $P2_12_12_1$ structures *via* neutron diffraction.[120] Among these materials, TbOHCO$_3$ and DyOHCO$_3$ demonstrated promising magnetocaloric properties with higher entropy changes than GdOHCO$_3$ for field changes lower than 2 T, the maximum field strength achievable using a permanent magnet at temperatures above 4 K, where they could be potentially used to replace liquid He for a wider range of cryogenic cooling applications. Specifically, DyOHCO$_3$ has a $-\Delta S_m^{max}$ of 33.3 J kg^{-1} K^{-1} (186 mJ cm^{-3} K^{-1}) at 4 K and a field change of 2 T while TbOHCO$_3$ has a $-\Delta S_m^{max}$ of 301.0 J kg^{-1} K^{-1} (169mJ cm^{-3} K^{-1}) compared to a value of 29.5 J kg^{-1} K^{-1} (158 mJ cm^{-3} K^{-1}) for GdOHCO$_3$ under the same conditions. The differences in $-\Delta S_m^{max}$ values between these compounds are even greater for a field change of 1 T (17.6 and 20.8 J kg^{-1} K^{-1} respectively for Dy and Tb; *cf.* 11.7 J kg^{-1} K^{-1} for Gd). These results are impressive when compared to the benchmark garnet oxides, with DyOHCO$_3$ showing improved magnetocaloric properties over GGG's maximum for a 2 T field change up to 8 K. Unfortunately, attempts to optimise magnetocaloric entropy change further through synthesising solid solutions Gd$_{1-x}$Tb$_x$OHCO$_3$ and Gd$_{1-x}$Dy$_x$OHCO$_3$ were unsuccessful, with heterometallic compounds having lower entropy changes compared to the homometallic materials.

A further study by Dixey *et al.*[121] indicated that the *Ln*OHCO$_3$ compounds with improved magnetocaloric properties above 4 K all exhibited significant magnetic diffuse

scattering in their correlated paramagnetic phases. Reverse Monte Carlo (RMC) fits indicated this was a result of having non-collinear ferromagnetically coupled Ising-like spins within the zig-zag chains packed into a frustrated antiferromagnetic lattice. They suggested such arrangements allows the ferromagnetic Ising chains to be readily aligned with low applied magnetic fields once the antiferromagnetic interactions are supressed by it, therefore maximising the change in magnetisation under these conditions, resulting in a higher MCE, as expressed by the Maxwell relation. This is in contrast to $GdOHCO_3$, which, as is typical in Gd coordination polymers, has predominantly antiferromagnetic coupling with a θ_{CW} of about -1 K.[55] Therefore, geometric frustration likely plays a key role in the optimisation of the MCE for this material, and indicates the important role structure plays in achieving such an optimisation, suggesting particular attention needs to be focused on fabricating materials with similar structural motifs.

Other inorganic coordination polymers have also been reported to have high magnetic entropy changes. These includes weakly antiferromagnetically coupled $Gd(OH)_3$ whose $-\Delta S_m^{max}$ is comparable to $GdOHCO_3$ at 62.0 J kg^{-1} K^{-1} (346 mJ cm^{-3} K^{-1}) at 2 K and 7 T, as determined from magnetisation data.[45] This material adopts $P6_3/m$ hexagonal symmetry with nine-coordinate Gd^{3+} connected *via* 9 different μ_3-OH$^-$ groups into a 3D structure with 1D hexagonal channels (see Figure 2.6). $Gd_2O(OH)_4(H_2O)_2$ is another promising material,[45] with $-\Delta S_m^{max}$ values, determined from magnetisation data, of 59.1 J kg^{-1} K^{-1} at 2 K and 7 T, although its lower density leads to a significant decreased value as a function of volume of 217 mJ cm^{-3} K^{-1}. This orthorhombic *Cmcm* structure features two distinct Gd^{3+} ions which are eight and nine coordinate, respectively. These are connected to form a 2D structure *via* connection of adjacent Gd2 ions through two OH$^-$ and one O^{2-} bridges along the *c*-axis with adjacent Gd1 ion connected through two OH$^-$ bridges along the same direction; adjacent Gd1 and Gd2 ions are connected through

three OH$^-$ bridges along the *b*-axis. These 2D structures are linked together along the

a-axis *via* hydrogen-bonding between the coordinated water molecules from adjacent 2D

layers thus generating a 3D framework.
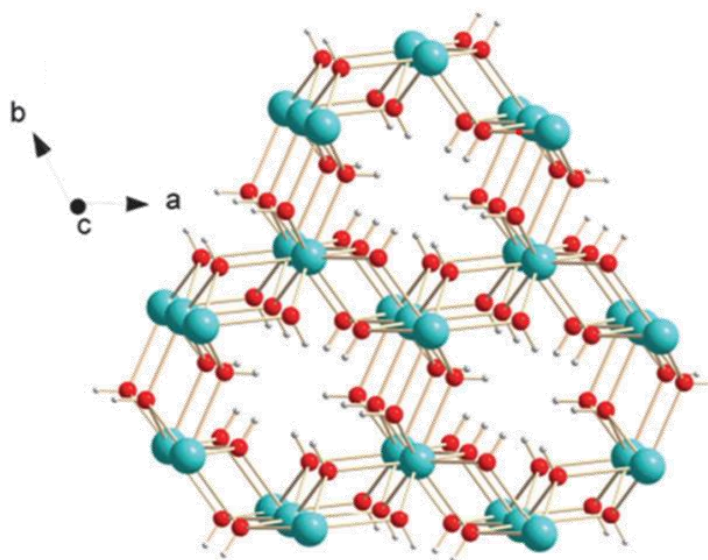
Figure 2.6: Crystal structure of Gd(OH)$_3$. Colour codes: Gd: cyan, O: red, H: white. Reproduced from *Chem. Commun.*, 2015, 51, 7317-7320 with permission from the Royal Society of Chemistry.

A final inorganic polymer with $-\Delta S_m^{max}$ above 40 J kg^{-1} K^{-1} is Gd$_6$(μ_6-O)(μ_3-

OH)$_8$(μ_4-ClO$_4$)$_4$(H$_2$O)$_6$](O)$_4$,[122] which crystallises in a monoclinic *C*2/*c* structure with

relatively strong antiferromagnetic coupling (θ_{CW} = -5.5 K) and has a $-\Delta S_m^{max}$ equal to

46.6 J kg^{-1} K^{-1} (207 mJ cm^{-3} K^{-1}) at 2.5 K for a field change of 7 T, based on

magnetisation data. This material has a complex structure comprised of hexanuclear

octahedral clusters and four crystallographically distinct Gd cations. The distorted

octahedral [Gd$_6$(μ_6-O)(μ_3-OH)$_8$]$^{8+}$ clusters have six Gd^{3+} around one central μ_6-oxo

central atom and are connected by eight face-capping μ_3-OH bridges. All Gd^{3+} cations

are coordinated to nine oxygen atoms in a mono-capped square antiprism geometry. The

octahedral clusters are connected to each other to form a 3D framework through ClO$_4^-$

bridges, with every cluster bridged *via* twelve ClO$_4^-$ ligands with every ligand linking

three Gd$_6$ clusters

2.3 Carboxylate-based Coordination Polymers

The other family of promising lanthanide coordination polymers that have shown significant promise as magnetocaloric materials are carboxylate-based frameworks. Amongst these materials, those with extended 2D and 3D structures can generally be considered MOFs, albeit most of these are dense and, thus, lacking significant porosity. Generally, these materials can be thought of as containing either small monocarboxylate ligands, slightly larger linear dicarboxylates or bulker aromatic carboxylates; where materials in this chapter contain more than one of these ligand types we have classified them according to the largest ligand type. The larger ligands involved in these materials, compared to purely inorganic coordination frameworks, lead to less densely packed structures, therefore, while their $-\Delta S_{m}^{max}$ as a function of weight are often similar, these coordination polymers typically have lower entropy changes as a function of volume.

2.3.1 Monocarboxylate-based Frameworks

The denser monocarboxylate frameworks, which amongst the polymers containing organic ligands are generally reported to have the highest $-\Delta S_{m}^{max}$, are based on either acetate or formate ligands. Acetate compounds commonly adopt 1D chain structures with coordination bonding only within these chains, with three such materials being reported to have high magnetocaloric entropy changes. Two examples of these are $Gd(OAc)_3(MeOH)$ and $Gd(OAc)_3(H_2O)_{0.5}$, which adopt monoclinic $P2_1/c$ and Cc symmetries, respectively (see Figure 2.7).[123]

In $Gd(OAc)_3(MeOH)$, the Gd^{3+} are in a nine-coordinate capped square antiprism geometry, while in $Gd(OAc)_3(H_2O)_{0.5}$, there are two Gd centres in nine-coordinate, capped square antiprismatic and eight-coordinate, square antiprismatic geometries respectively. In both cases, the Gd within the chains are bridged by three acetate ligands,

in a mixture of $\eta_2{:}\eta_1$ and *syn-syn* acetate geometries with Gd-Gd distances of 4.06 Å and

6.46 Å for $Gd(OAc)_3(MeOH)$ and $Gd(OAc)_3(H_2O)_{0.5}$, respectively. In $Gd(OAc)_3(H_2O)_{0.5}$

there are interchain hydrogen bonding interactions between the water and acetate

carboxylate groups while $Gd(OAc)_3(MeOH)$ only has weaker interchain interactions.

$Gd(OAc)_3(MeOH)$ and $Gd(OAc)_3(H_2O)_{0.5}$ have very weak ferromagnetic and

antiferromagnetic coupling, respectively, with θ_{CW} of -0.22 and 0.34 K. Magnetisation

measurements indicate a $-\Delta S_m^{max} = 45.0$ J kg^{-1} K^{-1} (96.8 mJ cm^{-3} K^{-1}) and 47.7 J kg^{-1} K^{-1} (106 mJ cm^{-3} K^{-1}) for a 7 T field change at 1.8 K for $Gd(OAc)_3(MeOH)$ and

$Gd(OAc)_3(H_2O)_{0.5}$ respectively.
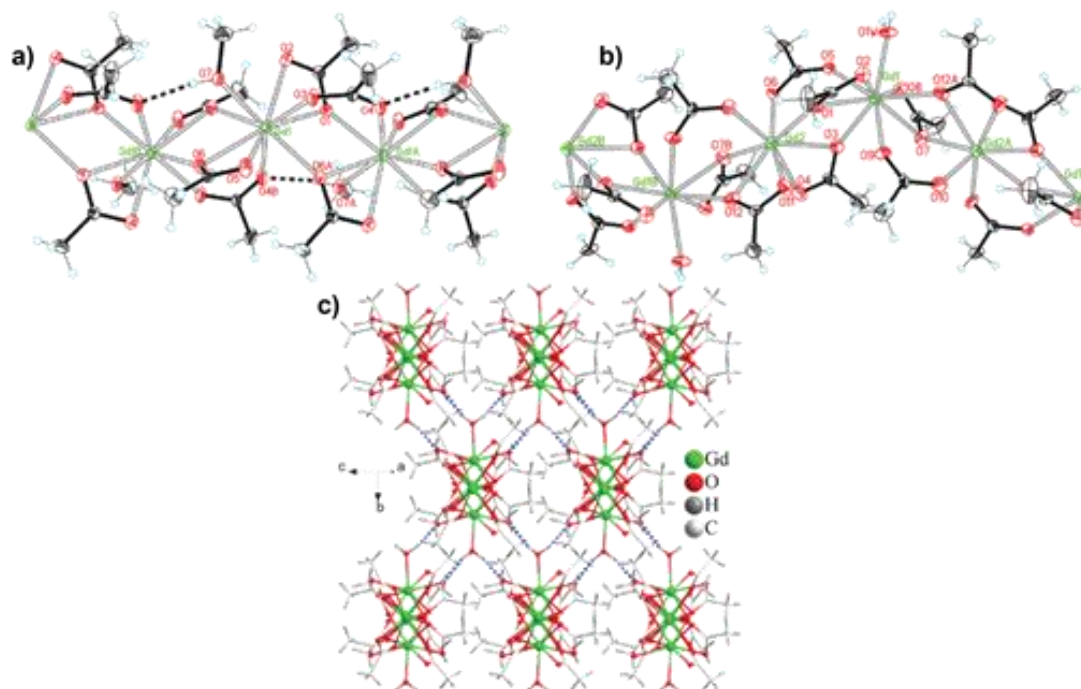
Figure 2.7: Chain structures of a) $Gd(OAc)_3(MeOH)$ and b) $Gd(OAc)_3(H_2O)_{0.5}$, shown with thermal ellipsoids at 30% probability. c) Three-dimensional hydrogen-bonded network of $Gd(OAc)_3(H_2O)_{0.5}$. Adapted with permission from *Inorg. Chem*., 2012, 51, 405–413.

A third 1D acetate compound reported to have a high magnetocaloric entropy

change is weakly antiferromagnetically coupled $Gd(HCO_2)(OAc)_2(H_2O)_2$[124], which

adopts monoclinic $P2_1/m$ symmetry. Here, it is the formate co-ligand which connects Gd

within the chain, with Gd-Gd distances of 6.58 Å (see Figure 2.8). Adjacent chains are

rotated by 180° which allows for the formation of a dense network of hydrogen bonds in

one direction perpendicular to the chain while chains in the third dimension are separated by methyl groups from the acetate ligand resulting in only weak intermolecular forces in this direction. The magnetocaloric properties of this compound were evaluated through both magnetisation and heat capacity data, both determining that $-\Delta S_m^{max}$ has a maximum of 45.9 J kg^{-1} K^{-1} (110 mJ cm^{-3} K^{-1}) at 1.8 K for a field change of 7 T.
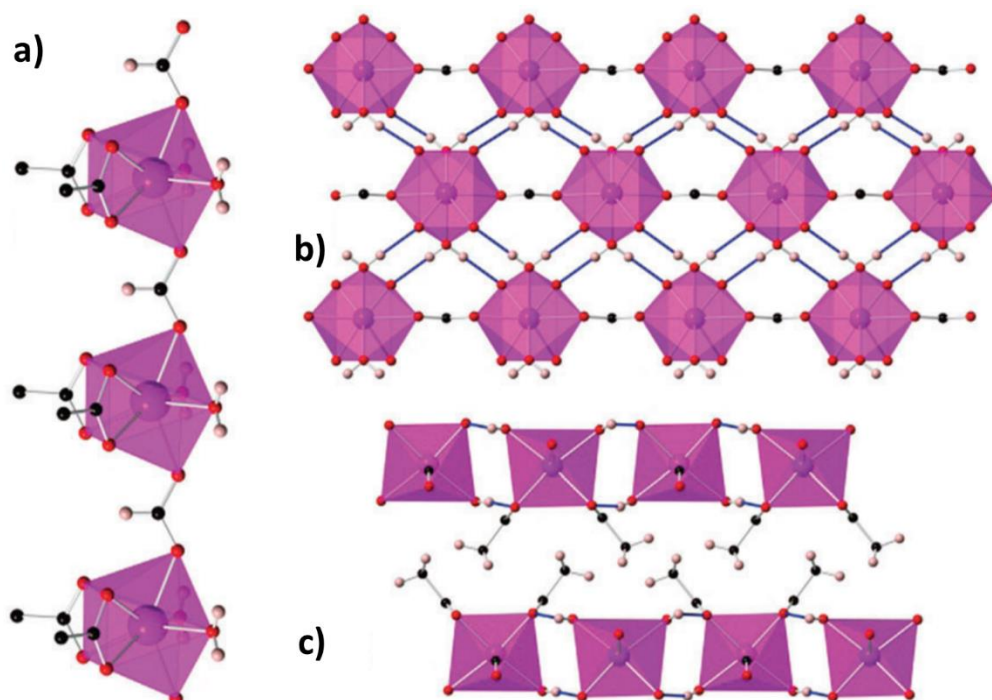
Figure 2.8: a) Coordination chains of Gd(HCO$_2$)(OAc)$_2$(H$_2$O)$_2$ along the *b*-axis; b) hydrogen-bonded chains forming sheets on the *bc*-plane; c) packing of the sheets along the *b*-axis. Colour codes: Gd: purple, O: red, C: black, H: pink. Reproduced from *Chem. Commun.*, 2012, 48, 7592–7594 with permission from the Royal Society of Chemistry.

The other formate-containing compound in this group reported to have significant magnetocaloric properties is Gd(HCO$_2$)$_3$,[53] which adopts a rhombohedral *R3m* structure featuring face-sharing chains with neighbouring chains connected through the formate ligand to yield a triangular lattice (see Figure 2.9). The Gd cations are nine-coordinate in a tricapped trigonal prismatic geometry. The MCE of Gd(HCO$_2$)$_3$ is evaluated both indirectly from the magnetisation data and directly from heat capacity measurements. In the former case, the magnetic entropy changes for different applied field changes are obtained, which are similar to those from heat capacity data. At ~1 K and for a field

change of 7 T , the $-\Delta S_m^{max}$ is 55.9 J kg^{-1} K^{-1} or 216 mJ cm^{-3} K^{-1}, with the large volumetric entropy change enabled by the dense structure. ΔT_{ad} was estimated to be approximately 22 K from heat capacity measurements. Direct measurements under quasi-adiabatic conditions suggest values of 2.47 and 0.51 K during magnetisation and demagnetisation for a 1-0 T field change, consistent with the values obtained from the indirect entropy-based measurements for such changes. The relative cooling power (RCP) of Gd(HCO$_2$)$_3$ was also estimated to be 522 mJ cm^{-3} K^{-1}, which is higher than the 479 mJ cm^{-3} K^{-1} reported for Gd$_3$Ga$_5$O$_{12}$.[30]
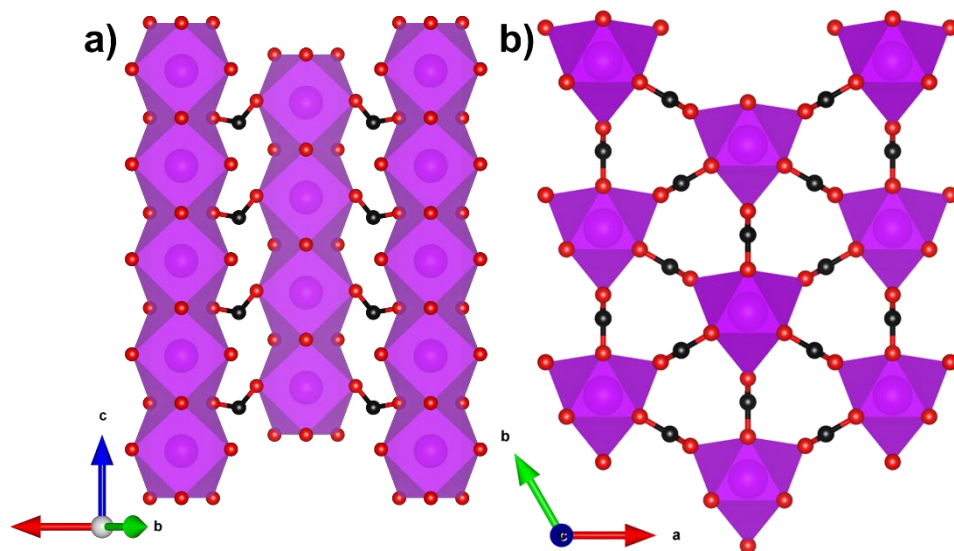
Figure 2.9: a) Crystal structure of Gd(HCO$_2$)$_3$ with chains propagating along the *c*-axis and b) arranged in a triangular lattice in the *bc*-plane. Colour codes: Gd: purple, C: black, O: red. The hydrogen atoms have been omitted for clarity.

The high entropy change of Gd(HCO$_2$)$_3$ has led to the investigation of analogues containing heavier lanthanides from Tb-Er.[5] While the $-\Delta S_m^{max}$ of these compounds is lower at high fields than for Gd(HCO$_2$)$_3$, for field changes less than 2 T and for temperatures above 4 K, Tb(HCO$_2$)$_3$ and, to a smaller extent, Ho(HCO$_2$)$_3$, have higher $-\Delta S_m^{max}$ compared to the Gd analogue. Specifically, Tb(HCO$_2$)$_3$ outperforms Gd(HCO$_2$)$_3$ above 6 K for a 2–0 T field change and both Tb(HCO$_2$)$_3$ and Ho(HCO$_2$)$_3$ do so above 4 K for a 1–0 T field change, although the difference between Ho(HCO$_2$)$_3$ and Gd(HCO$_2$)$_3$

is very modest. Unlike the LnOHCO$_3$ series, the mixing of lanthanide cations is shown

to be a promising route to optimising higher temperature and lower applied field MCE

behaviour. In the series, $Gd_{1-x}Tb_x(HCO_2)_3$, for $x = 0.2$ and 0.4 and a field change of 1 T,

there is improvement in the magnetic entropy change above 4 K compared to $Gd(HCO_2)_3$

with only a minimal loss in $-\Delta S_m^{max}$ at 2 K.[5]

Strong diffuse magnetic scattering is observed from neutron diffraction of the

paramagnetic phase of $Tb(HCO_2)_3$ with RMC fits indicating the presence of Ising-like

spins parallel to the chain direction with strong ferromagnetic correlations within these

units. There are also weaker frustrated interchain antiferromagnetic correlations within

the triangular lattice. It has been suggested that the high entropy change of $Tb(HCO_2)_3$

under low applied fields is caused by ready alignment of the ferromagnetic Ising chains

with the applied field once the interchain antiferromagnetic interactions are supressed.

Further work has shown that this combination of interactions in $Tb(HCO_2)_3$ leads to a

unique triangular Ising antiferromagnetic state below 1.6 K, which has long range

1D magnetic order with only short range antiferromagnetic correlations between these

chains.[54] Strong magnetic diffuse scattering has also been uncovered in $Ho(HCO_2)_3$

indicating the presence of similar magnetic interactions as in $Tb(HCO_2)_3$ while all other

$Ln(HCO_2)_3$ lack such correlations, suggesting the ferromagnetic Ising chains in these

systems are key to improving their $-\Delta S_m$ at higher temperatures as opposed to the

predominantly antiferromagnetic interactions in $Gd(HCO_2)_3$.[51]

2.3.2 Linear dicarboxylate ligands

Another extensively studied family of carboxylate magnetocalorics are those

using linear dicarboxylate ligands, principally those containing the relatively small

oxalate, succinate and citrate ligands. The oxalate ligand is the simplest of these, being

comprised of two connected carboxylate groups. The first promising magnetocaloric to be reported using the oxalate ligand was $Gd(C_2O_4)(H_2O)_3Cl$, a material that showed very weak antiferromagnetic coupling.[125] This material adopts a $P2_1/n$ monoclinic structure with the Gd in a nine-coordinate capped squared antiprismatic geometry. Gd dimers, formed by edge-sharing polyhedra with an intradimer separation of 4.42 Å, are connected into 2D layers with shorter Gd-Gd distances of 5.84 Å along the a-axis, through $\mu_4-\eta_1{:}\eta_2{:}\eta_1{:}\eta_2$ bonded oxalates, and 6.31 Å along the c-axis, through $\mu-\eta_2{:}\eta_2$ oxalates (see Figure 2.10).
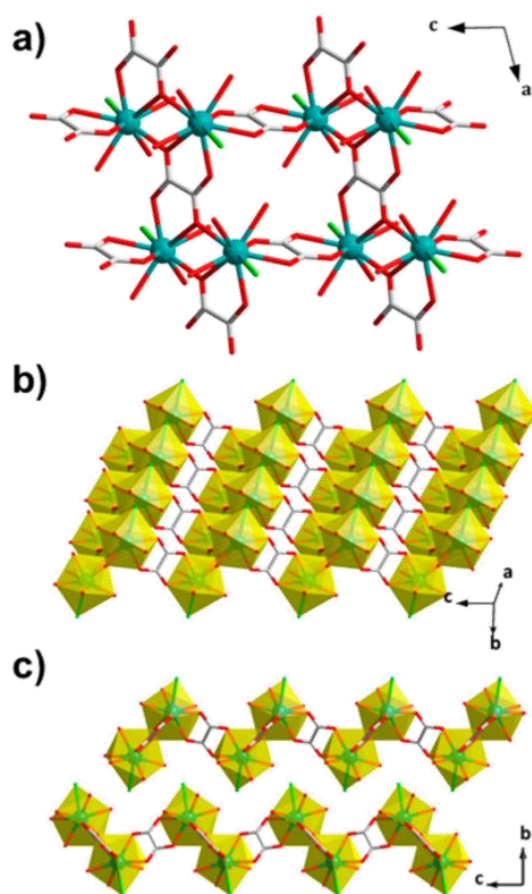
Figure 2.10: Crystal structure of $Gd(C_2O_4)(H_2O)_3Cl$, with a,b) 2D layers on the ac-plane and c) packing along the b-axis. Colour codes: Gd: cyan, C: grey, O: red. The hydrogen atoms have been omitted for clarity. Adapted with permission from *Inorg. Chem.*, 2014, 53, 17, 9052–9057. Copyright 2014 American Chemical Society.

The structure features intralayer O_{water}-H$\cdots O_{oxalate}$ and interlayer O_{water}-H$\cdots O_{water}$ and O_{water}-H$\cdots$Cl hydrogen bonds. Indirect methods of determining

magnetic entropy changes indicate a $-\Delta S_m^{max}$ of 48.0 J K^{-1} kg^{-1} (144 mJ cm^{-3} K^{-1}) at 2.2 K for a 7 T field change. Direct determination of the MCE effect *via* heat capacity measurements shows that the $-\Delta S_m^{max}$ values are consistent with those obtained from magnetisation data and that ΔT_{ad} is 16.9 K for the same magnetic field change.

Another oxalate family shown to have good magnetocaloric properties are the Gd(pda)(ox)$_{0.5}$(H$_2$O)$_x$ (x = 0, 1, 2, pda = propionate) phases.[126] All three compounds adopt $P\bar{1}$ triclinic symmetry with nine coordinate Gd cations in the anhydrous form, which increase to ten in the hydrated forms. The increase in the hydration state leads to a change from a 3D structure made of pillared layers in the anhydrous and monohydrate forms to a 2D dihydrate structure with only weak C-H$\cdots$O hydrogen bonding interactions between them. The layers in the 3D structure are connected by the carboxylate groups of the pda^{2-} ligands with the oxalates pillaring the layers. In the dihydrate, the layers are comprised of cationic zigzag Gd(pda) chains, which are connected to form 2D layers by the oxalate ligands. Despite the changes in dimensionality, all three materials retain similar weak ferromagnetic coupling with θ_{CW} ranging between 0.3 and 0.7 K. Magnetisation measurements indicate $-\Delta S_m^{max}$ for these compounds are similar with regards to mass density at 46.8 J kg^{-1} K^{-1}, 46.1 J kg^{-1} K^{-1} and 45.0 J kg^{-1} K^{-1} for the x = 0, 1 and 2 phases respectively for a 7 T field change at 2 K, although the greater density of the hydrated phases increases their volumetric entropy change (*cf.* 128 mJ cm^{-3} K^{-1}, 1512 mJ cm^{-3} K^{-1} and 159 mJ cm^{-3} K^{-1} for x = 0, 1 and 2, respectively).

The succinate (suc) ligand is expanded from an oxalate by inclusion of two CH$_2$ groups between its carboxylates. Two succinate frameworks have been reported to have promising magnetocaloric entropy changes, viz. Gd$_2$(OH)$_2$(suc)$_2$(H$_2$O)$\cdot$2H$_2$O and Gd$_6$(OH)$_8$(suc)$_5$(H$_2$O)$_2\cdot$4H$_2$O, which adopt $C2/c$ and $P2_1/c$ symmetry, respectively.[127] Gd$_2$(OH)$_2$(suc)$_2$(H$_2$O)$\cdot$2H$_2$O and Gd$_6$(OH)$_8$(suc)$_5$(H$_2$O)$_2\cdot$4H$_2$O both adopt ladder-like

structures with two and six distinct Gd cations, respectively, with one gadolinium in an eight coordinate environment in both structures and the remainder in nine coordinate environments (see Figure 2.11). $Gd_2(OH)_2(suc)_2(H_2O) \cdot 2H_2O$ crystallises as a Gd-OH ladder that grows parallel to the b-axis and is comprised of two rows of Gd^{3+} ions with Gd-Gd distances ranging from 3.655 to 4.065 Å. These ladders are then connected along the a-axis and the c-axis *via* succinate ligands which serve as pillars to form the 3D network. Similarly, $Gd_6(OH)_8(suc)_5(H_2O)_2 \cdot 4H_2O$ adopts a three rail Gd-OH ladder where three rows of Gd^{3+} ions, connected by the succinate ligand, from the rungs of the ladder. The ladders extend along the b-axis and neighbouring Gd$\cdots$Gd separations range from 3.656 and 4.049 Å. Magnetisation measurements of these weakly antiferromagnetically coupled phases indicate a $-\Delta S_m^{max}$ of 42.8 J kg^{-1} K^{-1} (120 mJ cm^{-3} K^{-1}) and 48.0 J kg^{-1} K^{-1} (144 mJ cm^{-3} K^{-1}) for a field change of 7 T at 2.6 K and 1.8 K, with ΔT_{ad} of 17 and 15 K, respectively.

One citrate (cit) coordination polymer, which is related to the succinate ligand *via* replacement of a CH_2 group with a $C(OH)(CHCO_2)$ group, has been reported to have potentially promising magnetocaloric entropy changes, namely $Gd(cit)(H_2O)$[128]. This compound adopts monoclinic $C2/c$ symmetry with GdO_9 polyhedra connected by carboxylate O atoms in a μ_2-η_2 bridging mode to form a dimer (see Figure 2.12). Neighbouring dimers are then bridged through carboxylate groups to form 1D ladders of Gd^{3+} chains which are bridged by citrate ligands to from a 2D layer structure with weak ferromagnetic coupling indicated by a θ_{CW} of 1.1 K. Magnetisation measurements indicate a $-\Delta S_m^{max}$ of 43.6 J kg^{-1} K^{-1} (115 mJ cm^{-3} K^{-1}) for field change of 7 T at 2 K
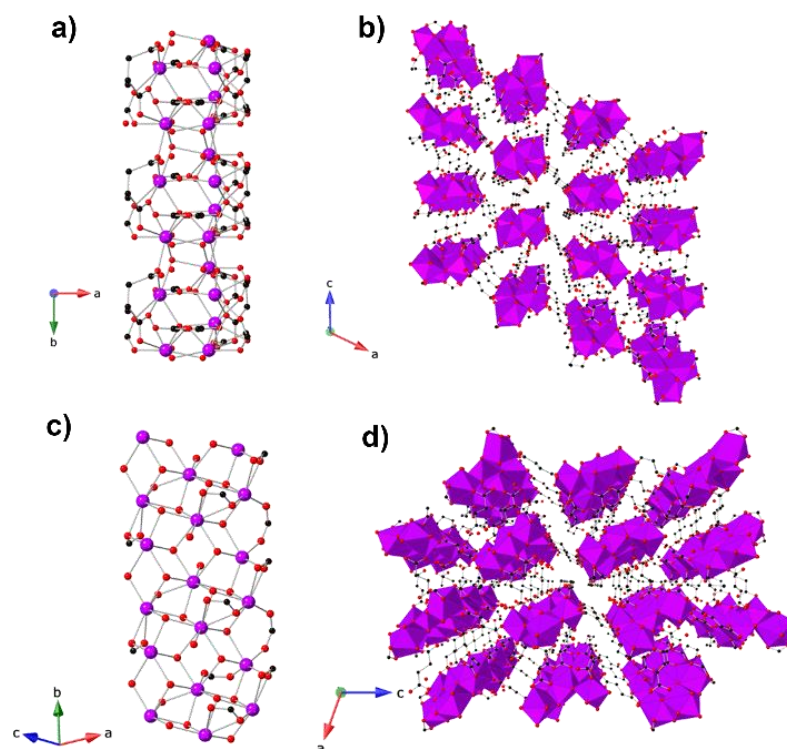
Figure 2.11: a) Crystal structure of $Gd_2(OH)(suc)_2H_2O \cdot 2H_2O$ with a two-rail Gd-OH ladder parallel to the *b*-axis and (b) the packing of the ladders on the *ac*-plane. (c) Crystal structure of $Gd_6(OH)_8(suc)_5(H_2O)_2 \cdot 4H_2O$ showing the three-rail Gd-OH ladder parallel to the *b*-axis and (d) the packing of the three-rail ladders on the *ac*-plane. Colour codes: Gd: purple, C: black, O: red. Hydrogens are omitted for clarity.
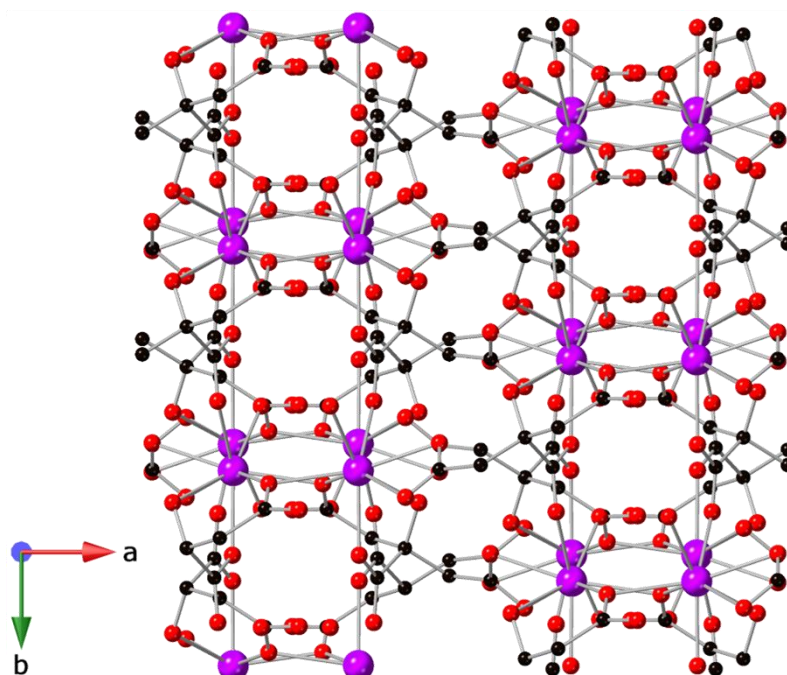
Figure 2.12: Two-dimensional layer structure of $Gd(cit)(H_2O)$ showing two Gd ladder chains propagating along the *b*-axis. Colour codes: Gd: purple, C: black, O: red. Hydrogens are omitted for clarity.

2.3.3 Cyclic Carboxylate Ligands

Compounds incorporating cyclic carboxylate ligands, which are amongst the most common ligands utilised in MOFs, have also been investigated as magnetocaloric materials. Amongst the first of these was $Gd(C_4O_4)(OH)(H_2O)_4$,[129] which adopts a monoclinic $P2_1/c$ structure with six coordinate Gd, which are bridged by the squarate ligand to form a 2D sheet in the bc-plane with an intralayer Gd-Gd separation of 6.48 Å (see Figure 2.13).

Interlayer coupling is *via* extensive hydrogen bonding between squarate oxygen atoms and water ligands. This phase has negligible magnetic interactions with indirect measurements of MCE properties indicating a $-\Delta S_m^{max}$ of 47.3 J kg^{-1} K^{-1} or 210 mJ cm^{-3} K^{-1} for a field change of 9 T at ~3 K, with the volumetric density particularly high for a MOF containing a cyclic unit due to the dense structure enabled by the smaller squarate ligand. Another high performing magnetocaloric framework containing a cyclic carboxylate is $Gd(HCO_2)(bdc)$,[130] where bdc is the aromatic 1,4-benzenedicarboxylate ligand commonly found in many MOFs structures. Here, it leads to a monoclinic $P2_1/c$ structure with edge-sharing dimeric GdO_8 distorted trigonal dodecahedra, which are connected through the oxygen atoms of two formate ligands with intradimer Gd-Gd distances of 3.95 Å. These dimers are connected through the bdc carboxylate groups to generate layers that are pillared through the bdc linkers, resulting in the $Gd(HCO_2)(bdc)$ network, and are found to be very weakly antiferromagnetically coupled, as indicated by the intradimer J ~ -0.04 K. The $-\Delta S_m^{max}$, calculated from magnetisation data, gives a value of 42.4 J kg^{-1} K^{-1} (113 mJ cm^{-3} K^{-1}) for a 5 T field change at 2.25 K, with this increasing to 47.0 J kg^{-1}K^{-1} (125 mJ cm^{-3} K^{-1}) for a field change of 9 T.

More recently, an evacuated porous benzenetricarboxylate (btc) framework, Gd(btc)(H$_2$O),[131] has been reported to have a surprisingly high θ_{CW} of –6.2 K and good magnetocaloric entropy change of 42 J kg^{-1} K^{-1} at 1.8 K for a 5 T field change as a function of weight. Its entropy change as a function of volume is, however, very modest at about 68 mJ cm^{-3} K^{-1}, due to the low density of the structure. This structure, which adopts the chiral space groups of $P4_122$ or $P4_322$,[132] features Gd cations connected *via* carboxylate groups of btc linkers to give 1D helical chains with Gd-Gd distances of
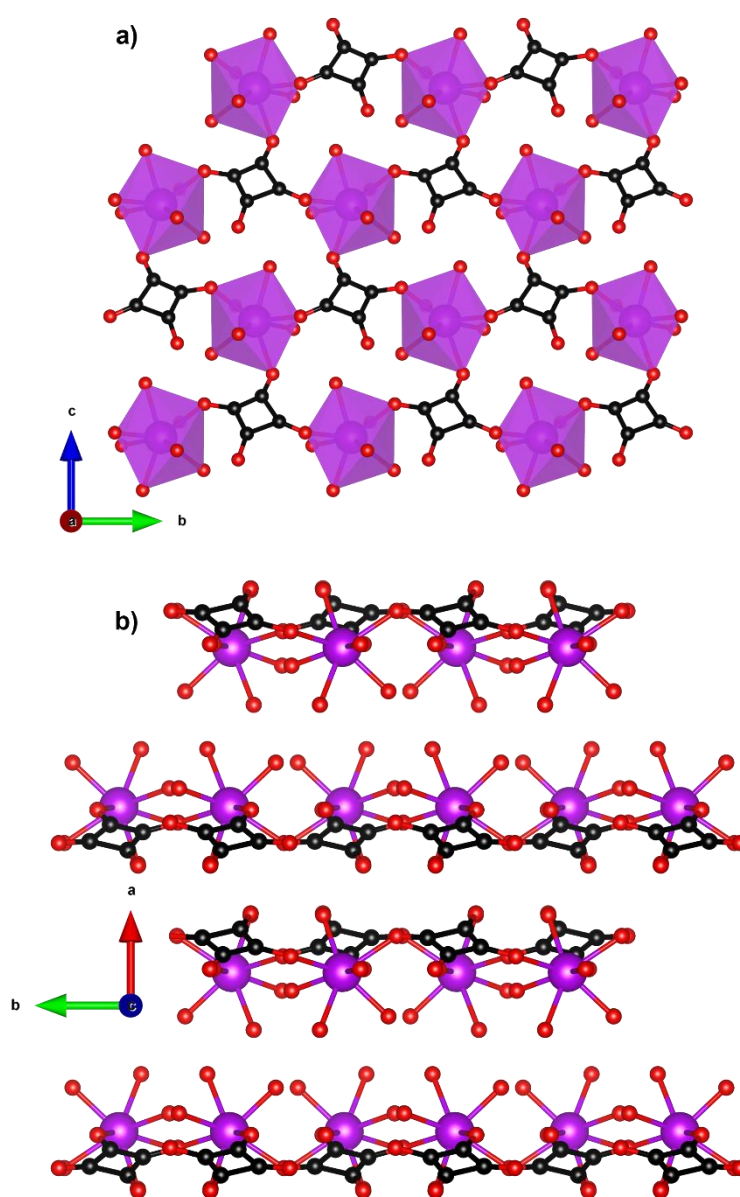
Figure 2.13: (a) Two-dimensional layers of Gd(C$_4$O$_4$)(OH)(H$_2$O)$_4$ on the *bc*-plane and (b) packing of the layers along the *a*-axis. Colour codes: Gd: purple, C: black, O: red. Hydrogens are omitted for clarity.

4.30 Å. These rods pack to give a 3D structure thanks to the connectivity of Gd^{3+} ions and btc^{3-} ligands and features helical-shaped channels, with well-spaced Gd cations between chains with a minimum separation of 8 Å.

Two other frameworks with potential voids featuring cyclic carboxylates and with $-\Delta S_m^{max}$ above 40 J kg^{-1} K^{-1} have been reported, namely the weakly antiferromagnetically coupled $Gd_5(\mu_3\text{-}OH)_6(TZI)_3(DMA)_{1.5}(H_2O)_{9.5}\cdot DMA$[133] (where H_3TZI is 5-(1H-tetrazol-5-yl)isophthalic acid and DMA is dimethylcetamide) and $Gd(2,5\text{-}FDA)_{0.5}(Glu)(H_2O)_2]\cdot xH_2O$[134] (where FDA^{2-} is furan-2,5-dicarboxylate and Glu^{2-} is glutarate) materials. Indirect measurements indicate a $-\Delta S_m^{max}$ of 41.3 J kg^{-1} K^{-1} and 40.6 J kg^{-1} K^{-1} at 2 K for a 7 T field change but, again, their porosity leads to a very modest volumetric $-\Delta S_m^{max}$ of 93.7 mJ cm^{-3} K^{-1} and 70.6 mJ cm^{-3} K^{-1} respectively. $Gd_5(\mu_3\text{-}OH)_6(TZI)_3(DMA)_{1.5}(H_2O)_{9.5}\cdot DMA$ forms a 3D framework in monoclinic $C2/m$ symmetry. Its structure is based on the $[Gd_5(OH)_6]^{9+}$ trigonal bipyramidal core built from eight and nine-coordinate Gd linked together by six μ_3-OH bridges and five *syn-syn* carboxylate bridges. These clusters are then connected by a μ_2-H_2O bridge to form 1D chains which are in turn connected by the carboxylate groups of the TZI ligand to create the 3D framework. $Gd(2,5\text{-}FDA)_{0.5}(Glu)(H_2O)_2\cdot xH_2O$ adopts orthorhombic *Pnma* symmetry consisting of nine-coordinate Gd in monocapped square-antiprismatic polyhedra[134] that are linked into Gd_2O_{16} dimers by two bidentate chelating-bridged carboxylates. The dimers connected into 1D zigzag chains *via* the 2,5-FDA ligand with neighbouring chains bridged together by two Glu ligands per dimer.

2.4 4*f*-3*d* Mixed-Metal Polymers

The other general group of magnetocaloric coordination polymers that should be considered are those containing transition metals, with the highest performing materials

amongst these typically combining d^5 Mn^{2+} with f^7 Gd^{3+} to maximise their magnetic spin. Mn^{2+} is the transition metal of choice in $3d$-$4f$ systems due to it being readily available and having the most unpaired electrons ($S = 5/2$) possible in a transition metal. Indeed, despite their lower number of unpaired electrons (*cf.* to Gd^{3+}), Mn^{2+} complexes can have high $-\Delta S_m^{max}$, with respect to weight even in the absence of a lanthanide, as seen in Mn(Me-ip)(DMF) (where Me-ipH$_2$ is 5-methylisophthalic acid).[135] This material adopts a *Pna*2_1 orthorhombic structure which contains distorted octahedral Mn^{2+} in a coordination polymer comprised of chains of Mn cations connected by two carboxylate ligands with a Mn-Mn intrachain distance of 3.88 Å (see Figure 2.14). Each chain is then connected to four adjacent ones *via* the Me-ip^{2-} ligand with interchain Mn-Mn distance of 7.49 Å. The $-\Delta S_m^{max}$ for this system is calculated at 42.4 J kg^{-1} K^{-1} (66. 7 mJ cm^{-3} K^{-1}) for a field change of 8 T at 2 K. This is accompanied by weak antiferromagnetic coupling, with a θ_{CW} of –0.59 K, indicating that despite the presence of only $3d$ cations, the emergence of magnetic order should not prevent its use as a magnetocaloric until much lower temperatures.

An interesting $3d$-$4f$ mixed coordination polymer is GdMn$_{0.5}$(OAc)$_4$(H$_2$O)$_2$·3H$_2$O,[136] which contains a low-dimensional motif, specifically the Gd^{3+}-Mn^{2+} acetate chains, with only very weak antiferromagnetic coupling within them. This compound has a $-\Delta S_m^{max}$ of 38.7 J kg^{-1} K^{-1} (78.7 mJ cm^{-3} K^{-1}) for a field change of 7 T at 2.5 K It should be noted that this compound also shows an interesting $-\Delta S_m^{max}$ of 31.1 J kg^{-1} K^{-1} (63.2 mJ cm^{-3} K^{-1}) for a field change of 3 T at ~2 K, which is higher than that of the commercially available GGG under the same conditions.
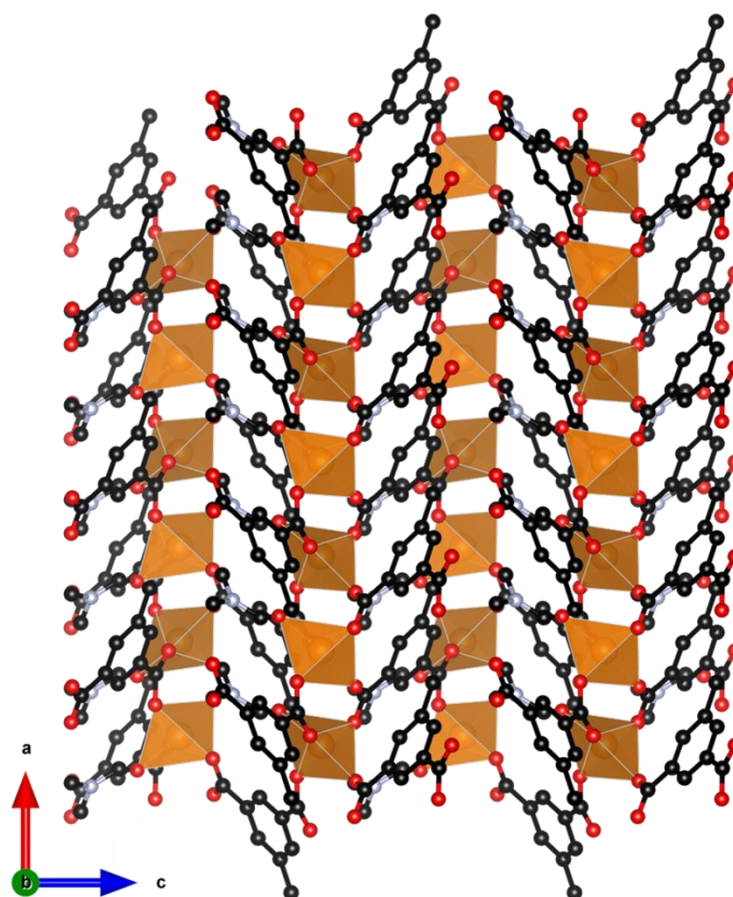
Figure 2.14: Crystal structure of Mn(Me-ip)(DMF) with MnO_8 octahedra forming chains along the a-axis, connected by the Me-ip2- ligand. Colour codes: Mn: orange, C: black, O: red. Hydrogens are omitted for clarity.

This compound crystallises in a triclinic $P\bar{1}$ structure where each Gd ion is in a capped square-antiprism geometry and each Mn adopts an octahedral geometry. Two adjacent Gd^{3+} ions are bridged by two acetates while adjacent Gd^{3+} and Mn^{2+} ions are bridged by three acetates (see Figure 2.15). This generates a 1D chain structure where pairs of Gd ions are separated by one Mn along the chain. Within the chains, the Gd-Gd distance is 4.277 Å, whereas the Gd-Mn distance is 4.030 Å. Intrachain hydrogen bonds are present between one coordinated water molecule and two acetate ligands. Water tetramers, formed by two guest water molecules, support the main interactions between chains by enabling hydrogen bonding between coordinating carboxylate and water molecules.
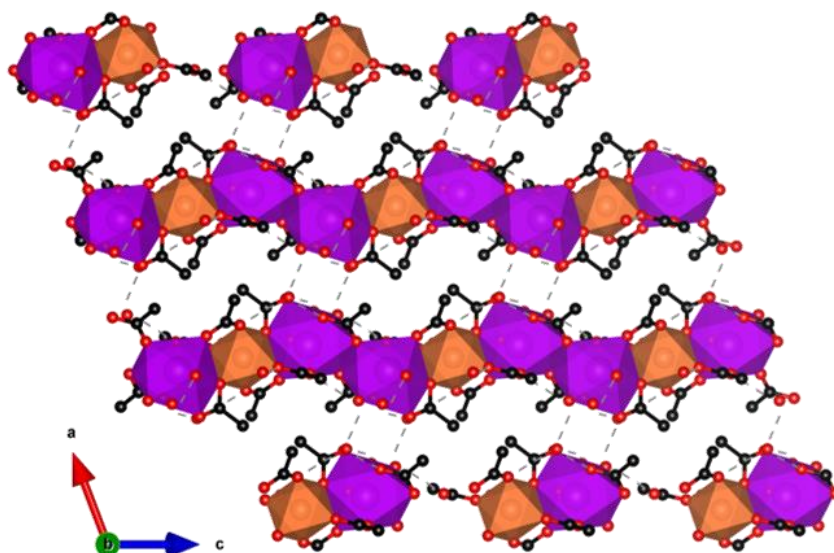
Figure 2.15: Crystal structure of [GdMn$_{0.5}$(OAc)$_4$(H$_2$O)$_2$]·3H$_2$O with chains of Mn and Gd polyhedra bridged together in a 2D network *via* hydrogen bonds. Colour codes: Gd: purple, Mn: orange, C: black, O: red. Hydrogens are omitted for clarity.

The remaining mixed 3d-4f coordination polymers with promising magnetocaloric properties are 3D frameworks with a net charge that is balanced by the presence of counterions in the pore space. These compounds all have respectable magnetocaloric entropy changes as a function of weight but, as for other porous magnetocalorics, they are much more modest as a function of volume. [Mn(H$_2$O)$_6$][MnGd(oda)$_3$]$_2$·6H$_2$O (where oda^{2-} is oxydiacetetate) is the only reported example of a promising magnetocaloric framework with an anionic charge.[137,138] The framework is composed of nine coordinate Gd in a distorted tricapped trigonal prismatic geometry while Mn in an octahedral environment, with each 3d cation connected *via* carboxylate oxygen atoms to six 4f cations and vice versa (see Figure 2.16).
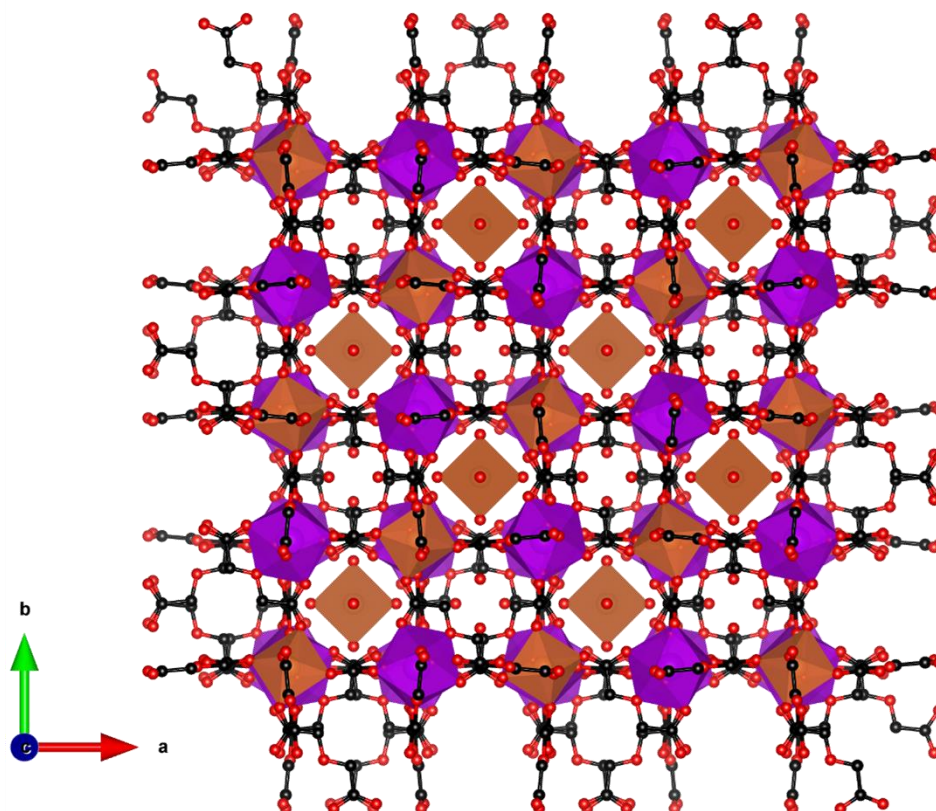
Figure 2.16: Crystal structure of $[Mn(H_2O)_6][MnGd(oda)_3]_2 \cdot 6H_2O$. The structure presents broad and narrow cavities, occupied by $[Mn(H_2O)_6]^{2+}$ and water molecules, respectively. Colour codes: Gd: purple, Mn: orange, C: black, O: red. Hydrogens are omitted for clarity.

This leads to a cubic lattice with voids of alternatingly broad and narrow cavities that are occupied by $[Mn(H_2O)_6]^{2+}$ units, which both balance the anionic charge of the framework and enhance the MCE of the material, and solvent water molecules, respectively. This weakly coupled ferromagnetic material (θ_{CW} of 1.2 K) has been determined indirectly to exhibit $-\Delta S_m^{max}$ of 50.1 J kg^{-1} K^{-1} (114 mJ cm^{-3} K^{-1}) at 1.8 K for field changes of up to 7 T. Heat capacity measurements under fields of up to 3 T were also performed and values were found to be consistent with those obtained from bulk magnetisation measurements with a ΔT_{ad} of 10.1 K for an applied field of 3 T. Weakly antiferromagnetically coupled $Gd_4Mn(L)_3(H_2O)_3(\mu_3\text{-}OH)_4(HCOO)_{1.5}](NO_3)_{2.5} \cdot 6H_2O$ (where H$_2$L is 2,2′-bipyridine-4,4′- dicarboxylic acid) has the highest $-\Delta S_m^{max}$ amongst a series of cationic mixed $3d$-$4f$ frameworks, between which L is varied, with a value of 46.0 J kg^{-1} K^{-1} (70.0 mJ cm^{-3} K^{-1}) for a field change of 7 T at 2 K.[139] This compound

adopts a cubic $I2_13$ structure with Gd^{3+} having two distinct coordination environments where Gd1 is eight coordinated with a dicapped trigonal prism geometry and Gd2 is six coordinated. These distinct cations are linked by OH^- groups into a distorted cubane $[Gd_4O_4]$ with Gd-Gd distances of 3.78 Å and 3.87 Å. The L^{2-} ligands both link each $[Gd_4O_4]$ cluster to three others but also the octahedral Mn which is coordinated only to nitrogen atoms from these ligands to six $[Gd_4O_4]$ clusters, forming a 6,9-connected sqc-topology. The clusters are bridged by formate ligands to form a 3D framework with two unusual types of helical channels, a larger L-helix with a pore diameter of 10.4 Å while the latter is an R-helix with the same helix pitch, that is the height of one complete helix turn, of 20.7 Å but a smaller pore diameter of 5.0 Å. Residual electron density has been used to suggest the pores of this compound are occupied by disordered H_2O molecules and NO_3^- anions, the latter being required for charge balancing, but there is no direct confirmation of this through other techniques. Weakly antiferromagnetically coupled $[Gd_5Mn(L)_3(H_2O)_{10}(\mu_3\text{-}OH)_6](NO_3)_5 \cdot 13H_2O$,[139] (where H_2L is 2,2′-dipyridine-4,4′-dicarboxylic acid) is another example of a 3D cationic framework with a high $-\Delta S_m^{max}$ of 38.3 J kg^{-1} K^{-1} (57.3 mJ cm^{-3} K^{-1}) at 3 K for a field change of 7 T. This compound adopts hexagonal $P3_12_1$ symmetry and contains $[Gd_5(COO)_6(H_2O)10(OH)_6]^{3+}$ cluster nodes in which the five Gd^{3+} cations are arranged in a distorted trigonal bipyramidal geometry, with the Gd cations bridged by six μ_3-OH groups and encapsulated by the six carboxyl groups of three L^{2-} ligands. Each cluster contains three crystallographically independent Gd^{3+} cations, all of which are eight-coordinated with dicapped trigonal prismatic geometries in the apical positions and square antiprism geometries in the equatorial plane of the cluster. Every cluster connects to six adjacent ones through the L^{2-} ligand which also connects the octahedral Mn to the Gd clusters,

forming an overall 6,6-connected topology. The resulting channels in the structure contain free water molecules and NO_3^- counter anions.

2.5 Summary and Perspective

This chapter has presented a review of coordination polymer materials, based on polyatomic ligands, exhibiting MCE and showing a high $-\Delta S_m^{max}$, the most readily available measure of their potential magnetic cooling properties. These are dominated by materials in which Gd is the magnetic cation and have been grouped across four categories based on the ligand type, *i.e.* inorganic, monocarboxylate, linear carboxylate and cyclic carboxylate (see Figure 2.17). Among these, the best performing magnetocaloric materials are typically found to incorporate only inorganic-based ligands, such as phosphates, borates and carbonates, likely because these smaller ligands yield structures containing higher densities of Gd^{3+} cations. One of the best performing magnetocalorics in this category is $GdPO_4$,[110] which features a high density of Gd^{3+} in combination with weak magnetic interactions and low magnetocrystalline anisotropy, with a magnetocaloric entropy change of up to 62.0 J kg^{-1} K^{-1} (376 mJ cm^{-3} K^{-1}) for a field change of 7 T, making this a very promising material for high field applications. Comparable materials are $GdBO_3$,[115] $Gd(OH)_3$,[45] and $GdOHCO_3$,[55] with the latter two having comparable and higher gravimetric magnetic entropy changes, respectively, but presenting a slightly lower volumetric entropy change due to their lower densities.
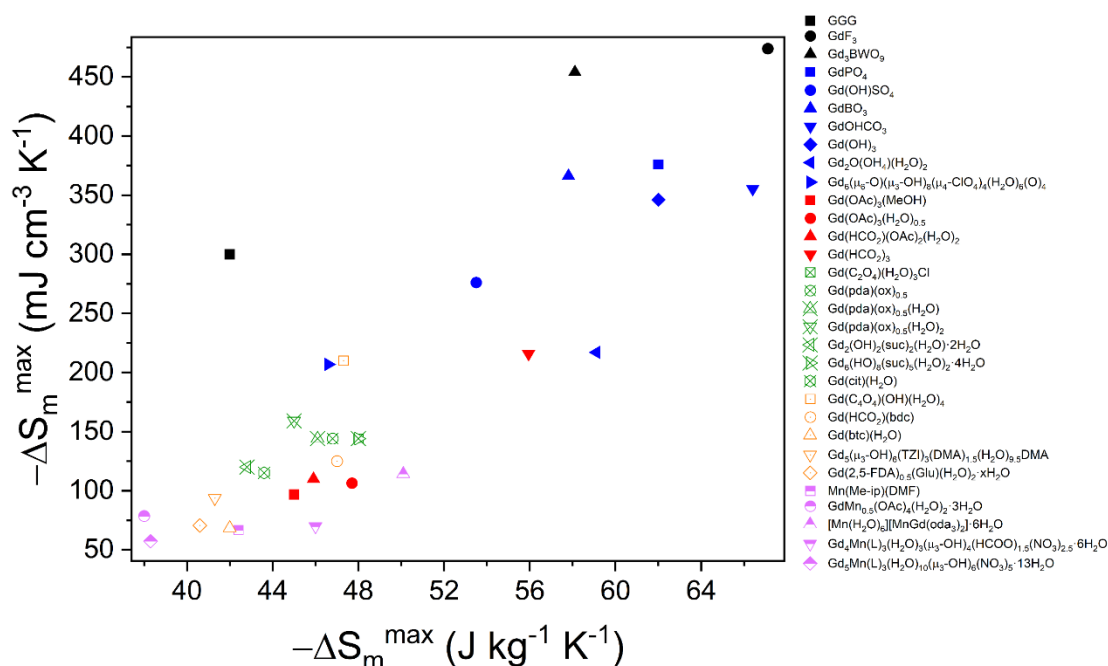
Figure 2.17: Plot of gravimetric and volumetric maximum entropy changes $-\Delta S_m^{max}$ of the materials discussed in this chapter. Presented here are inorganic-based (blue), monocarboxylate-based (red), linear carboxylate-based (green), cyclic carboxylate based (orange) and mixed $3d$-$4f$ (purple) materials along with selected high-performance conventional materials (black). The values presented here are for field changes of 7 T with the exception of those for which 9 T (GGG, Gd_3BWO_9, $GdBO_3$, $Gd(HCO_2)(bdc)$), 8 T ($Mn(Me\text{-}ip)(DMF)$) and only 5 T (GdF_3, $Gd(btc)(H_2O)$) values were available.

While there are a number of compounds associated with the other ligand groupings that exhibit $-\Delta S_m^{max}$ above 40 J kg^{-1} K^{-1}, and thus comparable to the commonly used benchmark material GGG, they generally exhibit more modest magnetic entropy change values with respect to those incorporating only inorganic ligands. There are, however, some notable exceptions to this, such as $Gd(HCO_2)_3$,[6,53] that highlight that magnetocalorics with simple carboxylates can offer comparable entropy changes to purely inorganic frameworks. It can be seen that coordination frameworks with more complex ligands, particularly where these lead to more porous structures, generally have much lower MCE due to their relatively low density of magnetic cations. Such MOFs, however, retain scope for multifunctionality that could be either used to enhance their magnetocaloric properties, e.g. *via* inclusion of simple magnetic guests in their pores such as simple neutral lanthanide complexes analogous to $[Mn(H_2O)_6][MnGd(oda)_3]_2\cdot 6H_2O$,[137,138] or by coupling another function with good, if not

excellent, magnetocaloric properties. In the pursuit of such multifunctionality, the use of simpler cyclic carboxylates, such as squarates,[129] and relatively small pore sizes that provide space for the desired guest or functionality, but does not unnecessarily reduce overall density, appears to be a sensible route forward. In contrast to the wide number of coordination polymers whose $-\Delta S_m$ have been characterised, further characterisation of the thermodynamic properties of even the most promising materials is still very limited. It will be important to address this in the future to enable the full potential of the most promising magnetocalorics to be determined. This is emphasised by examination of Table 2.1, which compares the ΔS_m^{max} and ΔT_{ad} of coordination polymers, for the limited number of materials where the later parameter has been reported. This shows that some materials with high $-\Delta S_m^{max}$ have relatively more modest ΔT_{ad}, which is often considered a more direct measure of magnetocaloric performance.

Looking beyond Gd-based materials, it has been noted that, amongst the 4f coordination polymers, there are a handful of examples where metal cations with significant magnetocrystalline anisotropy feature improved entropy changes for lower

Table 2.1: Available values of ΔT_{ad} for the compounds discussed in this chapter .

Compound	ΔT_{ad} (K)	$-\Delta S_m^{max}$ (J kg^{-1} K^{-1})	T_{max} (K)	ΔH (T)
GdPO$_4$	24.6	62.0	2.1	7
GdOHCO$_3$	24	66.4	2	9
Gd(HCO$_2$)$_3$	22	55.9	~1	7
Gd(C$_2$O$_4$)(H$_2$O)$_3$Cl	16.9	48.0	2.2	7
Gd$_2$(OH)$_2$(suc)$_2$(H$_2$O)·2H$_2$O	~17	42.8	2.6	7
Gd$_6$(OH)$_8$(suc)$_5$(H$_2$O)$_2$·4H$_2$O	15	48	1.8	7
Gd(btc)(H$_2$O)	~14	42	~20	5
[Mn(H$_2$O)$_6$][MnGd(oda)$_3$]$_2$·6H$_2$O	10.1	50.1	~2	3

field changes and higher temperatures compared to their Gd analogues. This renders these materials good candidates for a broader range of applications that require cooling above 4 K, as He is commonly used to do, rather than the < 2 K temperatures at which Gd materials typically show better performance. This is particularly the case when lower applied fields are needed, which are more readily achieved and offer the potential of using a permanent magnet rather than a more energy demanding superconducting magnet. Notably amongst these are $DyOHCO_3$ and $TbOHCO_3$,[120] which have higher $-\Delta S_m$ changes at and above 4 K than $GdOHCO_3$ for field changes below 2 T, and $Tb(HCO_2)_3$ and $Ho(HCO_2)_3$,[5] which offer similar improved magnetocaloric properties compared to $Gd(HCO_2)_3$. This suggests such properties are dependent on a combination of the single ion anisotropy and tailored magnetic interactions and thus designing structures where local magnetic interactions are optimised might be key to improving the magnetocaloric properties for cooling using low applied fields at higher temperature. Examples thus far focus on cases where there are strong ferromagnetic interactions within magnetic chain motifs but competing interactions between the chains due to geometric frustration. This enables the facile alignment of the moment on the chains along the direction of a modest external magnetic field while the frustration suppresses order to very low temperatures in the absence of an applied field. Similar behaviour might also be expected for well isolated chains in coordination polymers, such that the interchain interactions are weak enough that magnetic order does not occur until below the temperature at which these are useful magnetocalorics, although this would likely lead to lower $-\Delta S_m^{max}$ as a function of volume and, to a lesser extent, weight due to the dilution of the magnetic cations required by this additional spacing. It is also possible that other magnetic motifs may exhibit similar properties with anisotropic magnetic centres as indicated by the performance of $DyBO_3$ compared to its Gd analogue.[115] Thus,

investigation of the analogues of inorganic frameworks with anisotropic lanthanides offers a potential opportunity for improvement of magnetocaloric properties under lower applied fields with such materials including $Gd(OH)_3$, $Gd(OH)SO_4$ and $Gd_2O(OH)_4(H_2O)_2$.

Finally, $3d$-$4f$ mixed-metal coordination polymers have been discussed, with Gd-Mn polymers showing $-\Delta S_m^{max}$ comparable to the other classes of materials discussed with respect to weight. Although the lower density of these mixed metal MOFs leads to their entropy change as a function of volume being quite modest, it should also be considered that the materials reported thus far commonly have cyclic dicarboxylates that, even in purely $4f$ materials, commonly lead to poorer MC properties. The greater availability and lower cost of transition metals, however, makes $3d$-$4f$ frameworks or, as seen in $Mn(Me$-$ip)(DMF)$,[135] even $3d$ frameworks attractive as a way of enabling the use of magnetocalorics with a reduced dependence on the use of lanthanides. Thus, the magnetocaloric properties of $3d$-$4f$ and $3d$ frameworks based on inorganic ligands or small carboxylates, e.g. formate and oxalate, are worth further exploration. While it is possible these will have stronger magnetic coupling than the $3d$ containing polymers explored in this chapter, this should not prove an impediment to their application as magnetocalorics, provided magnetic order is supressed to below the desired ordering temperature by e.g. geometric frustration. Additionally, through the promising $-\Delta S_m^{max}$ of $GdMn_{0.5}(OAc)_4(H_2O)_2 \cdot 3H_2O$ for 3 T field changes,[136] there is some indication of there being a potential route for optimising MCE properties at lower applied magnetic fields.

In conclusion, a variety of coordination polymers featuring promising magnetocaloric properties have been described, highlighting the influence of a material's structure, including incorporation of smaller polyatomic ligands and optimisation of magnetic interactions, through use of low dimensional motifs and magnetic frustration,

as important factors to consider when designing materials for low temperature magnetic

cooling applications.

3 Experimental Techniques

3.1 Introduction

A variety of experimental techniques have been used throughout the research projects outlined in this dissertation and are presented in this chapter. The methods employed for the synthesis of the compounds under study will be discussed, followed by a description of the techniques used for the characterisation of the resulting target materials. The first and most fundamentally useful technique is powder X-ray diffraction, which is essential in rapidly determining the crystal structure of the products of a synthesis, provided the structure has already been solved, and identifying the presence of potential impurities. Single-crystal X-ray diffraction was also used for structural determination of those samples with single crystals of sufficient size for analysis. Neutron powder diffraction has been also employed as this technique allows probing of the position of the lighter atoms, such as hydrogen, in the nuclear phase, being complementary to X-ray diffraction in this respect, as well as the magnetic scattering indicative of average or local magnetic correlations. The results of the powder X-ray diffraction experiments have been analysed with methods such as Le Bail and Rietveld refinements. Superconducting quantum interference device (SQUID) magnetometry and heat capacity measurements have also been extensively used to determine the bulk magnetic properties of the materials under investigation. Thermogravimetric analysis (TGA), differential scanning calorimetry (DSC) and infrared spectroscopy (IR) have been used to gather further chemical insight regarding the properties of the materials studies throughout this thesis.

3.2 Synthetic Methods

The synthetic methods used to obtain the target materials will be described in this section for both "normal" and perdeuterated samples; the later are essential for high quality neutron diffraction experiments because ^{1}H possesses a very strong incoherent scattering component and, as a consequence, neutrons colliding with its nucleus and scattered from it will contribute significantly to the background of the measurements. Deuteration makes it possible to avoid this effect, greatly reducing the background of the signal and increasing the signal-to-noise ratio of neutron diffraction patterns.

3.2.1 Synthesis of the Lanthanide Formate Oxalate $Ln(HCO_2)(C_2O_4)$ Frameworks

Samples of $Ln(HCO_2)(C_2O_4)$ (Ln = Sm^{3+}–Er^{3+}) were synthesised under solvothermal conditions following a previously reported procedure with modifications.[140] 2 mmol of the appropriate $Ln(NO_3)_3 \cdot xH_2O$ (99%, x = 6 for Sm^{3+}, Eu^{3+}, and Tb^{3+}, Acros Organics and x = 5 for Dy^{3+}, Ho^{3+} and Er^{3+}, Alfa Aesar), 2 mmol oxalic acid (98%, Acros Organics), 0.8 mmol Na_2CO_3 (99.5%, Acros Organics), 3 ml N,N'-dimethylformamide (DMF, Fisher Scientific, 99%, reagent grade) and 3 ml distilled water were mixed in 25 mL Teflon-lined stainless steel autoclaves. These were then sealed and heated under autogenous pressure at 150 °C in an oven and left for 72 hours. After cooling to room temperature, the crystalline products were collected by vacuum filtration, washed with ethanol and allowed to air-dry.

About 2 g of deuterated samples of $Tb(DCO_2)(C_2O_4)$ and $Ho(DCO_2)(C_2O_4)$ for neutron diffraction experiments were synthesised by following the same procedure but were obtained from a combination of different batches of synthesis where D_2O (99.9%,

Acros Organics) and DMF-d_7 (99%, Goss Scientific) were used as solvents. The products were washed with ethanol-d_6 and left to dry in a desiccator.

3.2.2 Synthesis of Ce(HCO$_2$)$_3$, Pr(HCO$_2$)$_3$ and Nd(HCO$_2$)$_3$

Following a reported method,[51] samples of Ce(HCO$_2$)$_3$, Pr(HCO$_2$)$_3$ and Nd(HCO$_2$)$_3$ were synthesised by dissolving the metal precursors, namely Ce(NO$_3$)$_3$·6H$_2$O, Pr(NO$_3$)$_3$·6H$_2$O and Nd(NO$_3$)$_3$·5H$_2$O, in 4.75 ml formic acid (98+%, Fisher Chemicals) with the addition of 0.25 ml ethanol, used to dilute the solutions and slow the reactions down. After several minutes of stirring at ambient temperature, the release of NO$_x$ gases could be observed alongside the precipitation of pink products out of the solutions. The precipitates were collected by vacuum filtration, washed several times with ethanol and allowed to air-dry. Deuterated samples for the Ce and Nd members were synthesised following a similar procedure but employing deuterated formic acid (formic acid-d_2, 99+ atom % D, 95% solution in D$_2$O, Acros Organics) and deuterated ethanol (ethanol-d_6, 99 atom % D, Acros Organics) as solvents instead.

3.2.3 Synthesis of the Holmium/Erbium Formate Ho$_{1-x}$Er$_x$(HCO$_2$)$_3$ Solid Solutions

Following a literature procedure,[51] samples of Ho$_{1-x}$Er$_x$(HCO$_2$)$_3$ ($x = 0.1, 0.2, 0.3, 0.4, 0.5, 0.6, 0.7, 0.8, 0.9$) were synthesised by dissolving the metal precursors, Ho(NO$_3$)$_3$·5H$_2$O and Er(NO$_3$)$_3$·5H$_2$O, in the appropriate molar ratios, in 4.75 ml formic acid (98+%, Fisher Chemicals) with the addition of 0.25 ml ethanol. After several minutes of stirring at ambient temperature, the release of NO$_x$ gases could be observed alongside the precipitation of pink precipitates out of the solutions. The precipitates were collected by vacuum filtration, washed several times with ethanol and allowed to air-dry.

A sample of $Ho_{0.5}Er_{0.5}(DCO_2)_3$ for neutron diffraction experiments was synthesised *via* the same method, but using deuterated formic acid (formic acid-d_2, 99+ atom % D, 95% solution in D_2O, Acros Organics) and deuterated ethanol (ethanol-d_6, 99 atom % D, Acros Organics) as solvents instead.

3.2.4   Synthesis   of   the   Yittrium/Terbium   Formate $Y_{1-x}Tb_x(HCO_2)_3$ Solid Solutions

Samples of $Y_{1-x}Tb_x(HCO_2)_3$ (x = 0.20, 0.60, 0.80, 0.90, 0.95, 0.9750.975, 0.95, 0.90, 0.80, 0.60, and 0.20) were made by employing the same approach as above and reported in the literature,[51] by dissolving metal precursors, namely $Y(NO_3)_3 \cdot 6H_2O$ and $Tb(NO_3)_3 \cdot 6H_2O$, in appropriate molar ratios, in 4.75 ml formic acid (98+%, Fisher Chemicals) with the addition of 0.25 ml ethanol After several minutes of stirring at ambient temperature, the release of NO_x gases could be observed alongside the precipitation of white products out of the solutions. These precipitates were collected by vacuum filtration, washed several times with ethanol and allowed to air-dry.

3.3 Scattering Techniques

Techniques based on the phenomenon of the scattering of light or particles are among the most important in different fields of science, particularly in condensed matter physics. When a material is irradiated by an incident beam of electromagnetic (or particles) of wavevector k_i, the beam is scattered in multiple directions in space causing a change in direction described by a final wavevector k_f (see Figure 3.1).
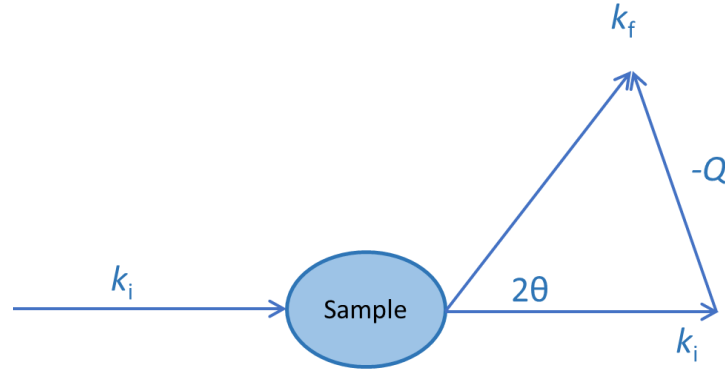
Figure 3.1 Diagram showing the phenomenon of elastic scattering from a sample.

To better understand this phenomenon, let's consider our ability to see objects in everyday life as an analogy: light from a source, such as the Sun, irradiates objects around us and the light is scattered across multiple directions. Some of this scattered light will then be collected by the human eye and an image of the objects is formed in the retina. Similarly, for much smaller objects, particularly those of microscopic size and for which optical microscopes are used, we make use of lenses that collect some of the scattered light, refract it and magnify the image of the object. Depending on the material irradiated and the wavelength of irradiating light, all of it can be scattered or some of it might be absorbed by the material due to waves of appropriate energy being responsible for excitation phenomena. In the first case, the phenomenon is said to be elastic and the wavevectors k_i and k_f differ only in direction while their magnitudes remain the same, that is $|k_i| = |k_f|$, whereas in the latter case the phenomenon is said to be inelastic and the two wavevector will have different magnitudes, that is $|k_i| \neq |k_f|$. The two wavevectors are then related by the momentum transfer Q, as shown in equation 3.1:

$$Q = k_i - k_f = \frac{2\pi}{d},$$
(3.1)

with d interatomic spacing. The smallest size of objects that can be seen with a microscope is set not simply by technical limitations in the manufacturing of lenses capable of sufficient magnification, but by the size of the objects themselves.

Wavelengths of visible light range from 400 to 700 nm in the electromagnetic spectrum, and bodies with a size below this range cannot be resolved using visible light. For this reason, the study of crystal structures, where the size of the atoms and their interatomic distances are in the order of magnitude of 10^{-10} m, or 1 Å, must occur by using light or particles of comparable wavelength. In the first case, we make use of X-rays whereas, in the latter, the particles most commonly used for the study of condensed matter are electrons and, more importantly in the context of this work, neutrons. It is then possible to collect information on the scattered waves, although it is not possible to immediately see an image of the crystal structure investigated as we would with macroscopic objects, with the exception of electron diffraction where appropriate lenses are available to reconstruct the image. When using x-rays and neutrons, it is necessary to make use of mathematical relationships between the object, *i.e.* the crystal, and the scattering pattern produced during the experiment.

3.3.1 Diffraction

The phenomenon of diffraction is regarded as one of the most powerful and useful techniques for the structural study of condensed matter materials and it is regarded as a non-destructive technique. Waves or particles hitting a sample are elastically scattered off the sample depending on the characteristics of the crystal structure and the interatomic distances of the atoms within it.

The physics and the mathematics behind the phenomenon of diffraction can be quite complex to use, but ground-breaking work carried by W.H. Bragg and L. Bragg allowed us to consider diffracted waves simply as waves reflected by planes of atoms in a crystal. While this is not a strictly correct physical interpretation of the phenomenon of diffraction, it significantly simplifies its mathematical treatment and has proven effective in interpreting the results of diffraction experiments. Let us consider two planes in a

crystal structure separated by interatomic distance d and an incident beam of waves or particles of wavelength λ irradiating the sample at an angle θ. Because each plane is
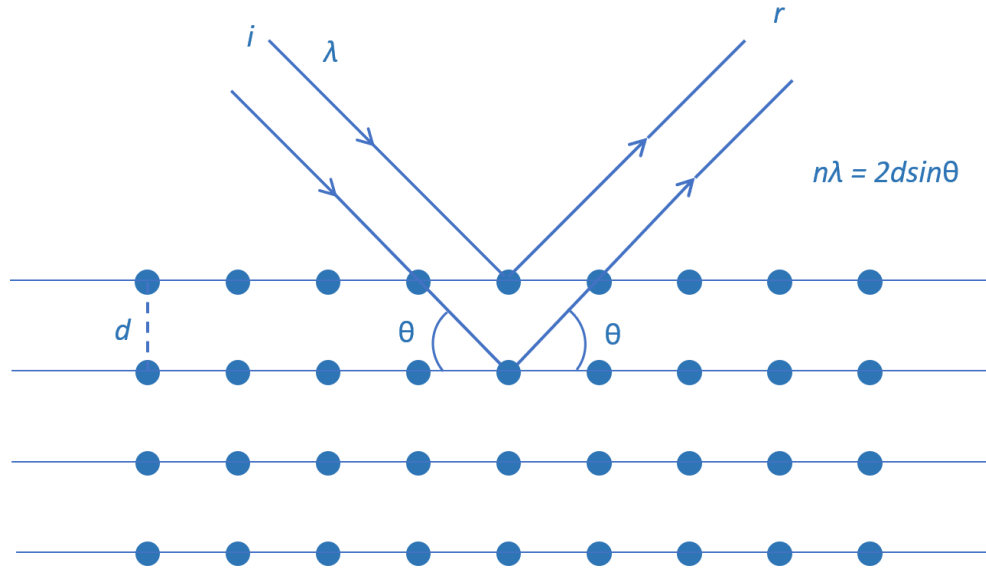
Figure 3.2 Two incident X-rays of wavelength λ and denoted by i, irradiating planes of atoms in a crystal structure separated by a distance d and being reflected (diffracted), as denoted by r, with θ being the incident and reflected angle.

reflecting the beam, reflected light with the same angle θ as the incident one will result. Furthermore, because the planes are separated from one another, both the incident and the reflected beam differ in pathlength. It is possible to have constructive interference only for those rays able to interact constructively, *i.e.* only for multiples of λ. This is clear in Figure 3.2 and it can be demonstrated that all the elements of this systems are related to one another *via* the following equation,[141] known as Bragg's law, which defines the condition for constructive interference:

$$n\lambda = 2dsin\theta. \tag{3.2}$$

Two or more waves reflected from a family of planes can then interfere constructively or destructively with one another. In the former case, the addition of the amplitudes of the waves results in a wave having an amplitude equal to the sum of the individual amplitudes, whereas in the latter case the same addition leads to the waves

cancelling each other, resulting in light and dark spots, respectively, on the diffraction pattern.

As mentioned in Section 3.3, it is possible to reconstruct an image of the object studied when using X-rays or particles thanks to mathematical relationships between an object and its corresponding diffraction pattern. The relationship between the crystal structure and the diffraction pattern produced during a diffraction experiment is known as the Fourier transformation.[141] Therefore, the diffraction pattern is the Fourier transform of the crystal structure and, *vice versa*, the crystal structure is the Fourier transform of the diffraction pattern. In principle, calculating the Fourier transform of the pattern allows us to obtain an image of the crystal under analysis. The Fourier transformation has the following form:

$$F(Q) = \int \rho(r) \cdot \exp(iQ\,r)\,dr\,, \tag{3.3}$$

where ρ is the electron density of an atom at a position r in the three-dimensional structure. The equation above can be applied for a continuous medium where an infinitely large number of particles are present, which is effectively true when considering a crystal of macroscopic size containing a very large number of particles in its structure. In reality, it is possible to express the same equation simply by considering the summation of a finite number of terms. Taking into account the dependence of Q on the atomic positions and the reciprocal lattice parameters, Eqn. 3.3 becomes:

$$F_{hkl} = \sum_j f_j(\theta) \cdot \exp\left[2\pi i\left(hx_j + ky_j + lz_j\right)\right], \tag{3.4}$$

where $f_j(\theta)$ is the atomic form factor for the j-th atom at a position defined by the coordinates x_j, y_j, z_j and h, k and l are the Miller indices defining the family of planes the atom lies on.[142] This form of the equation shows an important point: the intensity $I =$

$|F_{hkl}|^2$ of a diffracted beam on the pattern depends on individual atoms at their given position due to their form factors, the family of planes they belong to, and the collective effect of the diffraction itself as expressed by the summation operator. This equation is correct when X-rays are used to probe the structure. When neutrons are used instead, the atomic form factor $f_j(\theta)$ is replaced with the scattering length which will be discussed later on.

To obtain an image of the crystal structure, the reverse Fourier Transform must be calculated, and this provides information about the electron density $\rho(xyz)$. While it is possible to measure the intensities of the diffracted beams, proportional to $|F_{hkl}|^2$, and the contributions of the positions of the atoms for each family of planes, the information on the phases of the waves/particles used is lost during the diffraction experiment. This constitutes the well-known **phase problem**, and it is therefore not possible to use the Fourier transformation directly to obtain the image of the crystal, hence solve its structure. Fortunately, considerable effort has been put into finding methods to obtain the information necessary for the solution of the crystal structure.

3.3.2 X-ray Diffraction
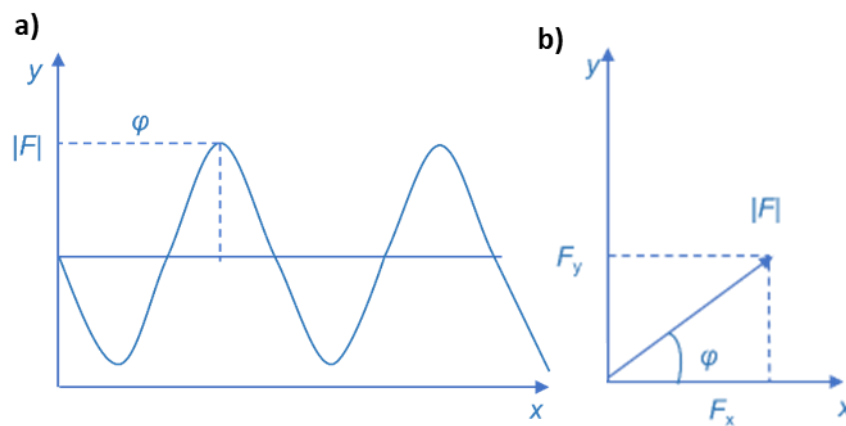
Figure 3.3 Two equivalent ways of representing radiation and particles: a) wave representation, with $|F|$ the amplitude of the wave and ϕ its phase, and b) vectorial representation, with $|F|$ the magnitude of the vector and ϕ the anticlockwise angle formed with the x-axis.

Diffraction experiments most commonly use X-ray radiation as the probe to determine crystal structures. This is because X-rays are easy to generate and there is a wide variety of equipment that can be used to conduct such experiments, ranging from large diffraction instruments to benchtop diffractometers. This makes X-ray diffraction one of the most readily available techniques for routine analysis of phase purity and quality of the crystalline phases when analysing powders or to determine novel crystal structures *ab initio* when single crystals are available. Of course, more sophisticated equipment exists, such as synchrotrons where intensities are orders of magnitude larger but here, only routine laboratory equipment will be considered, since this is used in the work presented in this thesis.

Traditionally, X-rays are generated using a Coolidge Tube in the following manner: a filament (the cathode) in a vacuum tube is electrically heated and electrons are emitted from it due to the thermionic effect. The electrons produced are then accelerated by a voltage, usually of 40–60 kV, towards a target material (the anode), typically made of copper or molybdenum, although other elements can also be used.[143] The collision of the electrons with the target material is responsible for a series of different phenomena. First, the kinetic energy of a great number of electrons is simply converted to heat, this being the reason for X-ray sources requiring a significant amount of continuous cooling to operate, lest the melting of the target material occurs. Meanwhile, the remainder of the electrons colliding with the target generates X-rays due to two main different processes.

In the first of these processes, the electrons are simply slowed down, and the energy lost is converted into X-ray radiation; this "white" radiation is often called **Bremmsstrahlung**, *i.e.* "braking radiation". In the second case, electrons of sufficient energy $E = h\nu$ cause the ejection of a core electron from the atoms of the target. The

vacancy is then filled by one electron of higher energy decaying into the lower energy orbital.

To do so, energy equal to the energy difference between the orbitals must be lost *via* the emission of X-rays, which has a **characteristic** radiation, $\lambda = hc/\Delta E$. As opposed to the Bremmsstrahlung radiation, which has a continuous profile with energy, X-rays emitted as a consequence of the decay of electrons to lower orbitals appear as sharp discrete peaks at defined energies depending on which material is being used and which inner orbital the outer electron is filling by losing its energy. Figure 3.4 shows this concept clearly, and depicts the radiation profile when copper is used as a source. It will be noted that the sharp, intense peaks of wavelengths 1.5418 and 1.3922 Å, respectively, are labelled using the symbols K_α and K_β, according to the Siegbahn notation, one way of describing spectral lines characteristic to elements. When copper is used as the anode these two different characteristic radiations are generated by the decay of electrons to the lowest energy orbital, as denoted by the letter K, but from different high-energy orbitals, as indicated by the letters α and β. It should be noted that the K_α radiation is the average of a doublet of two distinct radiations, K_{α_1} and K_{α_2}, of wavelengths 1.5406 and 1.5444 Å. The two peaks in Figure 3.4 have different intensities due to the different population of the energy levels and the probability of decay
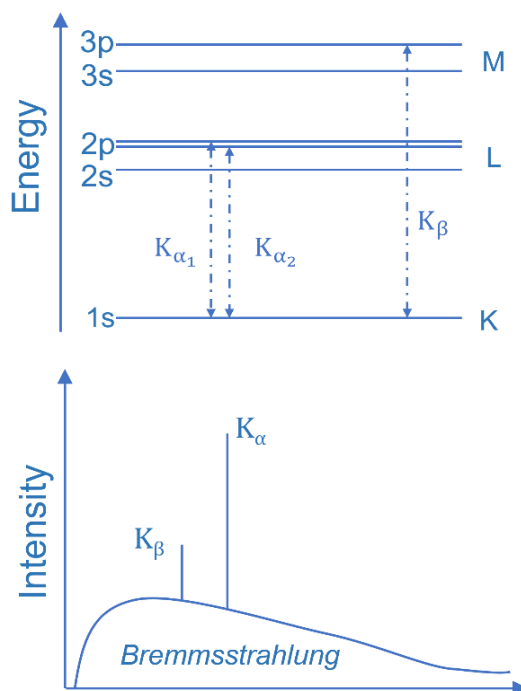
Figure 3.4 Diagram showing the energy levels involved in the generation of the characteristic radiation for copper (top) and the radiation profile resulting from the collision of electrons on a copper anode (bottom).

related to the energy itself. The most intense radiation is chosen by typically excluding all the other wavelengths *via* the use of filters and, for separating K_{α_1} and K_{α_2}, **monochromator** crystals that reflect only X-rays of the desired wavelength making use of Bragg's law.[143] In some cases, multiple monochromators can replace the filters for the same purpose, *e.g.* removing K_β.

The X-rays produced are then collimated and focused onto the sample using a series of slits of various dimensions which restrict the size of the beam and its divergence. The beams diffracted by the sample according to Bragg's law then travel towards detector slits and hit the detector where they are converted into electrical signals that can be recorded by computer software, hence generating the modern digital diffraction patterns used today as opposed to the obsolete, yet historically important, diffraction patterns on photographic film. Different devices are used nowadays to detect X-rays, including scintillation detectors or the more sophisticated line and area detectors, the latter allowing for the detection of X-rays at different angles simultaneously rather than one angle at a time, acting in many respects as "electronic films" analogous to the photographic ones.[141] The efficiency of each detector is obviously tied to the technologies employed for their fabrication and functionality, which are beyond the scope of this description. What has been described so far are the essential elements of any X-ray diffractometer, whether this is used for single-crystal or powder diffraction experiments.

Single-crystal X-ray diffraction is a powerful technique which enables the structure of a crystal to be determined *ab initio*, that is without any prior knowledge of what this structure might be. In a single-crystal diffractometer, a single crystal is rotated about three axes and the diffraction pattern is collected as a two-dimensional map from which an electron density map can be calculated and, ultimately, the structure determined. What is especially important is that the map acquired by such a technique

makes it possible to test for different potential symmetries when many are plausible, along with separating out reflections with different *hkl* with the same or similar *d*-spacings. On the other hand, powder X-ray diffraction is not sensitive to the orientation of the crystals. As a matter of fact, polycrystalline samples are used here, and they are ground in order to further randomise the orientation of the crystallites. This procedure ensures that any preferred orientation is minimised, and the pattern represents the average structure of the crystallites without any amongst them dominating the pattern, *e.g.* a particular family of planes of indices *{hkl}*. Furthermore, the information collected using powder diffraction is condensed into one dimension, with reflections having similar *d*-spacing easily overlapping, and no map is obtained. This makes it difficult, although not impossible, to solve a structure using powder diffraction without prior knowledge of it. Despite this limitation, the technique is still a powerful one. In addition to powders being easier to obtain than single crystals, powder diffraction is indeed a fast and easy to use technique, widely employed for the identification of the phases in a sample, to assess its purity and the quality of the crystals, and can be used to determine properties such as the size and the strain of the crystallites forming a polycrystalline sample. Similar considerations apply to single-crystal and powder neutron diffraction as well.

X-Ray Diffraction: Experimental Details

Within the context of this research, both powder and single-crystal diffraction have been employed for the study of the material synthesised in the laboratory. Powder X-ray diffraction was used on ground polycrystalline samples with a Malvern Panalytical X'pert 3 powder diffractometer equipped with an Empyrean Cu LFF source ($\lambda_{\text{CuK}_{\alpha_1}}$ = 1.5046 Å, $\lambda_{\text{CuK}_{\alpha_2}}$ = 1.5444 Å), a Ni filter for the CuK$_\beta$ radiation and an X'Celerator line detector, with samples mounted on zero-background silicon sample holders. The X-ray

generator operates at 40 kV and 40 mA and the sample holders are held in a reflection-transmission spinner PW3064, with the samples measured in a θ-θ configuration, *i.e.* the sample is fixed on an horizontal plane whereas the source and the detector move together in discrete steps according to the step size.

Single-crystal X-ray diffraction was used to determine the structures of $Tb(HCO_2)(C_2O_4)$ and $Ho(HCO_2)(C_2O_4)$ using a Supernova Rigaku Oxford Diffraction diffractometer. This instrument is equipped with two selectable microfocus sources, CuK_α — used in the measurement of the samples — and MoK_α ($\lambda = 0.71$ Å), and an Atlas S2 CCD area detector. The samples were cooled with nitrogen at 120 K using an Oxford Cryostream to reduce the thermal effects and improve the quality of the data. The data obtained from the experiment was indexed, integrated and reduced using the software CrysalisPro 1.171.40.53,[144] with absorption corrections performed using the same software package. The structures were then solved using SHELXT-2015,[145] and refinements of the structure were carried out using a least-squares method by SHELXL-2015 within the Olex2 graphical user interface.[146,147]

3.3.3 Neutron Diffraction

As mentioned earlier, particles such as neutrons, which possess wave-like properties, can also be used to study the structure of materials. One of the most widespread techniques using particles for the study of condensed matter is neutron diffraction. The use of neutrons offers several advantages. Firstly, neutrons are able to accurately probe the position of light atoms, such as deuterium, and hence indirectly that of hydrogen. While this is not possible with X-rays due to the direct correlation between the intensity of scattering and the number of electrons of an element, the scattering of neutrons has no such correlation. As will be later explained, neutrons interact mainly

with the nuclei of the atoms, and the scattering from light atoms can be significant. Secondly, neutrons of adequate energy have a higher penetration depth than X-rays both due to their zero-net charge — therefore being unaffected by the electron clouds of the atoms — and the interaction with the nuclei *via* the *strong interaction*, which only happens at very short distances and is responsible for the weak scattering of neutrons by the nuclei. This allows the bulk properties of the material to be probed. Finally, neutrons possess a magnetic moment, hence they are sensitive to the magnetic dipoles within a material, making them excellent probes for magnetic structures.

3.3.3.1 Production of Neutrons

Neutrons were discovered by James Chadwick in 1932, while irradiating beryllium with α-particles from the decay of polonium (^{210}Po).[148] The nuclear reaction that follows is responsible for the ejection of a neutron from the beryllium nucleus:

$$\alpha + \ {}^{9}Be \rightarrow {}^{12}C + n \ . \tag{3.5}$$

This process can produce 10^6 to 10^8 neutrons per second.[149] A much higher production of neutrons is possible thanks to nuclear **fission**.[149] During this process, a heavy nucleus splits into two lighter and more stable nuclei, generating γ-rays, neutrons and subatomic particles. For this purpose, uranium enriched with its rare isotope, ^{235}U, is used. Free neutrons, produced by a spontaneous fission of ^{235}U itself or by the interaction of cosmic rays in the atmosphere and matter, interact with ^{235}U. The unstable ^{236}U isotope results, and this decays in a number of different ways, including the following:

$$n + {}^{235}U \rightarrow {}^{236}U \rightarrow {}^{134}Xe + {}^{100}Sr + 2n. \tag{3.6}$$
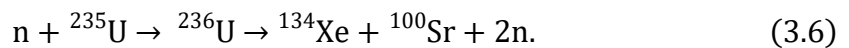
It must be noted that this mechanism generates two neutrons per reaction. A combination of all the mechanisms occurring will generate an average of 2.5 neutrons per event. In addition to this, as will be easily understood from Eqn. 3.6, the production of neutrons

results in a self-sustained chain reaction where ^{235}U is continuously bombarded, since

they initiate the fission events.[149] This allows for the generation of a neutron flux of 10^{15} s$^-$

^{1}cm^{-2} in research reactors. This happens only when neutrons of adequate
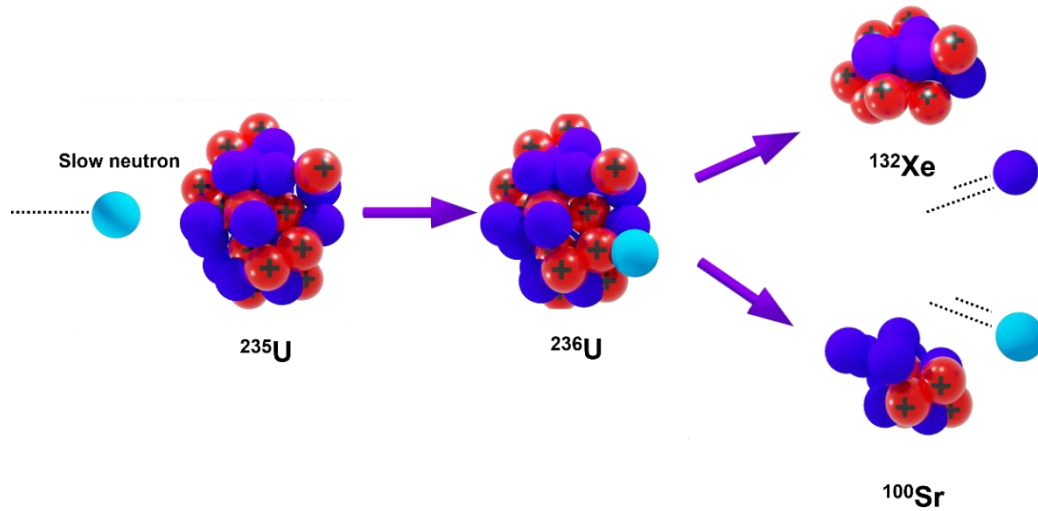
Figure 3.5 Pictorial diagram showing one of the mechanisms for the fission of ^{236}U following the collision of a neutron with a ^{235}U atom. In this case, ^{132}Xe and ^{100}Sr form as fission products, along with two neutrons per event. Other decay mechanisms are possible.

energy hit the ^{235}U nuclei. The nuclei ejected after the decay of ^{236}U are too fast, that is

they have a high kinetic energy. It is then necessary to use a **moderator** — typically

graphite or heavy water — that absorbs some of the kinetic energy of the neutrons within

the reactor core, effectively slowing them down. This process, called **thermalisation**, is

also vital for the diffraction experiments themselves as the energy of the probing neutrons

would be too high otherwise: the kinetic energy is related to the wavelength λ according

to the de Broglie equation:

$$\lambda_n = \frac{h}{m_n v_n},\qquad(3.7)$$

where m_n and v_n are the mass and the velocity of the neutrons and h Planck's constant

($6.62607015 \times 10^{-34}$ m^2 kg^{-1} s^{-1}). Hence, one or more moderators can be used to tune the

wavelength λ for the experiments, as necessary. Thermal neutrons therefore have an

average kinetic energy comparable to that of the atoms constituting the medium they are

interacting with. A single wavelength can then be selected by simply using a single-

crystal monochromator, allowing for constant-wavelength neutron diffraction experiments.

A second method used to produce neutrons is **spallation**.[149] This method is based on the acceleration of protons within a synchrotron. A flux of high-energy protons (typically ~1 GeV) hits a target material made of a heavy element, for example tungsten, and this ejects subatomic particles, mainly proton and neutrons. Following this, more neutrons will be ejected due to the relaxation of nuclei excited upon impact, these neutrons having a considerably lower energy than that of the previous batch and therefore easier to moderate for experiments. As opposed to neutrons generated in a nuclear reactor by fission, which provide a *continuous* flux of neutrons because of the chain reactions occurring within the reactor core, neutrons produced by spallation come in discrete pulses, hence the name "pulsed source". Pulses are characterised by their own duration (*i.e.* the window of time during which spallation is occurring and neutrons are produced) and by a repetition time τ between each pulse (*i.e.* the time necessary for a group of protons to reach the target material), as shown in Figure 3.6.
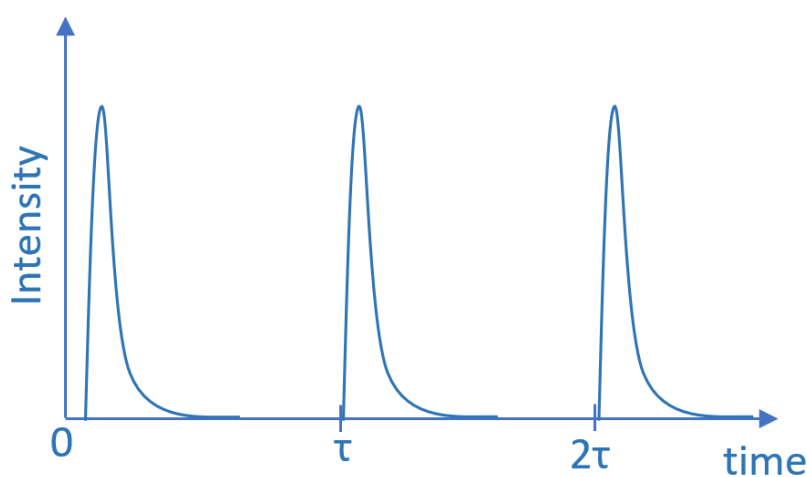
Figure 3.6 Schematic depiction of the pulses of thermal neutrons after the moderation step at a spallation source. The pulses are intense and repeat regularly after period τ.

One of the advantages of using the spallation method lies in the higher number of neutrons that can be generated for the experiment while also producing less heat, with nuclear sources producing four to five times as much. The selection of neutrons of a desired wavelengths after thermalisation does not occur by using monochromators, but *via* devices known as *choppers* which rotate at certain frequencies such that only neutrons having a sufficient speed can pass through a slit, while the rest of them are removed. This allows ranges of wavelengths to be selected with the result that polychromatic neutrons are used. Using a polychromatic beam is possible because the flight path L is known, as well as the time t from the collision of the protons onto the target material and the detection of the resulting neutrons from detectors, fixed around the sample container. Neutrons with different energies will be detected at different times due to their different wavelengths and velocities as shown by Eqn. 3.7. This forms the basis of the time-of-flight technique, with spallation sources existing since the 1980s, and becoming increasingly common in the last three decades. Important spallation sources are the ISIS Neutron and Muon Facility, UK,[150] the Spallation Neutron Source (SNS), Tennessee, USA,[151] the Japan Proton Accelerator Research Complex (J-Parc), Japan,[152] and the upcoming European Spallation Source (ESS), Sweden.[153]

3.3.4 Difference Between X-rays and Neutrons

Neutrons produced *via* the two methods above can be used for a variety of scattering experiments, both elastic or inelastic in nature, the latter type referred to as "spectroscopy". The main important difference between neutrons and X-rays lies in their interaction with matter. While the diffraction of X-rays is caused by the electrons surrounding the nuclei of an atom, neutrons interact with the nuclei themselves. As a result, in neutron experiments the structure factor F_{hkl} does not depend on the atom form factors $f(\theta)$, which are directly related to the number of electrons of an element. It is

necessary to consider the **scattering length** of an atom, b, which quantifies the scattering interaction of a neutron with its nucleus. This depends on the composition of the nucleus and the orientation of the nuclear spins. The scattering length b cannot be predicted from theory,[154] and for this reason there is no law to predict how b varies with the atoms, unlike the case for the atomic form factors in which the process is well understood and related to the atomic numbers. Due to the strong dependence on the nucleus composition, the scattering lengths of nuclei are specific to each isotope and do not vary in a monotonic way with the atomic number.[149] Furthermore, nuclear spins can adopt different configurations, leading to different values of b, hence an average scattering length $<b>$ must be used instead. Historically, this complexity has led to the determination of the scattering lengths using an entirely empirical and time-consuming approach. It is also necessary to point out that the scattering length has little to no dependence (as it is often assumed for elastic scattering, where no resonance phenomena are present) on the scattering angle and the wavelength used, in direct contrast to the atomic form factors $f(\theta)$, due to the

3.3.4.1 Neutrons and Magnetism

As mentioned previously, neutrons are excellent probes for the study of magnetic structures. This is because, despite having no net charge, neutrons have a ½-spin and therefore possess a magnetic dipole moment μ_n:

$$\mu_n = -1.913\mu_N, \quad\quad\quad (3.8)$$

with μ_N, the *nuclear magneton*, 960 times smaller than the Bohr magneton, which describes the magnetic moment produced by a single electron precessing around a unitary magnetic field, and with the discrepancy resulting from the different masses of heavy

nucleons and electrons. With a spin $s = $ ½, neutrons can adopt only two different spin configurations, either spin-up or spin-down.[149]

Understanding the magnetic dipole-dipole interactions of neutrons with the magnetic moments within a material can be made easy by picturing the interaction between two bar magnets. When such a simple experiment is carried out, it can be immediately noticed that the interactions between the two magnets depends on their relative orientation. Repulsion between the magnets occurs if their poles are alike (N-N or S-S) whereas attraction between different poles can be observed. Therefore, the magnetic interaction between two magnetic poles is strongly anisotropic. This phenomenon is identical at a microscopic level and influences the scattering by the magnetic lattice. When a neutron is scattered along a direction defined by the scattering vector Q, this implies that the neutron has been affected by the component of the magnetisation M that is perpendicular to it. The scattering length of a magnetic ion is described as:

$$F_{\mathrm{m}}^2 = b^2 + 2bpq \cdot \hat{v} + p^2 q^2,\qquad(3.9)$$

with b the nuclear scattering amplitude, p the magnetic scattering amplitude, $\hat{v}$ the unit vector direction of the scattered neutron and q given by:

$$q = \hat{\varepsilon}(\hat{\varepsilon} \cdot \hat{\kappa}) - \hat{\kappa},\qquad(3.10)$$

where $\hat{\varepsilon}$ is the unit vector describing the direction of the neutron beam and $\hat{\kappa}$ is the unit vector describing the direction of the magnetic moment. The term p in Eqn. 3.9 is described as:

$$p = \frac{e^2 \gamma}{2m_{\mathrm{e}}c^2} g_J J f,\qquad(3.11)$$

where $g_J J$ is the magnetisation perpendicular to the direction of the momentum transfer, e is the electron charge, m_e the mass of an electron, c the speed of light, γ the neutron magnetic moment (earlier described as μ_n) and f is the magnetic form factor. It can be seen from the above that for magnetic moments that are parallel to the direction of the neutron beam, q tends to zero, hence the scattering length F_m will depend on the nuclear scattering amplitude only.

As magnetic scattering is caused by magnetic dipoles — hence by unpaired electrons — the phenomenon can be described by using magnetic form factors which follow a similar trend to the atomic form factors for X-rays, that is f depends on the atom, the wavelength used for the experiment and decays with the angle θ.[149] It is important to note that the decay of the magnetic form factor occurs at a much faster rate than that of the atomic form factors. Indeed, while X-ray scattering depends on the entire electron density $\rho(xyz)$, magnetic scattering is affected only by the unpaired electrons of the atoms, therefore resulting in an increasingly smaller contribution to the cooperative diffraction from the electrons per atom with the angle. It is therefore essential to probe low Q regions in order to maximise the collection of signal arising from the magnetic structure of a sample. The spin-only contribution to the magnetic form factor can be described by $<j_0>$ having the following form:

$$< j_0 > = A^{-as^2} + Be^{-bs^2} + Ce^{-cs^2} + D. \tag{3.12}$$

The orbital contribution to the magnetic moment is described by:

$$< j_2 > = s^2 \left(A'e^{-a's^2} + B'e^{-b's^2} + C'e^{-C'e^{-c's^2}} + D' \right). \tag{3.13}$$

In both cases, the empirical constants A, a, B, b, C, c and D are listed in the International Tables for Crystallography Vol. C,[154] as well as on the Institut Laue-Langevin website.[155] The constant j_2 is essential when strong spin-orbit coupling is

present, such as in the case of lanthanides. The form factor of an atom is then described

as:

$$F = <j_0> + C_2 <j_2>,\tag{3.14}$$

with C_2 being the ratio between the orbital magnetic moment and the total contribution

of the magnetic form factor.

3.3.4.2 On Neutron Instruments

Neutron diffraction experiments presented in this work were carried out using

different diffractometers, namely the General Materials (GEM) diffractometer and the

"Wide Angle in a Single Histogram" (WISH) at the ISIS Muon and Neutron source,

Rutherford Appleton Laboratory,[156] with the help of Dr Ivan da Silva in carrying out the

experiments for the former and Dr Manuel Pascal for the latter, as well as the Wombat

high-intensity powder diffractometer at the OPAL reactor, located at the Australian

Nuclear Science and Technology Organisation (ANSTO),[157] thanks to the assistance of

Dr Andrew Studer, as access to the facilities was not allowed during the COVID

pandemic. The GEM beamline has been designed with the purpose of measuring high-

resolution scattering patterns over a wide range of Q, with minimal contributions from

background scattering. This is achieved by using ZnS scintillation detectors, which have

a low intrinsic background noise, and by collimation of the incident and scattered neutron

beam. The detectors are arranged in seven banks (numbered from 0 to 6) around the

sample at different scattering angles and offer a detection area of 14 m^2. The instrument

has a resolution of $\Delta d/d = 2$–3×10^{-3} in backscattering and $\Delta d/d = 5 \times 10^{-3}$ at a scattering

angle of 90° at all d-spacings. The fixed detector geometry also easily allows changing

the sample environment to suit specific needs for each experiment. Samples of

$Tb(DCO_2)(C_2O_4)$ and $Ho(DCO_2)(C_2O_4)$ were measured in a 1.6–300 K range, cooled in

a 8mm vanadium can using an Oxford Instruments Variox cryostat. Similarly, a sample

of $[Li(C_2O_4)]_2[(Co_5(OD)_8]$ was measured in a 8–300 K temperature range.

A sample of $Ho_{0.5}Er_{0.5}(DCO_2)_3$ was measured using WISH at 100, 10, 2 and

0.28 K at the ISIS Muon and Neutron source, Rutherford Appleton Laboratory,[158]

Dr Pascal Manuel carrying out the measurement as access was not allowed during the

COVID pandemic. WISH is a long-wavelength diffractometer designed to carry out large

d-spacing measurements in a range from 7–17 Å, both on powders and single-crystals.

Accessing long d-spacings is extremely useful for structures possessing large unit cells

and magnetic interactions, as this allows probing lower Q-spacings (see Eqn. 3.1) where

the magnetic reflections are the most intense. This is achieved by the combination of the

high-brilliance of solid-methane moderators, position-sensitive ^{3}He detectors covering

scattering angles from 10 to 170°, and tunable resolution. WISH can operate in three

different resolution modes — low, medium and high resolution — depending on the setup

of the piezoelectric slits that tune the divergence of the incident neutron beam. In

high-resolution mode, it is possible to achieve $\Delta Q/Q = 3\times10^{-3}$ at high-resolution frames.

WISH also possesses a low instrumental background that enables the detection of weak

magnetic Bragg-like or diffuse features in the scattering pattern which would otherwise

be hidden by instrumental noise. Measurements of $Ho_{0.5}Er_{0.5}(DCO_2)_3$ were carried out

between 0.28 K to 300 K, with the sample loaded into an 8 mm vanadium can and cooled

using an Oxford Instruments Variox cryostat.

Elastic neutron scattering experiments on samples of $Nd(DCO_2)_3$ and $Ce(DCO_2)_3$

were performed using Wombat. This constant wavelength instrument is used primarily

as a high-speed powder diffractometer, although its capabilities go beyond this purpose.

Its fast data collection rate is enabled by its continuous 120° area detector, having a low

intrinsic background level, a large beam guide and a large crystal monochromator. This

provides a high-flux of neutrons, up to 10^8 ns^{-1} cm^{-2} at the sample position, with a resulting high-count rate of 10^6 s^{-1}. Nd(DCO$_2$)$_3$ and Ce(DCO$_2$)$_3$ were measured from room temperature down to 140 and 50 mK respectively, with samples cooled using an Oxford Instruments Kelvinox DL1 low-temperature insert with a CF-10 top loading closed-cycle refrigerator.

3.4 Structure Refinement Techniques

After diffraction experiments are carried out and sufficient data is collected, it is necessary to produce a model that reproduces the data, therefore providing a representation of the average structure.[141] This is carried out with the use of software that employs statistical methods to fit a structural model to the data. This process is not completely automated and requires considerable effort depending on the complexity of the structure and the data collected, that is the refinement must be guided in order to produce a physically sensible model. The last step in the refinement process is to check if the final model is reasonable in terms of the chemistry; the software does not know if the calculated model structure is sensible or whether it contains components that would be impossible from a chemical point of view.

A wide variety of software packages is available to carry out structural refinements at the heart of which the same principles are shared, and these will be discussed first. Two of the main methods used for structure refinements are the Rietveld refinement and Le Bail extraction methods.[159,160]

3.4.1 The Rietveld Method

One of the most powerful ways to refine accurate average models of both nuclear and magnetic structures using the data collected from powder diffraction experiments is

the Rietveld method, first described by the Dutch crystallographer Hugo M. Rietveld in 1969.[159] This is a whole powder pattern fitting method, where model parameters, including cell parameters, are fitted to the whole pattern simultaneously using a least-squares approach. This is in contrast with older historical methods where the reflections were treated separately and their positions refined individually, without unit cell restraints.[161] In the Rietveld method, a pre-existing model, as close as possible to the structure to be refined, must be used. Therefore, prior knowledge of the crystal structure must be possessed before a refinement can be attempted. Model parameters are then optimised according to the sample and the instrument used, and they include the unit cell parameters, the atomic positions, the atomic displacement parameters, utilising either an isotropic or anisotropic model, the peak shape profile, the sample zero offset and the background. The parameters are refined gradually, ideally including them one at a time, and the sequence can vary considerably, although guidelines have been devised in order to optimise the process.[162,163] It should also be pointed out that the number of parameters used should be as low as possible to avoid over-fitting the data.

The brilliance of the Rietveld method relies on a simple concept: instead of extracting the integrated total intensities of the observed reflections directly, the contributions to that reflection are estimated on a point-by-point basis. Indeed, in powder diffraction, the observed reflections are often the results of a number of reflections overlapping due to the close *d*-spacing values. This implies that the extraction of intensities directly, employed in older methods, neglected a significant amount of information that is "hidden" in the powder diffraction pattern. The application of the Rietveld method was made possible by the advent of computers capable of handling more resource-demanding calculations. Before that, manually estimating the intensities of each expected reflection under a diffraction peak was too prohibitive to achieve.

During a Rietveld refinement, calculated intensity values, I(calc), are generated according to the crystallographic model: the atoms in the structure, their form factors and their positions, although not accurate during the initial stages of the refinement, all contribute to the estimation of groups of reflection intensities, $\sum I(hkl)$. The method then relies on a least-squares minimisation approach, where the quantity to be minimised is:

$$\sum_i w_i[y_i(obs) - y_i(calc)]^2 \, , \qquad (3.15)$$

where w_i is the weight, corresponding to the reciprocal of the estimated uncertainty, $1/\sigma^2[y_i(obs)]$, $y_i(obs)$ and $y_i(cal)$ are the observed and calculated intensities, respectively. The model parameters are therefore modified to achieve such a minimisation.

To estimate the quality of the fit resulting from a Rietveld refinement, hence understanding how closely the model is representing the data, a series of discrepancy terms have been proposed in the literature.[164] None of these parameters alone can be used to evaluate the quality of a refinement, but they rather need to be used together, along with the visual aid provided by the software used, showing clearly how the calculated pattern is overlapping with the observed data. It is indeed possible to obtain discrepancy terms that indicate a very good fit of the data, only to find out the data is significantly misrepresented due to the refinement reaching false minima during the least-squares minimisation. These discrepancy terms will be briefly discussed here, with details being provided in Appendix A.

The most used and straightforward of these discrepancy terms is the weighted profile R-factor, R_{wp}, with "R" standing for "reliability", obtained by considering the square root of the minimised quantity scaled by the weighted observed intensities. A much simpler version of this parameter, the R_p factor, simply ignores the weights. It is possible to obtain a third parameter, the expected R-factor, R_{exp}, which corresponds to

the best R_{wp} achievable while fitting the data in the ideal situation that the calculated values during the refinement are the "true" values of the observed intensities, that is $y_i(calc) = y_i(obs)$, the only error left in the refinement being only the intrinsic uncertainty from data collection.

Finally, an important term used to assess the quality of a refinement is known as the chi-squared value, χ^2. While this parameter should ideally be one, just like R_{exp}, in practice it only approaches unity depending on the quality of the fit. At the beginning of the refinements, χ^2 tends to assume very large values due to the high discrepancy between the starting model and the data against which it is refined, and ideally χ^2 should never increase during a least-squares refinement. In practice, small increases can occur when the parameters being refined are correlated with one another. It must also be noted that under no circumstance χ^2 should drop to values below one, as $\chi^2 < 1$ would imply that the fit is better than the uncertainty $\sigma[y_i(obs)]$ itself, implying that either the $\sigma[y_i(obs)]$ are overestimated or the refinement algorithm is attempting to fit noise in the powder pattern.

Other Factors in Rietveld Refinements

It was previously discussed how the Rietveld method calculates the intensities of the reflections in the powder data. We now briefly turn our attention to other factors that strongly influence the diffraction data and, therefore, the Rietveld refinement of the structural model.

The background of a diffraction pattern affects the refinements, and this must be estimated. Various ways of dealing with the background in the data are possible. One approach is to specify some points in the background, linearly interpolate them and subtract the resulting background from the data. In theory, this procedure needs to be

repeated several times during the refinement to represent the background contribution progressively better, mainly because in complex datasets, the peaks are rarely resolved to baseline. A different approach consists in fitting functions that represent the background, such as polynomial functions such as the Chebyshev polynomials,[165] amongst others. The use of functions allows for the automatic fitting of the background while refining the structural parameters. However, these functions tend to be empirical or semiempirical, meaning they will work only if they happen to well represent the background. A combination of the two methods can be employed in some software, *e.g.* fitting the background using a function and correcting deviations by means of interpolated fixed points.

The shape of the peaks needs to be calculated as well and will largely depend on the type of measurement being carried out. For X-rays and constant wavelength neutrons, the peak shapes can be represented by a combination of a Gaussian and a Lorentzian curve or pseudo-Voigt curve. The pseudo-Voigt function is a linear combination of a Gaussian and a Lorentzian component according to the ratio $\eta/(1 - \eta)$, where η is the pseudo-Voigt mixing parameter. This function is often used and represents very well the symmetric part of the peaks. However, the peaks contain an asymmetric component due to the axial divergence of the diffracted beams at low angles. This can be taken into account, for example using the Finger-Cox-Jephcoat (FCJ) asymmetry function,[166] but other functions can be used as well. In addition to that, the diffraction profile width changes with the angle 2θ. To take this into account, the Caglioti function is often used:

$$FWHM^2(\theta) = U \tan^2(\theta) + V \tan(\theta) + W, \qquad (3.16)$$

where FWHM is the full-width-half-maximum of a reflection and *U*, *V* and *W* are parameters to shape the function.[167] This function well represents how the Gaussian

component to the reflection changes with the angle, but not the Lorentzian component. For the latter, a separate function needs to be used:

$$FWHM(\theta) = X tan(\theta) + \frac{Y}{cos(\theta)}, \qquad (3.17)$$

where X and Y are the Lorentzian parameters. For X-rays and constant wavelength neutrons, the position of the reflections can be easily calculated from a modified version of Bragg's law (Eqn. 3.2) where the zero instrumental offset is included:

$$d = \frac{\lambda}{2 \sin(\theta + zero)}. \qquad (3.18)$$

When TOF neutrons are used, the situation is more complicated. An extra asymmetric component contributing to the peak shapes is present. This is related to the pulsed nature of the neutron beam, which causes an additional broadening effect. In 1982, Von Dreele et al.[168] developed an empirical function describing such a component, consisting of a series of back-to-back exponentials convoluted with a Gaussian function:

$$H(\Delta T) = N[\exp(u)\, erfc(x) + \exp(v)\, erfc(y)], \qquad (3.19)$$

where H is the peak-shape function for a reflection, *erfc* is the complementary error function and N, u, v and y depend on the d spacing of the reflection, the scattering angle of the detector and characteristics of the neutron source. The description of the diffraction profile is a more complex one as well, with the Gaussian and Lorentzian of the TOF peak shape described by the following equations:

$$FWHM_G = \sqrt{\sigma_0 + \sigma_1 d^2 + \sigma_2 d^4}, \qquad (3.20)$$

$$FWHM_L = \gamma_0 + \gamma_1 d + \gamma_2 d^2. \qquad (3.21)$$

The time of flight has a quadratic dependence on the d-spacing:

$$TOF = zero + DIFC \cdot d + DIFA \cdot d^2, \qquad (3.22)$$

where zero is the detector electronics delay in processing the signals (reported in microseconds), *DIFC* and *DIFA* are constants related to the instrument. In particular, *DIFC* is determined by the flight path *L*, the detector angle θ, the mass of the neutron m_n and the Planck constant *h*:

$$DIFC = \frac{2m_n L sin\theta}{h}. \tag{3.23}$$

The time-of-flight of neutrons is also affected by absorption, with the absorption cross-section of neutrons by atoms being proportional to the wavelength. Therefore, neutrons with a longer wavelength will be absorbed more easily, resulting in a change in penetration depth and, therefore, the time-of-flight. DIFA introduces small corrections related to this inevitable absorption effects and allows for the resulting peak shifts. More information about Rietveld refinements of both X-ray and neutron data along with a description of the equations can be found in the manual for the refinement software FullProf.[169]

In order to carry out average structure refinements, two refinement programs have been used in this research project. For laboratory X-ray data, LHPM-Rietica has been used,[170] whereas GSAS & EXPGUI has been the software of choice for the refinement of TOF neutron data.[171]

3.4.2 The Le Bail Method

The Le Bail method was first introduced by A. Le Bail in 1988 and is a whole-profile pattern fitting method.[160] The main difference between the Le Bail and Rietveld methods is that, while the latter requires prior knowledge of the atoms in the crystal structure and their form factors to calculate the intensity of the reflections, the Le Bail method does not require this information. While the unit cell parameters, instrumental

zero error and the peak parameters are refined using a least-square method, the intensities are not. Consequently, the calculations are very rapid which makes this method incredibly fast. This is made possible because the observed integrated intensities in the diffraction pattern, I(obs), which are the result of overlapping reflections from planes at similar d-spacings, can be approximated by calculating the integrated intensities, I(calc),
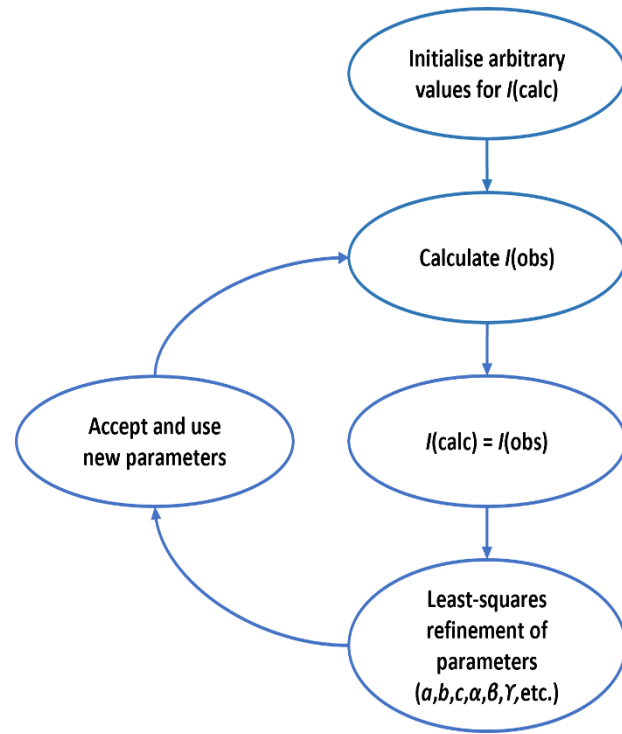
Figure 3.7: Scheme summarising the procedure behind the Le Bail fitting method.

contributing to the observed intensity. The initial values for I(calc) are arbitrary and are therefore not tied to the atoms in the structure and their form factors. The lack of a link to atomic types and positions means the insights available from this method are primarily limited to the symmetry and unit cell parameters. Re-injecting (sometime referred to as "recycling") the resulting values of I(obs) into the algorithm as I(calc) at every cycle, while the other parameters are refined, allows for the determination of newer and more accurate I(obs) values. This can be expressed as:

$$I_i(obs) = \sum_j w_{i,j} \cdot I_i^2(calc) \cdot \frac{y_j(obs)}{y_j(calc)} \ , \tag{3.24}$$

where I_i(obs) and I_i(calc) are the integrated observed and calculated intensities, respectively, $w_{i,j}$ is the contribution of the Bragg peak at the position $2\theta_i$ to the diffraction profile at the position $2\theta_j$, y_j(obs) is the experimental data point at position $2\theta_j$ and y_j(calc)

is the sum of the separate estimated points contributing to the reflections of the diffraction profile.

3.5 Physical Property Measurements

The study of magnetism in condensed matter requires a series of experimental techniques. These will be discussed in this section.

3.5.1 Magnetic Susceptibility and Magnetocaloric Properties

The first quantity measured to obtain an insight into the bulk magnetic properties of a material is the magnetic susceptibility. The main instrument used here is the Quantum Design Magnetic Properties Measurement System (MPMS), equipped with a ^{4}He cryostat. This is a very sensitive magnetometer that allows for the precise determination of the magnetic susceptibility by employing a superconducting magnet capable of producing magnetic fields up to 7 T in a temperature range of 1.2–400 K. In the context of this thesis, magnetic susceptibility measurements have been performed across a 1.8–300 K temperature range with an applied magnetic field of 1000 Oe while isothermal magnetisation measurements were measured to a maximum of 5 T.

The MPMS has many important components (see Appendix A), with the most important being its detector, the Superconducting Quantum Interference Device (SQUID). It is composed of Josephson junctions and exploits the Josephson effect.

The Josephson effect was proposed by Brian D. Josephson in 1962 and first observed in 1964.[172,173] For this discovery, Brian D. Josephson was awarded the Nobel prize in 1973. The Josephson effect is a supercurrent phenomenon where Cooper electron pairs can flow through a barrier in a circuit *via* quantum tunnelling. When two superconducting wires are separated by thin barrier (often referred to as "the weak link"

and often, though not exclusively, made of an insulating material), the Cooper electron pairs can tunnel through it in the absence of a voltage. This is the case for as long as the resulting superconducting current is lower than a critical current I_C. Applying a bias current I_B, greater than I_C, to both ends of the superconducting wires results in the production of an oscillating AC voltage. The Cooper pairs can also be described using wavefunctions. When a current is present, the Cooper pairs in the two superconducting wires will possess a different phase ϕ. The phase difference $\Delta\phi$ is responsible for the electron current and is proportional to I_B. A SQUID detector is built using two Josephson junctions in parallel, forming a ring, as shown in Figure 3.8.

The biasing current is applied to polarise the supercurrent through the junctions. When the loop is placed in a magnetic field, this current can only flow through the opening of the ring due to its superconductive properties. Additionally, it changes the phases across the two junctions, so that a phase difference results. The critical current in the ring changes and it oscillates with the magnetic flux. This can be altered by the motion of a magnetic sample within the loop. What is measured is the oscillating AC voltage associated to the current, making the SQUID a voltage-flux transducer. The change in oscillations enables for the determination of the magnetic properties of the sample. Because the magnetic flux in a superconducting ring is quantised, the SQUID can accurately detect magnetic fluxes on the order of 10^{-15} T m^2.[174]

In order to perform the measurements on our Quantum Design MPMS magnetometer, the samples were placed in gelatin capsules, loaded inside plastic straws with a uniform diamagnetic background. Samples of $Gd(HCO_2)(C_2O_4)$, $Ce(HCO_2)_3$, $Nd(HCO_2)_3$ and $[Li(C_2O_4)]_2[Co_5(OD)_8]$ have been measured using this instrument, across a 1~1.5 to 300 K temperature range. Measurements for the remainder of the $Ln(HCO_2)(C_2O_4)$ samples have been kindly carried out by Dr Gavin Stenning at the

Materials Characterisation Laboratory at the ISIS Muon and Neutron Source (Rutherford Appleton Laboratory, UK) using a Quantum Design MPMS 3 SQUID magnetometer, while samples of $Ho_{1-x}Er_x(HCO_2)_3$ have been analysed at the Inorganic Chemistry Laboratories, University of Oxford, using a MPMS 3, by Johnathan Bulled in the Goodwin group, with the exception of $Ho_{0.5}Er_{0.5}(HCO_2)_3$ which was measured down to 0.4 K by Dr Stenning at ISIS using a low-temperature insert.
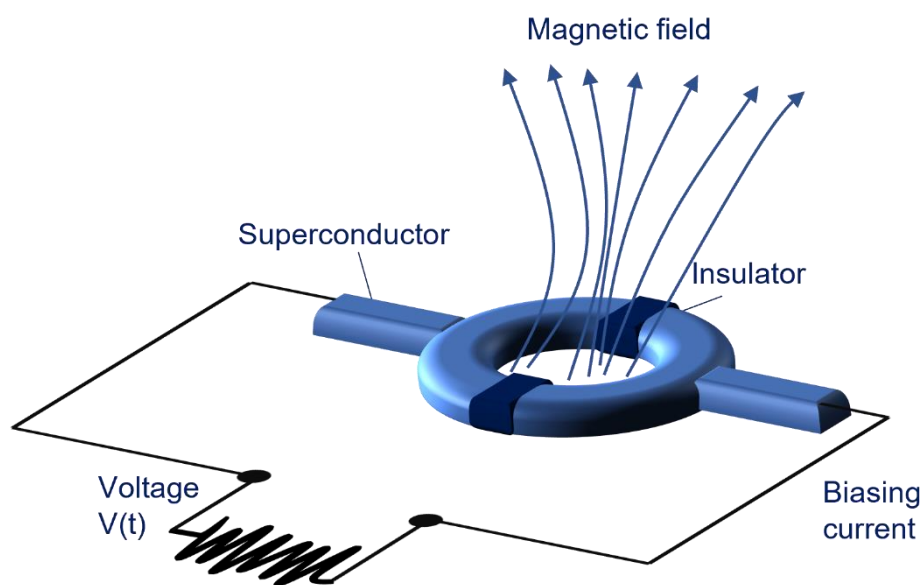
Figure 3.8: Depiction of a SQUID. Detector coils of the MPMS are connected to the ring by superconducting wires with a biasing current applied. The darker sections of the rings represent the Josephson junctions.

3.5.2 Measurement of the Magnetocaloric Properties

Indirect Measurements

As briefly mentioned in Chapter 2, the magnetocaloric properties of a material can be measured by using either direct or indirect methods, *i.e.* through the determination of the heat capacity as a function of temperature or through magnetisation measurements, respectively.[104] Throughout this work, the entropy change of the materials under study has been carried out using the latter method.

The magnetic entropy change of a material can be determined from isothermal magnetisation measurements using the Maxwell relation:

$$\Delta S_{\mathrm{m}}(T) = \int \left[\frac{\delta M(T,B)}{\delta T}\right]_B dB. \tag{3.25}$$

Measurements of the magnetocaloric properties of members of the $Ln(\mathrm{HCO_2})(\mathrm{C_2O_4})$ series, with Ln = $\mathrm{Gd^{3+}}$, $\mathrm{Tb^{3+}}$, $\mathrm{Dy^{3+}}$, $\mathrm{Ho^{3+}}$ and members of the $\mathrm{Y}_x\mathrm{Tb}_{1-x}(\mathrm{HCO_2})_3$ series, with x = 0.025, 0.05 and 0.10, were performed in a field range of 0–5 T and a temperature range of 2–12 K in 2 K steps.

Direct Measurements

When heat capacity data is available, the magnetic entropy change can be determined from it. The heat capacity of a material corresponds to the energy necessary to produce a unit change in temperature and can be thought as the rate of heat transfer with respect to the temperature. This relationship is more clearly described by the equation:

$$C_P = \left(\frac{dQ}{dT}\right)_P, \tag{3.26}$$

where C_p is the heat capacity at constant pressure, dQ the heat, P the pressure of the thermodynamic system and T is its temperature. Under isobaric conditions, *i.e.* constant pressure, the entropy of a system, dS, is related to the heat according to the second law of thermodynamics:

$$dQ = TdS. \tag{3.27}$$

As a consequence, the entropy is related to the heat capacity of a material by the following relationship:

$$dS = \int_0^{T_{max}} \left(\frac{C_P}{T} \right) dT .$$

(3.28)

At a microscopic level, the total heat capacity of a material, C_T is the sum of electronic, magnetic and nuclear contributions, as well as the contribution from the Schottky anomaly, a peak observed at low temperatures in solids due to the sudden increased probability in thermal excitations right above absolute zero. This can be expressed as:

$$C_T = C_{lattice} + C_{electron} + C_{magnetic} + C_{Schottky}.$$

(3.29)

At sufficiently high temperatures, no contribution due to the Schottky anomaly is present. As a consequence, only the first three terms need to be considered. While the contribution from the electrons is usually assumed to be zero in insulating materials, the lattice contribution can affect the total heat capacity considerably. It is possible to model the lattice contribution (the phonons being responsible for the lattice heat capacity) by using the Debye equation[175]:

$$C_{lattice} = \frac{9NRT^3}{\theta_D^3} \int_0^{\frac{\theta_D}{T}} \frac{x^4 e^x}{(e^x - 1)^2} \, dx ,$$

(3.30)

where R is the universal gas constant, T is the temperature, N is the number of atoms per unit cell and θ_D is the Debye temperature, corresponding to the temperature at which all the atoms in the crystal structure vibrate at the same frequency and is defined as:

$$\theta_D = \frac{\hbar}{k_B} \omega_D,$$

(3.31)

where k_B is the Boltzmann constant, $\hbar$ is the reduced Planck constant and ω_D is the Debye frequency, that is the frequency adopted by the atoms at this temperature. When the temperrature of the material is significantly lower than the Debye temperature, *i.e.* $T \ll \theta_D$, the following relation holds true:

$$C_{\text{lattice}} \cong \frac{12\pi^4}{5}\left(\frac{T}{\theta_{\text{D}}}\right)^3 . \tag{3.32}$$

It is difficult to deconvolute the contributions to the heat capacity from experimental data and, consequently, it is often necessary to model the lattice contribution and other anomalies and subtract those from the total heat capacity to estimate the magnetic heat capacity term and extract the magnetic entropy change.

Heat capacity measurements in zero-field conditions were carried out for $Dy(HCO_2)(C_2O_4)$, while both zero-field and non-zero field measurements were performed for the $Y_xTb_{1-x}(HCO_2)_3$ ($x = 0.05$, 0.10. 0.20, 0.40) were carried out using a Quantum Design Physical Properties Measurement System (PPMS) Dynacool across a 250 mK–4 K temperature range, achieved using of He-3 insert, at the Materials Characterisation Laboratory at the ISIS Muon and Neutron Source (Rutherford Appleton Laboratory, United Kingdom). To isolate the magnetic contribution for the measured samples, the lattice heat capacity was estimated using the Debye function in the low temperature limit (see Eqn. 3.32).

3.6 Other characterisation techniques

3.6.1 X-Ray Fluorescence

X-Ray Fluorescence (XRF) is a non-destructive analytical technique that allows for the determination of the elemental composition of a material. This is because the absorption of X-rays produce electrically excited ions which decay to their ground-state by electronic transitions from higher to lower energy levels. These transitions are characterised by the emission of X-rays, in a process similar to what has been described in Section 3.3.2. These X-rays have characteristic emission lines at defined energies

depending on the element excited and are always at higher wavelength than the irradiating X-rays from the source due to inelastic phenomena occurring during the excitation process.

XRF measurements were performed on all the members of the $Y_{1-x}Tb_x(HCO_2)_3$ and $Ho_{1-x}Er_x(HCO_2)_3$ families in order to experimentally assess their stoichiometries, using a Panalytical Epsilon 3 XRF spectrometer. Results obtained for the $Y_{1-x}Tb_x(HCO_2)_3$ were extracted by using a calibration curve determined from physically ground mixtures of $Y(HCO_2)_3$ and $Tb(HCO_2)_3$ with different Tb:Y molar ratios, namely 97.5:2.5, 95:5, 90:10, 75:25, 50:50 and 27:75. Similarly, results for the $Ho_{1-x}Er_x(HCO_2)_3$ series were obtained by using a calibration curve determined from mixtures of $Ho(HCO_2)_3$ and $Er(HCO_2)_3$ with different Ho:Er molar ratios, specifically 92:8, 75:25, 84:16, 60:40, 40:60, 16:84 and 8:92.

3.6.2 Scanning Electron Microscopy and Energy Dispersive X-Ray Spectroscopy

The Scanning Electron Microscope (SEM) is an instrument that enables the production of an energetic beam of electrons that is incident to the surface of a sample.[176] The interaction of the electrons with the sample is responsible for a series of phenomena, some electrons from the beam will simply be reflected from the sample (backscattered electrons or BSE) following an elastic interaction, whereas some electrons of sufficient energy will cause the sample to eject electrons from the outer orbitals (secondary electrons or SE) and the excitation and subsequent de-excitation of bound electrons causes the emission of characteristic X-rays,[176] a process explained in Section 3.3.2.

The detection of backscattered electrons and secondary electrons allows for an image of the sample surface to be produced. The scattering of electrons depends strongly

on the atomic number Z of the elements in the sample, causing a much stronger signal in proportion to the position of heavier elements. In other words, backscattered electrons provide an image where the main feature is the contrast between the elements present, allowing to distinguish different phases in the sample.[176]
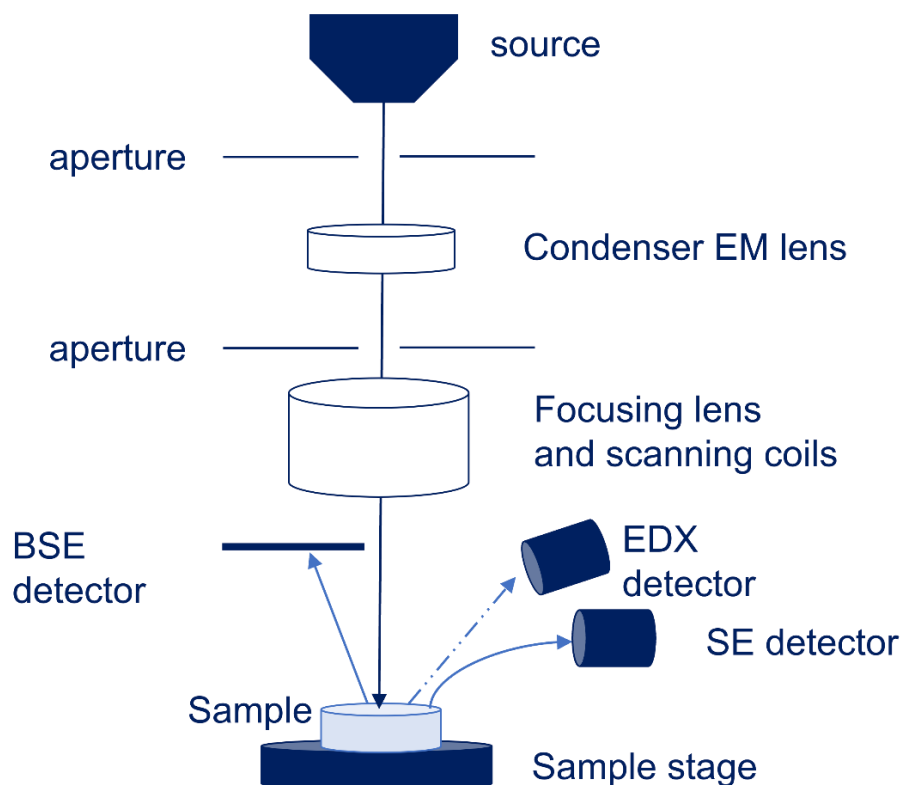
Figure 3.9: Schematic of the components of a Scanning Electron Microscope.

Secondary electrons are produced by the elements themselves and originate from the surface of the sample, with the resulting images providing visual information about the topography of a sample.[176] Since this technique allows high magnification images to be obtained with high resolution, very detailed pictures of the analysed samples can be achieved. This is possible thanks to the typical energies used to accelerate the electron beam, usually in the 0.2–0.4 keV range. Therefore, the beam itself possesses an average wavelength, thanks to the de Broglie relationship (Eqn. 3.7) which determines the resolution of the image. For this reason, the SEM allows the resolution limitation of

traditional optical microscopy to be overcome. A schematic of the SEM instrument is shown in Figure 3.9.

SEM measurements are typically carried out in a high vacuum, so that the electrons produced by the source, as well as those resulting from the interaction with the sample, do not interact with atmospheric atoms, resulting in them having too short a lifetime. Due to the vacuum, sample charging can occur, caused by the charge depositing on the sample, when this is non-conductive, and therefore not being dissipated. This can alter the brightness of the area under observation as well as the image produced. To overcome this issue, a conductive material, such as tape or coatings (*e.g.* gold or carbon), can be placed on the surface of the sample to earth it. In those instances when earthing the sample is not possible, variable pressure (VP) experiments can be conducted to introduce more atmospheric atoms in the sample chamber to allow the dissipation of the accumulated charge on the surface.

As mentioned above, X-rays are also produced when the electron beam hits the sample. These are characteristic of the elements constituting the sample, and it is therefore possible to carry out semi-quantitative and quantitative elemental analysis. Detecting these characteristic X-rays is possible thanks to energy-dispersive X-ray spectroscopy (EDX), with an appropriate X-ray detector coupled with the microscope and sampling different energy ranges thanks to multichannel analysers. Nonetheless, EDX suffers from low-energy resolution and the properties of the sample analysed, such as X-ray absorption due to surface roughness, which might lead to an erroneous quantification of the elements, usually requires the polishing of the surface.

The SEM used for the analysis of all the members of the $Y_{1-x}Tb_x(HCO_2)_3$ and $Ho_{1-x}Er_x(HCO_2)_3$ solid solutions is a Hitachi S3400N, equipped with a thermionic gun and employing the default high-vacuum mode.

3.6.3 Infrared Spectroscopy

Fourier-transform infrared spectroscopy (FT-IR) is a well-know, widespread, time- and cost-effective technique that probes the bonds in a material thanks to irradiation of samples with infrared light, typically in the 4000–500 cm^{-1} or mid-IR energy region. By detecting which wavelengths of light are transmitted to the detector — hence absorbed by the material — it is possible to obtain information pertaining to the functional groups present at a molecular level. This is because the frequency of the vibrational modes, *i.e.* the stretching and the bending motions, of a functional group are influenced by the masses of the atoms constituting the functional group and the type of covalent bond present, as shown by the relation:

$$\nu = \frac{1}{2\pi}\left(\frac{k}{\mu}\right)^{\frac{1}{2}}, \tag{3.33}$$

where ν is the frequency of the mode, k the force constant of the bond (which could be imagined as a spring joining two spheres together for simplicity) and μ is the reduced mass of the bonded atoms.

FT-IR spectra were acquired for the synthesised members of the $Ln(HCO_2)(C_2O_4)$ family, with $Ln = Sm^{3+}–Er^{3+}$, using a Shimadzu IRaffinity-1 Fourier-transform infrared spectrometer in the energy range 4000–500 cm^{-1}. The background was first measured, and this was automatically subtracted by the instrument software during the measurement of the samples. The collected spectra have been mainly used for comparison among the

samples and further confirmation of the ligands of the synthesised samples by recognition of the typical M-L bonds.

3.6.4 Thermogravimetric Analysis and Differential Scanning Calorimetry

Thermogravimetric analysis (TGA) and Differential Scanning Calorimetry (DSC) are two methods used to determine the thermal stability of materials, as well as the mass loss and absorption or release of heat with temperature. In particular, DSC is especially useful in the study of phase transitions or thermally induced reactions, as the heat released, or otherwise absorbed, is directly related to the thermodynamics of such phenomena. It is possible to conduct the experiments in different atmospheres, typically either atmospheric or an inert atmosphere, *e.g.* under nitrogen.

TGA and DSC measurements were simultaneously carried out for all the members of the $Ln(HCO_2)(C_2O_4)$ family synthesised using a Netzsch STA 409 PC TGA-DSC across a 20–800 °C range, with a heating temperature ramp of 10 °C min^{-1}, in order to assess the decomposition temperature of the members of the series. The measurements were performed under air and the background, automatically subtracted *via* the instrument software, previously measured using an empty ceramic crucible.

4 Structure and Magnetocaloric Properties of $Ln(HCO_2)(C_2O_4)$ Frameworks

4.1 Introduction

As discussed in Chapter 2, the best performing magnetocaloric coordination polymers are those featuring heavier lanthanides, from Gd-Er, with a densely packed structure. This is exemplified by the magnetocaloric performance of phases like the LnOHCO$_3$ and $Ln(HCO_2)_3$ frameworks,[5,32,177] in which the magnetostructural relationships and the exotic magnetic states play a key role. For example Tb(HCO$_2$)$_3$ and Ho(HCO$_2$)$_3$ exhibit the TIA state in the former case — this system in particular being its first experimental realisation —[51] and the ECO state for both,[56] due to the 1D chains achieving partial ferromagnetic 1D long-range ordering at 1.6 K, while the chains are antiferromagnetically correlated on a frustrated triangular lattice (see Section 1.9). The ferromagnetic chains and magnetic frustration in these materials also play a key role in their magnetocaloric properties.

Interest in these two families of frameworks led to posing the question about how structural and compositional changes would affect their observed properties, with the former being the major focus of this chapter. Introducing a different ligand while retaining a similar structure would modify the symmetry of the crystal structure and consequentially modify the magnetic properties and the MCE of analogous systems. This

has drawn our attention towards the $Ln(HCO_2)(C_2O_4)$ series of coordination frameworks, previously reported for Ce and Tb,[140,178,179] and the study of their magnetic properties. In these phases, two of the formate ligands in $Ln(HCO_2)_3$ are exchanged for one oxalate ligand, resulting in a lowering in symmetry from rhombohedral $R3m$ to orthorhombic $Pnma$. Similar to the $Ln(HCO_2)_3$ frameworks, these isostructural materials feature face-sharing LnO_9 polyhedra forming infinite 1D-chains, with a zig-zag shape rather than linear. In this chapter, we explore the range of lanthanides that can be incorporated in the $Ln(HCO_2)_3$ structure and explore the magnetocaloric properties of phases containing the later lanthanides, Gd-Ho. We find that while $Gd(HCO_2)(C_2O_4)$ is a promising magnetocaloric for 2 K applications, the disruption of the local magnetic correlations, likely due to the change in symmetry from the $Ln(HCO_2)_3$ to $Ln(HCO_2)(C_2O_4)$, means the Tb and Ho members of the latter series do not exhibit the promising high-temperature and low-field magnetocaloric properties found in the analogous $Ln(HCO_2)_3$ phases.

4.2 X-ray Diffraction and Characterisation of the $Ln(HCO_2)(C_2O_4)$ Phases

4.2.1 Single-Crystal X-ray Diffraction

Samples of $Ln(HCO_2)(C_2O_4)$ ($Ln = Sm^{3+}-Er^{3+}$) were synthesised as described in Section 3.2.1. Single-crystal diffraction data obtained at 120 K for $Ho(HCO_2)(C_2O_4)$ and $Er(HCO_2)(C_2O_4)$ indicated both coordination polymers are isostructural and crystallise in the orthorhombic $Pnma$ space group. The structure of $Ho(HCO_2)(C_2O_4)$ is described here and shown in Figure 4.1; the asymmetric units for both structures are shown in Figure 4.2; crystallographic parameters are given in Table 4.1 and a selection of bond distances are provided in Table B.1 and B.2 (see Appendix B).
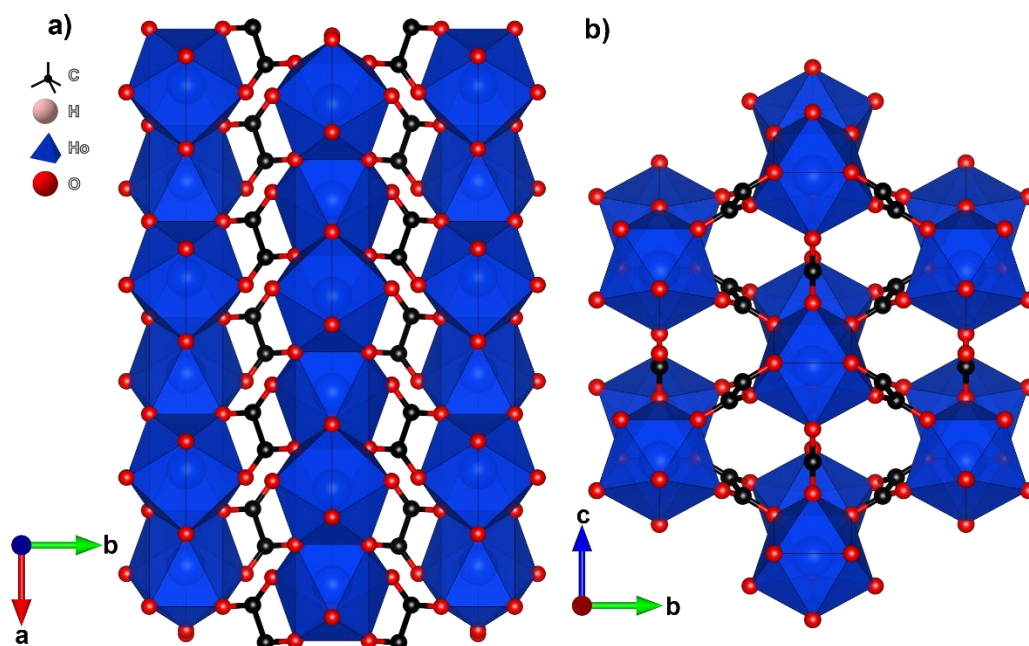
Figure 4.1: (a) Crystal structure of Ho(HCO₂)(C₂O₄) with infinite one-dimensional chains growing along the *a*-axis. (b) Arrangement of the chains in a triangular lattice on the *bc*-plane.
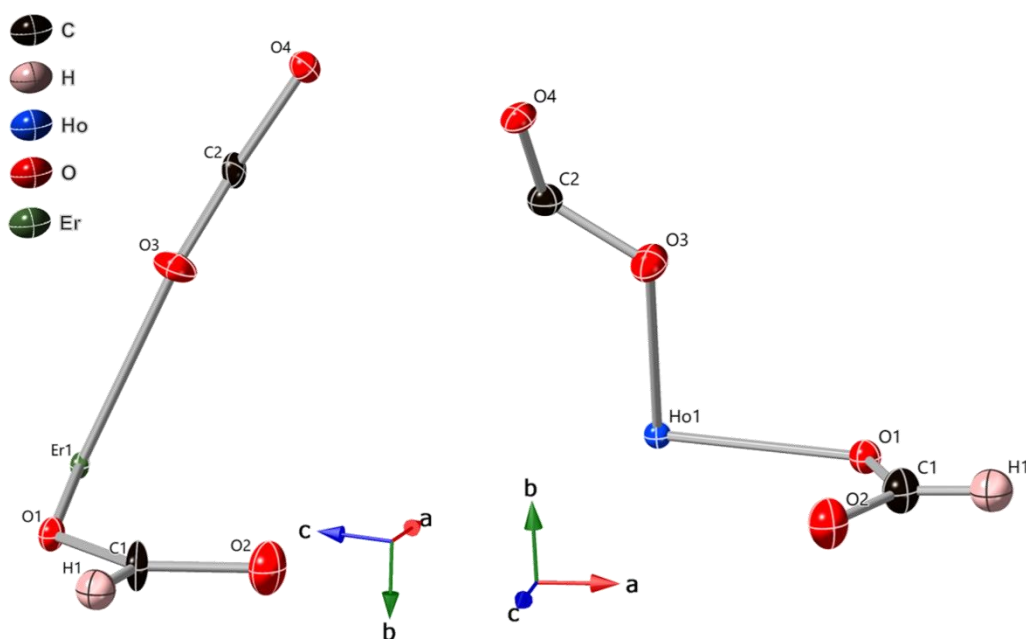
Figure 4.2: Asymmetric units of Er(HCO₂)(C₂O₄) (left) and Ho(HCO₂)(C₂O₄) (right), with atoms shown as ellipsoids with a 60% probability distribution.

The structure of Ho(HCO₂)(C₂O₄) contains Ho³⁺ cations occupying one unique

Ho site (Ho1) and coordinated by nine oxygen atoms from surrounding ligands, three

oxygens from three formates (one O2 and two O1) and six oxygens from three oxalates

(two O3 and four O4), with the latter acting as a bischelating ligand using both carboxylates groups.

Table 4.1: Crystallographic data for the structure of $Ho(HCO_2)(C_2O_4)$ and $Er(HCO_2)(C_2O_4)$ determined by single-crystal X-ray diffraction

Compound	$Ho(HCO_2)(C_2O_4)$	$Er(HCO_2)(C_2O_4)$
Formula	HoC_3HO_6	ErC_3HO_6
Formula weight (g mol^{-1})	297.97	300.30
Crystal system	Orthorhombic	Orthorhombic
Space group	*Pnma*	*Pnma*
Temperature (K)	120	120
a (Å)	6.9473(3)	6.9198(4)
b (Å)	10.5261(4)	10.4221(6)
c (Å)	6.5526(4)	6.5331(4)
V (Å^3)	479.18(4)	474.32(5)
Z	4	4
ρ_{calc} (g cm^{-3})	4.130	4.205
μ (cm^{-1})	30.72	32.72
Refl. meas./unique	2037/489 [R_{int} = 2.83%]	1003/483 [R_{int} = 2.33%]
Parameters refined	52	52
R_1, wR_2 (all)	2.03%, 4.56%	2.17%, 4.30%
R_1, wR_2 (obs)	1.89%, 4.50%	1.90%, 4.20%
Goodness of fit	1.04	1.04

This results in HoO_9 polyhedra which adopt a distorted monocapped square antiprism geometry, with Ho-O distances of 2.391(3) Å and 2.451(3) Å for O1, 2.402(3) Å for O2, 2.390(2) Å for O3 and 2.413(2) and 2.437(2) Å for O4. The face-sharing polyhedra propagate along the *a*-axis forming infinite zig-zag chains and with intrachain Ho-Ho distances of 3.7948(3) Å, and with angles of 103.21(12)° and 102.98(12)° for Ho-O1-Ho and Ho-O4-Ho, respectively. Each individual chain is then

joined to the neighbouring ones forming a distorted triangular lattice *via* the bridging formate ligand along the *c*-axis and oxalate ligands along the $[00\bar{1}]$ and $[01\bar{1}]$ axes. Interchain Ho-Ho distances are 6.5526(6) Å and 6.2367(3) Å for those connected by formate and oxalate ligands, respectively. Overall, this results in a coordination framework with three-dimensional connectivity of I^1O^2 type, according to the nomenclature of Cheetham *et al.*[180]

4.2.2 Powder X-ray Diffraction and Le Bail Fits

Powder X-ray diffraction measurements were acquired for all the members of this series, from Sm to Er, and showed these frameworks exhibit a similar diffraction pattern, indicating that they are isostructural at room temperature, and are shown in Figure 4.3. Attempts to make isostructural phases with lanthanides larger than Sm were unsuccessful (see Appendix B). Furthermore, the repeatability of the synthesis of the Er member proved unsuccessful, as this synthesis tends to yield significant amounts of $[(CH_3)_2NH_2]Er(HCO)_2(C_2O)_4$, which adopts a monoclinic *P*2/*n* structure with $[(CH_3)_2NH_2]^+$ in its cavities.[181]

Le Bail fits to the patterns, as shown in Figure 4.4 for Tb(HCO$_2$)(C$_2$O$_4$) (see Appendix B for fits to the remainder of the samples), confirmed that all the samples are phase pure and adopt an orthorhombic *Pnma* structure at room temperature. The lattice parameters and statistics obtained from the Le Bail refinements for all the members of the series are reported in Table 4.2 and the former are shown in Figure 4.5.
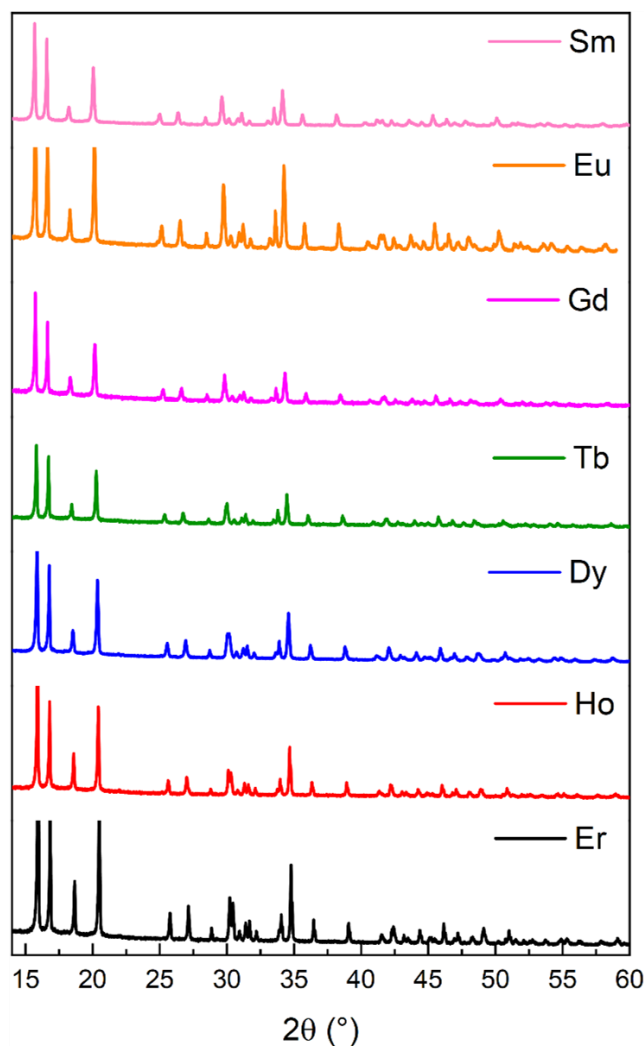
Figure 4.3: Conventional powder X-ray diffraction patterns of the synthesised $Ln(HCO_2)(C_2O_4)$, with Ln = Sm–Er, measured using a Cu source (λ = 1.54 Å).

Table 4.2: Lattice parameters and fitting statistics from Le Bail fits to PXRD patterns from $Ln(HCO_2)(C_2O_4)$ phases.

Ln	a (Å)	b (Å)	c (Å)	R_p (%)	R_{wp} (%)	χ^2
Sm	7.13136(14)	10.6840(2)	6.65763(15)	2.88	3.66	3.33
Eu	7.08694(14)	10.6524(2)	6.6324(2)	2.66	3.47	3.62
Gd	7.0431(3)	10.6194(4)	6.6070(3)	3.03	3.82	1.81
Tb	7.02274(18)	10.5980(3)	6.59748(18)	2.30	3.65	1.72
Dy	6.98194(13)	10.5752(2)	6.58162(14)	2.56	3.23	3.52
Ho	6.97292(19)	10.5811(4)	6.5821(2)	4.09	5.13	2.84
Er	6.92593(17)	10.5448(3)	6.55559(18)	4.36	5.58	4.63
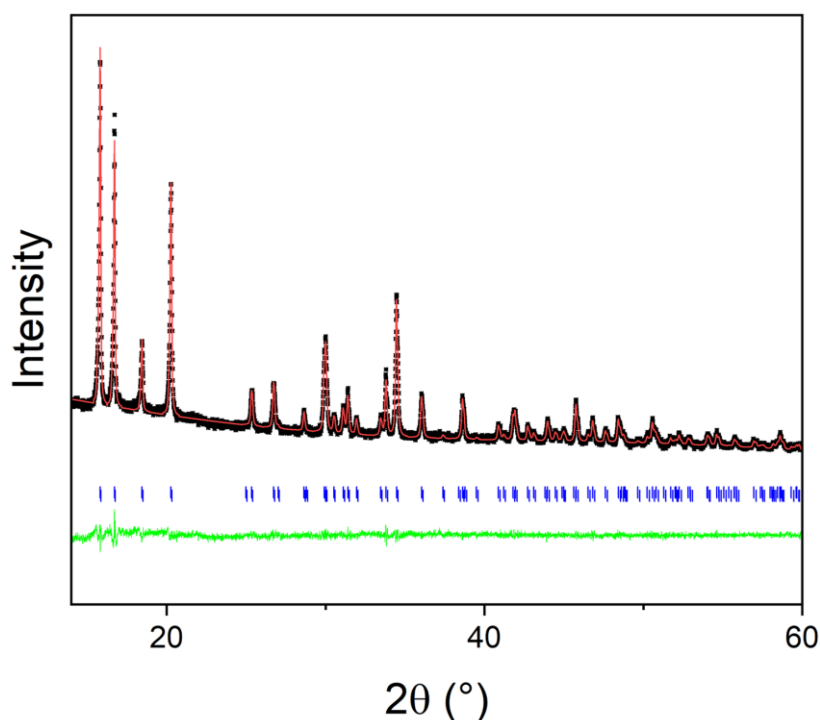
Figure 4.4: Conventional powder X-ray diffraction pattern of Tb(HCO$_2$)(C$_2$O$_4$) measured using a Cu source (λ = 1.54 Å) and fitted using the Le Bail method to highlight phase purity. The crosses, red and green lines are experimental and calculated intensities and the difference curve. Vertical markers indicate the position of the Bragg reflections.
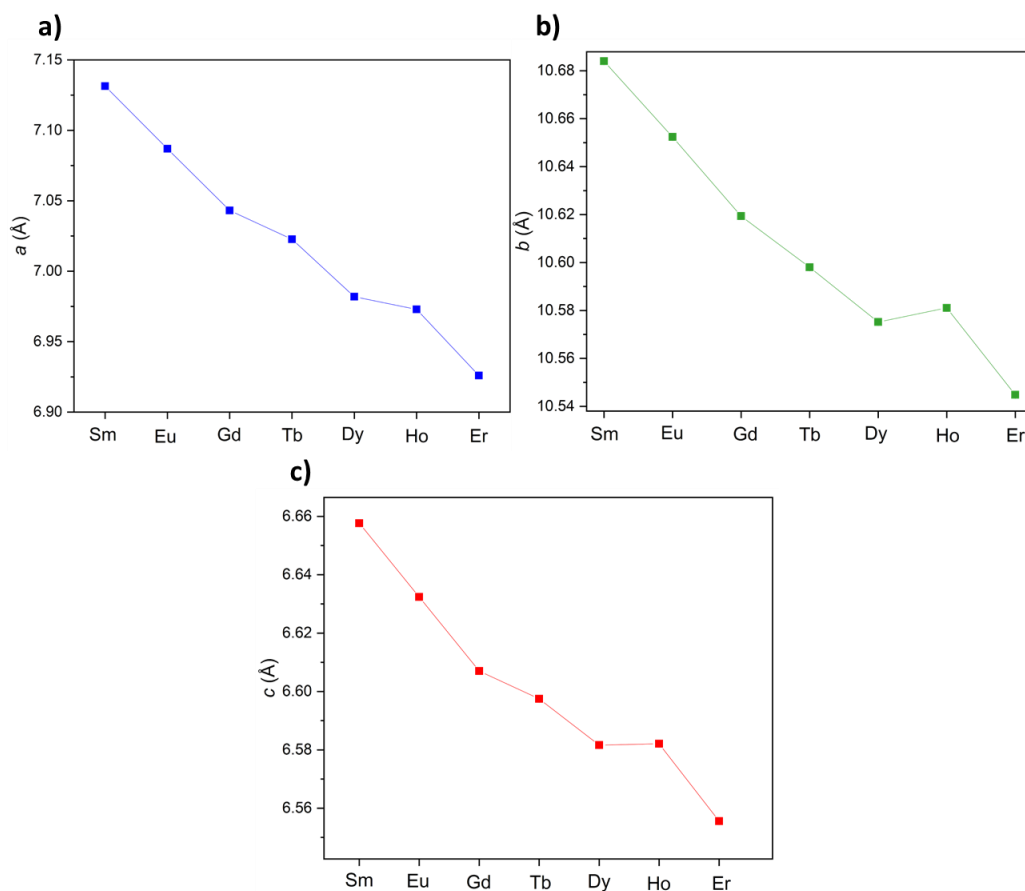
Figure 4.5: Plot of the lattice parameters *a*, *b* and *c* for *Ln*(HCO$_2$)(C$_2$O$_4$) (*Ln* = Sm^{3+}–Er^{3+}) obtained from Le Bail refinements of powder X-ray diffraction patterns.

4.3 Infrared Spectra of the *Ln*(HCO$_2$)(C$_2$O$_4$) Phases

Fourier-transform infrared spectra (FT-IR) for *Ln*(HCO$_2$)(C$_2$O$_4$) (*Ln* = Sm-Er), shown in Figure 4.6, reveal all members of the series have similar spectra, with a strong signal at ~1735 cm^{-1}, usually attributed to the stretching of the C=O group, here ascribable to a shortened C-O bond length, whereas bands at 1367 and 1345 cm^{-1}, as well as those at ~790 cm^{-1}, are attributed to C-H bending modes, due to the presence of the formate ligands in the structure. It is tentatively possible to attribute bands a ~1340 and ~1300 cm^{-1} to the stretching of C-O bonds.
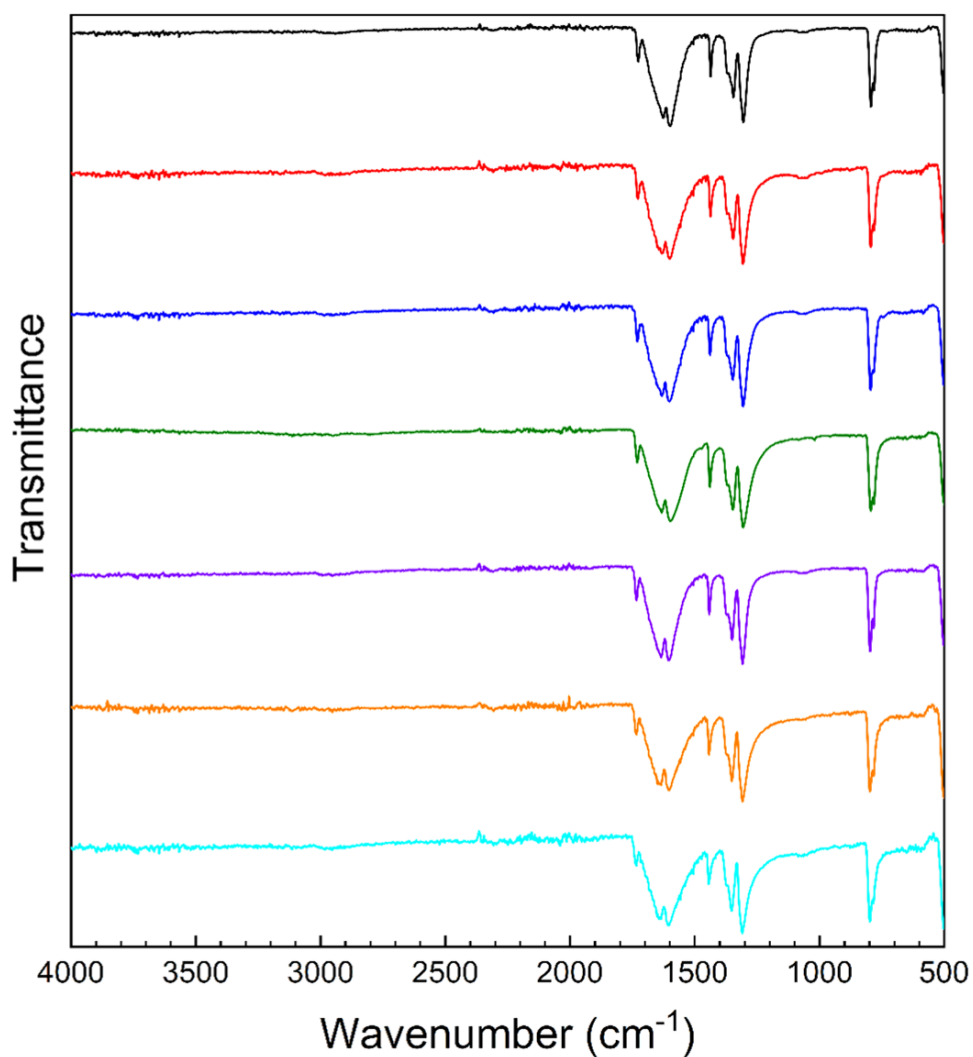
Figure 4.6: Fourier transform infrared spectra of *Ln*(HCO$_2$)(C$_2$O$_4$) (*Ln* = Sm–Er from top to bottom).

4.4 Thermal Behaviour of the *Ln*(HCO$_2$)(C$_2$O$_4$) Phases

TGA and DSC measurements of the *Ln*(HCO$_2$)(C$_2$O$_4$) frameworks (*Ln* = Sm-Er) were carried out between 24 and 800 °C in air to assess their thermal stability. The samples show similar TGA/DSC profiles, with those of the Sm, Eu, Tb, Dy, Ho and Er members shown in Figure 4.7. A significant loss of weight is observed between 440 and 450 °C, indicating all the samples decompose around this temperature. Furthermore, the DSC signal shows the decomposition to be exothermic in nature.
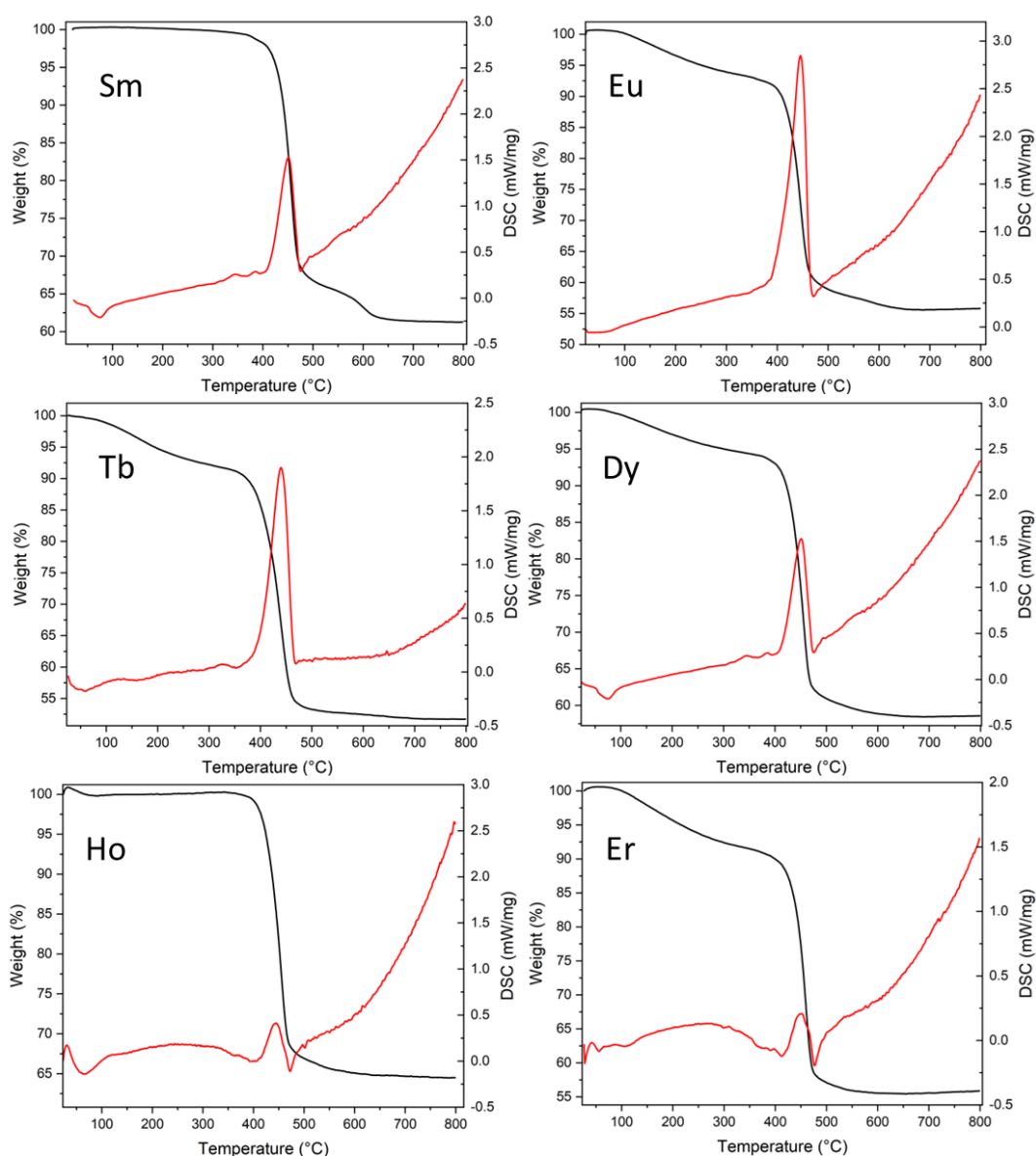
Figure 4.7: Thermogravimetric analysis for *Ln*(HCO$_2$)(C$_2$O$_4$) (*Ln* = Sm^{3+}, Eu^{3+}, Tb^{3+}, Dy^{3+}, Ho^{3+} and Er^{3+}) showing weight loss and differential curves at a heating rate of 10 °C/min from 24 to 800 °C.

The only exception to this behaviour is shown by $Gd(HCO_2)(C_2O_4)$, where the decomposition occurs at ~470 °C, with this appearing mildly endothermic in nature. A second measurement of this sample confirmed this behaviour with both results shown in Figure 4.8. We are unable to provide an explanation for the decomposition of $Gd(HCO_2)(C_2O_4)$ being endothermic rather than exothermic.
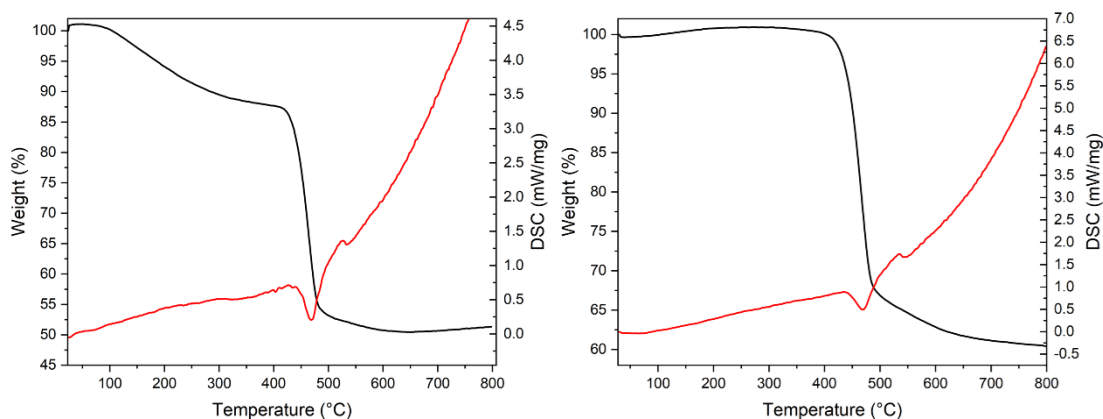
Figure 4.8: Thermogravimetric analysis of two samples of $Gd(HCO_2)(C_2O_4)$ showing weight loss and differential curves at a heating rate of 10 ºC/min from 24 to 800 ºC.

4.5 Magnetic properties of the *Ln*(HCO₂)(C₂O₄) phases

4.5.1 Bulk magnetic properties

Due to the similar structures that the $Ln(HCO_2)(C_2O_4)$ phases share with the $Ln(HCO_2)_3$ and LnOHCO₃,[182,119] the magnetic properties of the $A(HCO_2)(C_2O_4)$ (A = Gd^{3+}, Tb^{3+}, Dy^{3+} and Ho^{3+}) members of this family of frameworks were explored, with these lanthanides having been reported to have promising magnetocaloric properties in the $Ln(HCO_2)_3$ and LnOHCO₃ phases.[5,53,119,120]

Field cooled (FC) and zero-field cooled (ZFC) susceptibility $\chi(T)$ data of these compounds, measured in a 0.1 T magnetic field from 2 to 300 K, do not show any significant features, suggesting the materials remain paramagnetic down to 2 K, as shown in Figure 4.9. Inverse susceptibility, χ^{-1}, data were well-fitted using the Curie-Weiss law both between 50–300 K and 2-20 K, with the exception of $Ho(HCO_2)(C_2O_4)$, which was

fitted at low-temperature in a range of 8–20 K. The resulting values are reported in Table 4.3. The Curie-Weiss temperature (θ_{CW}) obtained for $Gd(HCO_2)(C_2O_4)$ is a clear indication of its antiferromagnetic behaviour. Other members of the series also have a negative θ_{CW}, consistent with antiferromagnetic interactions.
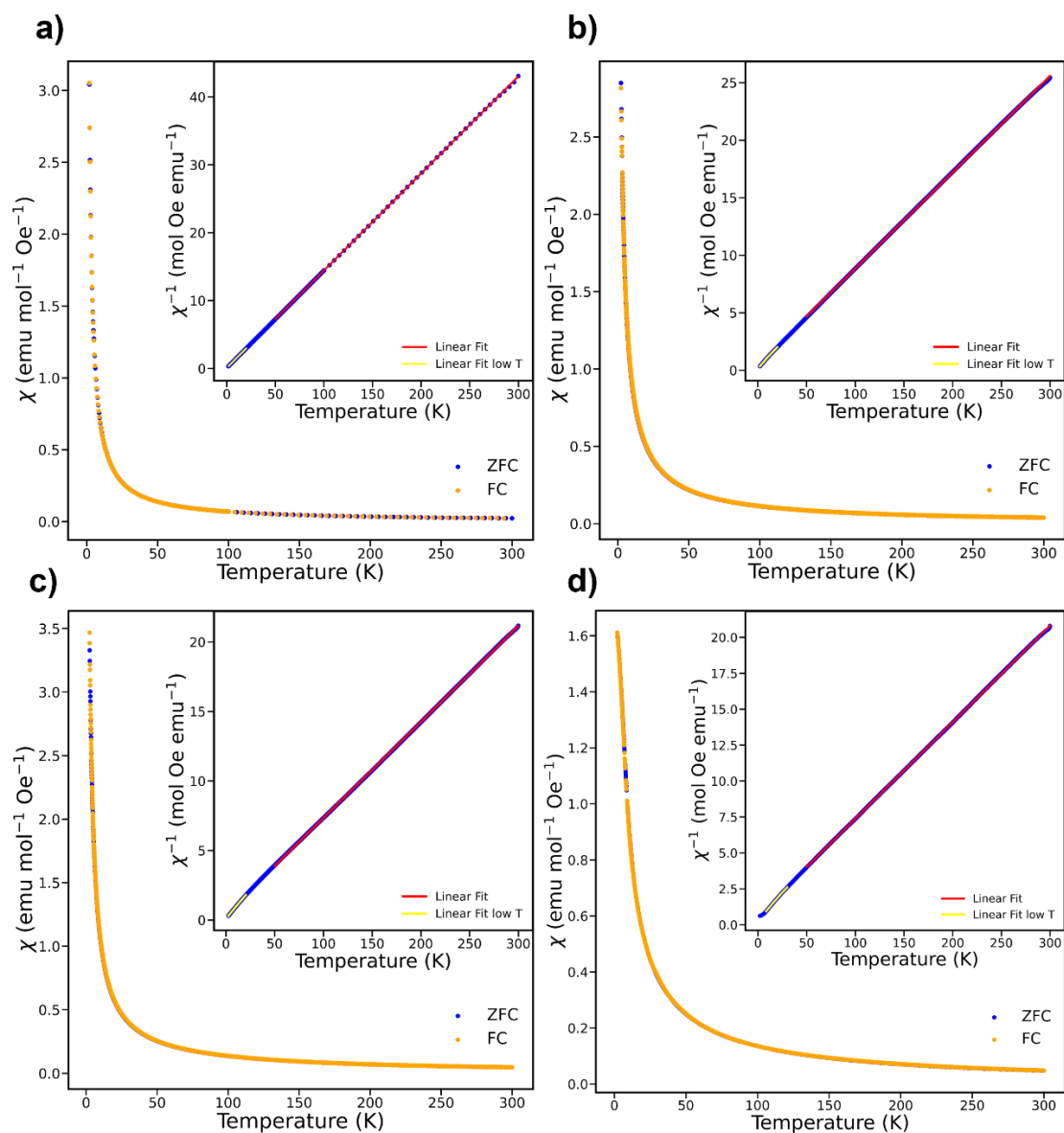
Figure 4.9: ZFC and FC susceptibility measurements for a) $Gd(HCO_2)(C_2O_4)$, b) $Tb(HCO_2)(C_2O_4)$, c) $Dy(HCO_2)(C_2O_4)$ and d) $Ho(HCO_2)(C_2O_4)$ in a 0.1 T field. Insert in each picture show the inverse susceptibility and the low- and high-temperature Curie-Weiss fits to the data.

Table 4.3: Bulk magnetic properties of A(HCO$_2$)(C$_2$O$_4$) with A = Gd–Ho.

Sample	Theoretical μ_{eff} (μ_B)	High-T fit (K)	θ_{CW} (K)	Experimental μ_{eff} (μ_B)	Low-T fit (K)	θ_{CW} (K)	Experimental μ_{eff} (μ_B)
Gd(HCO)$_2$(C$_2$O$_4$)	7.9	50–300	−0.8	7.5	2–20	−0.5	7.5
Tb(HCO)$_2$(C$_2$O$_4$)	9.7	50–300	−5.6	9.8	2–20	−1.9	9.3
Dy(HCO)$_2$(C$_2$O$_4$)	10.6	50–300	−6.4	10.8	2–20	−1.3	9.8
Ho(HCO)$_2$(C$_2$O$_4$)	10.6	50–300	−9.9	10.8	8–30	−4.2	10.2

The results for the Tb^{3+}–Ho^{3+} members of this series, however, must be interpreted more cautiously since their significant orbital angular momentum can also be quenched at low temperatures due to crystal-field effects. The θ_{CW} of these phases remain negative when fit across both high- and low-temperature ranges, which supports the existence of antiferromagnetic interactions. Effective magnetic moments, μ_{eff}, are found to be similar between the two temperature regimes and close to the expected values for Gd^{3+}, Tb^{3+}, Dy^{3+} and Ho^{3+}. The slightly lower effective magnetic moments resulting from fitting at lower temperatures can be attributed to the increasing strength of the antiferromagnetic interactions, as well as the effect of orbital angular momentum, *L*, quenching, due to the crystal field environment interacting more strongly with the 4*f* orbitals at these temperatures (see Table 1.1).

To better highlight any features of the inverse susceptibility curves, $C/\chi|\theta_{CW}|$-1 was plotted as a function of $T/|\theta_{CW}|$, with values of θ_{CW} being those from low-temperature fits.[183] These curves where then linearly fitted between $T/|\theta_{CW}|$ = 6–15, as seen in Figure 4.9. It can be observed that for Gd(HCO$_2$)(C$_2$O$_4$), the linear trend is maintained down to the lowest temperature, *i.e.* 2 K, indicating paramagnetic behaviour. For Tb(HCO$_2$)(C$_2$O$_4$) and Ho(HCO$_2$)(C$_2$O$_4$), there a small deviation from linearity below $T/|\theta_{CW}|$ = 2 can be observed; this is suggestive of very weak antiferromagnetic coupling

but may also be linked to crystal field effects. However, the deviation from linearity is especially significant in the Dy member, indicating a more significant coupling among the spins and presumably resulting in significant short-range order (see Figure 4.10).
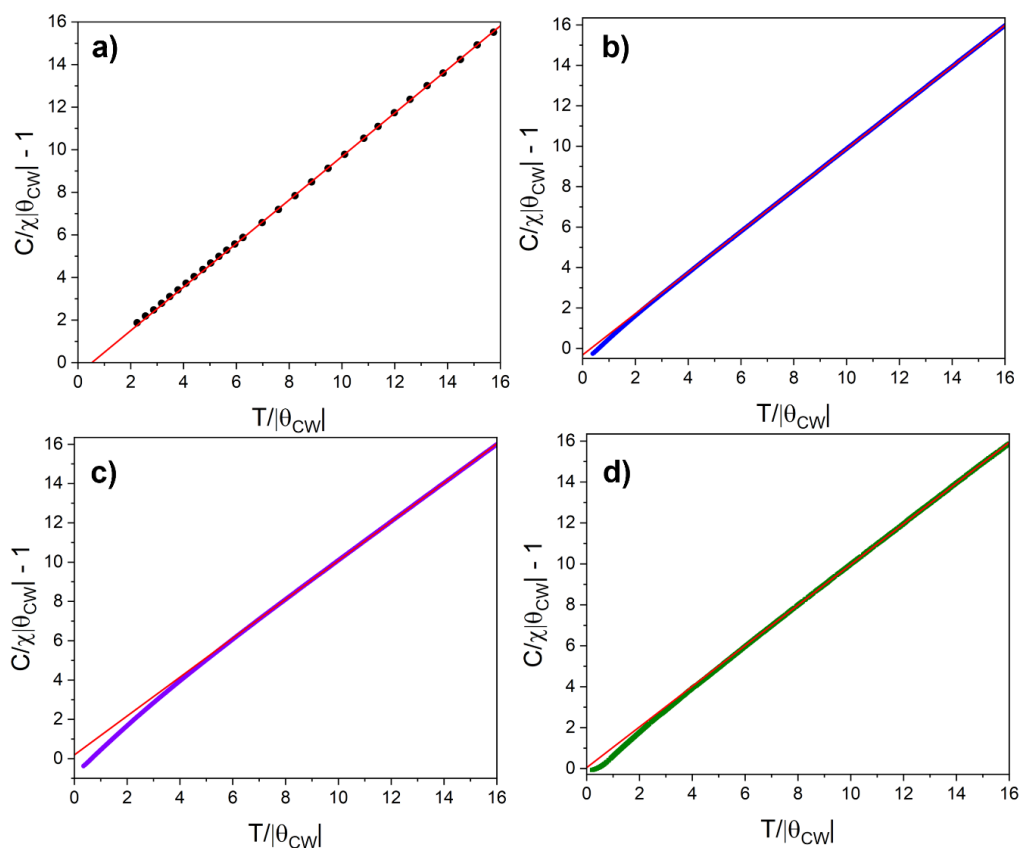
Figure 4.10: Plots of $C/\chi|\theta_{CW}| - 1$ as a function of $T/|\theta_{CW}|$ for a) Gd(HCO₂)(C₂O₄), b) Tb(HCO₂)(C₂O₄), c) Dy(HCO₂)(C₂O₄) and d) Ho(HCO₂)(C₂O₄).

Magnetisation measurements down to 2 K, shown in Figure 4.11, are consistent with paramagnetic behaviour. Values of saturation magnetisation, M_{sat}, allow to gain more insight about the behaviour of the spins, *e.g.* whether they possess an Ising- or Heisenberg-like behaviour, with systems containing the former expected to have saturation values, M_{sat}, close to $g_J J/2$, while systems of Heisenberg-like spins should have values close to $g_J J$. The observed values for the saturation magnetisation of Gd(HCO₂)(C₂O₄) are therefore consistent with Heisenberg spins, while those for the Dy³⁺, Tb³⁺ and Ho³⁺ compounds are closer to the Ising limit, albeit higher than the expected values, as reported in Table 4.4. These results suggest that these systems feature

significant single-ion anisotropy, although they are insufficient to conclusively suggest that the spins are Ising-like. We note similar deviations were found for the Ln(HCO₂)₃ and LnOHCO₃ phases, which were found to be Ising-like by neutron scattering.[5,120,51,121] Inelastic neutron measurements are required to confirm the precise nature of the anisotropy of these cations.
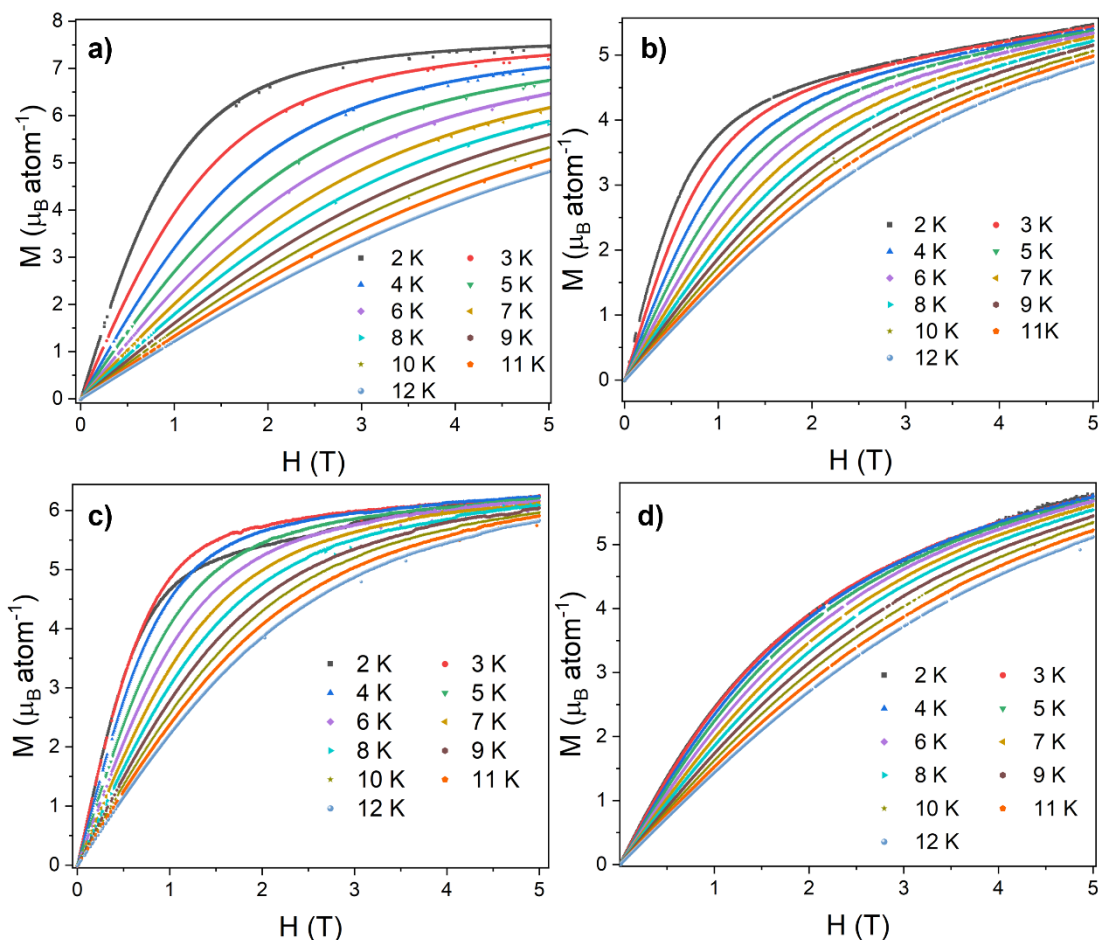
Figure 4.11: Isothermal magnetisation measurements for a) Gd(HCO₂)(C₂O₄); b) Tb(HCO₂)(C₂O₄); c) Dy(HCO₂)(C₂O₄); d) Ho(HCO₂)(C₂O₄).

It should be noted that, interestingly, Dy(HCO₂)(C₂O₄) shows a greater increase in magnetisation than Gd(HCO₂)(C₂O₄) for low applied fields and temperatures above 3 K. It can also be noted that the magnetisation of Dy(HCO₂)(C₂O₄) decreases between 3 and 2 K for fields higher than 0.1 T, suggesting a magnetic transition for Dy(HCO₂)(C₂O₄) close to 2 K. Furthermore, the observed decrease in magnetisation

Table 4.4: Theoretical and experimental saturation magnetisation values of A(HCO$_2$)(C$_2$O$_4$) with A = Gd–Ho.

Sample	Theoretical $M_{sat} = g_J$ (μ_B atom^{-1})	Theoretical $M_{sat} = g_J/2$ (μ_B atom^{-1})	M at T = 2 K, B = 5 T (μ_B atom^{-1})
Gd(HCO$_2$)(C$_2$O$_4$)	7	3.5	7.5
Tb(HCO$_2$)(C$_2$O$_4$)	9	4.5	5.5
Dy(HCO$_2$)(C$_2$O$_4$)	9.98	4.99	5.7
Ho(HCO$_2$)(C$_2$O$_4$)	10	5.0	5.7

suggests this transition is likely antiferromagnetic in nature. Heat capacity measurements for this sample, shown in Figure 4.12, are consistent with a magnetic phase transition, showing a peak at 0.6 K under zero-field conditions, indicating this compound undergoes a magnetic transition at these low temperatures. In addition to this, consistent with a magnetic phase transition, it can be observed that the feature in the heat capacity is partially supressed upon increasing the applied field up to 1 T, with the heat capacity increasing towards higher temperatures.
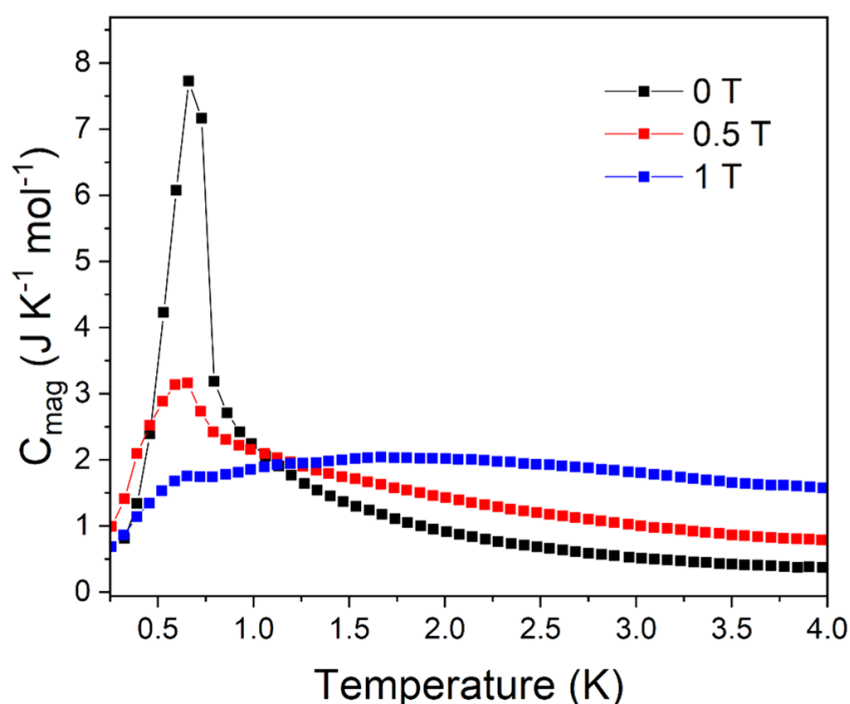
Figure 4.12: Magnetic heat capacity data for Dy(HCO$_2$)(C$_2$O$_4$) measured between 250 mK and 4 K with applied fields of 0, 0.5 and 1 T.

This is consistent with other reported systems, such as the lanthanide gallium garnets $Ln_3CrGa_4O_{12}$ ($Ln = Tb^{3+}$, Dy^{3+}, Ho^{3+}) where heat capacity data have shown higher applied magnetic fields result in the transition temperature shifting to higher values and a gradual broadening of the heat capacity maxima.[184]

4.5.2 Magnetocaloric properties of *Ln*(HCO$_2$)(C$_2$O$_4$)

Data from magnetisation measurements allowed for the determination of the magnetic entropy change using the Maxwell relation (see Eqn. 3.25). The resulting $-\Delta S_m^{max}$ values obtained are 55.97, 14.72, 16.45, 11.70 J kg^{-1} K^{-1} for a $\Delta B = 5$–0 T and a T_{max} of 2, 4, 5 and 9 K for Gd^{3+}, Tb^{3+}, Dy^{3+} and Ho^{3+}, respectively, with corresponding volumetric values of 218.42, 28.18, 66.44 and 48.33 mJ cm^{-3} K^{-1} (see Figure 4.13).
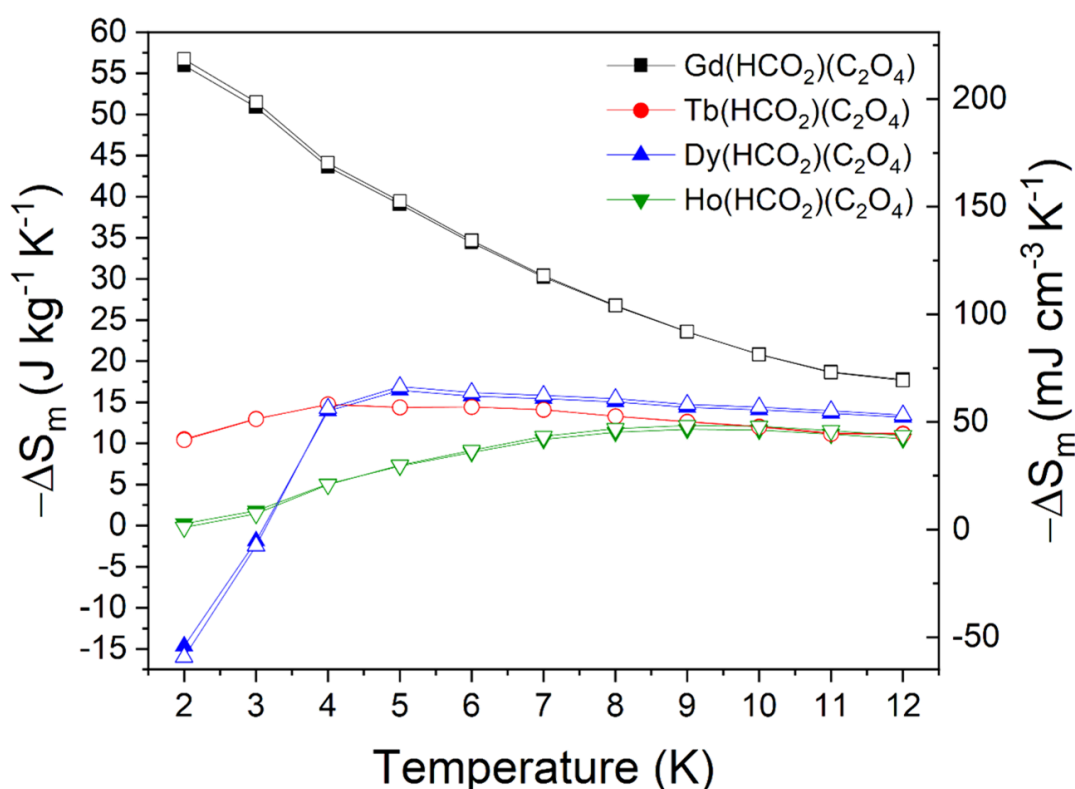
Figure 4.13: Magnetic entropy changes for the A(HCO$_2$)(C$_2$O$_4$) series for $\Delta B = 5$–0 T. The filled and hollow symbols mark the gravimetric and volumetric units, respectively.

The values found for Gd(HCO$_2$)(C$_2$O$_4$) are amongst the highest known for magnetocaloric coordination frameworks and the best performing coordination polymer

containing linear dicarboxylate ligands, discussed in Section 2.3.2, likely ascribable to the fact that the oxalate ligand is the shortest and simplest of the ligands discussed. The entropy changes observed in $Gd(HCO_2)(C_2O_4)$ slightly exceed that of the closely related $Gd(HCO_2)_3$,[5] and are well above that of $Ca_4GdO(BO_3)_3$,[185] and other carboxylate-based systems containing one-dimensional chains, such as $Gd(OAc)_3(MeOH)$, $Gd(OAc)_3(H_2O)_{0.5}$ or $Gd(HCOO)(OAc)_2(H_2O)_2$, where weaker interchain interactions are present.[123,124] $Gd(HCO_2)(C_2O_4)$ is also very likely superior to $Gd_6O(OH)_4(ClO_4)(H_2O)_6](OH)_4$, $Gd_4(SO_4)_4(OH)_4(H2O)$ and $Gd_4(SO_4)_3(OH)_4(C_2O_4)(H_2O)5H_2O$, which possess three-dimensional structures containing Gd clusters, and $Gd_2O(OH)_4(H_2O)_2$, which features a layered structure, with at least comparable values for a 5–0 T field change than these materials are reported to have for a 7–0 T change (5–0 T values are unavailable for these materials).[45,122,186] For the purpose of comparison with other systems previously discussed, we propose here Figure 4.14, similar to Figure 2.17, with $Gd(HCO_2)(C_2O_4)$ added. This shows more clearly this material can offer similar entropy changes to those of purely inorganic coordination frameworks. This makes $Gd(HCO_2)(C_2O_4)$ a very good candidate for ultra-low magnetic cooling at high magnetic fields.
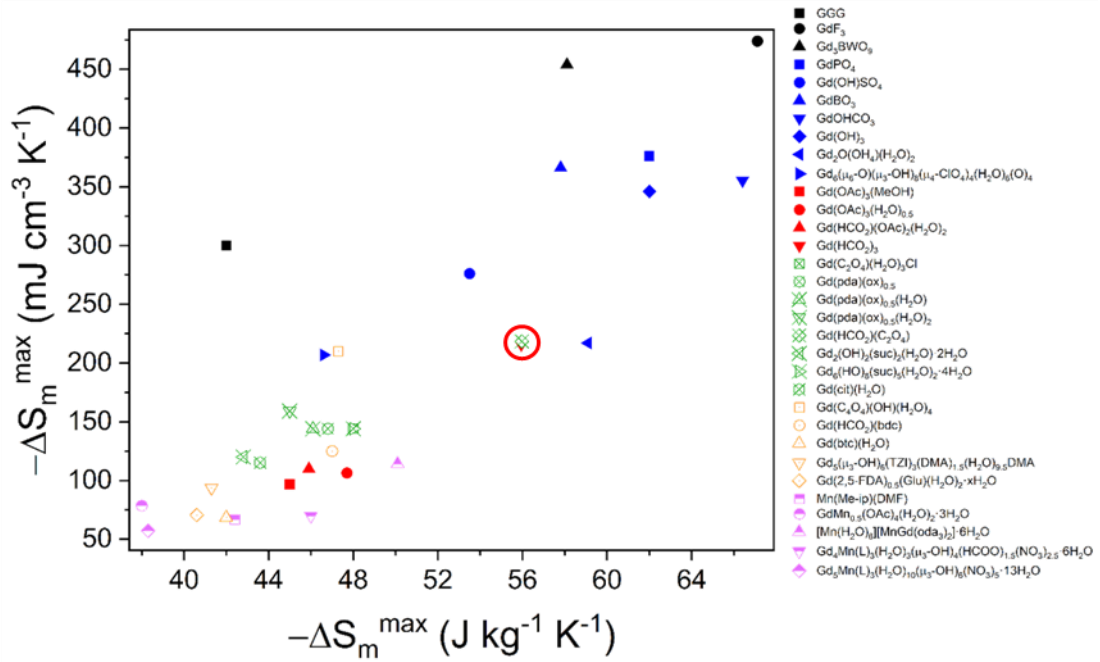
Figure 4.14: Plot of gravimetric and volumetric maximum entropy changes $-\Delta S_m^{max}$ of the materials discussed in Chapter 3, with the addition of Gd(HCO₂)(C₂O₄), circled in red. Presented here are inorganic-based (blue), monocarboxylate-based (red), linear carboxylate-based (green), cyclic carboxylate based (orange) and mixed 3*d*-4*f* (purple) materials along with selected high-performance conventional materials (black). The values presented here are for field changes of 7 T with the exception of those for which 9 T (GGG, Gd₃BWO₉, GdBO₃, Gd(HCO₂)(bdc)), 8 T (Mn(Me-ip)(DMF)) and only 5 T (GdF₃, Gd(HCO₂)(C₂O₄), Gd(btc)(H₂O)) values were available

For all the lanthanides other than Gd, the materials have a higher T_{max}, which facilitates use for higher temperature applications, with the exception of Tb(HCO₂)(C₂O₄) for small (1–0 T) field changes. In the context of the performance of related anisotropic materials in low applied fields, it is important to note that the $-\Delta S_m^{max}$ of these materials are 22.72, 24.10 and 5.66 mJ cm⁻³ K⁻¹ with T_{max} = 2, 4 and 6 K for Tb³⁺, Dy³⁺ and Ho³⁺, respectively, for a 1–0 T field change, as shown in Figure 4.15, whereas the values are 39.86, 47.00 and 17.02 mJ cm⁻³ K⁻¹ with T_{max} = 4, 5 and 7 K for a 2–0 T field change, with $-\Delta S_m$ curves shown in Figure 4.16. However, even at these lower fields, only Dy(HCO₂)(C₂O₄) appears to outperform the Gd material, which occurs at 5 K for a 1–0 T field change and above 7 K for a 2–0 T field change, with Dy(HCO₂)(C₂O₄) performing increasingly better than Gd(HCO₂)(C₂O₄) with increasing temperatures. This enhancement in performance is, however, smaller than that observed for some highly magnetocrystalline anisotropic cations in the *Ln*(HCO₂)₃ and *Ln*OHCO₃

series. Specifically, for the latter family of frameworks and a field change of 2–0 T, the $-\Delta S_m^{max}$ values are 168.62, 186.15 and 112.67 mJ cm^{-3} K^{-1} (T_{max} = 4 K) for Tb^{3+}, Dy^{3+} and Ho^{3+}, respectively,[120] while for the $Ln(HCO_2)_3$ series the values are 46.9, 61.2 and 46.2 mJ cm^{-3} K^{-1} with T_{max} = 3, 2 and 4 K, respectively.[5] In both cases, it has been shown that, for lower applied fields, compounds with magnetic anisotropy outperform their Gd-analogues at higher temperatures, typically above 4 K.

It should be noted that the $-\Delta S_m$ of Dy(HCO$_2$)(C$_2$O$_4$) decreases below 4 K and exhibits inverse MCE ($\Delta S_m > 0$) near 2 K. The reduction in entropy change is consistent with the drop in magnetisation observed for this compound and lower temperatures. Inverse MCE is not common but has been observed due to crystal field effects, such as in PrNi$_5$,[187,188] in transition metal alloys showing first-order magnetic transitions,[189] and more recently in Ba$_3$Tb(BO)$_3$.[190] In the case of Dy(HCO$_2$)(C$_2$O$_4$), the inverse MCE is likely due to approaching a magnetic transition, as indicated by heat capacity measurements. The behaviour of the magnetisation along with the deviation from linearity of χ^{-1} suggest this is antiferromagnetic in nature. It is, however, difficult to confirm the origins of the observed inverse MCE in Dy(HCO$_2$)(C$_2$O$_4$), *i.e.* whether this is due solely to the suppression of antiferromagnetic correlations under applied fields or other factors, as this would require further information about the magnetic structure, achievable *via* neutron diffraction; this would include its local structure since the material remains paramagnetic until well below the temperature at which negative entropy changes emerge. We anticipate this would present a significant challenge due to the high neutron absorption of Dy and, hence, require the use of isotopes with a lower absorption cross-section. This would be financially prohibitive to carry out for Dy(HCO$_2$)(C$_2$O$_4$), which cannot be made with the near 100% atomic efficiency of solid-state reactions.
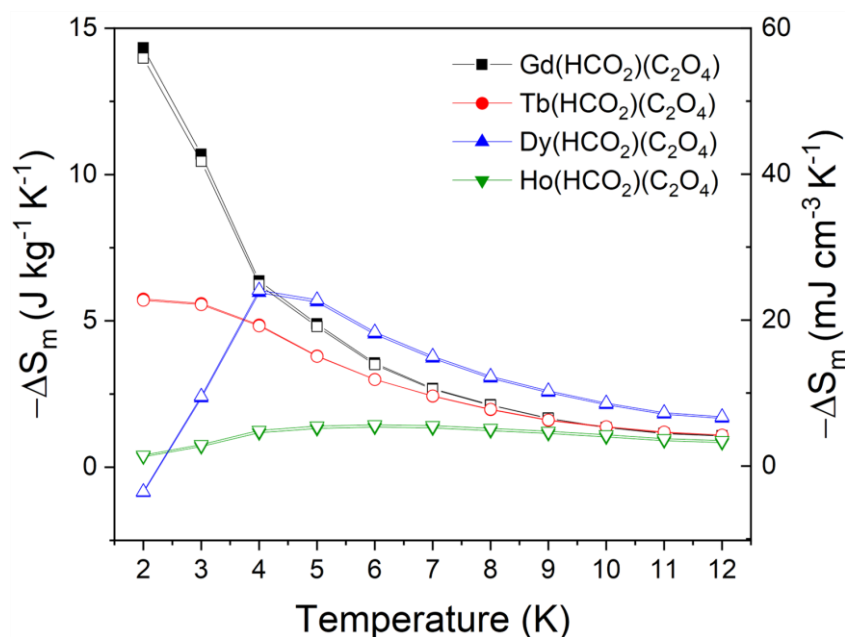
Figure 4.15: Magnetic entropy changes for the A(HCO₂)(C₂O₄) series for $\Delta B = 1$–0 T. The filled and hollow symbols mark the gravimetric and volumetric units, respectively.
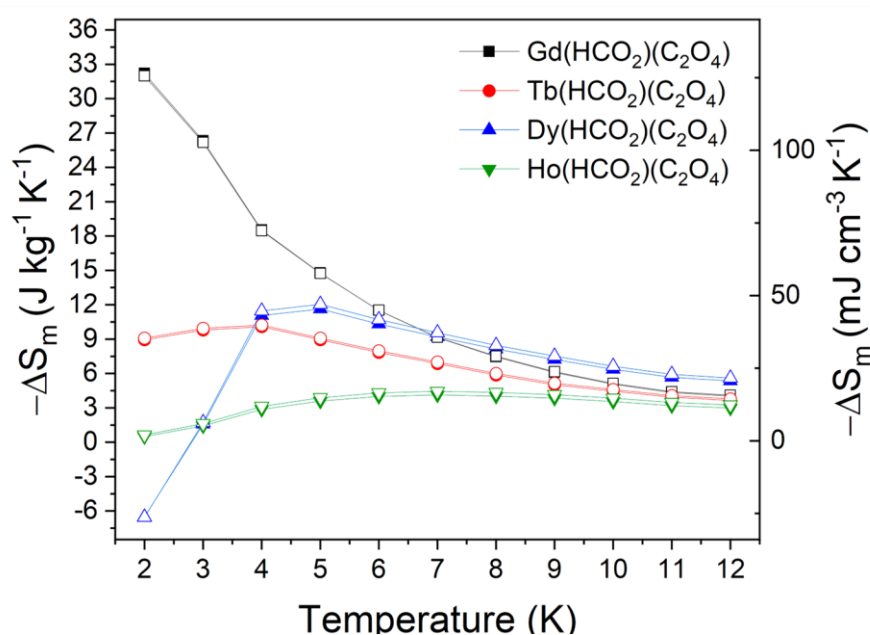
Figure 4.16: Magnetic entropy changes for the A(HCO₂)(C₂O₄) series for $\Delta B = 2$–0 T. The filled and hollow symbols mark the gravimetric and volumetric units, respectively.

In work that was completed and published in parallel with this study, similar values of $-\Delta S_m^{max}$ were found for Gd(HCO₂)(C₂O₄) by Xu *et al.*,[191] namely 58.9 J kg⁻¹ K⁻¹, corresponding to volumetric values of 228.5 mJ cm⁻³ K⁻¹, for a field change of 7 T and $T_{max} = 2$ K (*cf.* 55.97 J kg⁻¹ K⁻¹ and 218.42 mJ cm⁻³ K⁻¹ under the same conditions observed in our studies), while $-\Delta S_m^{max}$ was found to be 32.7 J kg⁻¹ K⁻¹, corresponding to 127 mJ cm⁻³ K⁻¹, for a 2 T field change, and with $T_{max} = 2$ K.

4.6   Low-Temperature   Neutron   Diffraction   of

Tb(HCO$_2$)(C$_2$O$_4$) and Ho(HCO$_2$)(C$_2$O$_4$)

In the related *Ln*(HCO$_2$)$_3$ and *Ln*OHCO$_3$ frameworks it has been shown that the enhancement of magnetocaloric properties at higher temperatures and lower field changes is associated with short range magnetic order, as indicated by the appearance of diffuse magnetic scattering in neutron diffraction patterns.[5,51,120] When comparing the behaviour of the A(HCO$_2$)(C$_2$O$_4$) compounds to the closely related *Ln*(HCO$_2$)$_3$ phases, there is a striking difference in the lack of improvement in the magnetocaloric entropy change of the Tb(HCO$_2$)(C$_2$O$_4$) and Ho(HCO$_2$)(C$_2$O$_4$) compounds at higher temperatures and lower applied fields. This offers the opportunity to confirm if the strong local magnetic interactions in the *Ln*(HCO$_2$)$_3$ phases are indeed related to their magnetocaloric properties. To confirm this, we measured the neutron diffraction patterns of both Tb(HCO$_2$)(C$_2$O$_4$) and Ho(HCO$_2$)(C$_2$O$_4$) at a series of temperatures between 1.5 K and 20 K. We were able to fit the data obtained on the GEM diffractometer at all the acquired temperatures, with Figure 4.17 showing fits to bank 2 and bank 6 at room temperature and Tables 4.5 and 4.6 reporting the crystallographic information extracted from the refinements at room temperature for Tb(HCO$_2$)(C$_2$O$_4$) and Ho(HCO$_2$)(C$_2$O$_4$), respectively. Crystallographic information at 20 and 1.6 K and patterns for the remainder of the fits are reported in Appendix B (see Figures S1–S96 in SI for fits to other temperatures). Only a variation in lattice parameters is observed upon lowering the temperature.
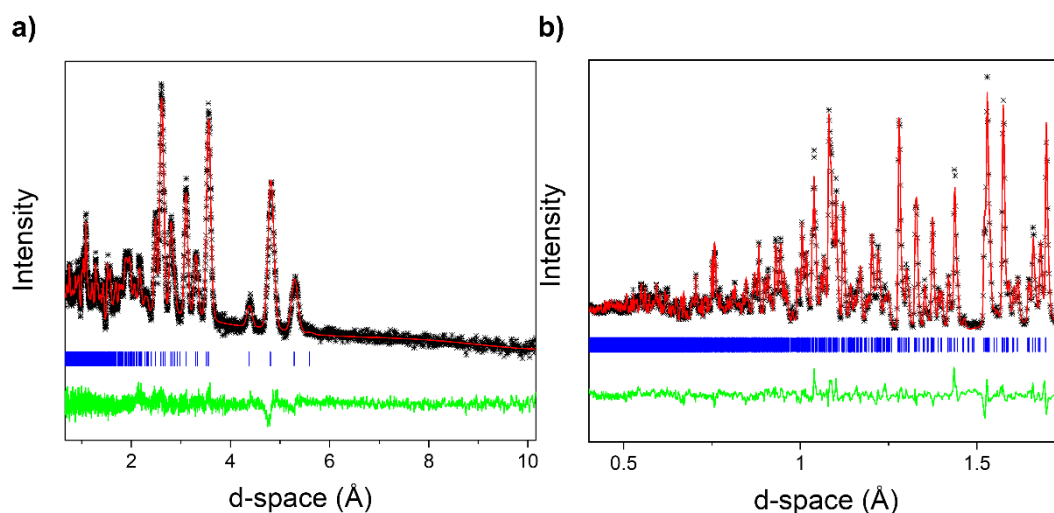
Figure 4.17: Fits to neutron diffraction patterns of Tb(HCO$_2$)(C$_2$O$_4$) collected at room temperature from (a) bank 2 and (b) bank 6 of the GEM diffractometer. Refinement statistics are $R_p = 2.67\%$ and 1.48%, and $R_{wp} = 3.16\%$ and 1.94%, for the two banks, respectively. The crosses, upper and lower lines indicate the observed and calculated intensities, and the differences between them. The markers indicate the reflection allowed by the structure.

Figure 4.18 shows the comparison of the neutron patterns acquired from bank 2 of the GEM diffractometer at 1.6 and 20 K for both systems. Indeed, it can be easily observed that no difference is present between patterns at these temperatures, either in terms of additional intensity of the Bragg reflections or diffuse scattering. The absence of the latter feature was confirmed by obtaining difference curves, which were rebinned to optimise signal to noise. The lack of observable diffuse scattering indicates that Tb(HCO$_2$)(C$_2$O$_4$) and Ho(HCO$_2$)(C$_2$O$_4$) likely lack significant magnetic correlations above 1.5 K, in sharp contrast to Tb(HCO$_2$)$_3$ and Ho(HCO$_2$)$_3$, where strong diffuse scattering is observed just below 10 K.[5,51]

Table 4.5: Crystallographic details of $Tb(HCO_2)(C_2O_4)$ obtained from neutron diffraction patterns collected at 300 K. Final total refinement statistics R_p and R_{wp} were 2.88 % and 3.27 %, respectively.

Space Group	a (Å)	b (Å)	c (Å)	Volume (Å³)	
Pnma	7.01686(13)	10.5978(2)	6.59239(12)	490.23(2)	
Site	x	Y	z	U_{iso}(Å²)	Fractional Occupancy
Tb	0.20348	3/4	0.63422	0.00153(18)	1
O1	0.53263(18)	3/4	0.5380(2)	0.0053(3)	1
O2	0.5526(3)	3/4	0.1993(2)	0.0131(4)	1
O3	0.23803(15)	0.54453(9)	0.47981(13)	0.0069(2)	1
O4	0.08552(13)	0.37694(8)	0.35167(16)	0.0064(2)	1
C1	0.6190(2)	3/4	0.3726(2)	0.0124(3)	1
C2	0.09644(13)	0.47884(7)	0.45248(11)	0.00331(17)	1
D	0.7711(3)	3/4	0.3766(3)	0.0681(7)	1

These results support the hypothesis that 1D ferromagnetic correlations in $Tb(HCO_2)_3$ and $Ho(HCO_2)_3$ play a key role in enhancing the rate of change in their magnetisation under low external applied fields, and the lack of these correlations in $Tb(HCO_2)(C_2O_4)$ and $Ho(HCO_2)(C_2O_4)$ might lead to them not showing such enhanced properties. We have found, as discussed in Section 4.2.1, that the replacement of the two formates with one oxalate ligand lowers the symmetry from the rhombohedral $R3m$ space group of the $Ln(HCO_2)_3$ frameworks to the orthorhombic $Pnma$ structure of the $Ln(HCO_2)(C_2O_4)$, with a modification of the LnO_9 polyhedra such that the chains propagate in a zig-zag fashion rather than being linear.

Table 4.6: Crystallographic details of $Ho(HCO_2)(C_2O_4)$ obtained from neutron diffraction patterns collected at 300 K. Final total refinement statistics R_p and R_{wp} were 2.88% and 3.31%, respectively.

Space Group	a (Å)	b (Å)	c (Å)	Volume (Å^3)	
Pnma	6.94353(14)	10.5424(2)	6.55458(13)	479.81(2)	

Site	x	y	z	U_{iso}(Å^2)	Fractional Occupancy
Ho	0.20113	¼	0.36659	−0.00065(16)	1
O1	0.08687(14)	0.62422(9)	0.64978(17)	0.00554(14)	1
O2	0.24041(15)	0.45462(10)	0.52007(14)	0.00554(14)	1
O3	0.5517(3)	¼	0.8024(2)	0.00782(2)	1
O4	0.5304(2)	¼	0.4619(2)	0.00782(2)	1
C1	0.09750(14)	0.52095(8)	0.54864(13)	0.00507(15)	1
C2	0.6180(2)	¼	0.6269(2)	0.00507(15)	1
D	0.7726(3)	¼	0.6240(4)	0.0725(8)	1
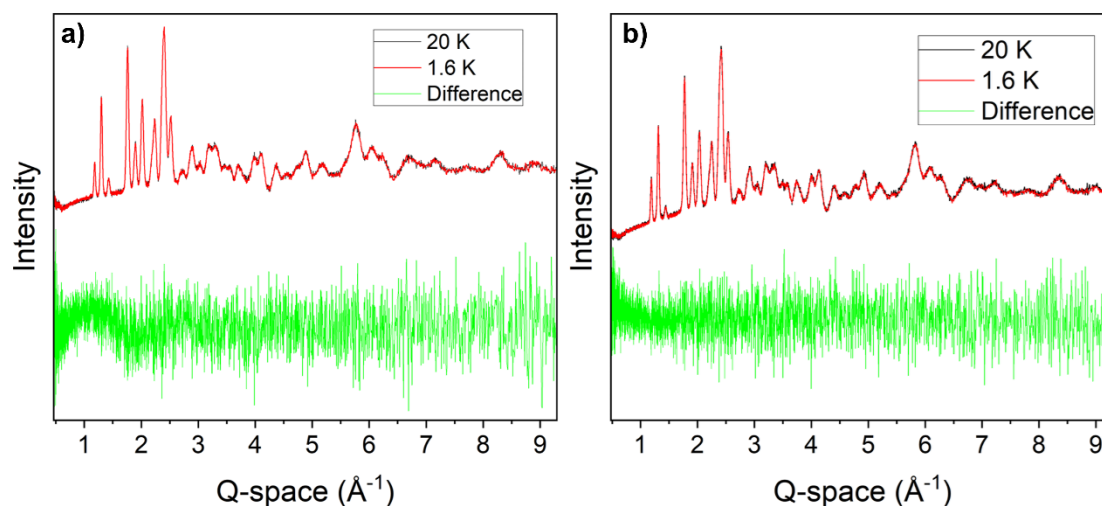
F**igure 4.18:** Comparison of neutron diffraction patterns collected at 20 K and 1.6 K from bank 2 on GEM for (a) $Tb(HCO_2)(C_2O_4)$ and (b) $Ho(HCO_2)(C_2O_4)$. For both compounds, the difference line has been magnified ten times and shows no appreciable variation upon lowering the temperature.

Despite these modifications, we have found the superexchange pathways remain quite similar among the two families of compounds, with these found to have a total length of 4.975(3) Å in $Tb(HCO_2)_3$ and 4.937(2) Å and 4.887(2) Å in $Tb(HCO_2)(C_2O_4)$ for O1 and O4, respectively. Similarly, the Tb-O-Tb angles in $Tb(HCO_2)(C_2O_4)$ have an

average value of 103.04(8)°, close to the 105° found in $Tb(HCO_2)_3$. As a consequence, we expected the interactions within the chains in both series to remain similar for a given f-configuration, despite small changes in the pathways that may affect the nature of these interactions. The superexchange interactions were estimated in the mean-field isotropic approximation using the equation:

$$J_1 = J_{nn}S(S + 1) = \frac{3k_B\theta_{CW}}{2n} \, , \tag{4.1}$$

where S is the total spin quantum number, n is the number of nearest neighbour spins — equal to 2 in the case of 1D-chains — and θ_{CW} is the Curie-Weiss temperature obtained from the lowest-temperature fit. J_1 values are reported in Table 4.5. These values can be compared with the dipolar interactions D within the system, estimated using the equation:

$$D = \frac{-\mu_0\mu_{eff}^2}{4\pi r^3} \, , \tag{4.2}$$

where r is the distance between two neighbouring lanthanide cations in a chain or between two chains. It should be noted that the structure is such that any given chain is surrounded by six neighbouring ones, four of which can be found along the [011] direction and are at the same distance from any given Ln site, whereas the other two neighbouring chains are found along the [001] direction and are slightly further apart. It should also be pointed out that, as single-crystal data for $Gd(HCO_2)(C_2O_4)$ and $Dy(HCO_2)(C_2O_4)$ is lacking, the same Ln-Ln distances found in $Tb(HCO_2)(C_2O_4)$ from refinements of neutron diffraction data at 1.6 K are used to estimate the dipolar interactions in these two coordination polymers, whereas for $Ho(HCO_2)(C_2O_4)$ the Ho-Ho distances determined from refinements of the neutron data at the same temperature are used. For instance, in $Tb(HCO_2)(C_2O_4)$, the interchain distances are 6.26232(4) and 6.59095(7) Å for neighbouring chains along the [011] and the [001] directions, respectively, while the Tb-Tb intrachain distance is 3.83106(4) Å. Similarly,

in $Ho(HCO_2)(C_2O_4)$, the corresponding values are 6.22692(6), 6.52620(8) and 3.79706(5) Å, respectively. Despite the above-mentioned approximation for those $Ln(HCO_2)(C_2O_4)$ members where crystallographic information is not available, we do not expect the Ln-Ln distances to differ to such an extent as to affect the values of the dipolar interactions significantly and this would still allow us to compare these interactions with the superexchange J_1 ones, especially in terms of their magnitude. Values of superexchange J_1 and dipolar interactions $D_{intrachain}$ and $D_{interchain}$ are reported in Table 4.7.

These results show that both intrachain and interchain dipolar interactions are quite close to the superexchange ones. We therefore concluded the change in symmetry plays a significant role in suppressing the strong magnetic interactions found in $Tb(HCO_2)_3$ and $Ho(HCO_2)_3$ in their $Ln(HCO_2)(C_2O_4)$ analogues.

These results highlight the importance of searching for lanthanide frameworks with strong local magnetic correlations when looking for enhanced magnetocaloric properties and that small changes in the structures of these materials can have a significant impact on their performance.

Table 4.7: Estimated values of superexchange coupling constant J_1 along the chains, and dipolar D intrachain and interchain interactions in *Ln*(HCO$_2$)(C$_2$O$_4$) (*Ln* = Gd^{3+}, Tb^{3+}, Dy^{3+}, Ho^{3+})

Sample	J_1 (K)	$D_{\text{intrachain}}$ (K)	$D_{\text{interchain}}$ along [001] (K)	$D_{\text{interchain}}$ along [011] (K)
Gd(HCO$_2$)(C$_2$O$_4$)	−0.375	−1.24	−0.24	−0.57
Tb(HCO$_2$)(C$_2$O$_4$)	−1.425	−2.11	−0.41	−0.96
Dy(HCO$_2$)(C$_2$O$_4$)	−0.975	−2.57	−0.50	−1.18
Ho(HCO$_2$)(C$_2$O$_4$)	−3.15	−2.74	−0.53	−1.24

4.7 Conclusions

The synthesis of the members of the *Ln*(HCO$_2$)(C$_2$O$_4$) (*Ln* =Sm^{3+}–Er^{3+}) family of coordination frameworks proved to be successful and the magnetic — including magnetocaloric — properties of the A(HCO$_2$)(C$_2$O$_4$) members (A = Gd^{3+}–Ho^{3+}) have been studied. It was found that Gd(HCO$_2$)(C$_2$O$_4$) exhibits a high magnetocaloric performance, with a peak entropy change $-\Delta S_{\text{m}}^{\text{max}} = 55.97$ J kg^{-1} K^{-1}, corresponding to a volumetric entropy change of 218.42 mJ cm^{-3} K^{-1}, comparable to that of some of the best performing coordination frameworks, at 2 K and for a field change of 5–0 T. For this reason, Gd(HCO$_2$)(C$_2$O$_4$) is an excellent candidate for magnetic cooling applications at low temperature and high magnetic fields, and shows that coordination frameworks with organic ligands can indeed offer entropy changes comparable to purely inorganic frameworks. Dy(HCO$_2$)(C$_2$O$_4$) was found to outperform Gd(HCO$_2$)(C$_2$O$_4$) at higher temperatures for field changes of less than 2 T, despite this not being as significant as observed in related families of coordination polymers. Indeed, this study has shown that Tb(HCO$_2$)(C$_2$O$_4$) and Ho(HCO$_2$)(C$_2$O$_4$) lack significant magnetic correlations above 1.5

K, in contrast with the isoelectronic *Ln*(HCO$_2$)$_3$ analogues. The lack of significant magnetic correlations is likely the cause of the poorer MCE of these coordination frameworks compared to the analogous magnetically anisotropic formates. Hence, these results highlight the importance of optimising the local magnetic correlations in magnetocalorics materials in order to enhance their performance at lower applied magnetic fields and higher temperatures and they have also shown how these optimisations are vulnerable to disruption by relatively small structural changes.

5 Tuning the Magnetic Interactions in Solid Solutions of $Ln(HCO_2)_3$ (Ln = Tb, Ho)

5.1 Introduction

Following from the previous chapter on the effects of structural modifications between $Ln(HCO_2)_3$ and $Ln(HCO_2)(C_2O_4)$ phases on the magnetocaloric properties of these materials, we now turn to the effects of doping the $Ln(HCO_2)_3$ phases with other cations to modulate their magnetic properties. The interesting properties found in $Tb(HCO_2)_3$ and $Ho(HCO_2)_3$,[51] which host ferromagnetic correlations within their chains, as discussed in Section 1.9, have sparked our interest about the possibility of doping with diamagnetic cations or those that support antiferromagnetic coupling within the chains of the $Ln(HCO_2)_3$ structure. While Y^{3+} provides an obvious option as a diamagnetic cation, being approximately the same size as Tb^{3+} and Ho^{3+} (*cf.* 1.075, 1.095 and 1.072, for 9-coordinated Y^{3+}, Tb^{3+} and Ho^{3+}, respectively),[192] of the $Ln(HCO_2)_3$ frameworks examined thus far only $Er(HCO_2)_3$ has antiferromagnetic ordering within its chains; unfortunately this appears to be far weaker than in $Tb(HCO_2)_3$ and $Ho(HCO_2)_3$ as it only leads to magnetic ordering at ~50 mK as opposed to ~1 K in the $Tb(HCO_2)_3$ and $Ho(HCO_2)_3$ phases (see Section 1.9). Thus, given that the magnetic behaviour of $Ln(HCO_2)_3$ (Gd–Er) only had been studied in detail so far,[5,51,55,56] the first goal for this chapter was to explore the magnetic properties of the $Ln(HCO_2)_3$ frameworks containing

earlier lanthanides, namely Ce^{3+}, Pr^{3+} and Nd^{3+}, which had been largely neglected thus far and lack the high neutron absorptions of Sm and Eu, or the radioactivity of Pm.

As will be discussed below, unfortunately, none amongst the $Ce(HCO_2)_3$, $Pr(HCO_2)_3$ or $Nd(HCO_2)_3$ frameworks exhibit any indication of magnetic ordering at low temperature. Given the weaker interactions in $Ho(HCO_2)_3$ compared to $Tb(HCO_2)_3$, this leaves a solid solution of $Ho_{1-x}Er_x(HCO_2)_3$ as the best series in which to look for the effect of mixing ferromagnetic and antiferromagnetic intrachain interactions in a material that would potentially allow for neutron scattering experiments. Interest in such a system emerges from a similar 1D series reported in the literature, namely the $SrCuPt_{1-x}Ir_xO_6$ series.[42] While the parent compounds, Sr_3CuPtO_6 and Sr_3CuIrO_6 feature structures containing one-dimensional Heisenberg chains with antiferromagnetic and ferromagnetic interchain coupling respectively, it was shown that in the $Sr_3CuPt_{1-x}Ir_xO_6$ series variations in composition allow for the tuning of the magnetic properties of its different members. In particular $Sr_3CuPt_{0.5}Ir_{0.5}O_6$ has been previously shown to be a random spin-chain paramagnet due to the 1:1 mixing of Pt and Ir on the same crystallographic site.[42] A random spin-chain paramagnet is a system where the probability P of finding a neighbouring site antiferromagnetically or otherwise ferromagnetically coupled is 50%, achieved when the distribution of both sites is random, such as in $Sr_3CuPt_{0.5}Ir_{0.5}O_6$,[42] with the result that the magnetic susceptibility $\chi(T)$ resembles that of free spins down to low temperatures, not because the spins are actually free but rather because they are locked together in clusters of size $\xi(T)$ and forming a large effective spin, S_{eff}, and with these still randomly oriented overall when $P = 0.5$. To date, the mixture of the high absorption of Ir and the need to use high pressures to fabricate $Sr_3CuPt_{0.5}Ir_{0.5}O_6$, however, have prevented the study of this material using neutron scattering, restricting the understanding of its structure. The realisation of such a phase in the $Ho_{1-x}Er_x(HCO_2)$

series would allow a more in-depth study of this exotic state. We have therefore synthesised the Ho$_{1-x}$Er$_x$(HCO$_2$)$_3$ series and characterised the magnetic properties of its members. Among these, we have probed the Ho$_{0.5}$Er$_{0.5}$(HCO$_2$)$_3$ sample *via* neutron diffraction using the WISH diffractometer.

Another series that has attracted our interest is that of Tb$_{1-x}$Y$_x$(HCO$_2$)$_3$, where Y is a diamagnetic dopant, with diamagnetic impurities known to disrupt low-dimensional magnetic states.[193–197] Therefore, our interest was drawn by the possibility of doping the Tb(HCO$_2$)$_3$ structure and observe how its TIA state would be affected by the presence of such a non-magnetic impurity. This proved to be successful, and the characterisation of this new family of Y-doped MOFs, the Tb$_{1-x}$Y$_x$(HCO$_2$)$_3$ frameworks, is here reported. We have studied this series using a combination of magnetic and ultra-low temperature heat capacity measurements, to assess the magnetic — including magnetocaloric — properties of some of its members, with the observation of interesting effects, ascribed to be entropic in nature and due to the fragmentation of the spin-chains in the structure.

5.2 Ce(HCO$_2$)$_3$, Pr(HCO$_2$)$_3$ and Nd(HCO$_2$)$_3$: Bulk Properties and Neutron Diffraction

5.2.1 Powder X-ray Diffraction and Bulk Magnetic Properties of Ce(HCO$_2$)$_3$, Pr(HCO$_2$)$_3$ and Nd(HCO$_2$)$_3$

Samples of Ce(HCO$_2$)$_3$, Pr(HCO$_2$)$_3$ and Nd(HCO$_2$)$_3$, and deuterated analogues, Ce(DCO$_2$)$_3$ and Nd(DCO$_2$)$_3$, were synthesised *via* the method reported in Section 3.2.2. Characterisation using PXRD revealed the samples to be isostructural with the rest of the $Ln(HCO_2)_3$ series, adopting a $R3m$ rhombohedral structure, with Le Bail fits showing phase purity, as shown in Figure 5.1, with lattice parameters and statistics from the fits reported in Table 5.1, with the former also plotted in Figure 5.2.

Table 5.1: Lattice parameters from Le Bail refinements for $Ln(HCO_2)_3$ (Ln = Ce^{3+}, Pr^{3+}, Nd^{3+}) and corresponding refinement statistics.

Sample	a (Å)	c (Å)	R_p%	R_{wp}%	χ^2
Ce(DCO$_2$)$_3$	10.68723(12)	4.11429(5)	3.25	4.10	3.20
Pr(HCO$_2$)$_3$	10.64861(15)	4.08739(6)	3.47	4.70	8.50
Nd(DCO$_2$)$_3$	10.60441(13)	4.06361(13)	2.49	3.26	3.83
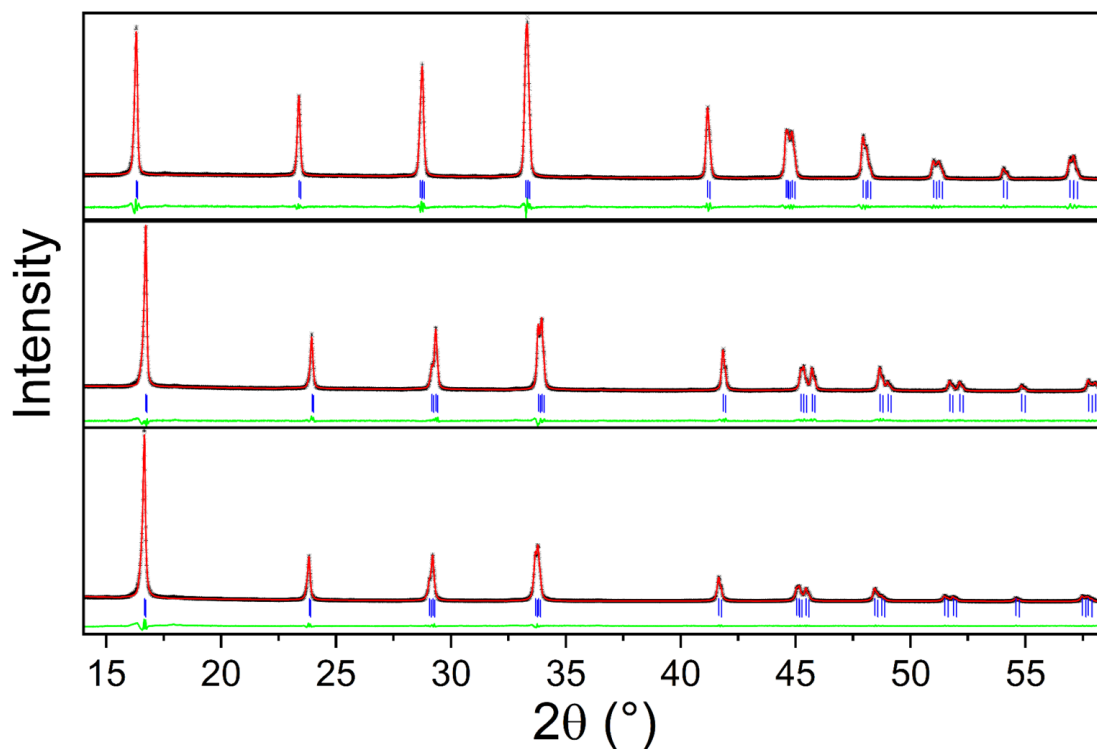
Figure 5.1: Conventional powder X-ray diffraction patterns of Ce(DCO₂)₃, Pr(HCO₂)₃ and Nd(DCO₂)₃, measured using a Cu source ($\lambda = 1.54$ Å) and fitted using the Le Bail method to highlight phase purity. The crosses, red and green lines are experimental and calculated intensities and the difference curve. Vertical markers indicate the position of the Bragg reflections.
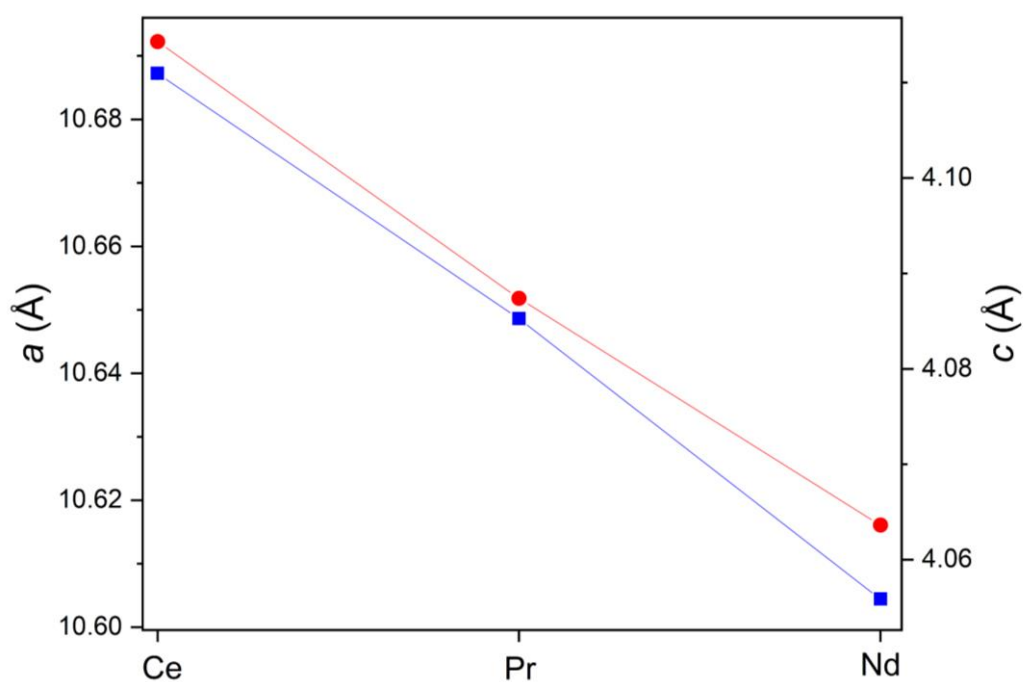
Figure 5.2: Lattice parameters *a* (in blue) and *c* (in red) of Ce(DCO₂)₃, Pr(HCO₂)₃ and Nd(DCO₂)₃ determined *via* Le Bail refinements of the powder X-ray diffraction patterns.

Measurements of the bulk magnetic properties of the $Nd(HCO_2)_3$, $Pr(HCO_2)_3$ and $Ce(HCO_2)_3$ samples *via* SQUID magnetometry have shown both samples to be paramagnetic down to 1.8 K, as shown in Figure 5.3. Interestingly, it is possible to observe a significant deviation from the Curie-Weiss law occurring at ~80 , ~20 and ~60 K for $Nd(HCO_2)_3$, $Pr(HCO_2)_3$ and $Ce(HCO_2)_3$, respectively, which might indicate the onset of stronger short-range interactions within the magnetic lattice as well as crystal field effects becoming more significant. Two linear regions have therefore been identified for both samples, at high and low temperature, respectively. Results from fits to the Curie-Weiss law carried out both in the high- and low-temperature regimes are shown in Table 5.2 and suggest these samples possess antiferromagnetic behaviour, as shown by the negative values of the Curie-Weiss temperature θ_{CW}. Furthermore, values of effective magnetic moment, μ_{eff}, at high-temperature are close to the expected values for Ce^{3+}, Pr^{3+} and Nd^{3+}, and decrease upon cooling. It should be noted that data for $Pr(HCO_2)_3$ contains some degree of noise, and some data points have been excluded in order to reduce its effect on the fit. The observed decrease of the Curie-Weiss temperature, θ_{CW}, and effective magnetic moments in the low-temperature regime can be ascribed to the effects of orbital quenching resulting from interactions with the crystal field environment, which become more significant at lower temperature. As such, the values determined from the fit to the Curie-Weiss law in the low-temperature regime are more representative of the weakly antiferromagnetic behaviour in these materials.

Heat capacity measurements for $Pr(HCO_2)_3$, shown in Figure 5.4, were also carried out between 0.5 and 4 K in zero-field conditions. The lack of any significant feature in the data shows that $Pr(HCO_2)_3$ does not undergo any noticeable transition in this temperature range.

Table 5.2: Results from fits of the Curie-Weiss law to the inverse susceptibility χ^{-1} in the high- and low-temperature regimes for Ce(HCO₂)₃, Pr(HCO₂)₃, and Nd(HCO₂)₃.

Sample	High-T range (K)	θ_{CW} (K)	μ_{eff} (μ_B)	Low-T range (K)	θ_{CW} (K)	μ_{eff} (μ_B)
Ce(HCO₂)₃	100–300	−19.59	2.32	1.8–10.6	−0.16	1.88
Pr(HCO₂)₃	100–300	−45.28	3.57	1.8–10.6	−9.87	1.80
Ce(HCO₂)₃	100–300	−67.62	3.67	1.8–10.6	−0.54	2.30
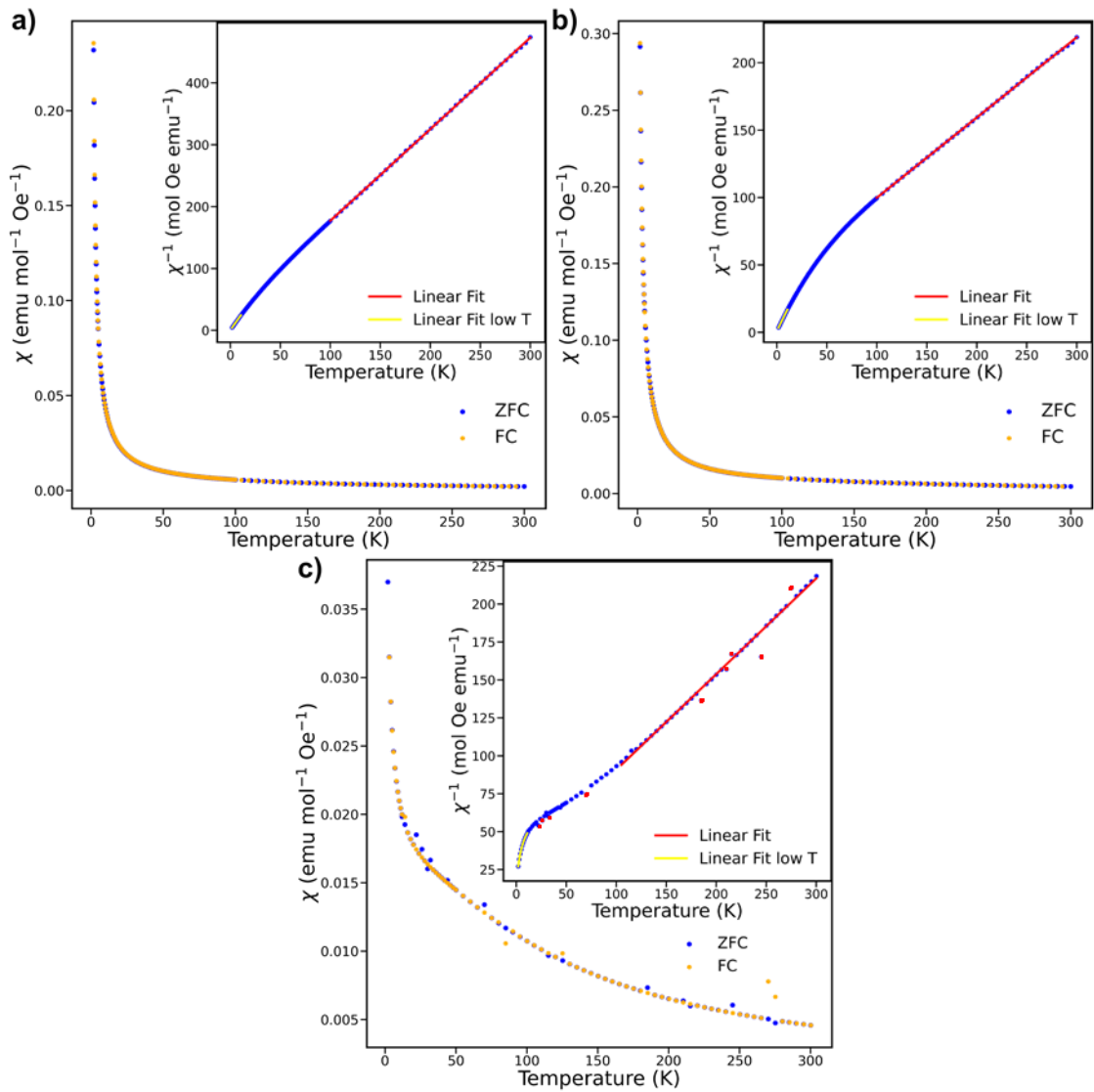
Figure 5.3: Bulk magnetic properties of a) Ce(HCO₂)₃, b) Nd(HCO₂)₃ and c) Pr(HCO₂)₃ measured from 1.8 to 300 K. The inverse susceptibilities, χ^{-1}, are shown in the insets. Red data points in c) were excluded from the fits.
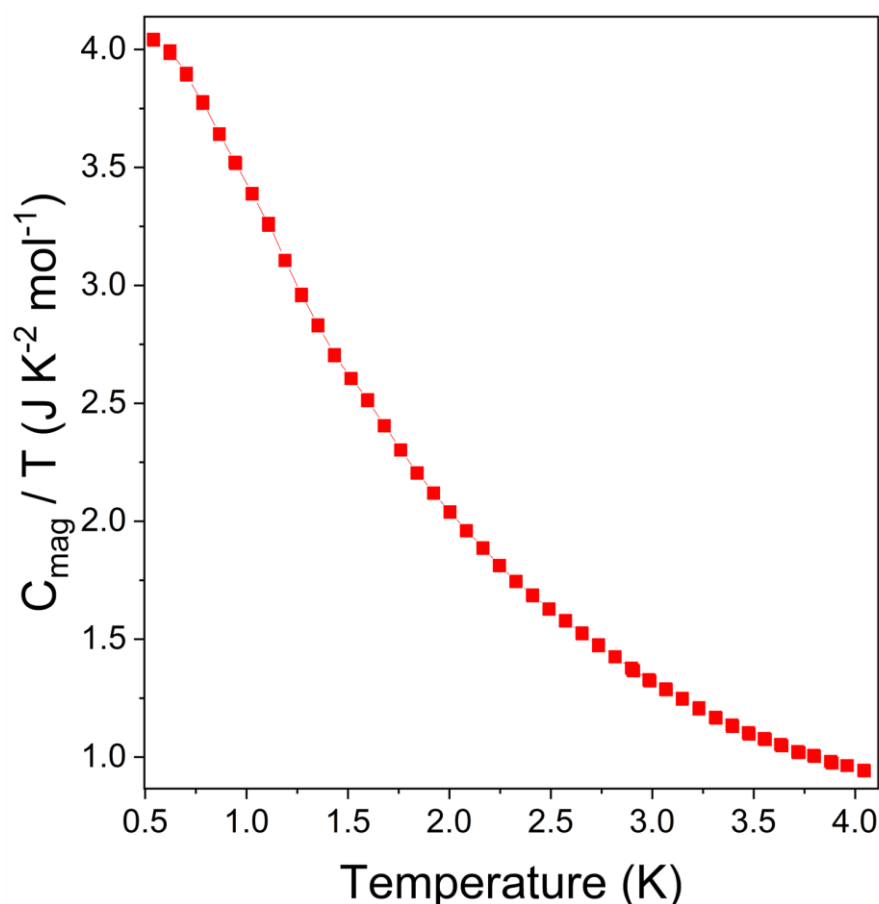
Figure 5.4: Heat capacity of $Pr(HCO_2)_3$ between 0.5 and 4 K in zero-field conditions.

As the Kramer's theorem states, in a system containing an odd number of electrons, at least a two-fold degeneracy must remain in the absence of a magnetic field, and the resulting doublets can be split by an applied field. Ions containing an odd number of electrons are therefore named Kramer's ions and will show some magnetic behaviour under any condition. Conversely, non-Kramer ions possess an even number of electrons, which can be paired, resulting in the removal of the degeneracy. This might therefore result in the material becoming diamagnetic if some conditions are satisfied in its ground state. Ce^{3+} and Nd^{3+} are examples of Kramer's ions, as their electronic configuration is $4f^1$ and $4f^3$, whereas Pr^{3+} possesses only two electrons in its $4f$ orbitals, and therefore constitutes a non-Kramer ion. For this reason, following the results so-far discussed, we focused on $Ce(DCO_2)_3$ and $Nd(DCO_2)_3$ for neutron diffraction experiments, carried out using the Wombat diffractometer (ANSTO, Australia) and performed by Dr Andrew

Studer, to ascertain these two materials do not exhibit any significant magnetic behaviour, such as magnetic frustration which diffuse scattering might indicate, if present, upon cooling at even lower temperatures. Results have shown both materials maintain their nuclear phase down to 50 mK and 140 mK for Ce(DCO$_2$)$_3$ and Nd(DCO$_2$)$_3$, respectively. The absence of additional Bragg-like or diffuse features in the patterns down to these temperatures, as shown in Figure 5.5 and Figure 5.6, suggests no magnetic ordering emerges down to these temperatures and no significant short-range interactions are present either in Ce(DCO$_2$)$_3$ and Nd(DCO$_2$)$_3$.
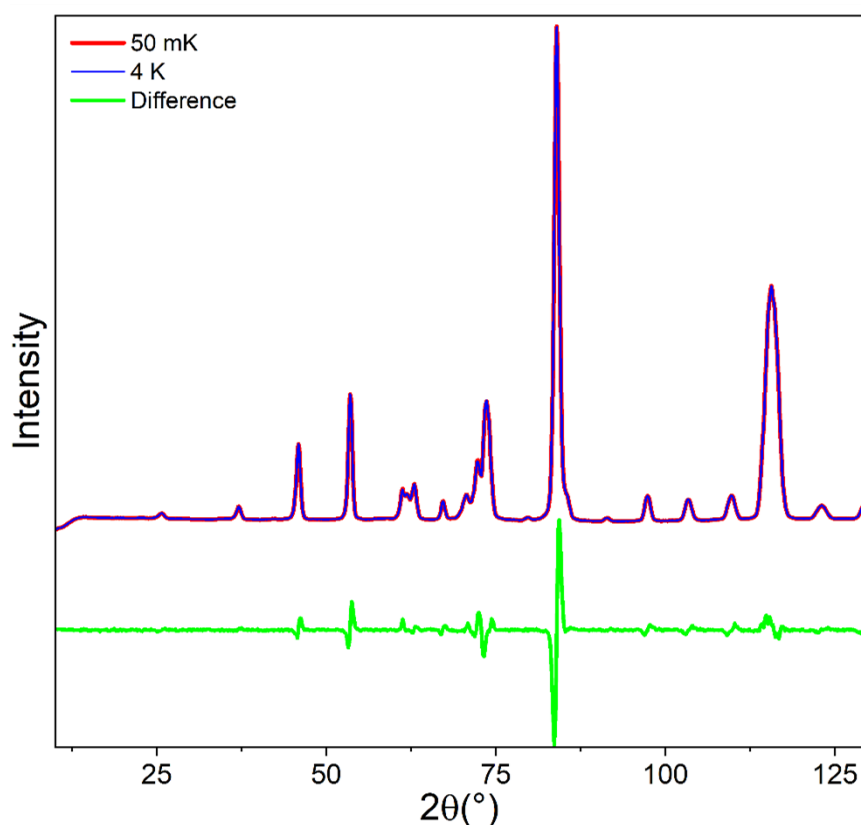
Figure 5.5: Neutron diffraction patterns of Ce(DCO$_2$)$_3$ acquired on Wombat at 50 mK and 4 K with a wavelength $\lambda = 2.41$ Å. The difference curve has been magnified ten times and shows no appreciable variation upon lowering the temperature.
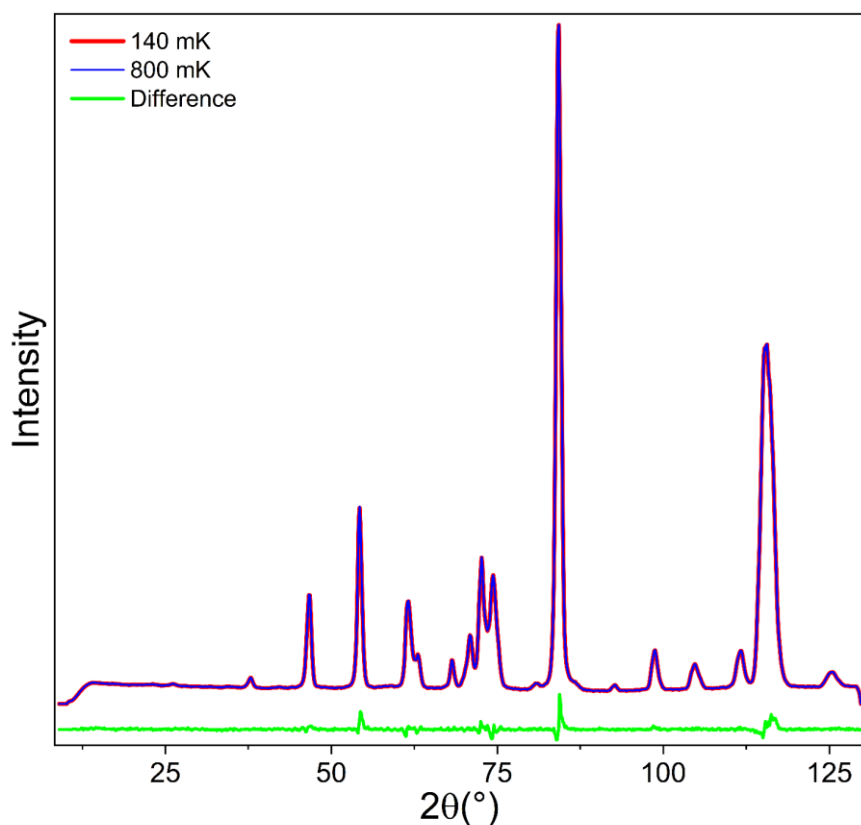
Figure 5.6: Neutron diffraction patterns of $Nd(DCO_2)_3$ acquired on Wombat at 140 and 800 mK with a wavelength $\lambda = 2.41$ Å. The difference curve has been magnified ten times and shows no appreciable variation upon lowering the temperature.

Indeed, as shown in Figure 5.7, heavily constrained Rietveld refinements of both $Ce(DCO_2)_3$ and $Nd(DCO_2)_3$ models using the patterns obtained at the lowest temperatures showed that the nuclear phases account for the reflections observed, confirming no transition occurs upon cooling.
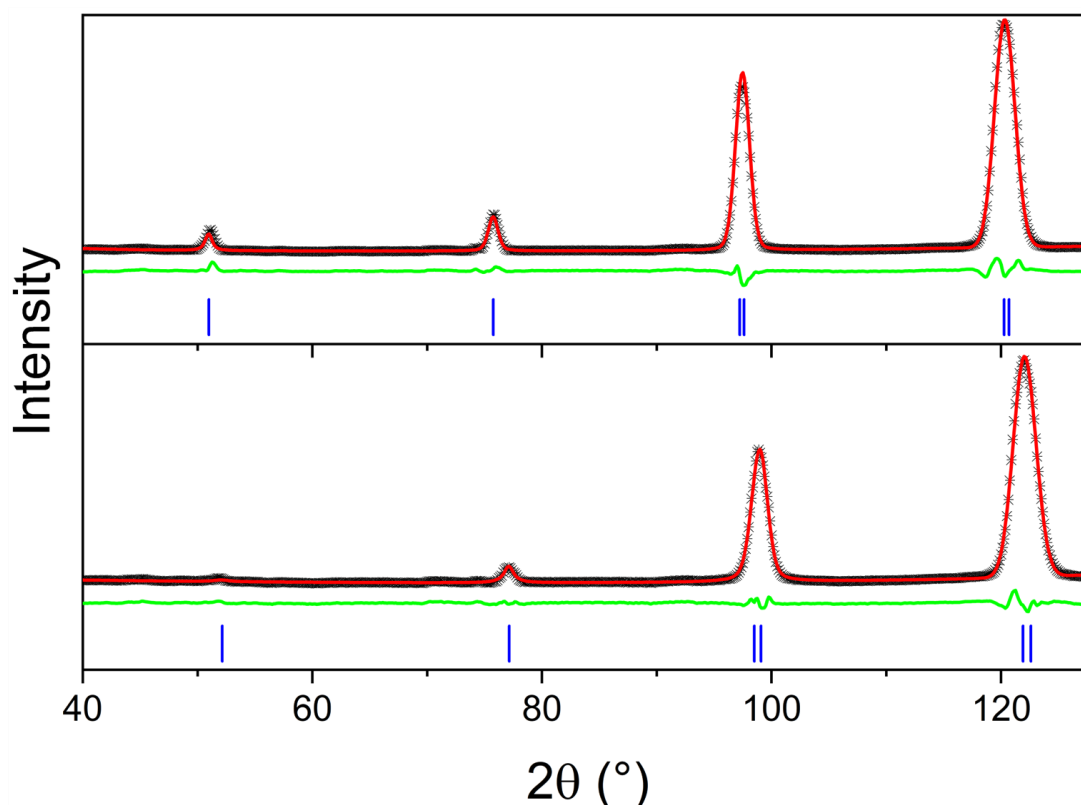
Figure 5.7: Partial refinements of patterns for $Ce(DCO_2)_3$ (top) and $Nd(DCO_2)_3$ (bottom) measured using Wombat with a wavelength $\lambda = 4.61$ Å. The crosses, red and green lines are experimental and calculated intensities and the difference curve. Vertical markers indicate the position of the Bragg reflections.

5.3 Magnetic properties of $Ho_{1-x}Er_x(HCO_2)_3$

Given the lack of short- or long-range order in the $Ln(HCO_2)_3$ frameworks containing the earlier lanthanides, as discussed in the sections above, the next sensible step consisted of the synthesis of a series of $Ho_{1-x}Er_x(HCO_2)_3$ solid solutions; this represented the best way to explore a $Ln(HCO_2)_3$ family containing a mixture of ferromagnetic and antiferromagnetic intrachain 1D interactions, given the interest in the $SrCuPt_{1-x}Ir_xO_6$ series as discussed in Section 5.1.[42]

5.3.1. Composition and structure of the $Ho_{1-x}Er_x(HCO_2)_3$ series

Samples of $Ho_{1-x}Er_x(HCO_2)_3$ ($x = 0.1, 0.2, 0.3, 0.4, 0.5, 0.6, 0.7, 0.8$ and 0.9) were synthesised *via* the method reported in Section 3.2.3. The experimental stochiometric compositions of the $Ho_{1-x}Er_x(HCO_2)_3$ members were determined *via* XRF with the

results, shown in Table 5.3, suggesting these to be close to the nominal compositions, the targets of our syntheses.

Additional elemental analysis was carried out *via* EDX on selected regions of the samples — with results reported in Appendix C, along with pictures of the regions acquired using SEM — and showed good agreement with values determined from bulk XRF experiments with no obvious indication of sample inhomogeneity. Powder X-ray diffraction measurements of Ho$_{1-x}$Er$_x$(HCO$_2$)$_3$ ($x = 0.1, 0.2, 0.3, 0.4, 0.5, 0.6, 0.7, 0.8$ and 0.9) have shown the members of this series to be isostructural, adopting a rhombohedral $R3m$ structure, hence retaining that of the parent materials, namely Ho(HCO$_2$)$_3$ and Er(HCO$_2$)$_3$, (see Figure 5.8 for fits to patterns). Statistics for the Le Bail fits carried out on the patterns and lattice parameters *vs*. composition plots are reported in Appendix C, with the latter showing these decrease overall with increasing concentrations of Er, although this trend is not linear due to fluctuations mainly attributed to the fact the Ho^{3+} and Er^{3+} ionic radii differ by less than 1% (*cf*. 1.072 and 1.062 Å for 9-coordinated Ho^{3+} and Er^{3+}, respectively).[192]
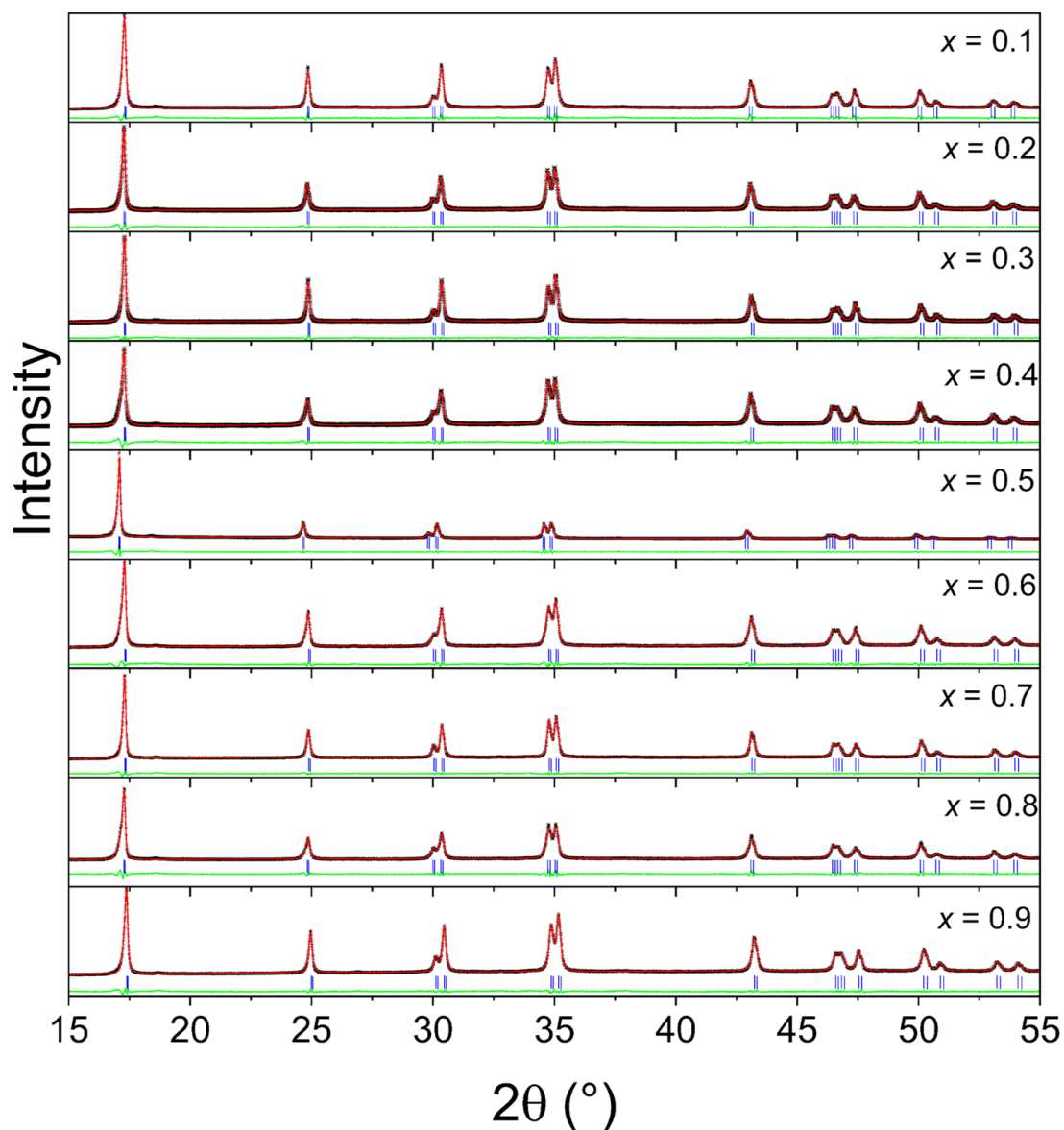
Figure 5.8: Conventional powder X-ray diffraction pattern of $Ho_{1-x}Er_x(HCO_2)_3$ ($x = 0.10, 0.20, 0.30, 0.40,$ $0.50, 0.60, 0.70, 0.80$ and 0.90) measured using a Cu source ($\lambda = 1.54$ Å) and fitted using the Le Bail method to highlight phase purity. The crosses, red and green lines are experimental and calculated intensities and the difference curve with the blue markers indicating expected positions of Bragg reflections.

Table 5.3. Comparison of the nominal and experimental compositions for $Ho_{1-x}E_x(HCO_2)_3$ determined *via* X-ray fluorescence.

Nominal composition	Experimental composition
$Ho_{0.90}Er_{0.10}(HCO_2)_3$	$Ho_{0.93(2)}Er_{0.07(2)}(HCO_2)_3$
$Ho_{0.80}Er_{0.20}(HCO_2)_3$	$Ho_{0.83(1)}Er_{0.17(1)}(HCO_2)_3$
$Ho_{0.70}Er_{0.30}(HCO_2)_3$	$Ho_{0.73(1)}Er_{0.27(1)}(HCO_2)_3$
$Ho_{0.60}Er_{0.40}(HCO_2)_3$	$Ho_{0.63(1)}Er_{0.37(1)}(HCO_2)_3$
$Ho_{0.50}Er_{0.50}(HCO_2)_3$	$Ho_{0.53(1)}Er_{0.47(1)}(HCO_2)_3$
$Ho_{0.40}Er_{0.60}(HCO_2)_3$	$Ho_{0.44(1)}Er_{0.56(1)}(HCO_2)_3$
$Ho_{0.30}Er_{0.70}(HCO_2)_3$	$Ho_{0.34(1)}Er_{0.66(1)}(HCO_2)_3$
$Ho_{0.20}Er_{0.80}(HCO_2)_3$	$Ho_{0.24(1)}Er_{0.76(1)}(HCO_2)_3$
$Ho_{0.10}Er_{0.90}(HCO_2)_3$	$Ho_{0.14(2)}Er_{0.86(2)}(HCO_2)_3$

5.3.2 Bulk magnetic properties of the $Ho_{1-x}Er_x(HCO_2)_3$ series

Bulk magnetic measurements were carried out for $Ho_{1-x}Er_x(HCO_2)_3$, with $x = 0.20$, 0.40, 0.60 and 0.80, as well as $x = 0.5$, as shown in Figures 5.9 and 5.10, respectively. All the samples measured showed paramagnetic behaviour down to 1.8 K, similar to that of the parent structures. With $Ho_{0.5}Er_{0.5}(HCO_2)_3$ potentially being a realisation of a random spin-chain paramagnet, as explained in Section 5.1, further analysis was carried out down to 0.4 K to ascertain this material remained paramagnetic well below the transition temperature observed for $Ho(HCO_2)_3$ (see inset Figure 5.9).[51] Indeed, the data suggests this material remains paramagnetic down to 0.4 K. This is in sharp contrast to the pure $Ho(HCO_2)_3$, which showed, as previously discussed, a transition at ~1.5 K both in bulk magnetic properties and elastic neutron scattering measurements, and the behaviour of this material is conversely closer to that of the $Er(HCO_2)_3$ parent material, which showed paramagnetic behaviour down to 0.4 K in bulk magnetic measurements.[56]
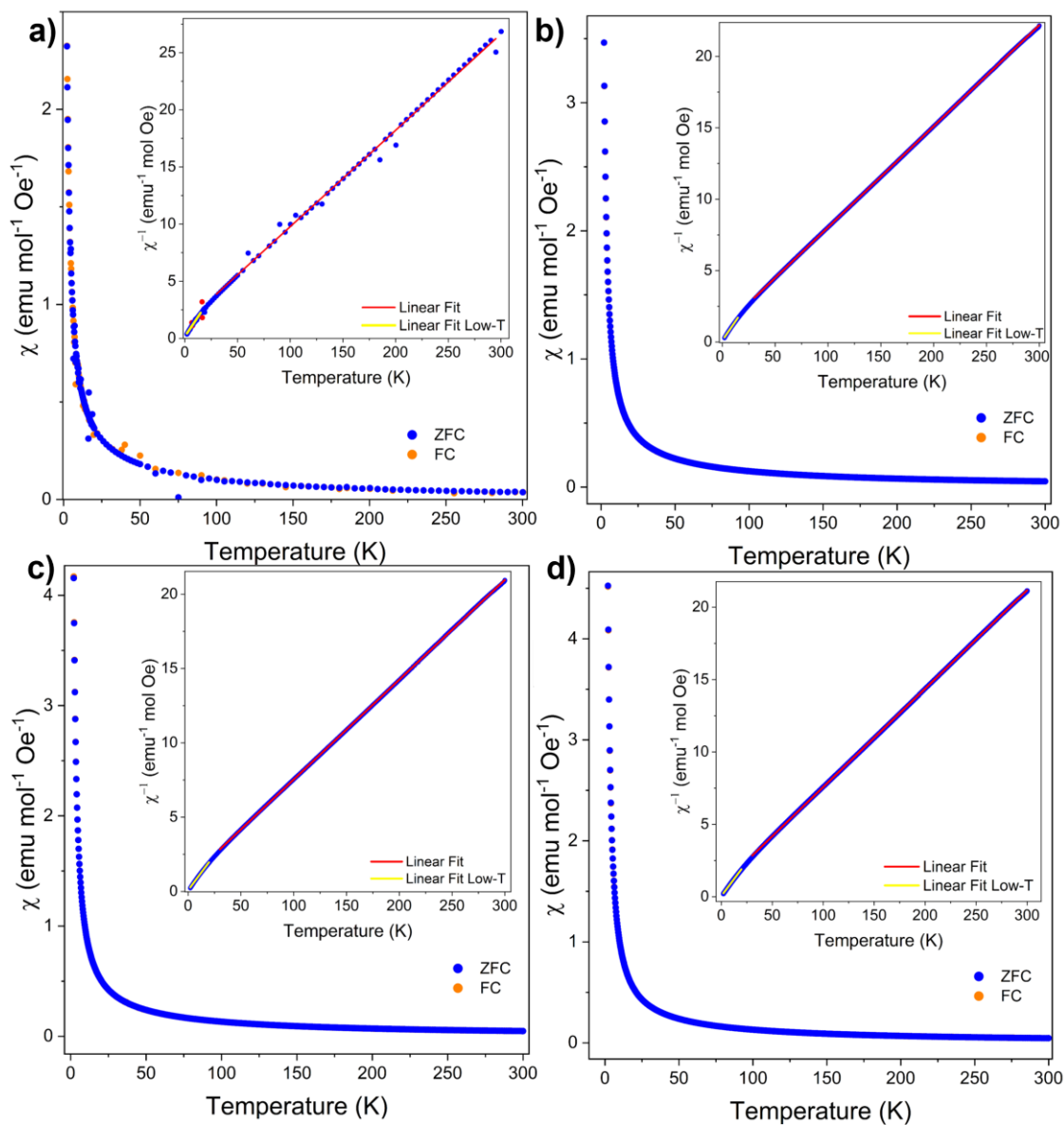
Figure 5.9: Bulk magnetic properties of Ho$_{1-x}$Er$_x$(HCO$_2$)$_3$ with a) $x = 0.80$, b) $x = 0.60$, c) $x = 0.40$, d) $x = 0.20$, measured from 1.8 to 300 K. The inverse susceptibility, χ^{-1}, and Curie-Weiss fits are shown in the insets.
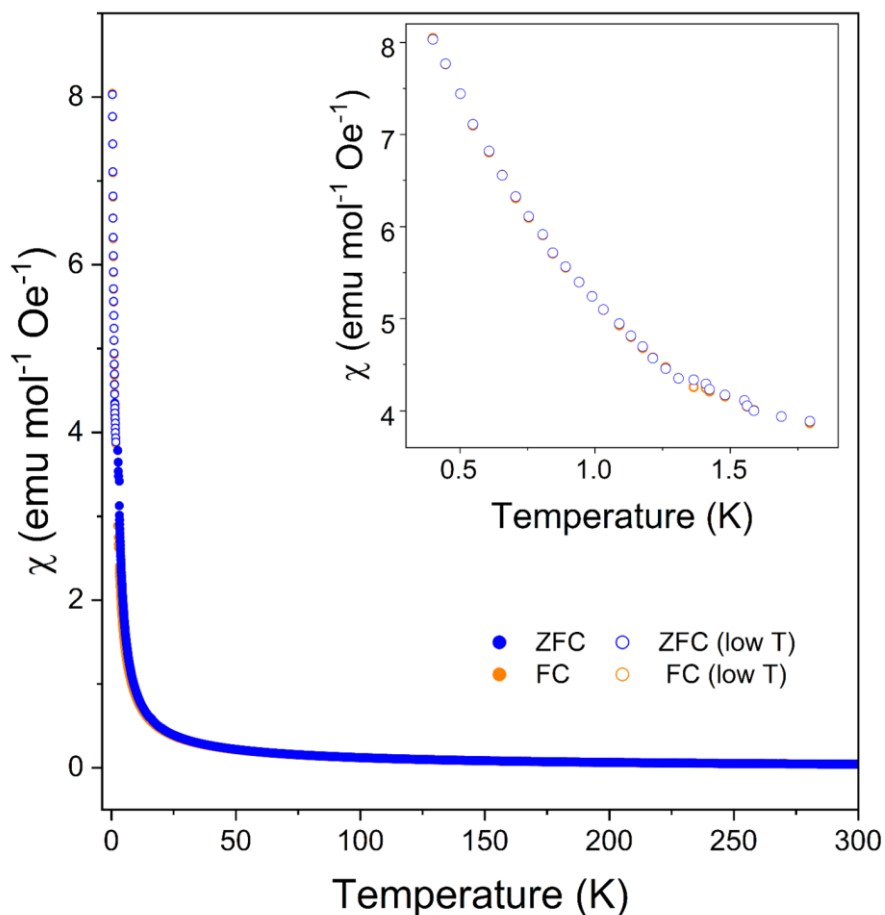
Figure 5.10: Bulk magnetic properties of $Ho_{0.5}Er_{0.5}(HCO_2)_3$ measured between 0.4 and 1.8 K (hollow symbols) and from 1.8 to 300 K (full symbols). The inset shows the lower temperature range.

Linear behaviour of the inverse susceptibility, $\chi^{-1}(T)$, consistent with the Curie-Weiss law, can be observed down to ~30 K, with deviation from linearity below this temperature. Fits to the inverse susceptibility using the Curie-Weiss law were therefore carried out from 30 to 300 K and 2 to ~15 or ~20 K, for lower temperatures, with the exception of $Ho_{0.5}Er_{0.5}(HCO_2)_3$, for which low-temperature fits were carried out from 0.4 to 1.5 K. (see Figure 5.9 for $x = 0.80$, 0.60, 0.40 and 0.20 and Figure 5.11 for $x = 0.5$), with results reported in Table 5.4 (see also Figure C.??).
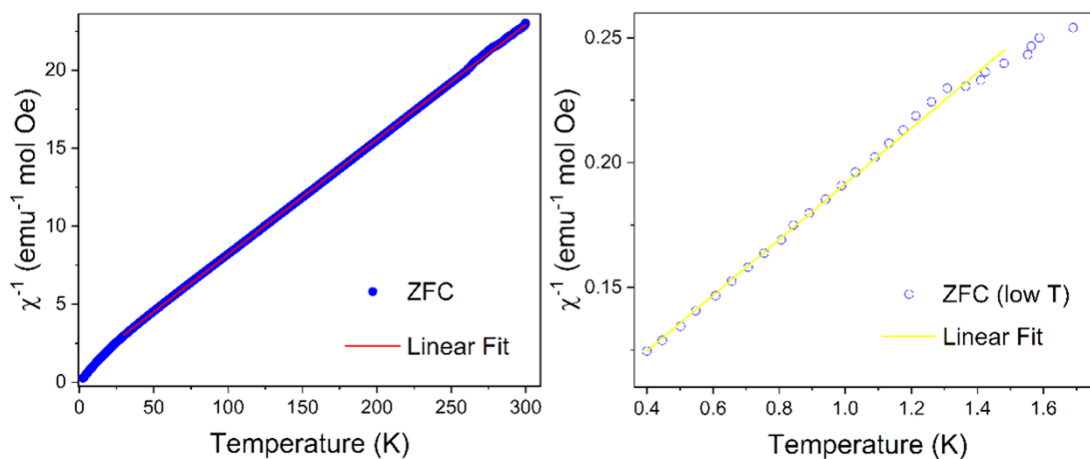
Figure 5.11: Inverse magnetic susceptibility, χ^{-1}, and Curie-Weiss fits to the inverse the high-temperature (left) and low-temperature regimes (right) for $Ho_{0.5}Er_{0.5}(HCO_2)_3$

Table 5.4: Curie-Weiss temperature θ_{CW} and effective magnetic moments μ_{eff} from the Curie-Weiss fit of the inverse susceptibility χ^{-1} of $Ho_{1-x}Er_x(HCO_2)_3$ (x = 0.20, 0.40, 0.50, 0.60 and 0.80)

x	Range (K)	θ_{CW} (K)	μ_{eff} (μ_B)	Range (K)	θ_{CW} (K)	μ_{eff} (μ_B)
0.20	30–300	−11.60(5)	10.850(2)	2–15	−0.62(4)	7.61(4)
0.40	30–300	−12.21(4)	10.9145(14)	2–15	−0.96(6)	8.59(2)
0.50	30–300	−11.00(2)	10.4154(8)	0.4–1.5	−0.72(2)	8.47(5)
0.60	30–300	−13.38(4)	10.6284(10)	2–20	−0.99(6)	9.18(2)
0.80	30–300	−15.98(1.34)	9.74(4)	2–20	−1.22(10)	9.243(15)

Isothermal magnetisation measurements of $Ho_{1-x}Er_x(HCO_2)_3$ (x = 0.2, 0.4, 0.6 and 0.8) performed at 2 K for fields up to 5 T, shown in Figure 5.12, confirm the paramagnetic behaviour of these materials.
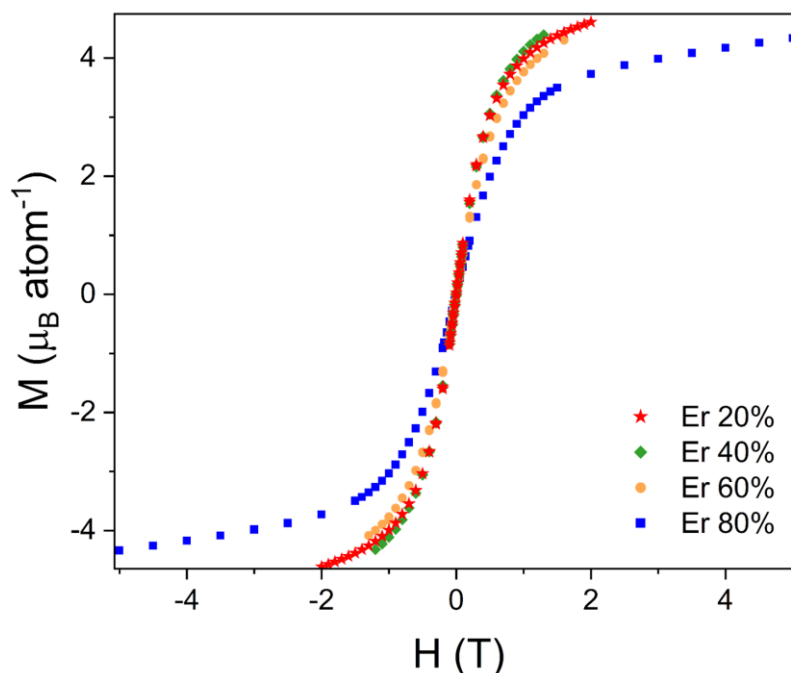
Figure 5.12: Isothermal magnetisation measurements of $Ho_{1-x}Er_x(HCO_2)_3$ ($x = 0.20$, 0.40, 0.60 and 0.80) carried out at 2 K for fields up to 5 T.

5.3.3 Neutron Diffraction of Ho₀.₅Er₀.₅(DCO₂)₃

Due to the results obtained from bulk measurements of $Ho_{0.5}Er_{0.5}(HCO_2)_3$, discussed in the previous section, the next sensible step in studying the magnetic structure of this material led to analysing a perdeuterated analogue *via* neutron diffraction. Patterns collected on $Ho_{0.5}Er_{0.5}(DCO_2)_3$ down to 0.28 K showed no additional Bragg-like or structured diffuse features down to base temperature, with a comparison at low Q between patterns at 10 and 0.28 K from bank 1 of the WISH diffractometer clearly demonstrating this, as shown in Figure 5.13. Interestingly, it is possible to observe a noticeable yet small difference between the two patterns at lower Q values (see inset of Figure 5.13) which might be indicative of diffuse scattering, but unfortunately it is difficult to draw any such conclusions from this data alone given the very weak and structureless feature. Nonetheless, it is clear that $Ho_{0.5}Er_{0.5}(HCO_2)_3$ remains paramagnetic down to 0.28 K and behaves quite differently from the parent material, $Ho(HCO_2)_3$.[51]

Ideally, inelastic neutron scattering would provide more insight about the nature and magnitude of the interactions within the parent structures, which would in turn offer initial parameters for simulations of the magnetic behaviour of this sample to probe how diffuse scattering might appear for a random chain paramagnet possessing this structure to compare to the weak signal detected. Attempts were therefore made to apply for beamtime to study $Ho(DCO_2)_3$ and $Er(DCO_2)_3$ at ANSTO. However, due to the limited beamtime availability caused by a combination of other facilities undergoing long shutdowns and the COVID-19 pandemic, such measurements were not possible during the course of this PhD project.

Therefore, the question is open as to whether this system behaves as a Random Spin-Chain paramagnet, with the formation of clusters of spins of size $\xi(T)$ and effective spin S_{eff} expected to form at sufficiently low-temperature,[42] and anticipated to be responsible for some degree of diffuse scattering, due to short-range interactions becoming significant in the formation of the clusters.
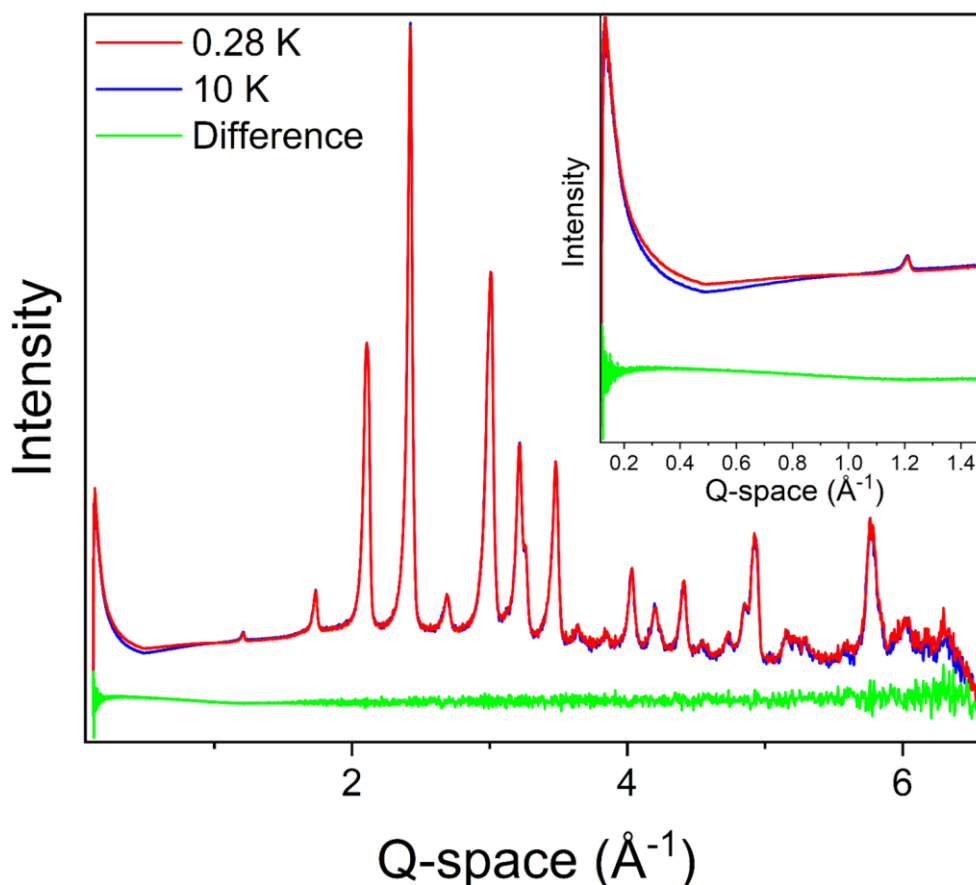
Figure 5.13: Neutron diffraction patterns of Ho$_{0.5}$Er$_{0.5}$(HCO$_2$)$_3$ from bank 1 of the WISH diffractometer collected at 10 K and 0.28 K, and difference line. The inset shows bank 1 zoomed in the low-*Q* range.

5.4 Magnetic Properties of the Tb$_{1-x}$Y$_x$(HCO$_2$)$_3$ Series and Anomalous Evolution of its Magnetocaloric Effect with Diamagnetic Doping

5.4.1 Composition and Structure of the Tb$_{1-x}$Y$_x$(HCO$_2$)$_3$ Series

Samples of Tb$_{1-x}$Y$_x$(HCO$_2$)$_3$ (x = 0.025, 0.05, 0.10, 0.20, 0.40, 0.60 and 0.80) were synthesised *via* the method reported in Section 3.2.4. The experimental stochiometric compositions of the Tb$_{1-x}$Y$_x$(HCO$_2$)$_3$ members were determined *via* XRF,

with results, shown in Table 5.5 suggesting these to be within experimental error of the nominal compositions targeted in the synthesis.

Additional elemental analysis was carried out *via* EDX on selected regions of the samples — with results reported in Appendix C, along with pictures of the regions acquired using SEM — and show good agreement with values determined from bulk XRF experiments.

Room-temperature powder X-ray diffraction measurements showed that all the members of the series share the same rhombohedral *R*3*m* structure as the parent Tb(HCO$_2$)$_3$ and Y(HCO$_2$)$_3$ phases. Le Bail fits to the patterns, shown in Figure 5.14, confirmed the phase purity of the samples and refinement statistics are shown in Table 5.6. The absence of peak broadening upon higher Y doping suggests relatively high homogeneity of the samples. Plots of lattice parameters and volume *vs* composition, shown in Figure 5.15, reveal these decrease with increasing Y concentration, as expected due to its smaller ionic radius.[192]

Table 5.5. Comparison of the nominal and experimental compositions for Tb$_{1-x}$Y$_x$(HCO$_2$)$_3$ determined from X-ray fluorescence.

Nominal composition	Experimental composition
Tb$_{0.975}$Y$_{0.025}$(HCO$_2$)$_3$	Tb$_{0.99(6)}$Y$_{0.01(6)}$(HCO$_2$)$_3$
Tb$_{0.95}$Y$_{0.05}$(HCO$_2$)$_3$	Tb$_{0.96(5)}$Y$_{0.04(5)}$(HCO$_2$)$_3$
Tb$_{0.90}$Y$_{0.10}$(HCO$_2$)$_3$	Tb$_{0.91(4)}$Y$_{0.09(4)}$(HCO$_2$)$_3$
Tb$_{0.80}$Y$_{0.20}$(HCO$_2$)$_3$	Tb$_{0.819(19)}$Y$_{0.181(19)}$(HCO$_2$)$_3$
Tb$_{0.60}$Y$_{0.40}$(HCO$_2$)$_3$	Tb$_{0.63(3)}$Y$_{0.37(3)}$(HCO$_2$)$_3$
Tb$_{0.40}$Y$_{0.60}$(HCO$_2$)$_3$	Tb$_{0.44(8)}$Y$_{0.56(8)}$(HCO$_2$)$_3$
Tb$_{0.20}$Y$_{0.80}$(HCO$_2$)$_3$	Tb$_{0.25(12)}$Y$_{0.75(12)}$(HCO$_2$)$_3$

Table 5.6: Refinements statistics for the Le Bail refinements of powder X-ray diffraction patterns of $Tb_{1-x}Y_x(HCO_2)_3$.

Sample	R_p	R_{wp}	χ^2
$Tb(HCO_2)_3$	2.18	2.84	1.91
$Tb_{0.975}Y_{0.025}(HCO_2)_3$	2.17	2.80	1.58
$Tb_{0.95}Y_{0.05}(HCO_2)_3$	3.65	4.65	1.30
$Tb_{0.90}Y_{0.10}(HCO_2)_3$	4.07	5.16	1.26
$Tb_{0.80}Y_{0.20}(HCO_2)_3$	2.30	2.94	1.31
$Tb_{0.60}Y_{0.40}(HCO_2)_3$	2.46	3.12	1.17
$Tb_{0.40}Y_{0.60}(HCO_2)_3$	2.48	3.17	1.32
$Tb_{0.20}Y_{0.80}(HCO_2)_3$	2.24	2.83	1.41
$Y(HCO_2)_3$	2.25	3.03	2.73
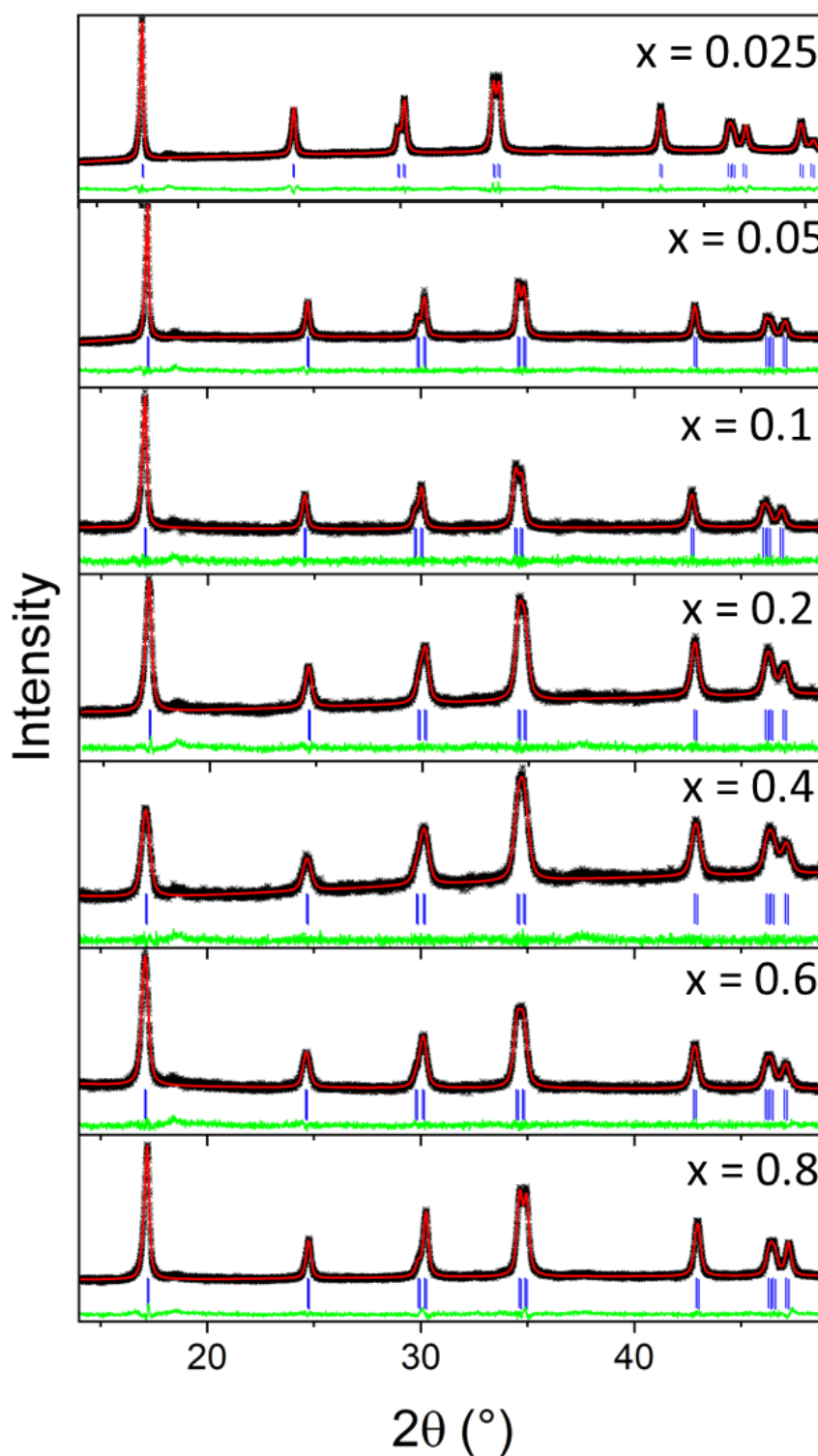
Figure 5.14: Conventional powder X-ray diffraction patterns of $Tb_{1-x}Y_x(HCO_2)_3$ measured using a Cu source ($\lambda = 1.54$ Å) and fitted using the Le Bail method to highlight phase purity. The crosses, red and green lines are experimental and calculated intensities and the difference curve. Vertical markers indicate the positions of the Bragg reflections.
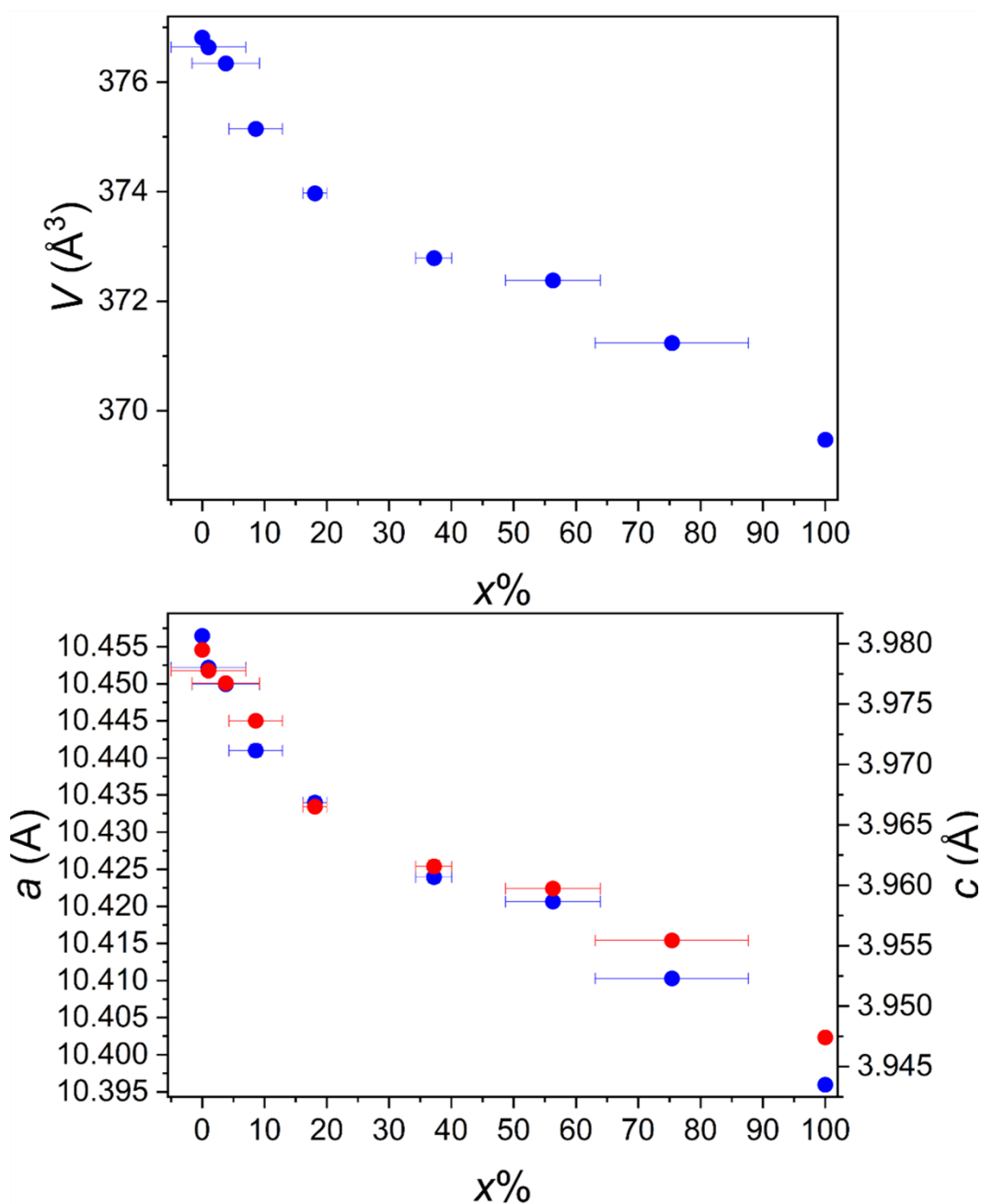
Figure 5.15 Plots of the unit cell volume (top) and lattice parameters a and c (bottom), the latter shown in blue and red, respectively, for the orthorhombic unit cell of $Tb_{1-x}Y_x(HCO_2)_3$. Horizontal error bars show the uncertainty on the composition determined *via* X-ray fluorescence for the solid solutions.

5.4.2 Bulk Magnetic Properties of the $Tb_{1-x}Y_x(HCO_2)_3$ Series.

Field cooled (FC) magnetic susceptibility $\chi(T)$ measurements of the $Tb_{1-x}Y_x(HCO_2)_3$ frameworks, with $x = 0.025$, 0.05 and 0.10, were carried out in a 0.1 T field from 2 K to 300 K and are shown in Figure 5.16. The susceptibility data did not

show any indication of long-range magnetic ordering within this temperature range. This observation is consistent with previous magnetic susceptibility measurements on Tb(HCO$_2$)$_3$, for which no deviation from paramagnetic behaviour is observed to well below 2 K.[5,51,54] The inverse susceptibilities of the Tb$_{1-x}$Y$_x$(HCO$_2$)$_3$ samples were well fitted using the Curie-Weiss law from 10 to 300 K, with corresponding θ_{CW} values given in Table 5.7.

From mean-field theory, θ_{CW} is expected to scale with Tb^{3+} concentration if there is no variation in the strength of magnetic interactions, as these are diluted by the presence of diamagnetic impurities. Our data reflects this trend, and so we assume that the coupling among Tb^{3+} spins is likely to be similar across the whole series to that present in the parent Tb(HCO$_2$)$_3$ framework, *i.e.* ferromagnetic intrachain and antiferromagnetic interchain coupling. Effective magnetic moments, μ_{eff}, reported in Table 5.7, were found to be close to the reported experimental value for Tb(HCO$_2$)$_3$ and also the 9.75 μ_B value expected from the Russel-Saunders coupling scheme.[5]

Isothermal magnetisation measurements from 12 K down to 2 K are consistent with paramagnetic behaviour and are shown in Figure 5.17. Observed normalised values of saturation magnetisation, M_{sat}, at 2 K and a magnetic field of 5 T, also reported in Table 5.7, are close to the theoretical value of 4.50 μ_B atom^{-1} expected for Ising behaviour, for which M_{sat} is expected to be close to $g_J J/2$, suggesting significant single-ion anisotropy. They are, however, significantly lower than the value of 5.77(4) μ_B atom^{-1} previously reported for Tb(HCO$_2$)$_3$.
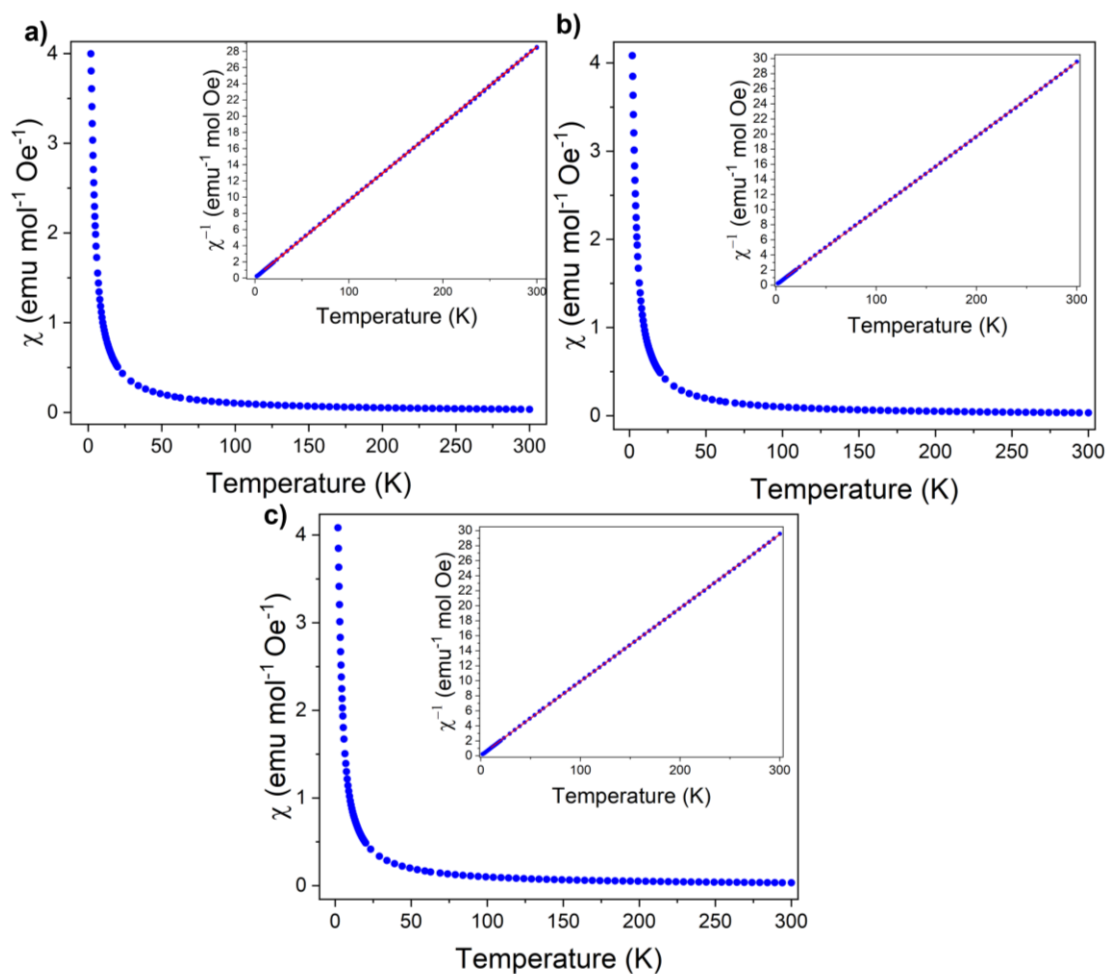
Figure 5.16: FC molar susceptibility, $\chi(T)$, for $Tb_{1-x}Y_x(HCO_2)_3$ with (a) $x = 0.025$, (b) $x = 0.05$ and (c) $x = 0.10$, measured from 2–300 K in a field of 0.1 T. The inverse molar susceptibility, $\chi^{-1}(T)$, for each sample is presented in the insets.

Table 5.7. Magnetic properties extracted from FC susceptibility and magnetisation measurements of $Tb_{1-x}Y_x(HCO_2)_3$ samples. Magnetic properties for $x = 0$ were obtained from Saines *et al.*[5]

x	θ_{CW} (K)	$|\theta_{CW}|/(1-x)$ (K)	Tb^{3+} Magnetic moment (μ_B)	M_{sat} (μ_B atom^{-1})	M_{sat} (μ_B atom$_{Tb}^{-1}$)
0.0	−0.9	0.9	9.62	5.77(4)	5.77(4)
0.025	−0.86(5)	0.88(5)	9.417(2)	4.73(2)	4.86(2)
0.05	−1.11(8)	1.17(8)	9.511(2)	4.34(2)	4.57(2)
0.10	−0.79(8)	0.88(8)	9.771(2)	4.25(2)	4.73(2)
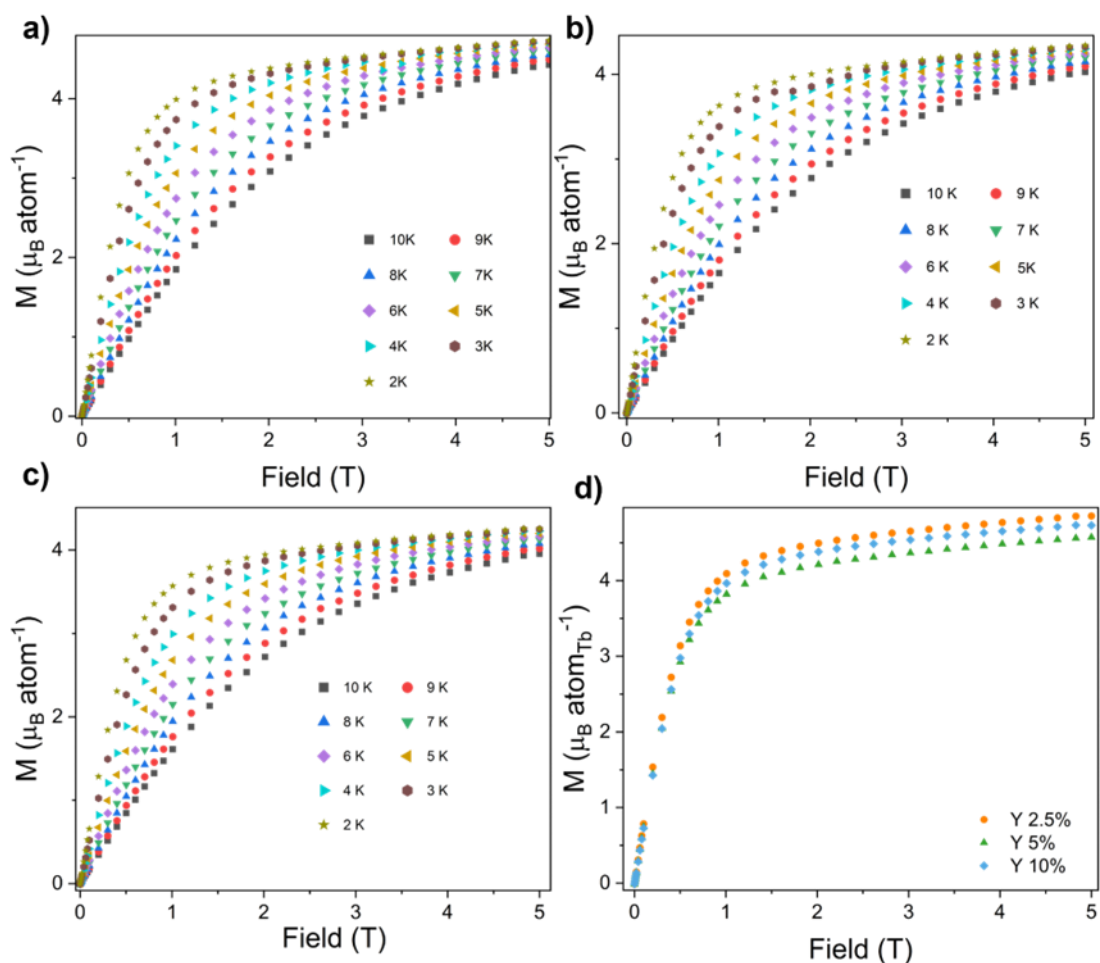
Figure 5.17: Isothermal magnetisation measurements as a function of the applied magnetic field of $Tb_{1-x}Y_x(HCO_2)_3$ with (a) $x = 0.025$, (b) $x = 0.05$ and (c) $x = 0.10$. Plot (d) shows the comparison of normalised magnetisations of the three samples at 2 K.

5.4.3 Heat Capacity of the $Tb_{1-x}Y_x(HCO_2)_3$ Series

Heat capacity $C(T)$ data were measured for $Tb(HCO_2)_3$ and $Tb_{1-x}Y_x(HCO_2)_3$, with $x = 0.05$, 0.10, 0.20 and 0.40, in zero-field conditions. Lattice contributions were subtracted by taking a common Debye temperature of $156.2(1.8)$ K, determined by fitting the high-temperature heat capacity data for $Tb(HCO_2)_3$ using Eqn. 3.32, *i.e.* the Debye model in the lower-temperature limit, between 8 to 14 K, where lattice contributions are more significant (see Figure 5.18). This was then subtracted from the total heat capacity to yield, the magnetic heat capacity, C_{mag}. Determining C_{mag} this way leads to it including

a contribution from the Schottky anomaly, which arises below 0.8 K because of magnetic hyperfine coupling of the electronic spins in the $4f$ orbitals of terbium and the magnetic moment of the terbium nucleus ($I = 3/2$).
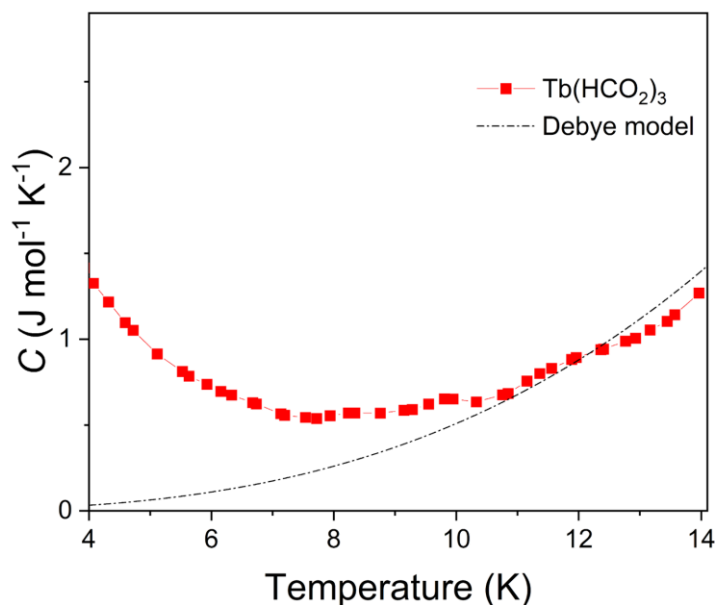
Figure 5.18: Heat capacity data for Tb(HCO$_2$)$_3$ between 4 to 14 K and Debye Model fit between 8 to 14 K.

This contribution was estimated by fitting to the low-temperature data, *i.e.* in the 0.4–0.8 K range, using the expression:

$$C_N = \frac{\Delta^2 R}{9T^2} \frac{\exp\left(-\frac{\Delta}{3T}\right)\left[1 + \exp\left(-\frac{\Delta}{3T}\right)\right]^4 + 4\exp\left(-\frac{\Delta}{T}\right)}{\left[1 + \exp\left(-\frac{\Delta}{3T}\right) + \exp\left(-\frac{2\Delta}{3T}\right) + \exp\left(\frac{\Delta}{T}\right)\right]^2},$$
(5.1)

where the single adjustable parameter Δ represents the hyperfine splitting.[198] We found $\Delta = 0.437(2)$ K for Tb(HCO$_2$)$_3$, reported in Table 5.8, which is consistent with other systems, including Tb metal,[198–200] suggesting this solely depends on the internal electronic structure of Tb and is not significantly affected by the local environment. Therefore, this parameter is here assumed to be constant with respect to stoichiometry and was subtracted from the measured heat capacity for all samples. This leads to the curious result that this hyperfine coupling contribution does not account for the entirety

of the observed low-temperature heat capacity of those members with higher concentrations of Y^{3+}.

Table 5.8: Hyperfine coupling Δ parameter for other Tb-containing systems.

System	Oxidation state	Δ (K)	Ref.
Tb-metal	0	0.45	197
Tb@SrF$_2$	3	0.476	198
Tb(CF$_3$SO$_3$)$_{3.9}$H$_2$O	3	0.470	199

The C_{mag} heat capacity curves, presented in Figure 5.19, show that Tb(HCO$_2$)$_3$ has the highest magnetic heat capacity, with this decreasing with higher Y^{3+} concentration in the other samples, as would be expected. The maxima of the heat capacity curves, indicative of the transition temperature and the strength of the correlations within the system, was found to be centred at 1.54 K for Tb(HCO$_2$)$_3$, close to the reported transition temperature to the TIA state for this system (see inset in Figure 5.19b). Surprisingly, there is only a modest decrease in this transition temperature with Y^{3+} doping such that even where almost half of the Tb^{3+} cations are replaced with Y^{3+} in Tb$_{0.60}$Y$_{0.40}$(HCO$_2$)$_3$, the TIA transition still occurs at a similar temperature, being reduced by less than 30% of the undoped Tb(HCO$_2$)$_3$. Further heat capacity measurements were performed under different applied fields on the Tb$_{1-x}$Y$_x$(HCO$_2$)$_3$ series with x = 0.10, 0.20 and 0.40. The data, shown in Figure 5.20 as C_{mag}/T as a function of T, reveal that the magnetic component of the heat capacity C_{mag} is suppressed at higher applied fields, confirming that the features observed are magnetic in nature.
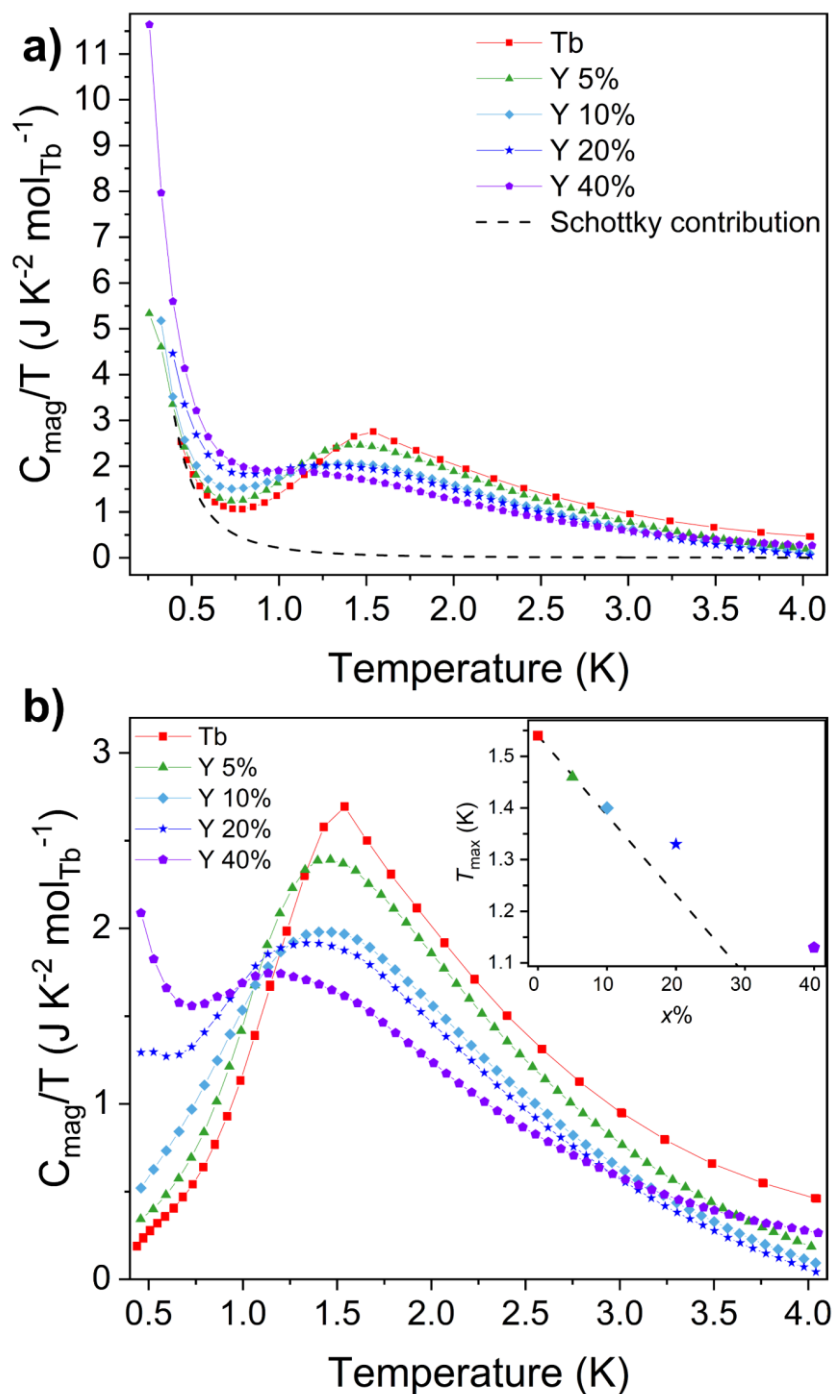
Figure 5.19: Plot of magnetic heat capacity C_{mag}/T, normalised per moles of Tb, for $Tb_{1-x}Y_x(HCO_2)_3$ ($x = 0$, 0.05, 0.10, 0.20 and 0.40) (a) measured between 300 mK and 4 K in zero field conditions and (b) after subtracting the hyperfine coupling contribution for the Tb cations. In the latter case, the data is shown down to 0.4 K, the lowest limit for the fits for the hyperfine coupling. Values of T_{max} are shown in the inset, with the dashed line representing the trend as predicted by mean-field theory.
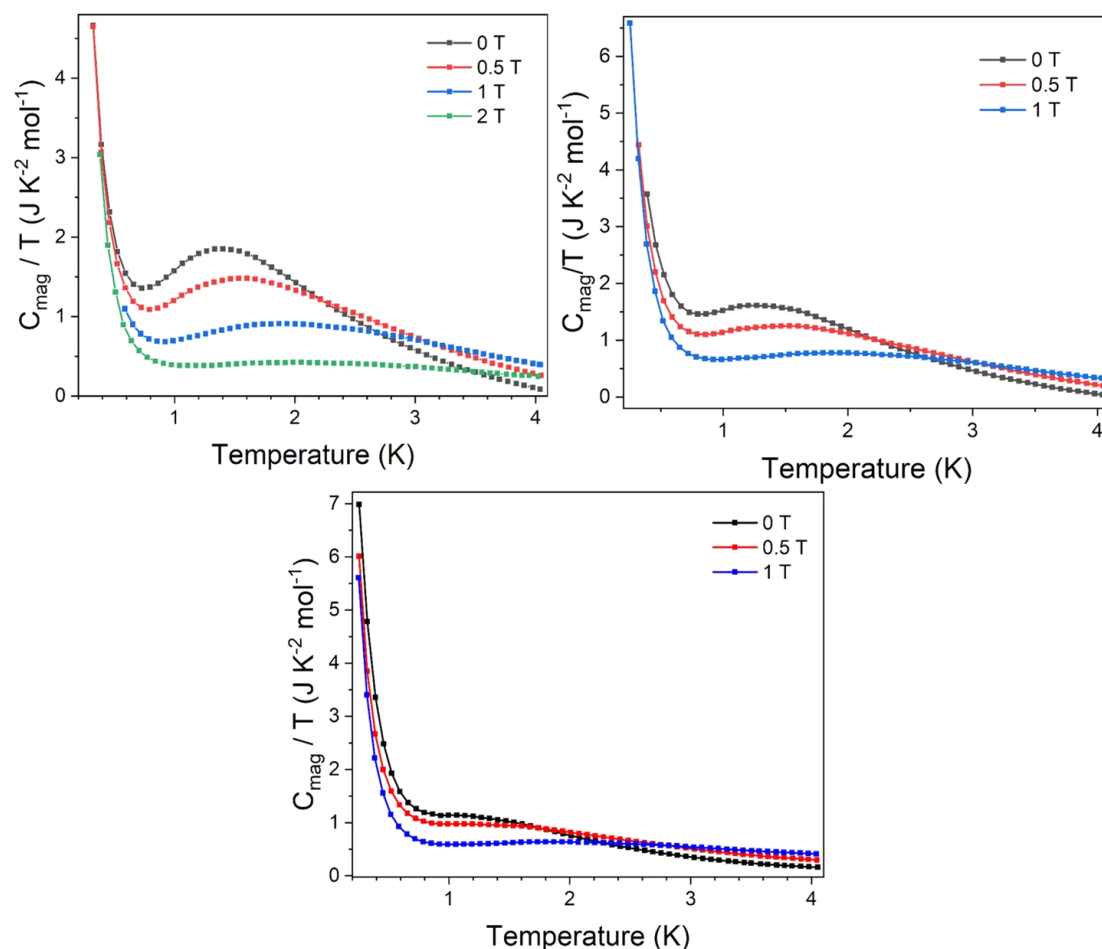
Figure 5.20: Heat capacity measurement under applied fields for Tb$_{1-x}$Y$_x$(HCO$_2$)$_3$, with x = 0.10, 0.20 and 0.40.

Attempts were made at fitting the normalised heat capacity C_{mag}/T curves to capture their features and, hence, follow the evolution of the heat capacity with increasing Y concentration, for which the following equation, suggested by collaborators in the group of Professor Andrew Goodwin (University of Oxford), was used:

$$C_{mag}(T) = \frac{aT^b}{(T-c)^2 + d^2} + \frac{e}{T^3} , \tag{5.2}$$

with the first term describing the maximum of the heat capacity curve, while the second term describes the entropic contribution observed at lower temperatures. Results from the fits are shown in Table 5.9 and Figure 5.21.

Table 5.9: Values of the coefficients of Eqn 5.1 resulting from the fits to the C_{mag}/T. The asterisk denotes a coefficient constrained to a value.

x	a (K)	b	c (K)	d (K^2)	e (K^3)
0	0.66(2)	1.33(3)	1.369(7)	0.648(8)	0*
0.05	0.99(9)	0.80(9)	1.38(2)	0.74(3)	0.00(1)
0.10	0.38(12)	0.32(10)	1.42(4)	0.88(3)	0.000(11)
0.20	1.86(8)	0*	1.437(16)	0.98(2)	0.0032(8)
0.40	2.20(6)	0.14(3)	1.22(2)	1.168(14)	0.104(3)
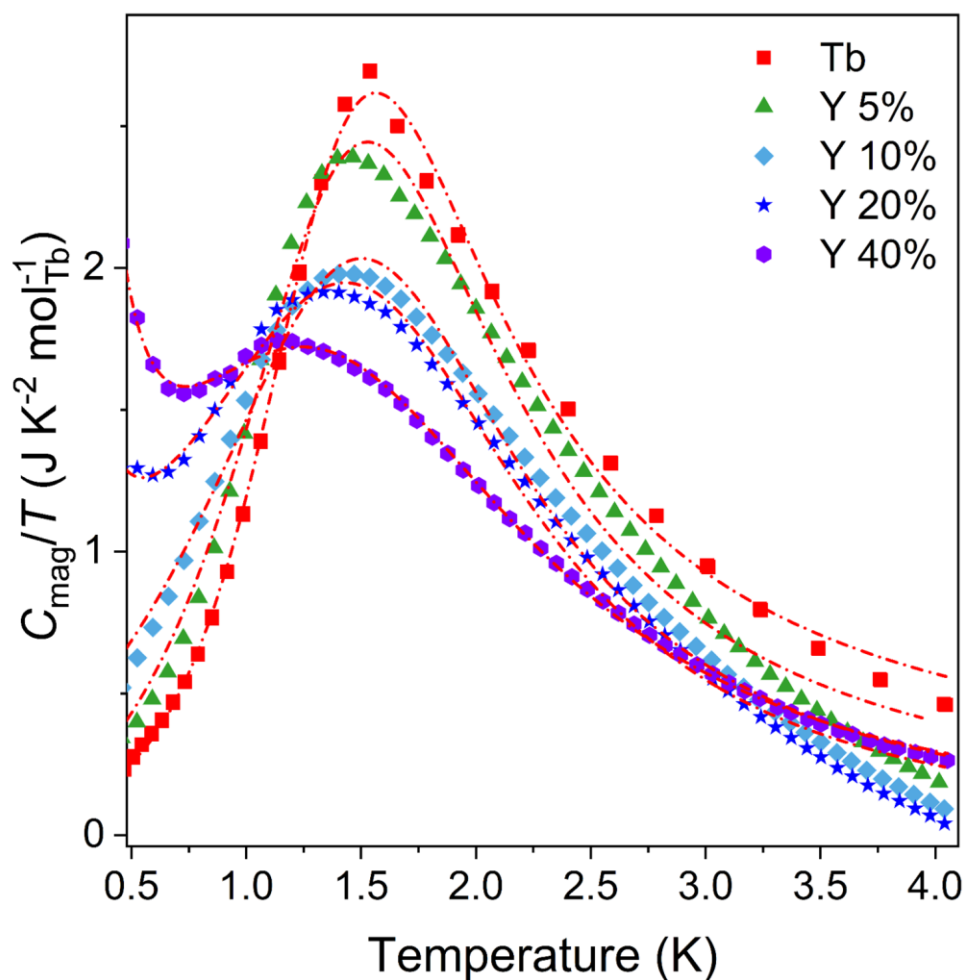
Figure 5.21: Fits to the normalised C_{mag}/T curves for Tb$_{1-x}$Y$_x$(HCO$_2$)$_3$ ($x = 0$, 0.05, 0.10, 0.20 and 0.40) using Eqn. 5.2.

It should be noted that the fit to $x = 0.40$ did not reach convergence when the coefficient e is refined, likely due to the broadness of this heat capacity curve. Attempts to fit C_{mag}/T acquired in non-zero field conditions were also made, but this proved to be unsuccessful, in that fits did not reach convergence, due to the progressively broader features of the curves. An estimate of the values for the temperature corresponding to the maxima of the curves, T_{max}, can be obtained from the derivative of Eqn. 5.2, and these can be compared to the experimental values, with Table 5.10 showing calculated and experimental values following a similar trend, although the derivative of the fitting equation clearly overestimates T_{max}. Overall, it was concluded that this model shows that the entropic effect for zero-field heat capacity measurements increases with Y concentration, as shown by the increase in the e parameter, although the fits are also quite limited by Eqn. 5.2 not representing any physical quantity.

Table 5.10: Comparison of experimental values for T_{max} and those derived from fitting the C_{mag}/T curves.

x	Experimental T_{max} (K)	Estimated T_{max} (K)
0	1.54	1.56
0.05	1.46	1.53
0.10	1.40	1.50
0.20	1.36	1.44
0.40	1.13	1.29

The magnetic entropy associated with the TIA transition, S_m^{TIA}, was extracted from the zero-field heat capacity data using Eqn. 3.28, with values shown in Table 5.11 and Figure 5.22. It should be noted that $T = 0.5$ K was chosen as the lowest temperature for which we have reliable data, due to the limitations in the fitting the Schottky anomaly. It can be observed that the decline in the S_m^{TIA} is steeper than the change in the TIA ordering temperature even when normalised by the amount of Tb present. It should be

noted that the entropy curves tend to intersect at lower temperatures, which is attributed

to the higher contribution observed for the Y-doped samples at lower temperatures.

Table 5.11. Maximum magnetic entropies associated with the TIA transition for the $Tb_{1-x}Y_x(HCO_2)_3$ solid solution with $x = 0$, 0.05, 0.10, 0.20 and 0.40.

x	S_m^{TIA} (J kg^{-1} K^{-1})	S_m^{TIA} (J mol$_{Tb}^{-1}$ K^{-1})
0	15.41	4.62
0.05	14.31	4.25
0.10	11.38	3.74
0.20	9.54	3.73
0.40	7.95	3.64
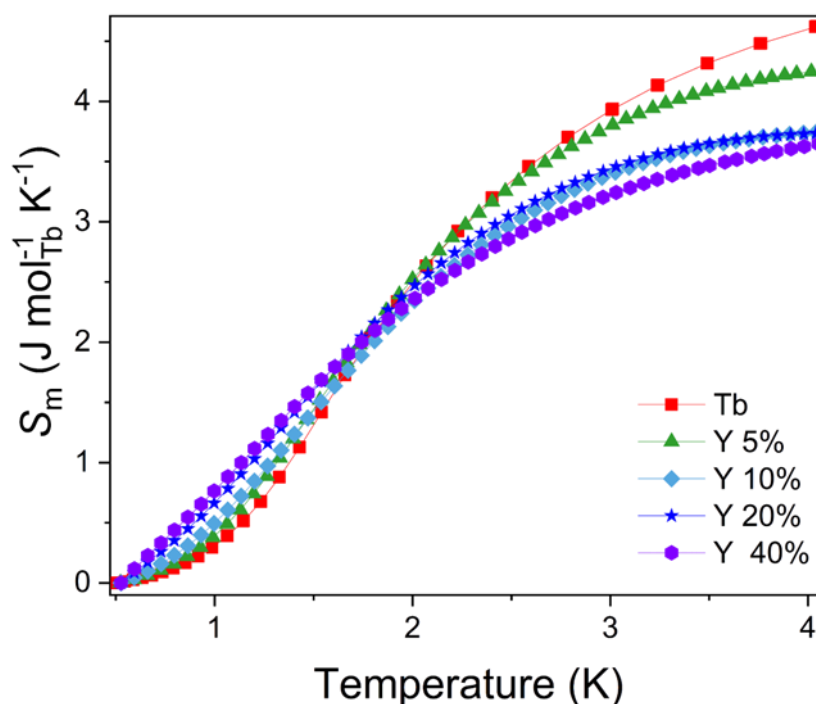
Figure 5.22: Magnetic entropies per moles of Tb extracted from the heat capacity data for the $Tb_{1-x}Y_x(HCO_2)_3$ ($x = 0$, 0.05, 0.10, 0.20 and 0.40) series in zero-field conditions.

We observe that the peak at ~1.5 K, associated with the formation of the TIA state in

$Tb(HCO_2)_3$, broadens and shifts to only moderately lower temperature with Y^{3+} doping.

This suggests that the formation of the TIA state caused by the ordering of the 1D chains

within $Tb_{1-x}Y_x(HCO_2)_3$ is surprisingly robust to doping with a diamagnetic impurity,

although it should be noted that the extent to which ordering occurs reduces somewhat

more quickly than the transition temperature at which it occurs as indicated by the greater reduction in S_m^{TIA} associated with the phase transition with Y^{3+} doping. Another key observation is the presence of an additional low-temperature contribution to the heat capacity at high levels of diamagnetic impurity fraction. We interpret this as arising from an entropic contribution due to the presence of short chains, which are a result of the Y^{3+} ions breaking the *quasi*-1D chains into small segments. Because of the much weaker interchain interactions, we would not expect these short chains to order until significantly below the TIA transition, at which temperature they contribute to the upturn in C$_{mag}$/T seen at the lowest temperatures. Computational studies would enable us to gain more insight about the behaviour of these shorter chains.

5.4.4 Magnetocaloric properties of the Tb$_{1-x}$Y$_x$(HCO$_2$)$_3$ series

The magnetic entropy change $-\Delta S_m$ as a function of applied magnetic field was extracted from the magnetisation data using the Maxwell relation (see Eqn. 3.25) from 2 K to 12 K. In determining the volumetric values, the crystallographic densities of each of the measured members of the series, reported in Table 5.12, were calculated by considering the volumes determined from the Le Bail fits for each member of the series. Values for $-\Delta S_m$ are shown in Figure 5.23 (see also Appendix C for $\Delta B = 1$–0 T), and the maximum values are reported in Table 5.13.

Table 5.12: Estimated density values δ for Tb$_{1-x}$Y$_x$(HCO$_2$)$_3$ with $x = 0.025$, 0.05, 0.10, 0.20 and 0.40, respectively.

x	0.025	0.05	0.10	0.20	0.40
δ (g cm^{-3})	3.86	3.84	3.81	3.73	3.55

Compared to the values reported for Tb(HCO$_2$)$_3$,[5] the entropy change values found for the doped samples clearly show that the magnetocaloric performance of this material decreases due to Y-doping as a function of sample weight or volume. However,

while normalised values per mole of Tb^{3+} are lower compared to the $-\Delta S_m^{max}$ for the parent compound Tb(HCO$_2$)$_3$, the decrease in $-\Delta S_m^{max}$ with respect to Y-doping is more dramatic for low values of x, particularly for more modest applied field changes. This trend is then reversed at higher concentrations, with Tb$_{0.90}$Y$_{0.10}$(HCO$_2$)$_3$ having the highest $-\Delta S_m^{max}$ amongst the Y-doped samples with respect to the amount of Tb^{3+} present for all field changes considered. This suggests two competing factors are responsible for the change of $-\Delta S_m^{max}$ in Tb(HCO$_2$)$_3$ with Y^{3+} doping. These should be viewed in the context of the promising Tb(HCO$_2$)$_3$ $-\Delta S_m^{max}$ emerging from the ability of its strongly coupled ferromagnetic chains to align readily with each other once the frustrated antiferromagnetic coupling between them is suppressed by the applied field.[5,55] The initial decrease in normalised $-\Delta S_m^{max}$ is likely caused by the hindrance of this ability due to the addition of diamagnetic impurities breaking the chains into shorter segments, which reduces the rate at which the ferromagnetic state emerges under applied fields. This is reflected in the initial decrease in normalised $-\Delta S_m^{max}$ being somewhat greater for more modest applied fields. Conversely, as the concentration of Y^{3+} increases further there are likely a higher number of short chains present, which leads to a significantly more disordered state in the absence of an applied magnetic field and thus a greater change in the normalised $-\Delta S_m^{max}$. When compared to other MCE materials doped with non-magnetic impurities, such as the Ga-doped La$_{0.7}$(Ba, Sr)$_{0.3}$Mn$_{1-x}$Ga$_x$O$_3$ ($x = 0, 0.1$ and 0.2),[201] the Cr-doped La$_{0.65}$Eu$_{0.05}$Sr$_{0.3}$Mn$_{1-x}$Cr$_x$O$_3$ ($x = 0.05, 0.1$ and 0.15),[202] and the Sn-substituted RCo$_2$ (R = Gd, Tb and Dy) alloys, the Tb$_{1-x}$Y$_x$(HCO$_2$)$_3$ series follows similar trends with respect to its initial decrease in $-\Delta S_m^{max}$ with Y^{3+} doping, $i.e.$ lower transition temperatures and lower values of $-\Delta S_m^{max}$ when higher concentrations of non-magnetic impurities are present. Cases where non-magnetic impurities improve the MCE of the material, such as for Tm$_{1-x}$Lu$_x$B$_4$,[203] have, however been reported. This has been

ascribed to the formation of sufficiently large and nearly independent magnetic clusters that increase the degeneracy of the ground state and therefore of the entropy change which results from the application of the external magnetic field.[203]
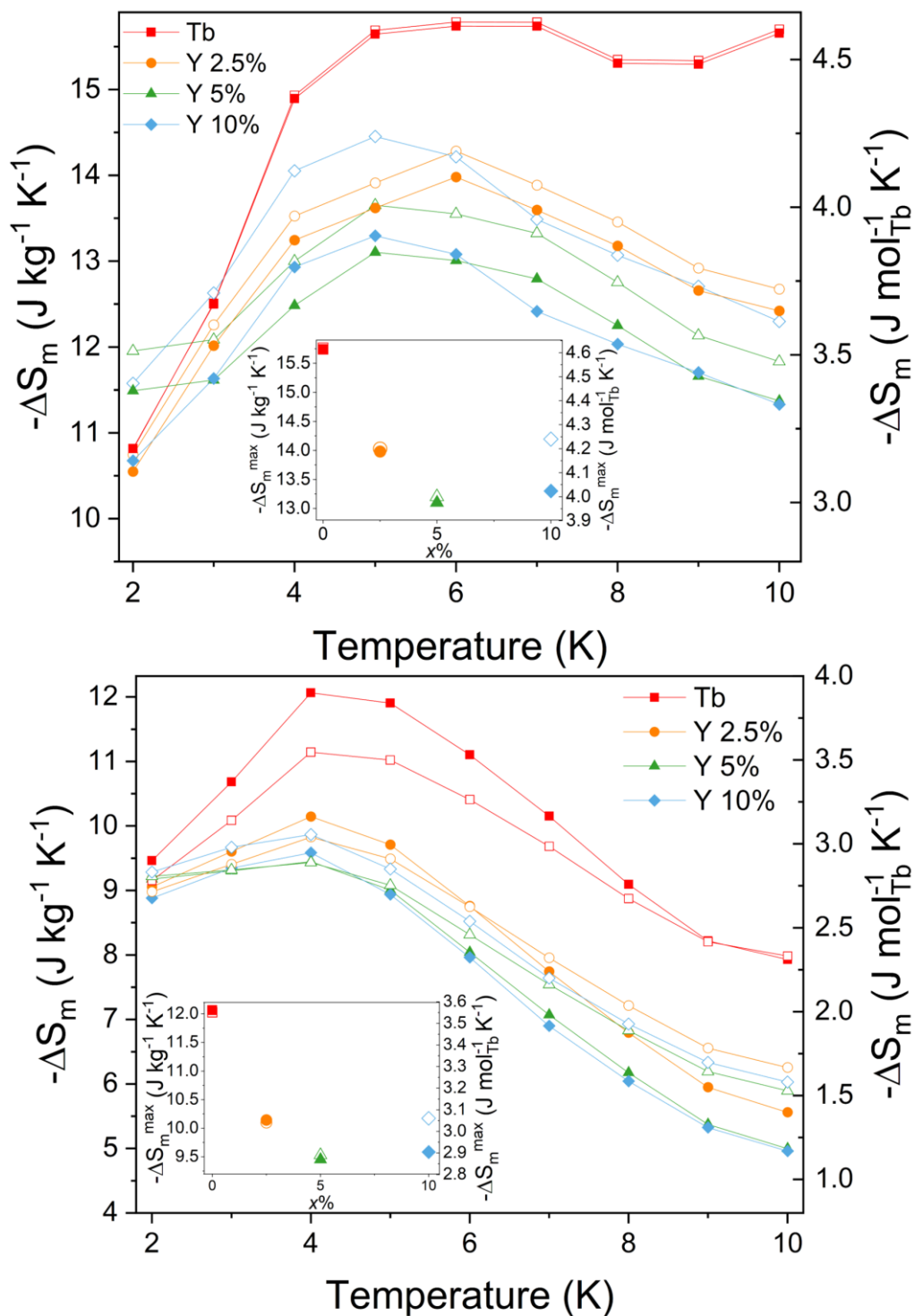
Figure 5.23: Magnetic entropy changes extracted from the magnetisation data for $Tb_{1-x}Y_x(HCO_2)_3$ ($x = 0$, 0.025, 0.05 and 0.10) series for $\Delta B = 5\text{–}0$ T (top) and $\Delta B = 2\text{–}0$ T (bottom). The hollow symbols represent normalised molar values per amount of Tb. Insets show the values of $-\Delta S_m^{max}$ for each sample.

Table 5.13. Maximum entropy changes extracted from magnetisation data for the Tb$_{1-x}$Y$_x$(HCO$_2$)$_3$ solid solutions ($x = 0$, 0.025, 0.05, 0.10) for field changes of 5-0, 2-0 and 1-0 T.

Sample	ΔB = 5-0 T			ΔB = 2-0 T			ΔB = 1-0 T		
	$-\Delta S_m^{max}$ (J kg^{-1} K^{-1})	$-\Delta S_m^{max}$ (mJ cm^{-3} K^{-1})	$-\Delta S_m^{max}$ (J mol$_{Tb}^{-1}$ K^{-1})	$-\Delta S_m^{max}$ (J kg^{-1} K^{-1})	$-\Delta S_m^{max}$ (mJ cm^{-3} K^{-1})	$-\Delta S_m^{max}$ (J mol$_{Tb}^{-1}$ K^{-1})	$-\Delta S_m^{max}$ (J kg^{-1} K^{-1})	$-\Delta S_m^{max}$ (mJ cm^{-3} K^{-1})	$-\Delta S_m^{max}$ (J mol$_{Tb}^{-1}$ K^{-1})
Tb(HCO$_2$)$_3$	15.74	61.62	4.62	12.06	47.23	3.55	8.08	31.64	2.38
Tb$_{0.975}$Y$_{0.025}$(HCO$_2$)$_3$	13.98	54.04	4.20	10.14	39.21	3.04	6.42	24.82	1.92
Tb$_{0.95}$Y$_{0.05}$(HCO$_2$)$_3$	13.10	50.39	4.00	9.45	36.33	2.89	6.15	23.64	1.88
Tb$_{0.90}$Y$_{0.10}$(HCO$_2$)$_3$	13.29	50.67	4.24	9.58	36.52	3.06	6.07	23.13	1.93

5.5 Conclusions

In this chapter, studies on the $Ln(HCO_2)_3$ frameworks with $Ln = Nd^{3+}$, Pr^{3+} and Ce^{3+}, as well as those carried out on two new families of coordination polymers, namely the $Ho_{1-x}Er_x(HCO_2)_3$ and $Tb_{1-x}Y_x(HCO_2)_3$ solid solutions, have been discussed.

We observed that $Nd(HCO_2)_3$, $Pr(HCO_2)_3$ and $Ce(HCO_2)_3$, show paramagnetic behaviour down to 1.8 K as bulk magnetic property measurements suggest, with fits to the Curie-Weiss law indicating these members possess antiferromagnetic interactions. Heat capacity measurements carried out for $Pr(HCO_2)_3$ down to 500 mK confirm this behaviour for this sample. We therefore focused on the Nd and Ce members due to these being Kramer ions with neutron diffraction patterns measured down to 140 and 50 mK for the two samples, respectively, with these not showing any indication of short- or long-range magnetic order, as the lack of additional Bragg-like or diffuse features clearly indicates, despite their structures being the same as that of $Tb(HCO_2)_3$ and $Ho(HCO_2)_3$,[51] *i.e.* they feature one-dimensional chains arranged on a triangular lattice.

Members of the $Ho_{1-x}Er_x(HCO_2)_3$ ($x = 0.1, 0.2, 0.3, 0.4, 0.5, 0.6, 0.7, 0.8$ and 0.9) series have been successfully synthesised, their stoichiometries verified *via* a combination of XRF and EDX, and their bulk magnetic properties characterised. We observed that different Ho/Er stoichiometric ratios result in a modification of the magnetic properties of these materials. The magnetic properties of the $Ho_{0.5}Er_{0.5}(HCO_2)_3$ material, a potential realisation of a Random Spin-Chain paramagnet, were measured down to 0.4 K, and results have shown the behaviour of this material to be paramagnetic down to this temperature. Given this promising result indicating paramagnetism, as expected by such a system,[42] neutron diffraction experiments were successfully carried out for this material down to 0.28 K, where no additional Bragg-like or clearly structured

diffuse features emerged. This is in contrast to the behaviour of one of its parent structures, namely $Ho(HCO_2)_3$,[51] and confirms this Ho/Er 1:1 ratio to be responsible for the paramagnetic behaviour of this material. Only a small difference between low-temperature neutron diffraction patterns was observed, which may indicate some weak degree of diffuse scattering is present. However, with this difference being small, further confirmation is needed *via* computational studies, for which more insight about the nature of the interactions within the parent structures is needed. Such information, measurable from inelastic neutron experiments, was not obtained due to beamtime in neutron facilities being severely limited during the COVID-19 pandemic, which has severely impacted this aspect of the project. Therefore, the question is still open as to whether this material behaves like a Random Spin-Chain Paramagnet and whether the difference observed in the curves might contain information about the spin clusters that constitute such a system.[42]

Finally, studies on the magnetocaloric properties of the novel $Tb_{1-x}Y_x(HCO_2)_3$ family of coordination polymers were carried out. Members of this family with $x = 0.025$, 0.05, 0.10, 0.20, 0.40, 0.60 and 0.80 have been synthesised and their stoichiometric compositions measured using a combination of XRF and EDX. The magnetic properties, including magnetocaloric, and the heat capacity were measured to study the evolution of these properties with the increasing concentration of Y. Heat capacity data for samples up to $x = 0.40$ have allowed us to monitor the evolution of the TIA transition *vs.* Y concentration, and has confirmed all of them undergo such a transition, but with this shifting to slightly lower temperatures. The small extent of the temperature variations suggests the TIA state is quite robust to diamagnetic impurities, while smaller entropy changes extracted from this data indicate that 1D order decreases with doping. An additional contribution to the magnetic heat capacity data was observed

with increasing concentrations of Y, and this was attributed to arising from entropic effects caused by the Y cations breaking the Tb 1D chains into smaller segments, therefore increasing the entropy of the system. The diamagnetic impurity impacts the magnetocaloric properties negatively, as values of $-\Delta S_m^{max}$ are lower than that of the parent Tb(HCO$_2$)$_3$. However, when normalised per amount of Tb present in the structure, $-\Delta S_m^{max}$ values are lowest for $x = 0.05$ but higher for $x = 0.10$, independent of the applied fields. A mechanism for this peculiar behaviour has been proposed, where two competing effects arise from diamagnetic doping. Further investigation *via* computational studies, such as those involving Monte-Carlo simulations, would be required to predict the behaviour of these systems with diamagnetic doping.

6 Antiferromagnetic Structure of [Li(C$_2$O$_4$)]$_2$[Co$_5$(OH)$_8$], a Complex 2D Framework

6.1 Introduction

Decarbonisation of transport and limiting the impact of CO$_2$ production on climate change have become of great importance in recent years, with efforts focusing on the fabrication and distribution of electric vehicles (EVs) in the mass market as the next-generation means of transport.[204] Li-based rechargeable batteries are necessary for this purpose, as they are widely used in EVs, as well as many electronic devices, such as laptops, mobile phones and wearables, and their demand is increasing significantly, with lithium cobalt oxide LiCoO$_2$ (LCO) being the main material for electrodes for lithium-ion batteries (LIBs).[204,205] However, obtaining cobalt to fabricate battery components for electric vehicles is quite challenging as its abundance is low and obtaining such a resource often involves mining, which in turn results in the violation of human rights, including exploitation of child labour, in those countries where cobalt is found the most, *e.g.* Congo.[206] As a consequence, in order to overcome such issues, developing methods for a full circular economy of lithium and cobalt used in batteries is key.[204,207] Optimising the energy and cost efficiency of synthesis and recycling of LIBs is an important aspect of this goal. The Lithium Cobalt Recycling Innovation in the Circular Economy (LiCoRICE) project has been working on a novel, low-energy and fast-turnaround

process aimed at recycling existing batteries and producing LCO for new ones.[208] During studies for the optimisation of this process, the group of Dr Tony Keene — member of the LiCoRICE team — at University College Dublin, Ireland, synthesised a dense coordination framework, [Li(C₂O₄)]₂[Co₅(OH)₈]. This 2D material has well-separated Li$^+$ and Co^{2+} layers, which makes this system an ideal host for two-dimensional magnetism. The Co^{2+} layers are also based on a triangular motif, while also potentially featuring geometric frustration (see Section 1.6). In this chapter, we present our study of the magnetic structure of this 2D-layered framework.

6.2 Crystal Structure of [Li(C₂O₄)]₂[Co₅(OH)₈]

Information on the crystal structure of [Li(C₂O₄)]₂[Co₅(OH)₈] has been obtained by Dr Tony Keene's group and is herein reported. [Li(C₂O₄)]₂[Co₅(OH)₈] was synthesised in aqueous environment by the Keene group by mixing CoCl₂·6H₂O, LiOH·H₂O, LiBr and H₂C₂O₄·2H₂O in a Teflon-lined autoclave, with this heated at ~230 °C for four hours.[209] Deuteration for neutron diffraction measurements was carried out by synthesising the compound in D₂O. Single-crystal X-ray data have previously shown this material adopts a triclinic $P\bar{1}$ structure, with layers of [Co(OH)₈]$^{2+}$ lying on the *ab*-plane, well-separated from one another due to the presence of [Li(C₂O₄)]$^-$ layers, alternating along the *c*-axis, as shown in Figure 6.1a.[209] Three crystallographically independent Co^{2+} sites are present — namely Co1, Co2 and Co3 — with the oxidation state of the Co cations confirmed *via* calculation of the bond valences using the following equation:

$$V_i = \sum_{ij} v_{ij} = \sum_{ij} e^{\frac{R_{ij} - d_{ij}}{b}} , \qquad (6.1)$$

with V_i the valence of the *i* atom, v_{ij} the valence of a bond between the atoms *i* and *j*, d_{ij} the length of the bond between the two atoms, *b* is known as the "universal" constant and

is equal to 0.37 Å, and R_{ij} is the bond-valence parameter, equal to 1.692 Å for bonds between Co(II) centres and oxygen anions.[210] The calculated Co cation valences, V_{Co}, and the distances, $d_{Co\text{-}O}$, for each Co site at room temperature are shown in Table 6.1. While Co1 and Co2 adopt an octahedral coordination environment, Co3 adopts a tetrahedral geometry, with tetrahedra situated above and below each layer and directly connected to the [Li(C$_2$O$_4$)]$^-$ layers *via* Co-O-Li bonds.
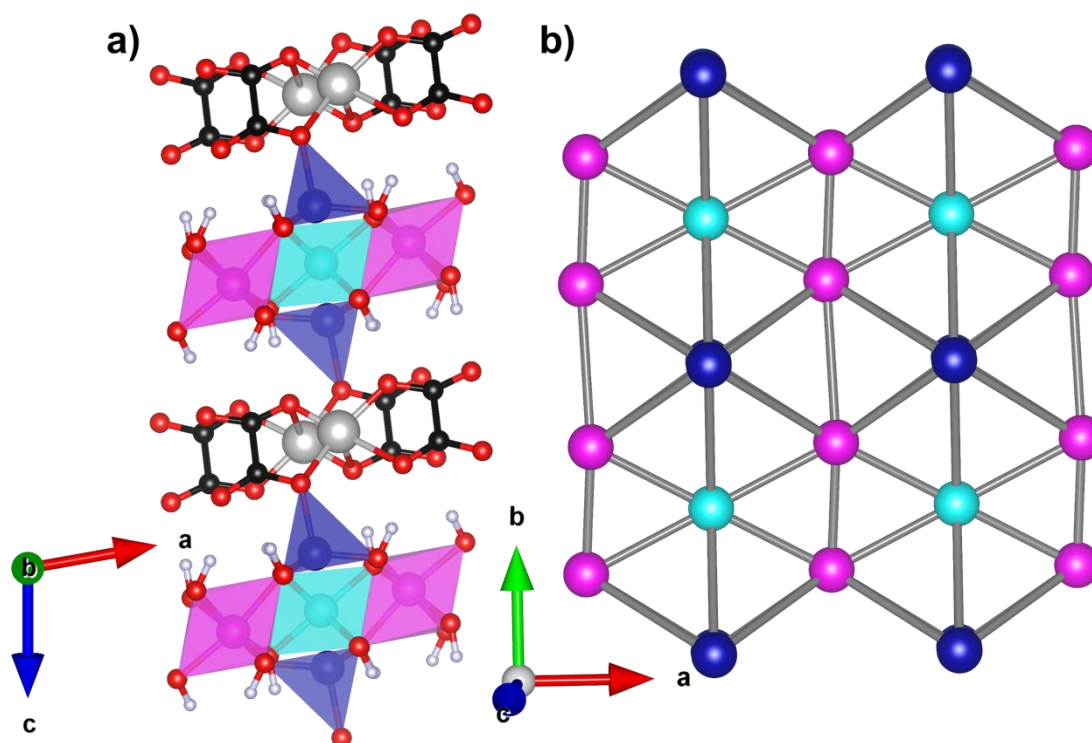
Figure 6.1: (a) Crystal structure of [Li(C$_2$O$_4$)]$_2$[Co$_5$(OH)$_8$]: Co^{2+} layers are well-separated by Li$^+$ layers and connected to these *via* tetrahedral cobalt sites; (b) triangular arrangement of Co sites within a layer, with bonds showing Co sites bridged by oxygens. Colour codes are Co1 site: cyan, Co2 site: magenta, Co3 site: blue, C: black, O: red and H: white.

Table 6.1: Co-O bond distance for each Co site at room temperature and corresponding Co oxidation state.

	Co1	Co2	Co3
d_{Co-O} (Å)	2.001(5)	1.880(13)	1.834(11)
	2.001(5)	2.066(12)	1.947(12)
	2.169(5)	2.134(15)	1.961(13)
	2.169(5)	2.182(15)	2.070(12)
	2.157(6)	2.228(12)	-
	2.157(6)	2.341(14)	-
V_{Co}	1.99	1.94	2.02

The Co^{2+} cations can be viewed as being arranged in a significantly distorted arrangement of edge-sharing triangles, as shown in Figure 6.1b. Co-Co distances, as well as Co-O-Co pathway distances where superexchange interactions are likely to occur, are reported in Table 6.2 and Co-O-Co angles are reported in Table 6.3. These values show these triangles are somewhat distorted from being equilateral as a consequence of the low symmetry of the structure. Despite this, the well-separated distorted triangular lattices may still be expected to lead to geometric frustration, as discussed in Section 1.6, if they featured antiferromagnetic interactions between neighbouring Co cations.

Table 6.2: Co-Co and Co-O-Co superexchange pathway distances in $[Li(C_2O_4)]_2[Co_5(OH)_8]$ at room temperature.

Sites	Distance (Å)
2×Co1-Co2	3.032(10)
2×Co1-Co2	3.080(10)
2×Co1-Co3	3.486(10)
2×Co1-Co3	3.624(9)
Co2-Co2	2.96(2)
Co2-Co2	3.35(2)
Co2-Co3	3.463(13)
Co2-Co3	3.526(12)
Co2-Co3	3.623(13)
Co2-Co3	3.625(14)
Co1-O10-Co2	4.084(11)
Co1-O11-Co2	4.307(13)
Co1-O12-Co2	4.262(13)
Co1-O11-Co3	4.038(12)
Co1-O12-Co3	4.144(11)
Co2-O10-Co2	4.080(15)
Co2-O13-Co2	4.358(15)
Co2-O11-Co3	4.097(16)
Co2-O12-Co3	4.078(16)
Co2-O13-Co3	4.010(14)

Table 6.3: Co-O-Co superexchange angles in $[Li(C_2O_4)]_2[Co_5(OH)_8]$ at room temperature.

Sites	Angle (°)
Co1-O10-Co2	95.9(4)
Co1-O11-Co2	91.3(4)
Co1-O12-Co2	90.7(3)
Co1-O11-Co3	119.3(3)
Co1-O12-Co3	121.9(3)
Co2-O10-Co2	92.9(5)
Co2-O13-Co2	100.3(4)
Co2-O11-Co3	124.3(4)
Co2-O12-Co3	125.4(5)
Co2-O13-Co3	119.3(5)

6.3 Powder X-ray Diffraction and Le Bail Fits

Powder X-ray diffraction patterns were measured for $[Li(C_2O_4)]_2[Co_5(OD)_8]$, with Le Bail fits performed to assess the purity of the sample, as shown in Figure 6.2. The fits indicate good phase purity of the sample, however, a small amount of $Co(OD)_2$ is present in the perdeuterated sample, an impurity resulting from the basic synthesis conditions of $[Li(C_2O_4)]_2[Co_5(OD)_8]$.[209] The inclusion of this phase in our Le Bail fits led to a significant improvement of the refinement statistics.
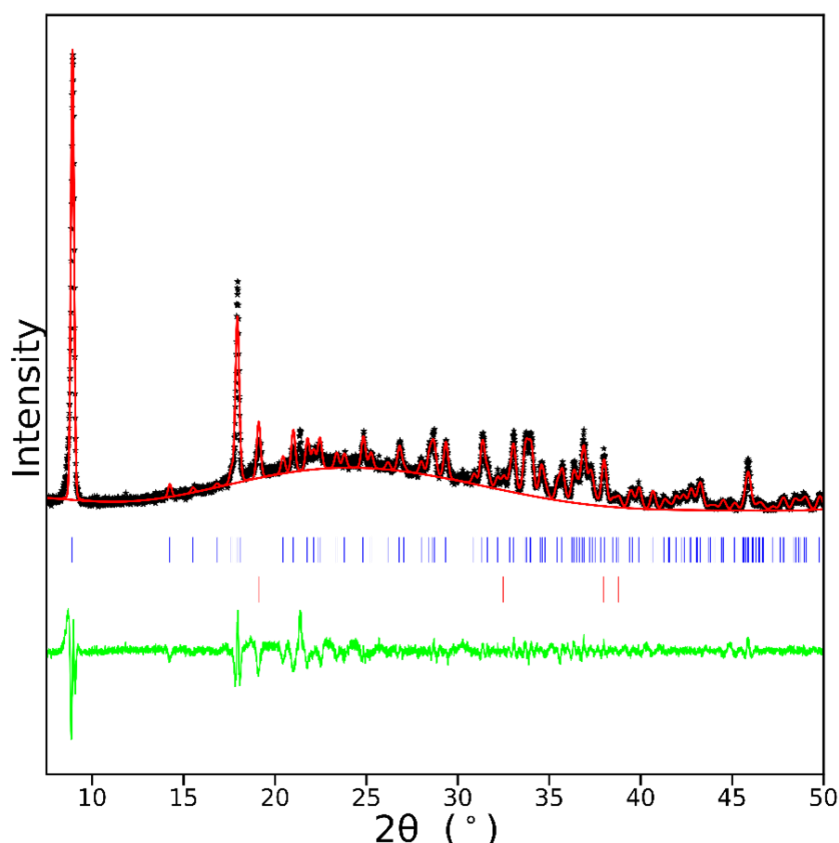
Figure 6.2: Conventional powder X-ray diffraction pattern of $[Li(C_2O_4)]_2[Co_5(OD)_8]$ measured using a Cu source (λ = 1.54 Å) and fitted using the Le Bail method to highlight phase purity. The crosses, red and green lines are experimental and calculated intensities and the difference curve. Blue and red vertical markers indicate the position of the Bragg reflections of the $[Li(C_2O_4)]_2[Co_5(OD)_8]$ and $Co(OD)_2$ phases, respectively. R_p and R_{wp} of 6.79 % and 9.58 % are obtained from the refinement, with a = 5.3433(13) Å, b = 6.2906(19) Å, c = 10.167(6) Å, α = 99.51(2)°, β = 99.931(11)° and γ = 90.101(6)° for $[Li(C_2O_4)]_2[Co_5(OD)_8]$.

6.4 Bulk Magnetic Properties of [Li(C₂O₄)]₂[Co₅(OH)₈]

and [Li(C₂O₄)]₂[Co₅(OD)₈]

Bulk magnetic properties for $[Li(C_2O_4)]_2[Co_5(OH)_8]$ and its deuterated analogue $[Li(C_2O_4)]_2[Co_5(OD)_8]$, the former collected by Dr Paul Saines, were measured in a 1 kOe magnetic field. Magnetic susceptibility $\chi(T)$ plots are shown in Figure 6.3. For both samples, the data showed a sharp cusp at ~54 K, with divergence of the zero-field cooled (ZFC) and field cooled (FC) curves below this temperature, which is suggestive of weak ferromagnetism. A second cusp centred at ~13 K can be identified, suggesting a further transition may be occurring at these temperatures. This feature could be ascribed

to the presence of the Co(OH)$_2$ impurity, which is expected to order antiferromagnetically below T_N ~11 K.[211] The inverse susceptibility data, $\chi^{-1}(T)$, shows linear behaviour in the paramagnetic regime down to ~150 K, consistent with the Curie-Weiss law (see Eqn. 1.13), with the loss of linearity below ~150 K suggesting interactions amongst magnetic moments within the triangular lattice may become significant below this temperature. Fits of the linear region using the Curie-Weiss law were carried out, with results reported in Table 6.4.
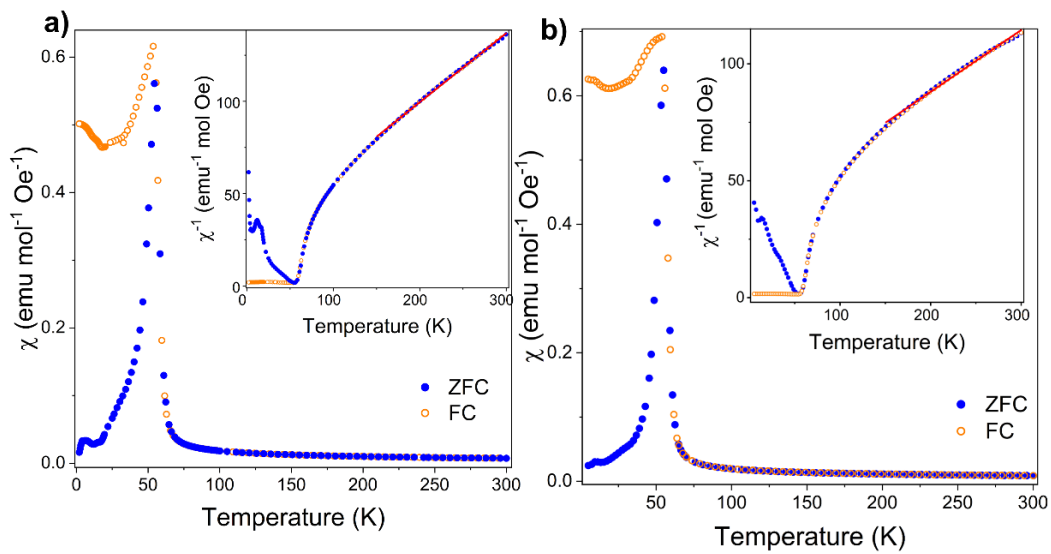
Figure 6.3: Bulk magnetic properties of (a) [Li(C$_2$O$_4$)]$_2$[Co$_5$(OH)$_8$] and (b) [Li(C$_2$O$_4$)]$_2$[Co$_5$(OD)$_8$] from 1.8 to 300 K. The inverse susceptibilities, χ^{-1}, are shown as insets.

Table 6.4: Results from Curie-Weiss fits to inverse susceptibility, χ^{-1}, data carried out from 150–300 K for [Li(C$_2$O$_4$)]$_2$[Co$_5$(OH)$_8$] and [Li(C$_2$O$_4$)]$_2$[Co$_5$(OD)$_8$].

Sample	θ_{CW} (K)	μ_{eff} (μ_B)
[Li(C$_2$O$_4$)]$_2$[Co$_5$(OH)$_8$]	−67.0(1.9)	4.63(2)
[Li(C$_2$O$_4$)]$_2$[Co$_5$(OD)$_8$]	−133(5)	5.50(3)

Values of the Curie-Weiss temperature, θ_{CW}, are negative for both samples, indicating this material has antiferromagnetic behaviour. Interestingly, the $|\theta_{CW}|$ value is higher for the deuterated sample, which would suggest its antiferromagnetic behaviour is more significant. Regardless, the frustration indices $f = \frac{|\theta_{CW}|}{T_N}$ ~ 1 and 2 for [Li(C$_2$O$_4$)]$_2$[Co$_5$(OH)$_8$] and the deuterated sample, respectively, with their difference

likely due to the different amount of $Co(OH)_2$ and $Co(OD)_2$, present in the two samples, respectively, would suggest this material does not show magnetic frustration based on bulk property measurements.

Isothermal magnetisation measurements of $[Li(C_2O_4)]_2[Co_5(OD)_8]$ have shown hysteresis is present upon magnetisation of the samples, and this increases upon cooling down to 5 K, as shown in Figure 6.4. These results support the idea that the material exhibits weak ferromagnetic behaviour but it is not possible, particularly given the complex nature of the structure, to confirm if this is due to antiferromagnetic canting or ferrimagnetic ordering based on bulk property measurements. We therefore turned to neutron diffraction in combination with density functional theory calculations to give us a better understanding of the behaviour of this material on the atomic scale.
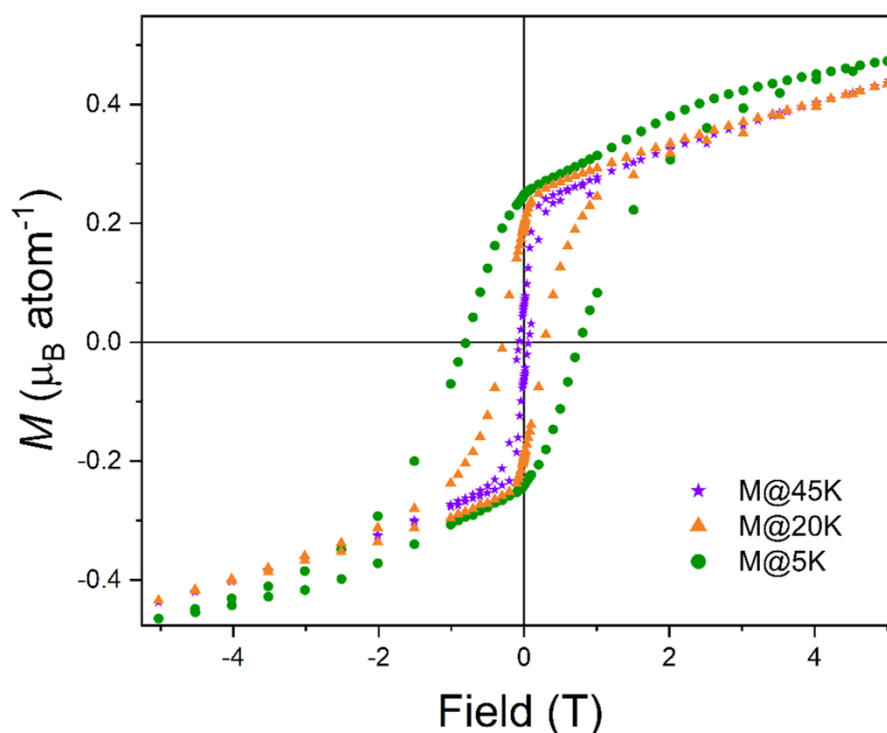
Figure 6.4: Isothermal magnetisation measurements of $[Li(C_2O_4)]_2[Co_5(OD)_8]$.

6.5   Probing   the   Magnetic   Structure   of

[Li(C$_2$O$_4$)]$_2$[Co$_5$(OD)$_8$]

To determine the magnetically ordered state in [Li(C$_2$O$_4$)]$_2$[Co$_5$(OD)$_8$], neutron diffraction patterns were collected using the GEM diffractometer at the ISIS Neutron and Muon Source. These were obtained for temperatures down to 8 K using a closed cycle refrigerator, with analysis carried out using Rietveld refinements.[159] Fits to the room temperature data, shown in Figure 6.5 for bank 2 and 6 (see Appendix D ad Figures S97–S252 in the SI for lower temperatures), were carried out using the model for [Li(C$_2$O$_4$)]$_2$[Co$_5$(OH)$_8$] determined *via* single-crystal diffraction data along with the inclusion of Co(OD)$_2$ as a secondary phase; we found the phase fraction of Co(OD)$_2$ to be ~35%, indicating a significant amount of this phase is present. Fits to room temperature patterns have allowed us to determine the position and the occupancy of the deuterium atoms in the structure, as reported in Table 6.5, for the first time. This provided additional confirmation of the presence of hydroxide rather than oxide groups in this material. The structures determined from these refinements, however, had lower precision that the structure determined *via* single-crystal X-ray diffraction due to the complex and low symmetry structure of [Li(C$_2$O$_4$)]$_2$[Co$_5$(OH)$_8$]. It should be noted that during the refinement process, soft and hard constraints have been introduced to aid in achieving convergence. For instance, in the former case, C-C and C-O bond distances have been restrained, whereas, in the latter case, isotropic displacements parameters for atoms in the Li layers and, separately, the Co layers were constrained to remain equal. Similarly, thermal displacement parameters for all the D atoms were constrained to remain equal to one another (see Appendix D for details).
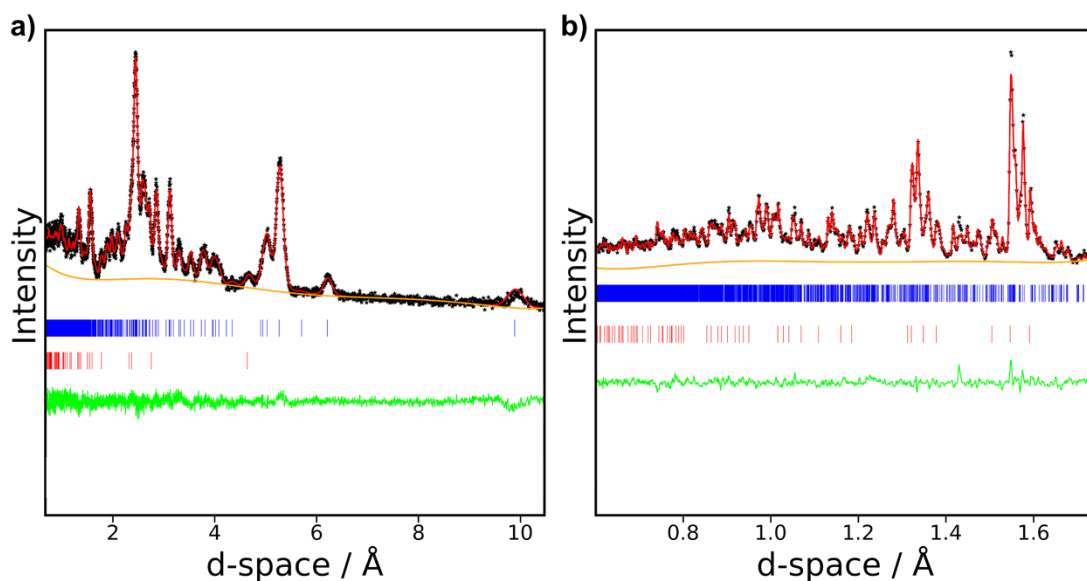
Figure 6.5: Neutron diffraction patterns of [Li(C$_2$O$_4$)]$_2$[Co$_5$(OD)$_8$] from bank 2 and 6 of the GEM diffractometer, measured at room temperature. The crosses, red, orange and green lines are experimental and calculated intensities, the estimated background and the difference curve, respectively. Blue and red vertical markers indicate the position of the Bragg reflections of the [Li(C$_2$O$_4$)]$_2$[Co$_5$(OD)$_8$] and Co(OD)$_2$ phases, respectively.

It should be noted that the decision was taken to exclude bank 1 from the refinements for the data sets collected above the magnetic transition, mainly due to the fact that the patterns containing reflections at high *d*-spacings from the bank 1 detectors do not contain significant nuclear phase information. On the contrary, significant information about the magnetic phase is expected to be observed at high *d*-space, with bank 1 therefore becoming more relevant in the refinement process when fitting to lower temperature data.

Table 6.5: Crystallographic details of $[Li(C_2O_4)]_2[Co_5(OD)_8]$ obtained from neutron diffraction patterns collected at room temperature. Final total refinement statistics R_p, R_{wp} and χ^2 were 2.21%, 2.36% and 2.94, respectively.

Space group	a (Å)	b (Å)	c (Å)	Volume (Å^3)	
$P\bar{1}$	5.34880(19)	6.3002(2)	10.1843(4)	333.26(3)	
	x	y	z	U_{iso} (Å^2)	occupancy
Co1	−0.5	0.5	0.5	0.0011(2)	1
Co2	−0.0030(17)	0.7358(15)	0.5046(10)	0.0011(2)	1
Co3	0.4612(15)	0.9433(15)	0.3336(7)	0.0011(2)	1
Li1	−0.382(2)	0.7157(18)	0.0050(14)	0.0047(3)	1
O10	−0.2087(7)	0.4732(7)	0.3933(5)	0.0011(2)	1
O11	0.2902(7)	0.7049(6)	0.3784(4)	0.0011(2)	1
O12	0.2929(7)	1.2184(6)	0.3796(4)	0.0011(2)	1
O13	0.8119(7)	0.9607(6)	0.3846(4)	0.0011(2)	1
O22	−0.1238(7)	0.6258(6)	−0.1209(4)	0.0047(3)	1
O23	0.3133(7)	0.5999(6)	−0.1118(4)	0.0047(3)	1
O24	−0.0498(7)	0.8667(6)	0.1237(4)	0.0047(3)	1
O25	0.3814(7)	0.8712(6)	0.1244(4)	0.0047(3)	1
D10	0.2153(8)	0.6152(6)	0.2984(4)	0.0133(5)	0.984(4)
D11	1.2449(7)	1.5475(7)	0.6973(4)	0.0133(5)	0.984(4)
D12	1.2213(9)	1.2771(7)	1.2940(4)	0.0133(5)	0.984(4)
D13	1.1250(6)	1.0494(7)	0.6993(4)	0.0133(5)	0.984(4)
C20	0.1126(6)	0.6695(6)	−0.0733(4)	0.0047(3)	1
C21	0.1466(6)	0.8242(6)	0.0737(4)	0.0047(3)	1

Upon cooling down to 199 K, a mismatch between the intensity of the measured data points and the calculated line was noticed, particularly for reflections centred at ~2.4, ~3.4 and ~4.5 Å, which could not be accounted for by the two phases used so far. Upon discussions with the GEM instrument scientist, Dr Ivan da Silva, it was concluded that

water ice (phase Ih), which adopts a hexagonal P6₃/*mmc* structure,[212] formed in the sample environment at this temperature. Indeed, the inclusion of a model of this phase for refinements — using deuterium atoms rather than hydrogens — has allowed the reflections where the mismatch was observed to be fitted. This may suggest the sample was not completely dried prior to measurement.

Upon cooling down to 55.6 K, additional Bragg-like features were observed in the diffraction pattern, with those centred at ~20, ~6.5 and ~4.5 Å being the most noticeable, as shown in Figure 6.6. We attribute the emergence of these reflections to the onset of magnetic order at this temperature, consistent with bulk magnetic property data. It was possible to index these reflections by considering a triclinic $P\overline{1}$ unit cell with the same lattice parameters as the nuclear phase one, but with the *c*-axis doubled, therefore suggesting a *k*-vector of (0, 0, ½). This *k*-vector implies that the Co sites on adjacent layers are coupled antiferromagnetically to one another. ISODISTORT was used to determine the possible irreducible representations of the magnetic structure, using the determined *k*-vector and the nuclear phase model as the starting structure.[213,214] Two possible irreducible representations were identified, namely mZ^+ and mZ^-, both corresponding to the $P\overline{1}$ magnetic space group. The former irreducible representation allows only Co2 and Co3 sites to be magnetically active, whereas the latter allows all the Co sites to be magnetically active.
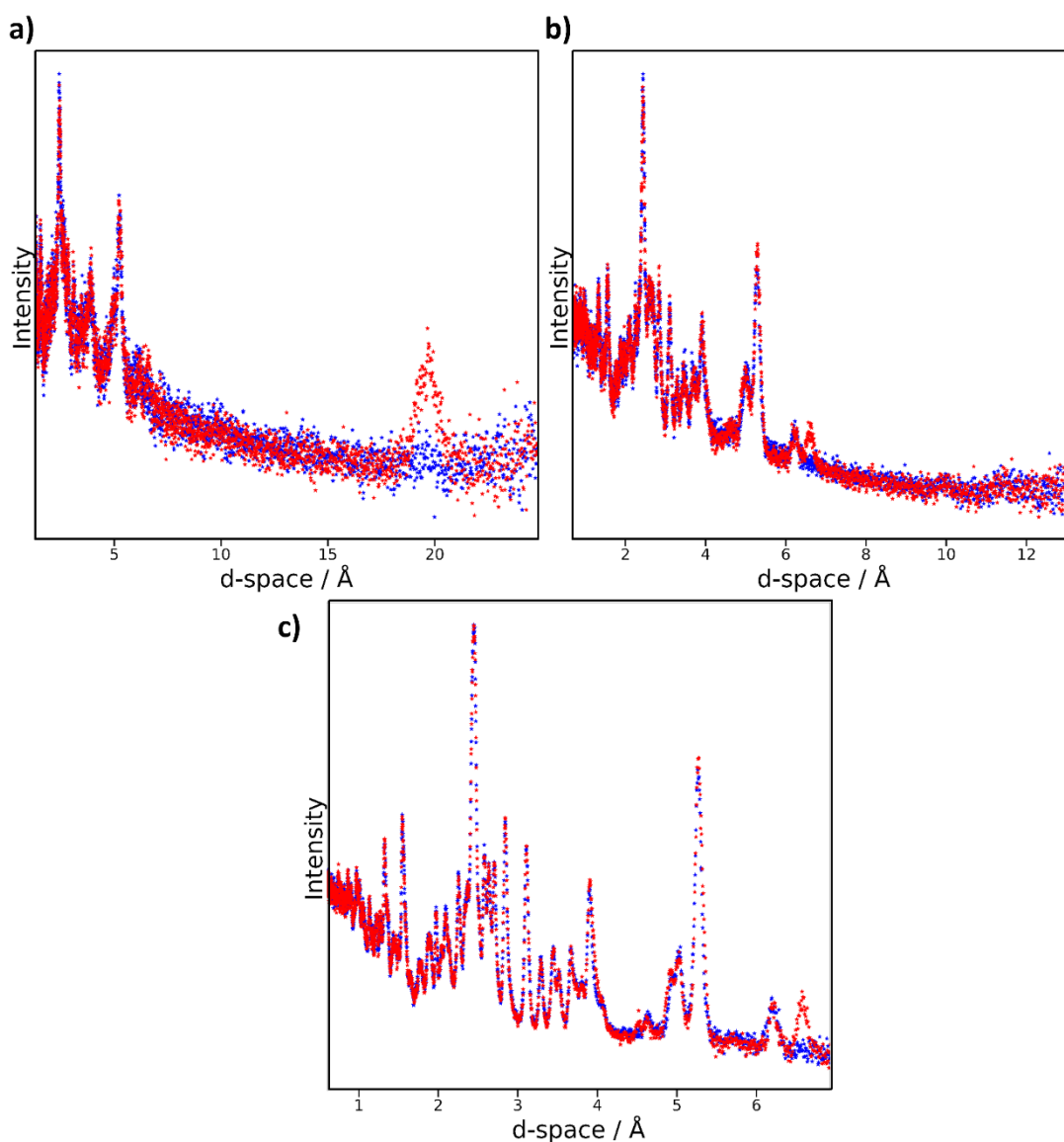
Figure 6.6: Comparison of neutron diffraction patterns acquired at 60 K (blue) and 55.6 K (red) obtained from (a) bank 1, (b) bank 2 and (c) bank 3 of the GEM diffractometer.

Simulated Annealing (SA) carried out by Dr Emma McCabe (Durham University), using TOPAS-Academic,[215] have shown that the mZ⁻ irreducible representation best fits the data obtained at 55.6 K (R_p = 2.76% and R_{wp} = 2.85%). This corresponds to a $P\bar{1}$ magnetic structure and provided the magnetic moment vectors belonging to each Co site, shown in Table 6.6. It can be observed that the magnetic moments lay mainly along the *b*-axis, with no component on the *c*-axis and a negligible component along the *a*-axis. SA therefore suggested interactions within a layer to be ferromagnetic between Co1-Co2,

Co2-Co2 and Co3-Co3 sites, with Co1-Co3 and Co2-Co3 sites being antiferromagnetically coupled.

Table 6.6: Components of the magnetic moment vectors for the Co^{2+} sites in $[Li(C_2O_4)]_2[Co_5(OD)_8]$ at 55.6 K, as determined by Simulated Annealing.

Site	a-component	b-component	c-component
Co1	1×10^{-5}	0.14(7)	0
Co2	2.3×10^{-4}	2.44(3)	0
Co3	1.6×10^{-4}	−1.75(4)	0
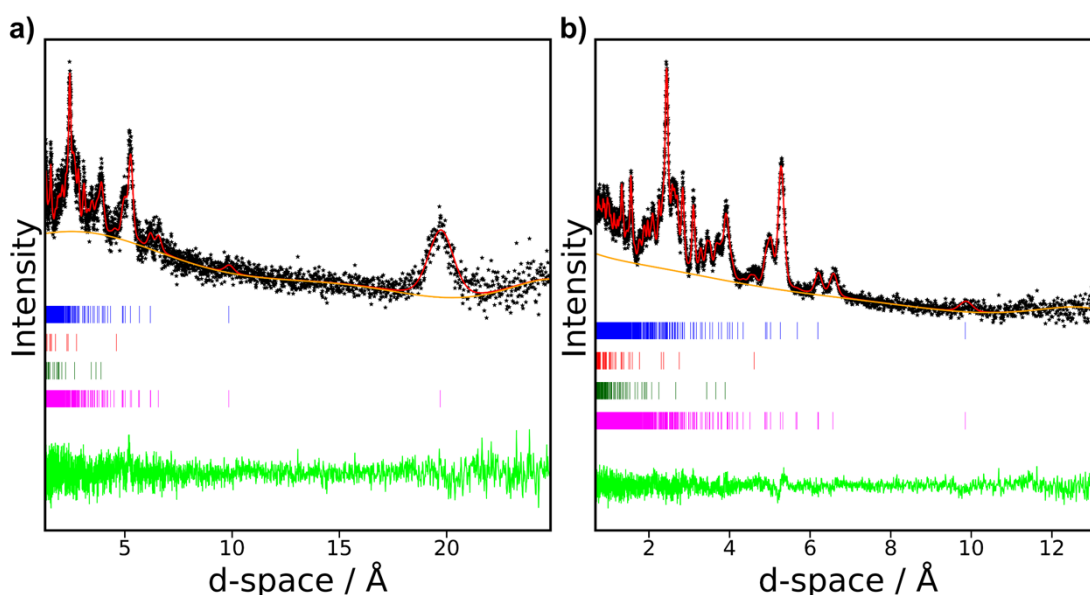
Figure 6.7: Neutron diffraction patterns of $[Li(C_2O_4)]_2[Co_5(OD)_8]$ from a) bank 1 and b) bank 2 of the GEM diffractometer, measured at 55.6 K. The crosses, red, orange and green lines are experimental and calculated intensities, the estimated background and the difference curve, respectively. Blue, red, green and magenta vertical markers indicate the position of the Bragg reflections of the $[Li(C_2O_4)]_2[Co_5(OD)_8]$, $Co(OD)_2$, D_2O and magnetic phases, respectively.

Rietveld refinements carried out following these findings and using the initial magnetic model determined *via* SA as a starting point, have allowed for the fitting of the data obtained at 55.6 K, as shown in Figure 6.7. It should be noted that, initially, despite the initial non-zero values found from SA, the component along the *a*-axis for the magnetic moments belonging to the Co1 site was set and fixed to zero, as fitting this parameter was found to lead to divergence of the refinements when fitting to patterns immediately below the magnetic phase transition. Conversely, a significant component

of the magnetic moment was obtained for both Co2 and Co3 along the *a*-axis at this temperature.

It was found that the model obtained at 55.6 K for the magnetic structure did not account for changes in the intensity observed for the magnetic reflections upon cooling below 45 K. For this reason, we excluded these variations to be caused by the $Co(OD)_2$ phase present in the sample, since this is known to order at ~11 K.[211] Including the *a*-axis component for the magnetic moment of the Co1 site as a refinable parameter at this temperature enabled the variations of intensity observed upon cooling to be accounted for, as it can be observed for refinements at 8 K, shown in Figure 6.8. This has led to the interesting conclusion that, while the magnetic moments on the Co sites are primarily oriented along the *b*-axis, they all cant towards the *a*-axis at lower temperature; those of Co1 and Co3 progressively rotate towards the *a*-axis on cooling below 45 K, as shown in Figure 6.9. Ultimately, the *a*-axis component for the Co1 site approaches similar values as those of the moments belonging to the Co2 site.
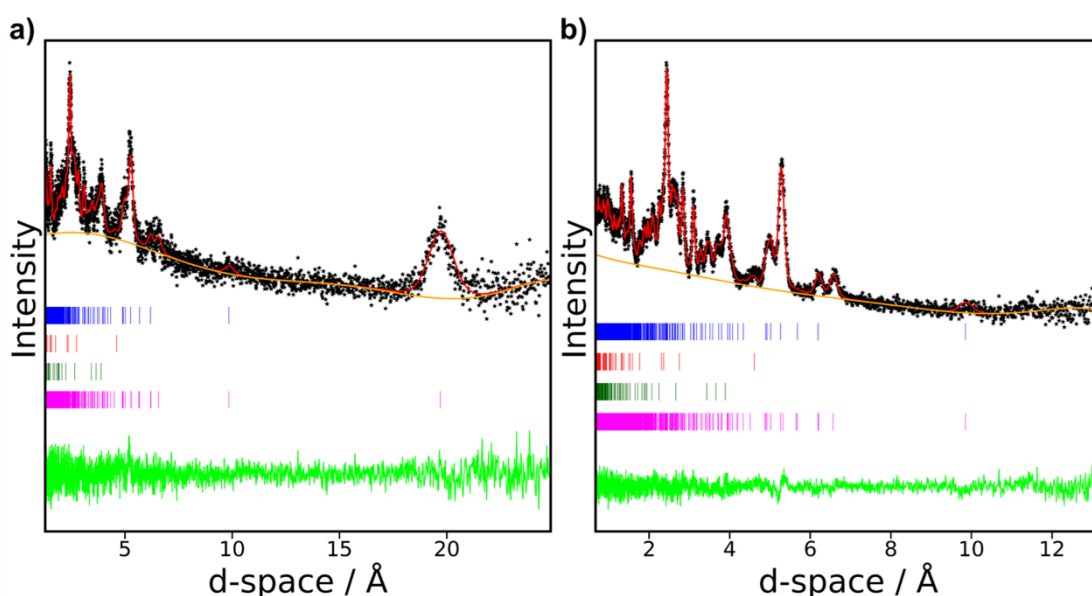
Figure 6.8: Neutron diffraction patterns of $[Li(C_2O_4)]_2[Co_5(OD)_8]$ from a) bank 1 and b) bank 2 of the GEM diffractometer, measured at 8 K. The crosses, red, orange and green lines are experimental and calculated intensities, the estimated background and the difference curve, respectively. Blue, red, green and magenta vertical markers indicate the position of the Bragg reflections of the $[Li(C_2O_4)]_2[Co_5(OD)_8]$, $Co(OD)_2$, D_2O and magnetic phases, respectively.
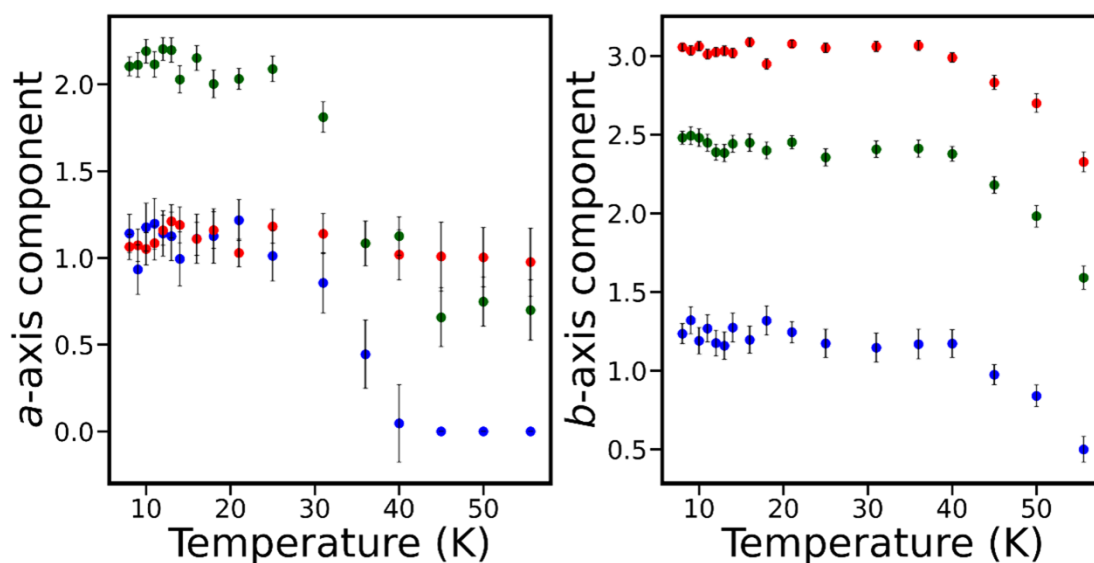
Figure 6.9: Plots of *a*-axis (left) and *b*-axis components (right) of the magnetic moment vectors as a function of temperature determined *via* Rietveld refinements. The *a*-axis component for the Co1 site magnetic moment above 45 K are fixed to a zero value to avoid instability of the refinements. Colour codes are blue: Co1 site, red: Co2 site and green: Co3 site.

Refinements down to 8 K proved to be successful, enabling us to determine the magnetic structure of $[Li(C_2O_4)]_2[Co_5(OD)_8]$ at this temperature, represented in Figure 6.10, and with the final magnetic moment vectors reported in Table 6.7. Overall, particularly when considering the lattices of the magnetic moments for the Co2 and Co3 sites, it can be concluded that the magnetic structure of $[Li(C_2O_4)]_2[Co_5(OD)_8]$ is that of a canted antiferromagnet. However, the smaller magnetic moments for Co1 are aligned with those belonging to the Co2 sites, which implies this complex material shows behaviour resembling that of a ferrimagnet. Furthermore, the very small value of the magnetic moment vector for Co1, compared to the expected value of 3 μ_B atom^{-1} for fully ordered Co^{2+} spins, suggests this material might exhibit magnetic frustration, despite the bulk magnetic properties not showing any indication of this (see Section 6.4).

Table 6.7 Vector components and values for the magnetic moments in [Li(C$_2$O$_4$)]$_2$[Co(OD)$_8$] at 8 K, as determined from Rietveld refinements.

Site	*a*-component	*b*-component	*c*-component	Moment
Co1	1.07(11)	1.22(6)	0	1.62(6)
Co2	1.10(7)	3.07(2)	0	3.26(3)
Co3	2.18(6)	2.52(4)	0	3.34(5)

6.6 Density Functional Theory Study of the Magnetic Structure of [Li(C$_2$O$_4$)]$_2$[Co$_5$(OD)$_8$]

To confirm the validity of our model, Density Functional Theory (DFT) simulations were carried out by Dr Nicholas Bristowe (Durham University). These considered the magnetic structure obtained at $T = 8$ K in the collinear spin limit and different configurations obtained by varying the nature of the coupling among magnetic moments belonging to the Co sites. Each configuration of a layer was simulated both using the experimentally observed *k*-vector (0, 0, 0.5), as well as a *k*-vector (0, 0, 0), allowing consideration of antiferromagnetic and ferromagnetic alignment of the layers. One of the configurations, labelled AFM1, where the Co1-Co2, Co1-Co1, Co2-Co2 and Co3-Co3 sites are ferromagnetically coupled, whereas the Co1-Co3 and Co2-Co3 sites are antiferromagnetically coupled, proved to be the lowest-energy configuration and this confirmed that the experimentally obtained magnetic structure is, in the collinear limit, the lowest energy configuration. This also allowed some insight into the relative strength of the different magnetic coupling pathways in the material, i.e. the possible *J* values.

Further DFT calculations allowing for non-collinear spins by including spin-orbit coupling were performed for the lowest-energy magnetic structure for

[Li(C$_2$O$_4$)]$_2$[Co$_5$(OD)$_8$] with a *k*-vector = (0, 0, ½). This is shown in Figure 6.10 and is broadly consistent with the spin orientations in our model, determined *via* Rietveld refinements.
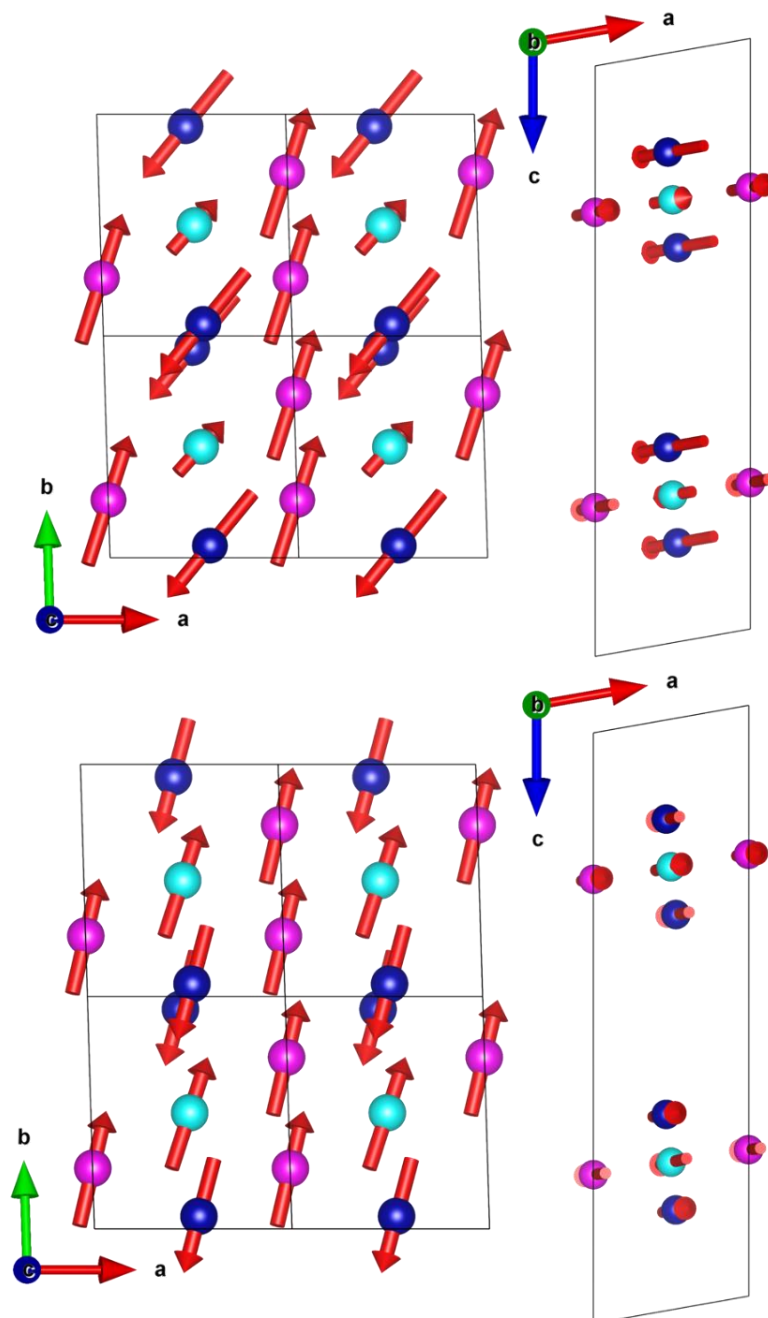
Figure 6.10: Representation of the magnetic structure of [Li(C$_2$O$_4$)]$_2$[Co$_5$(OD)$_8$] at 8 K determined from Rietveld refinements of neutron elastic scattering data (top) and the lowest-energy configuration (AFM1) resulting from DFT simulations (bottom). Note that for the DFT models, the magnitude of the spins are fixed to have the same magnetic moment for representation purposes. Colour codes are Co1 site: cyan, Co2 site: magenta, Co3 site: blue.

When considering individual layers of $[Li(C_2O_4)]_2[Co_5(OH)_8]$, it is possible to identify four different superexchange coupling pathways, as shown in Figure 6.11, namely J_1, J_2, J_3 and J_5, among Co1-Co2, Co2-Co3, Co1-Co3 and Co2-Co2 sites, respectively. In addition to these, a direct exchange pathway between Co3-Co3 sites, J_4 can be identified as well (see Figure 6.11b). The interlayer Co3-Co3 distance along the c-axis is 3.252(10) Å, and this interaction can be attributed to some degree of overlap of the three degenerate d orbitals, namely d_{xz}, d_{xy}, d_{yz}. These comprise the t_2 set, which results from the splitting of the d orbitals in the tetrahedral environment, and which contains the three unpaired electrons in Co(II). Finally, an additional interlayer pathway between Co3 sites placed in adjacent layers, J_6, can be identified. Due to the low symmetry of the structure, this is somewhat of a simplification of the distinct magnetic coupling pathways possible in this material but is required to simplify the equations describing the configurations simulated using DFT.
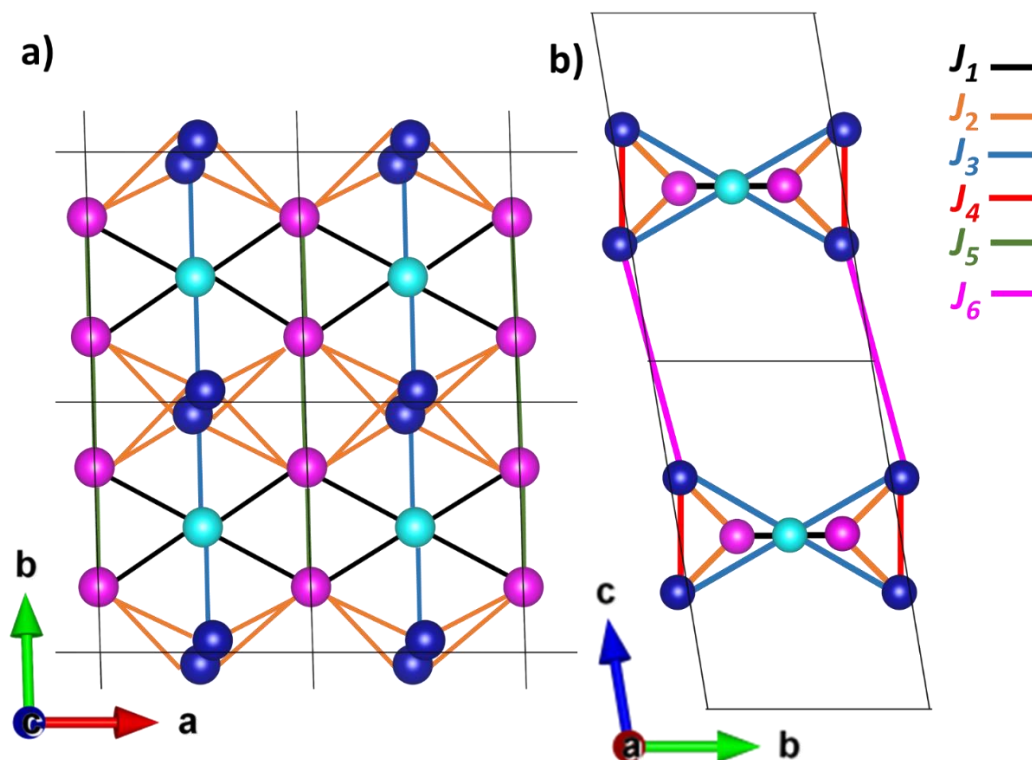
Figure 6.11: Coupling constants J in $[Li(C_2O_4)]_2[Co_5(OH)_8]$ seen in two different views a) along the c-axis and b) along the a-axis, respectively. Colour codes are Co1 site: cyan, Co2 site: magenta, Co3 site: blue.

When considering the Hamiltonian for a system of interacting spins:

$$\hat{H} = \sum_{i,j} J_{i,j} \vec{S}_i \cdot \vec{S}_j \,, \tag{6.1}$$

with $S = \frac{1}{2}$ being the spin for unpaired electrons, equations of the form

$$E = (n_1 J_1 + n_2 J_2 + n_3 J_3 + n_4 J_4 + n_5 J_5 + n_6 J_6) \left(\frac{N_{Co}^2}{4}\right) + K \,, \tag{6.2}$$

can be written, where the coefficients n_i are the number of interactions with J_i coupling, $N_{Co} = 3$ the number of unpaired electrons in high-spin Co^{2+}, K is an additional term that takes into account electronic effects in the simulated system, and E is the energy of a given configuration

Constructing systems of equations which describe each configuration simulated using DFT allows in turn for the estimation of the values of the coupling constants J. These equations, reported in Appendix D, were determined by Dr Nicholas Bristowe and indeed enabled us to estimate the values of J, reported in Table 6.8. These were found to be broadly consistent regardless of the equations from which they were solved. This justified the simplified magnetic coupling pathways included in the equations which, as indicated above, did not separately consider all the possible crystallographically distinct pathways.

Table 6.8: Values of magnetic coupling constants J estimated solving systems of equations written following Eqn. 6.2.

J_1 (K)	J_2 (K)	J_3 (K)	J_4 (K)	J_5 (K)	J_6 (K)
−2.84	−36.96	−38.84	−52	12	−2.08

It can be noticed that the value of J_4 indicates that the direct exchange among Co3 sites within the same layer has significant antiferromagnetic character, in contrast with what their orientation suggests (see Figure 6.10). However, for any given Co3 site, only

one of these interactions is present, *i.e.* coupling with only one other Co3 site occurs, whereas two J_2 and two J_3 interactions per Co3 site with the Co2 and Co1 sites, respectively, are present. It could be therefore stated that these interactions might overcome the one J_4, forcing the Co3 sites to be oriented towards the same direction. It can also be noticed that the value of interlayer coupling, J_6, is significantly smaller than the others and corroborates the idea that $[Li(C_2O_4)]_2[Co_5(OH)_8]$ constitutes an example of a two-dimensional magnetic framework. In addition to this, when considering the J_2, J_3 and J_4 interactions within a Co layer on the *bc*-plane, it can be observed how these interactions constitute two sets of triangles — as more clearly shown in Figure 6.12 — where all the Co sites sitting at the vertices would be antiferromagnetically coupled, with these interactions being potentially frustrated as a result.
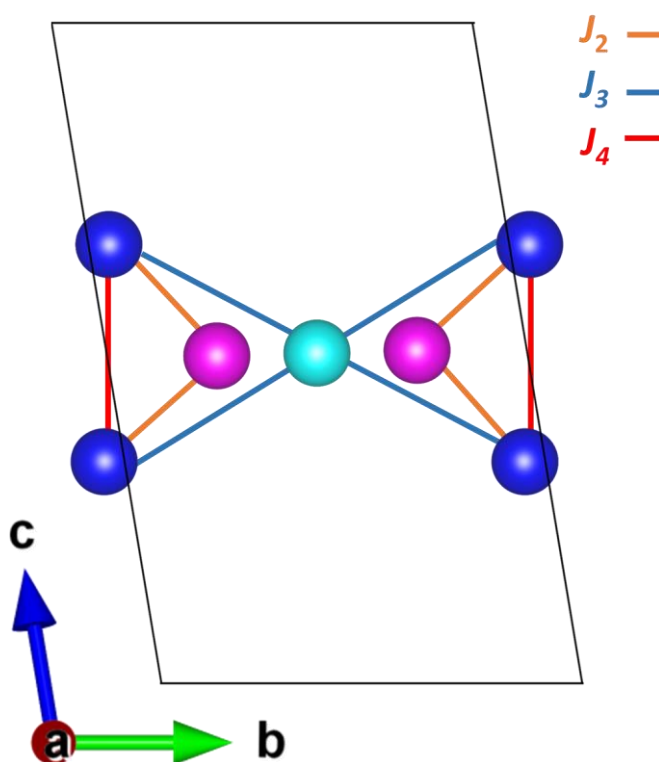
Figure 6.12: Coupling constants J forming triangular lattices in $[Li(C_2O_4)]_2[Co_5(OH)_8]$ along the *a*-axis . Colour codes are Co1 site: cyan, Co2 site: magenta, Co3 site: blue.

The canting of the spins observed in our experimental model could indeed be the result of these frustrated interactions and partially relieves it.

6.6 Conclusions

[Li(C$_2$O$_4$)]$_2$[Co$_5$(OH)$_8$], a coordination framework synthesised by Dr Tony Keene (University College Dublin), attracted our interest due to the presence of two-dimensional motifs in its $P\bar{1}$ triclinic structure, thought to be potential hosts for two-dimensional magnetism. Furthermore, due to the low symmetry, three crystallographically independent Co^{2+} sites are present in the [Co$_5$(OH)$_8$]$^{2+}$ layers. The arrangement of the Co sites within each layer is triangular, raising the question as to whether this system features magnetic frustration.

Bulk magnetic property measurements of both [Li(C$_2$O$_4$)]$_2$[Co$_5$(OH)$_8$] and its deuterated analogue, [Li(C$_2$O$_4$)]$_2$[Co$_5$(OD)$_8$], have shown this framework to be paramagnetic down to ~55 K, where a sharp cusp indicates a paramagnetic-to-antiferromagnetic transition occurs. Antiferromagnetic behaviour was confirmed by fits to the Curie-Weiss law in the paramagnetic regime, showing both materials possess negative Curie-Weiss temperatures.

Neutron diffraction measurements performed down to 8 K confirmed the transition temperature of ~55 K, with the emergence of extra Bragg-like features, indicating the onset of long-range magnetic order. These features were indexed with a k-vector = (0, 0, ½) and the magnetic structure was shown to be triclinic $P\bar{1}$, as confirmed by Simulated Annealing carried out by Dr Emma McCabe (Durham University), with magnetic moments oriented along the *ab*-plane and with orientation of these, initially aligned along the *b*-axis, suggesting the Co1-Co2, Co2-Co2 and Co3-Co3 sites to be FM coupled, whereas the Co1-Co3 and Co2-Co3 sites are AFM coupled. Upon cooling, it is

found that the magnetic moments, rotate on the *ab*-plane towards the *a*-axis. Refinements down to 8 K have allowed to determine the magnetic structure at this temperature, with Co1 showing a significantly smaller magnetic moment than that expected for fully-ordered Co^{2+} sites.

DFT calculations carried out in the collinear spin limit were performed by Dr Nicholas Bristowe (Durham University) and have confirmed the lowest-energy configuration to be consistent with the model determined using neutron diffraction data *via* Rietveld refinements. Estimating values of the *J* coupling constants was possible, and these show that the calculated interactions are consistent with our model. However, the value of J_4, describing the strength of the intralayer interactions between Co3-Co3 sites, was shown to be strongly AFM, in contrast with the relative orientation of the magnetic moments of these sites, which initially suggested FM coupling instead. This peculiar feature can be explained when considering the number and the nature of the coupling between Co3 and the other Co sites, whose net effect is thought to be responsible for the orientations of the Co3 magnetic moments observed in our model. The strong antiferromagnetic character of J_2, J_3 and J_4 would suggest the Co1, Co2 and Co3 sites are arranged in two sets of triangles, with this being the cause of potential magnetic frustration in this system and with the spin canting observed in our model possibly being the result of such frustration being relieved. Finally, the small value of the interlayer interactions confirms this material is an experimental realisation of a two-dimensional magnet.

7 Conclusions

The thesis has mainly explored the effects of symmetry changes and doping on the magnetic behaviour of a series of families of coordination polymers, the $Ln(HCO_2)(C_2O_4)$ (Ln = Gd–Ho) family of compounds, the $Ho_{1-x}Er_x(HCO_2)_3$ and the $Tb_{1-x}Y_x(HCO_2)_3$ solid solutions. The study of bulk magnetic properties and neutron diffraction experiments carried out for $Ln(HCO_2)_3$ containing earlier lanthanides, specifically Ce^{3+}, Pr^{3+} and Nd^{3+}, has also been presented. Finally, the magnetic properties and the nuclear and magnetic structures of a complex 2D-layered canted antiferromagnet, $[Li(C_2O_4)]_2[Co_5(OH)_8]$, *via* a combination of SQUID magnetometry, neutron diffraction experiments and DFT simulations has been discussed.

It was found that $Gd(HCO_2)(C_2O_4)$ exhibits a high magnetocaloric performance, with a peak entropy change $-\Delta S_m^{max}$ = 55.97 J kg^{-1} K^{-1} (218.42 mJ cm^{-3} K^{-1}) at 2 K and for a field change of 5–0 T, which makes $Gd(HCO_2)(C_2O_4)$ a promising material for magnetic cooling applications at low temperature and high magnetic fields, and proves that coordination frameworks with organic ligands can show performances similar to those of purely inorganic coordination polymers. The enhancement of magnetocaloric properties for lower field changes, where permanent magnets could be used, was not achieved for other members of the series, in contrast with the observations on the $Ln(HCO_2)_3$ family of MOFs.[5] Only $Dy(HCO_2)(C_2O_4)$ was found to outperform $Gd(HCO_2)(C_2O_4)$ for field changes of less than 2 T. It was also shown in this study that $Tb(HCO_2)(C_2O_4)$ and $Ho(HCO_2)(C_2O_4)$ lack the significant magnetic correlations found in the $Tb(HCO_2)_3$ and $Ho(HCO_2)_3$ analogues above 1.5 K, which is likely the cause of the lower MCE of these coordination frameworks compared to the analogous formates.

These findings highlight the potential role of local magnetic interactions in enhancing the MCE at lower applied fields, also suggesting how these factors are strongly susceptible to small structural changes. Future work would comprise the use of ligands other than $C_2O_4^{2-}$, although of similar size, to further study the effect of modifying the distance between low-dimensional motifs as well as the consequence of slight changes in the symmetry of the crystal structure.

Further studies on $Ce(HCO_2)_3$, $Pr(HCO_2)_3$ and $Nd(HCO_2)_3$ have shown these samples remain paramagnetic down to 1.8 K, with susceptibility data suggesting antiferromagnetic interactions are present in these systems. Greater attention was focused on the Nd and Ce members, being these Kramer ions. Neutron diffraction patterns were measured down to 140 and 50 mK for the two samples, respectively. The data obtained does not show any additional Bragg-like or diffuse features, which confirms these materials stay paramagnetic down to the measured temperatures.

Members of the $Ho_{1-x}Er_x(HCO_2)_3$ (x = 0.1, 0.2, 0.3, 0.4, 0.5, 0.6, 0.7, 0.8 and 0.9) series have been successfully synthesised, their stoichiometries verified *via* a combination of XRF and EDX, and their bulk magnetic properties characterised. We observed that different Ho/Er ratios lead to their magnetic properties changing. We measured the bulk magnetic properties of $Ho_{0.5}Er_{0.5}(HCO_2)_3$, a potential realisation of a Random Spin-Chain paramagnet, down to 0.4 K, and results revealed this material to be paramagnetic down to this temperature, a promising result given the properties expected by this system.[42] Neutron diffraction experiments were carried out for this material down to 0.28 K, and have shown no presence of additional Bragg-like or structured diffuse scattering, in contrast to the behaviour of $Ho(HCO_2)_3$.[51] This further suggests the Ho/Er 1:1 ratio is responsible for the paramagnetic behaviour of this material. We point out a small difference between low-temperature neutron diffraction patterns was present,

which may indicate some weak degree of diffuse scattering is present. However, this difference is too small to draw any conclusion and future work might consisnt of computational studies, beneficial to gain further insight about the behaviour of this material. For this purpose, it would be necessary to obtain data about the interactions in the parent materials from inelastic neutron experiments, not possible during the course of this PhD degree due to beamtime in neutron facilities being severely limited during the COVID-19 pandemic. Results from this suggested future work might answer the question as to whether this material behaves like a Random Spin-Chain Paramagnet. [42]

Studies on the magnetocaloric properties of the novel $Tb_{1-x}Y_x(HCO_2)_3$ family of coordination polymers were carried out. The magnetic properties, including magnetocaloric, and the heat capacity were measured to study the evolution of these properties with the increasing concentration of Y. Heat capacity data for samples up to $x = 0.40$ have allowed us to monitor the evolution of the TIA transition $vs.$ Y concentration. This has confirmed all of them show TIA transition, although this shifts to slightly lower temperatures, suggesting the TIA state is quite robust to diamagnetic impurities. An additional contribution to the magnetic heat capacity data was observed with increasing concentrations of Y, ascribed to entropic effects caused by the Y cations fragmenting the Tb 1D chains, increasing the entropy of the system. The magnetocaloric properties are negatively affected by the diamagnetic impurity, as shown by the decrease of $-\Delta S_m^{max}$ compared to those of the parent $Tb(HCO_2)_3$. However, it was noted that when normalising per amount of Tb present in the structure, $-\Delta S_m^{max}$ values are lowest for $x = 0.05$ but higher for $x = 0.10$, independent of the applied fields. This behaviour could be explained by the presence of two competing effects caused by diamagnetic doping. Computational studies would be beneficial in explaining these observed effects with increasing dopant concentration.

Finally, [Li(C$_2$O$_4$)]$_2$[Co$_5$(OH)$_8$], a coordination framework synthesised by Dr Tony Keene (University College Dublin) and containing two-dimensional motifs in its $P\bar{1}$ triclinic structure was studied as this was thought to be potential hosts for two-dimensional magnetism. Due to the arrangement of the Co sites within each layer being, the potential presence of geometric frustration was also postulated. Bulk magnetic property measurements of both [Li(C$_2$O$_4$)]$_2$[Co$_5$(OH)$_8$] and its deuterated analogue, [Li(C$_2$O$_4$)]$_2$[Co$_5$(OD)$_8$]. Results have shown this material stays paramagnetic down to ~55 K, where a paramagnetic-to-antiferromagnetic transition occurs. Fits to the Curie-Weiss law have confirmed antiferromagnetic behaviour in the paramagnetic regime, showing both samples possess negative Curie-Weiss temperatures. Neutron diffraction experiments have been carried out down to 8 K and these confirmed the transition occurs at ~55 K, where additional Bragg-like reflections were observed, suggesting long-range magnetic order. The magnetic structure was found to be triclinic $P\bar{1}$, with this further confirmed by SA, which has also shown the magnetic moments lie on the *ab*-plane and are oriented along the *b*-axis. This indicated the Co1-Co2, Co2-Co2 and Co3-Co3 sites are FM coupled, whereas the Co1-Co3 and Co2-Co3 sites are AFM coupled. The magnetic moments were found to rotate on the *ab*-plane towards the *a*-axis upon cooling down. The magnetic structure at 8 K was determined *via* refinements of the patterns acquired down to this temperature. Our model was confirmed by DFT, performed by Dr Nicholas Bristowe (Durham University). DFT also allowed to estimate values of the *J* coupling constants. These indicated the calculated interactions are consistent with our model, although *J* values suggested the interactions between Co3-Co3 sites were AFM, in contrast with the relative orientation of the magnetic moments of these sites. An explanation for this feature could be found in the number and the nature of the coupling between Co3 and the other Co sites, with the net effect of all the interactions potentially

being the cause for the observed orientations of the Co3 magnetic moments. The strong antiferromagnetic character of J_2, J_3 and J_4 would suggest the Co1, Co2 and Co3 sites are arranged in two sets of triangles, with this being the cause of potential magnetic frustration in this system. This combined with the spin canting observed in our model are potentially a consequence of frustration being relieved. Finally, the small value of the interlayer interactions confirms this material is an experimental realisation of a two-dimensional magnet.

References

1   M. Brand, S. Neaves and E. Smith, in *Museum of Electricity and Magnetism, Mag Lab U*, 1995.

2   R. Moessner and A. P. Ramirez, *Phys Today*, 2006, **59**, 24–29.

3   R. L. Comstock, *Journal of Materials Science: Materials in Electronics*, 2002, **13**, 509–523.

4   C. Mitra, *Nat Phys*, 2015, **11**, 212–213.

5   P. J. Saines, J. A. M. Paddison, P. M. M. Thygesen and M. G. Tucker, *Mater Horiz*, 2015, **2**, 528–535.

6   M. Falsaperna, G. B. G. Stenning, I. da Silva and P. J. Saines, *J Mater Chem C Mater*, 2021, **9**, 13209–13217.

7   L. Gyongyosi and S. Imre, *Comput Sci Rev*, 2019, **31**, 51–71.

8   S. Maniam, *World J Radiol*, 2010, **2**, 309–322.

9   Y.-D. Xiao, R. Paudel, J. Liu, C. Ma, Z.-S. Zhang and S.-K. Zhou, *Int J Mol Med*, 2016, **38**, 1319–1326.

10   P. Weiss, *Journal de Physique Théorique et Appliquée*, 1907, **6**, 661–690.

11   L. D. Landau, *Phys. Z. Sowjet*, 1933, **4**, 675.

12   M. L. Néel, *Ann Phys (Paris)*, 1948, **12**, 137–198.

13   T. C. Arnoldussen and E.-M. Rossi, *Annual Review of Materials Science*, 1985, **15**, 379–409.

14   P. Gomez-Romero, *Advanced Materials*, 2001, **13**, 163–174.

15   J. R. Li, R. J. Kuppler and H. C. Zhou, *Chem Soc Rev*, 2009, **38**, 1477–1504.

16   D. Britt, D. Tranchemontagne and O. M. Yaghi, *Proceedings of the National Academy of Sciences*, 2008, **105**, 11623–11627.

17   F. Monforte, M. Falsaperna, A. L. Pellegrino, C. Bongiorno, A. Motta, G. Mannino and G. G. Condorelli, *The Journal of Physical Chemistry C*, 2019, **123**, 28836–28845.

18   Y. Cui, Y. Yue, G. Qian and B. Chen, *Chem Rev*, 2012, **112**, 1126–1162.

19   Z. Hu, C. A. Tao, H. Liu, X. Zou, H. Zhu and J. Wang, *J Mater Chem A Mater*, 2014, **2**, 14222–14227.

20   D. J. Wales, J. Grand, V. P. Ting, R. D. Burke, K. J. Edler, C. R. Bowen, S. Mintova and A. D. Burrows, *Chem Soc Rev*, 2015, **44**, 4290–4321.

21   E. V. Ramos-Fernandez, M. Garcia-Domingos, J. Juan-Alcañiz, J. Gascon and F. Kapteijn, *Appl Catal A Gen*, 2011, **391**, 261–267.

22   N. V. Maksimchuk, O. V. Zalomaeva, I. Y. Skobelev, K. A. Kovalenko, V. P. Fedin and O. A. Kholdeeva, *Proceedings of the Royal Society A: Mathematical, Physical and Engineering Sciences*, 2012, **468**, 2017–2034.

23   X. Li, W. Guo, Z. Liu, R. Wang and H. Liu, *Appl Surf Sci*, 2016, **369**, 130–136.

24   X. Li, W. Guo, Z. Liu, R. Wang and H. Liu, *J Hazard Mater*, 2017, **324**, 665–672.

25   J. He, Y. Zhang, X. Zhang and Y. Huang, *Sci Rep*, 2018, **8**, 1–8.

26   M. Hoop, C. F. Walde, R. Riccò, F. Mushtaq, A. Terzopoulou, X. Z. Chen, A. J. deMello, C. J. Doonan, P. Falcaro, B. J. Nelson, J. Puigmartí-Luis and S. Pané, *Appl Mater Today*, 2018, **11**, 13–21.

27   O. K. Farha, I. Eryazici, N. C. Jeong, B. G. Hauser, C. E. Wilmer, A. A. Sarjeant, R. Q. Snurr, S. T. Nguyen, A. Ö. Yazaydın and J. T. Hupp, *J Am Chem Soc*, 2012, **134**, 15016–15021.

28   M. Falsaperna and P. J. Saines, *Dalton Transactions*, 2022, **51**, 3394–3410.

29   A. H. Olafsdottir and H. U. Sverdrup, *Biophysical Economics and Sustainability*, 2020, **5**, 1–18.

30   Y. Z. Zheng, G. J. Zhou, Z. Zheng and R. E. P. Winpenny, *Chem Soc Rev*, 2014, **43**, 1462–1475.

31   P. J. Saines and N. C. Bristowe, *Dalton Transactions*, 2018, **47**, 13257–13280.

32   M. Falsaperna and P. J. Saines, *Dalton Transactions*, 2022, **51**, 3394–3410.

33   J.-L. Liu, Y.-C. Chen and M.-L. Tong, *Chem Soc Rev*, 2018, **47**, 2431–2453.

34   S. Blundell, *Magnetism in Condensed Matter*, Oxford University Press, 1st edn., 2001.

35   R. Scatena, R. D. Johnson, P. Manuel and P. Macchi, *J Mater Chem C Mater*, 2020, **8**, 12840–12847.

36   L. Landau, *Nature*, 1936, 138, 840–841.

37   S. K. Pati and C. N. R. Rao, *Chemical Communications*, 2008, 4683.

38   C. Castelnovo, R. Moessner and S. L. Sondhi, *Annu Rev Condens Matter Phys*, 2012, **3**, 35–55.

39   C. Castelnovo, R. Moessner and S. L. Sondhi, *Nature*, 2008, **451**, 42–45.

40   M. Mekata, Y. Ajiro, T. Sugino, A. Oohara, K. Ohara, S. Yasuda, Y. Oohara and H. Yoshizawa, *J Magn Magn Mater*, 1995, **140–144**, 1987–1988.

41   K. Kakurai, R. Pynn, B. Dorner and M. Steiner, *Journal of Physics C: Solid State Physics*, 1984, **17**, L123–L128.

42   T. N. Nguyen, P. A. Lee and H.-C. zur Loye, *Science (1979)*, 1996, **271**, 489–491.

43   M. Kurmoo, *Chem Soc Rev*, 2009, **38**, 1353–1379.

44   D. Ghoshal, T. Kumar Maji, T. Mallah, T.-H. Lu, G. Mostafa and N. R. Chaudhuri, *Inorganica Chim Acta*, 2005, **358**, 1027–1033.

45   Yan Yang, Qian-Chong Zhang, Yin-Yin Pan, La-Sheng Long, Lan-Sun Zheng, Y. Yang, Q.-C. Zhang, Y.-Y. Pan, L.-S. Long and L.-S. Zheng, *Chemical Communications*, 2015, **51**, 7317–7320.

46   D. T. Tran, X. Fan, D. P. Brennan, P. Y. Zavalij and S. R. J. Oliver, *Inorg Chem*, 2005, **44**, 6192–6196.

47   D. S. Yufit, J. A. K. Howard, D. J. Price, S. O. H. Gutschke, A. K. Powell and P. T. Wood, *Chemical Communications*, 1999, **0**, 1561–1562.

48   M. Kurmoo, H. Kumagai, K. W. Chapman and C. J. Kepert, *Chemical Communications*, 2005, 3012–3014.

49   J. L. Manson, J. S. Miller, J. L. Manson, C. Campana and J. S. Miller, *Chemical Communications*, 1998, **0**, 251–252.

50   R. Feyerherm, A. Loose and J. L. Manson, *Journal of Physics: Condensed Matter*, 2003, **15**, 663–673.

51   R. J. C. Dixey, F. Orlandi, P. Manuel, P. Mukherjee, S. E. Dutton and P. J. Saines, *Philosophical Transactions of the Royal Society A: Mathematical, Physical and Engineering Sciences*, 2019, **377**, 20190007.

52   A. E. Thorarinsdottir and T. D. Harris, *Chem Rev*, 2020, **120**, 8716–8789.

53   G. Lorusso, J. W. Sharples, E. Palacios, O. Roubeau, E. K. Brechin, R. Sessoli, A. Rossin, F. Tuna, E. J. L. L. McInnes, D. Collison and M. Evangelisti, *Advanced Materials*, 2013, **25**, 4653–4656.

54   D. R. Harcombe, P. G. Welch, P. Manuel, P. J. Saines and A. L. Goodwin, *Phys Rev B*, 2016, **94**, 174429.

55   R. J. C. Dixey, P. Manuel, F. Orlandi, P. Mukherjee, S. E. Dutton, G. B. G. Stenning and P. J. Saines, *J Mater Chem C Mater*, 2020, **8**, 12123–12132.

56   R. Dixey, University of Kent, 2020.

57   J.-L. Dupont, P. Domasnki, P. Lebrun and F. Ziegler, *38th Informatory Note on Refrigeration Technologies*, 2019.

58   S. A. Tassou, J. S. Lewis, Y. T. Ge, A. Hadawey and I. Chaer, *Appl Therm Eng*, 2010, **30**, 263–276.

59   L. P. Ichkitidze, N. A. Bazaev, D. V. Telyshev, R. Y. Preobrazhensky and M. L. Gavrushina, *Biomed Eng (NY)*, 2015, **48**, 305–309.

60   J. C. Doane and H. D. Stein, *J Int Coll Surg*, 1951, **16**, 346—349.

61   O. Sari and M. Balli, *International Journal of Refrigeration*, 2014, **37**, 8–15.

62   V. Franco, J. S. Blázquez, B. Ingale and A. Conde, *Annu Rev Mater Res*, 2012, **42**, 305–342.

63   J. F. Scott, *Annu Rev Mater Res*, 2011, **41**, 229–240.

64   P. F. Liu, J. L. Wang, X. J. Meng, J. Yang, B. Dkhil and J. H. Chu, *New J Phys*, 2010, **12**, 023035.

65   G. G. Wiseman and J. K. Kuebler, *Physical Review*, 1963, **131**, 2023–2027.

66   W. N. Lawless, *Phys Rev B*, 1977, **16**, 433–439.

67   H.-X. Cao and Z.-Y. Li, *J Appl Phys*, 2009, **106**, 094104.

68   W. N. Lawless and A. J. Morrow, *Ferroelectrics*, 1977, **15**, 159–165.

69   I. N. Flerov and E. A. Mikhaleva, *Physics of the Solid State*, 2008, **50**, 478–484.

70   S. Qian, Y. Geng, Y. Wang, J. Ling, Y. Hwang, R. Radermacher, I. Takeuchi and J. Cui, *International Journal of Refrigeration*, 2016, **64**, 1–19.

71   J. Tušek, K. Engelbrecht, R. Millán-Solsona, L. Mañosa, E. Vives, L. P. Mikkelsen and N. Pryds, *Adv Energy Mater*, 2015, **5**, 1500361.

72   K. Otsuka and C. M. Wayman, *Shape memory materials*, Cambridge University Press, First Edition., 1998.

73   C. M. Miliante, A. M. Christmann, E. O. Usuda, W. Imamura, L. S. Paixão, A. M. G. Carvalho and A. R. Muniz, *Macromolecules*, 2020, **53**, 2606–2615.

74   S. Crossley, N. D. Mathur and X. Moya, *AIP Adv*, 2015, **5**, 067153.

75   L. Mañosa and A. Planes, *Advanced Materials*, 2017, 29, 1603607.

76   C. Cazorla, *Appl Phys Rev*, 2019, **6**, 041316.

77   W. Imamura, É. O. Usuda, L. S. Paixão, N. M. Bom, A. M. Gomes and A. M. G. Carvalho, *Chinese Journal of Polymer Science*, 2020, **38**, 999–1005.

78   A. M. G. Carvalho, W. Imamura, E. O. Usuda and N. M. Bom, *Eur Polym J*, 2018, **99**, 212–221.

79   E. O. Usuda, N. M. Bom and A. M. G. Carvalho, *Eur Polym J*, 2017, **92**, 287–293.

80   N. M. Bom, W. Imamura, E. O. Usuda, L. S. Paixão and A. M. G. Carvalho, *ACS Macro Lett*, 2017, **7**, 31–36.

81   B. Li, Y. Kawakita, S. Ohira-Kawamura, T. Sugahara, H. Wang, J. Wang, Y. Chen, S. I. Kawaguchi, S. Kawaguchi, K. Ohara, K. Li, D. Yu, R. Mole, T. Hattori, T. Kikuchi, S. Yano, Z. Zhang, Z. Zhang, W. Ren, S. Lin, O. Sakata, K. Nakajima and Z. Zhang, *Nature*, 2019, **567**, 506–510.

82   L. Mañosa, D. González-Alonso, A. Planes, E. Bonnot, M. Barrio, J.-L. Tamarit, S. Aksoy and M. Acet, *Nat Mater*, 2010, **9**, 478–481.

83   J. M. Bermúdez-García, M. Sánchez-Andújar, S. Yáñez-Vilar, S. Castro-García, R. Artiaga, J. López-Beceiro, L. Botana, Á. Alegría and M. A. Señarís-Rodríguez, *Inorg Chem*, 2015, **54**, 11680–11687.

84   J. M. Bermúdez-García, M. Sánchez-Andújar, S. Castro-García, J. López-Beceiro, R. Artiaga and M. A. Señarís-Rodríguez, *Nat Commun*, 2017, **8**, 15715.

85   J. M. Bermúdez-García, S. Yáñez-Vilar, A. García-Fernández, M. Sánchez-Andújar, S. Castro-García, J. López-Beceiro, R. Artiaga, M. Dilshad, X. Moya and M. A. Señarís-Rodríguez, *J Mater Chem C Mater*, 2018, **6**, 9867–9874.

86   J. Salgado-Beceiro, A. Nonato, R. X. Silva, A. García-Fernández, M. Sánchez-Andújar, S. Castro-García, E. Stern-Taulats, M. A. Señarís-Rodríguez, X. Moya and J. M. Bermúdez-García, *Mater Adv*, 2020, **1**, 3167–3170.

87   E. Warburg, *Ann Phys*, 1881, **249**, 141–164.

88   P. Weiss and A. Piccard, *Comptes Rendus*, 1918, **166**, 352–354.

89   A. Waske, M. E. Gruner, T. Gottschall and O. Gutfleisch, *MRS Bull*, 2018, **43**, 269–273.

90   C. Zimm, A. Jastrab, A. Sternberg, V. Pecharsky, K. Gschneidner, M. Osborne and I. Anderson, in *Advances in Cryogenic Engineering*, Springer US, Boston, MA, 1998, pp. 1759–1766.

91   K. A. Gschneidner and V. K. Pecharsky, *International Journal of Refrigeration*, 2008, **31**, 945–961.

92   V. K. Pecharsky and K. A. Gschneidner, *Phys Rev Lett*, 1997, **78**, 4494–4497.

93   U. Cardella, L. Decker and H. Klein, *Int J Hydrogen Energy*, 2017, **42**, 13329–13338.

94   P. Martin, A. S. Royet, F. Guellec and G. Ghibaudo, *Solid State Electron*, 2011, **62**, 115–122.

95   A. Cho, *Science (1979)*, 2009, **326**, 778–779.

96   V. K. Pecharsky and K. A. Gschneidner Jr, *J Magn Magn Mater*, 1999, **200**, 44–56.

97   I. Niknia, P. V. Trevizoli, T. V. Christiaanse, P. Govindappa, R. Teyber and A. Rowe, *J Appl Phys*, 2017, **121**, 064902.

98   A. Giguère, M. Foldeaki, B. Ravi Gopal, R. Chahine, T. K. Bose, A. Frydman and J. A. Barclay, *Phys Rev Lett*, 1999, **83**, 2262–2265.

99   V. K. Pecharsky and K. A. Gschneidner, *J Appl Phys*, 1999, **86**, 565–575.

100   A. M. Tishin, *J Alloys Compd*, 1997, **250**, 635–641.

101   M. Evangelisti and E. K. Brechin, *Dalton Transactions*, 2010, **39**, 4672–4676.

102   N. R. Ram, M. Prakash, U. Naresh, N. S. Kumar, T. S. Sarmash, T. Subbarao, R. J. Kumar, G. R. Kumar and K. C. B. Naidu, *J Supercond Nov Magn*, 2018, **31**, 1971–1979.

103   K. A. Gschneidner and V. K. Pecharsky, *Annual Review of Materials Science*, 2000, **30**, 387–429.

104   Y. Mozharivskyj, *Magnetocaloric Effect and Magnetocaloric Materials*, Elsevier Inc., 2016.

105   S. R. Batten, N. R. Champness, X.-M. Chen, J. Garcia-Martinez, S. Kitagawa, L. Öhrström, M. O'Keeffe, M. P. Suh and J. Reedijk, *CrystEngComm*, 2012, **14**, 3001.

106   A. P. Ramirez, *Annual Review of Materials Science*, 1994, **24**, 453–480.

107   M. Mekata, *Phys Today*, 2003, **56**, 12–13.

108   S. S. Sosin, L. A. Prozorova, A. I. Smirnov, A. I. Golov, I. B. Berkutov, O. A. Petrenko, G. Balakrishnan and M. E. Zhitomirsky, *Phys Rev B*, 2005, **71**, 094413.

109   O. A. Petrenko, D. M. Paul, C. Ritter, T. Zeiske and M. Yethiraj, *Physica B Condens Matter*, 1999, **266**, 41–48.

110   E. Palacios, J. A. Rodríguez-Velamazán, M. Evangelisti, G. J. McIntyre, G. Lorusso, D. Visser, L. J. de Jongh and L. A. Boatner, *Phys Rev B*, 2014, **90**, 214423.

111   D. F. Mullica, D. A. Grossie and L. A. Boatner, *Inorganica Chim Acta*, 1985, **109**, 105–110.

112   Y. Han, S.-D. Han, J. Pan, Y.-J. Ma and G.-M. Wang, *Mater Chem Front*, 2018, **2**, 2327–2332.

113   R. A. Zehnder, C. S. Wilson, H. T. Christy, K. S. Harris, V. Chauhan, V. Schutz, M. Sullivan, M. Zeller, F. R. Fronczek, J. A. Myers, K. Dammann, J. Duck, P. M. Smith, A. Okuma, K. Johnson, R. Sovesky, C. Stroudt and R. A. Renn, *Inorg Chem*, 2011, **50**, 836–846.

114   B. Daudin, R. Lagnier and B. Salce, *J Magn Magn Mater*, 1982, **27**, 315–322.

115   P. Mukherjee, Y. Wu, G. I. Lampronti and S. E. Dutton, *Mater Res Bull*, 2018, **98**, 173–179.

116   L. C. Chapon, P. Manuel, F. Damay, P. Toledano, V. Hardy and C. Martin, *Phys Rev B*, 2011, **83**, 024409.

117   A. I. Smirnov, L. E. Svistov, L. A. Prozorova, A. Zheludev, M. D. Lumsden, E. Ressouche, O. A. Petrenko, K. Nishikawa, S. Kimura, M. Hagiwara, K. Kindo, A. Ya. Shapiro and L. N. Demianets, *Phys Rev Lett*, 2009, **102**, 037202.

118   T. Tahara, I. Nakai, R. Miyawaki and S. Matsubara, *Zeitschrift für Kristallographie*, 2007, **222**, 326–334.

119   Y.-C. Chen, L. Qin, Z.-S. Meng, D.-F. Yang, C. Wu, Z. Fu, Y.-Z. Zheng, J.-L. Liu, R. Tarasenko, M. Orendáč, J. Prokleška, V. Sechovský and M.-L. Tong, *J. Mater. Chem. A*, 2014, **2**, 9851–9858.

120   R. J. C. Dixey and P. J. Saines, *Inorg Chem*, 2018, **57**, 12543–12551.

121   R. J. C. Dixey, G. B. G. Stenning, P. Manuel, F. Orlandi and P. J. Saines, *J Mater Chem C Mater*, 2019, **7**, 13111–13119.

122   Y.-L. Hou, G. Xiong, P.-F. Shi, R.-R. Cheng, J.-Z. Cui and B. Zhao, *Chemical Communications*, 2013, **49**, 6066–6068.

123   F.-S. Guo, J.-D. Leng, J.-L. Liu, Z.-S. Meng and M.-L. Tong, *Inorg Chem*, 2012, **51**, 405–413.

124   G. Lorusso, M. A. Palacios, G. S. Nichol, E. K. Brechin, O. Roubeau and M. Evangelisti, *Chemical Communications*, 2012, **48**, 7592–7594.

125   Y. Meng, Y.-C. Chen, Z.-M. Zhang, Z.-J. Lin and M.-L. Tong, *Inorg Chem*, 2014, **53**, 9052–9057.

126   S.-J. Liu, C. Cao, S.-L. Yao, T.-F. Zheng, Z.-X. Wang, C. Liu, J.-S. Liao, J.-L. Chen, Y.-W. Li and H.-R. Wen, *Dalton Transactions*, 2017, **46**, 64–70.

127   Y.-C. Chen, F.-S. Guo, Y.-Z. Zheng, J.-L. Liu, J.-D. Leng, R. Tarasenko, M. Orendáč, J. Prokleška, V. Sechovský and M.-L. Tong, *Chemistry - A European Journal*, 2013, **19**, 13504–13510.

128   S.-J. Liu, C.-C. Xie, J.-M. Jia, J.-P. Zhao, S.-D. Han, Y. Cui, Y. Li and X.-H. Bu, *Chem Asian J*, 2014, **9**, 1116–1122.

129   S. Biswas, A. Adhikary, S. Goswami and S. Konar, *Dalton Transactions*, 2013, **42**, 13331–13334.

130   R. Sibille, T. Mazet, B. Malaman and M. François, *Chemistry - A European Journal*, 2012, **18**, 12970–12973.

131   V. Zeleňák, M. Almáši, A. Zeleňáková, P. Hrubovčák, R. Tarasenko, S. Bourelly and P. Llewellyn, *Sci Rep*, 2019, **9**, 15572–15580.

132   L.-H. Xie, Y. Wang, X.-M. Liu, J.-B. Lin, J.-P. Zhang and X.-M. Chen, *CrystEngComm*, 2011, **13**, 5849–5857.

133   F. Liu, H. Huang, W. Gao, X.-M. Zhang and J.-P. Liu, *CrystEngComm*, 2017, **19**, 3660–3665.

134   M. Kumar, L.-H. Wu, M. Kariem, A. Franconetti, H. N. Sheikh, S.-J. Liu, S. C. Sahoo and A. Frontera, *Inorg Chem*, 2019, **58**, 7760–7774.

135   C.-B. Tian, R.-P. Chen, C. He, W.-J. Li, Q. Wei, X.-D. Zhang and S.-W. Du, *Chem. Commun*, 2014, **50**, 1915–1917.

136   Y. Y. Pan, Y. Yang, L. S. Long, R. Bin Huang and L. S. Zheng, *Inorg Chem Front*, 2014, **1**, 649–652.

137   T. K. Prasad, M. V. Rajasekharan and J.-P. Costes, *Angewandte Chemie International Edition*, 2007, **46**, 2851–2854.

138   F. S. Guo, Y. C. Chen, J. L. Liu, J. D. Leng, Z. S. Meng, P. Vrábel, M. Orendác, M. L. Tong, M. Orendáč and M. L. Tong, *Chemical Communications*, 2012, **48**, 12219–12221.

139   P.-F. Shi, C.-S. Cao, C.-M. Wang and B. Zhao, *Inorg Chem*, 2017, **56**, 9169–9176.

140   C. Kittipong, P. Khemthong, F. Kielar and Y. Zhou, *Acta Crystallogr E Crystallogr Commun*, 2016, **72**, 87–91.

141   W. Clegg, *X-ray crystallography* , Oxford University Press, Second Edition., 2015.

142   C. Kittel, *Introduction to Solid State Physics*, Wiley, Eighth Edition., 2005.

143   D. A. Skoog and D. M. West, *Principles of instrumental analysis*, Saunders College, Second Edition., 1980.

144   *CrysAlisPRO, Oxford Diffraction /Agilent Technologies UK Ltd, Yarnton, England.*

145   G. M. Sheldrick, *Acta Cryst. A*, 2008, **64**, 112–122.

146   G. M. Sheldrick, *Acta Cryst. C*, 2015, **71**, 3–8.

147   O. V. Dolomanov, L. J. Bourhis, R. J. Gildea, J. A. K. Howard and H. Puschmann, *J Appl Crystallogr*, 2009, **42**, 339–341.

148   J. W. G. Thomason, *Nucl Instrum Methods Phys Res A*, 2019, **917**, 61–67.

149   D. S. Sivia, *Elementary Scattering Theory : For X-ray and Neutron Users*, Oxford University Press, 2011.

150   J. W. G. W. G. Thomason, *Nucl Instrum Methods Phys Res A*, 2019, **917**, 61–67.

151   M. M. White, *AIP Conf Proc*, 2002, **613**, 15–24.

152   S. Nagamiya, *Progress of Theoretical and Experimental Physics*, 2012, **2012**, 02B001.

153   M. Lindroos, S. Bousson, R. Calaga, H. Danared, G. Devanz, R. Duperrier, J. Eguia, M. Eshraqi, S. Gammino, H. Hahn, A. Jansson, C. Oyon, S. Pape-Møller, S. Peggs, A. Ponton, K. Rathsman, R. Ruber, T. Satogata and G. Trahern, *Nucl Instrum Methods Phys Res B*, 2011, **269**, 3258–3260.

154   E. Prince, *International Tables for Crystallography Volume C: Mathematical, physical and chemical tables*, Springer Dordrecht, Chester, England, 3rd edn., 2004.

155   P.   J.   Brown,   Magnetic   Form   Factors,
       https://www.ill.eu/sites/ccsl/ffacts/ffachtml.html.

156   W. G. Williams, R. M. Ibberson, P. Day and J. E. Enderby, *Physica B Condens Matter*, 1997, **241–243**, 234–236.

157   A. J. Studer, M. E. Hagen and T. J. Noakes, *Physica B Condens Matter*, 2006, **385–386**, 1013–1015.

158   L. C. Chapon, P. Manuel, P. G. Radaelli, C. Benson, L. Perrott, S. Ansell, N. J. Rhodes, D. Raspino, D. Duxbury, E. Spill and J. Norris, *Neutron News*, 2011, **22**, 22–25.

159   H. M. Rietveld, *J Appl Crystallogr*, 1969, **2**, 65–71.

160   A. Le Bail, H. Duroy and J. L. Fourquet, *Mater Res Bull*, 1988, **23**, 447–452.

161   A. Le Bail, *Powder Diffr*, 2005, **20**, 316–326.

162   R. J. Hill, *Powder Diffr*, 1991, **6**, 74–77.

163   L. B. McCusker, R. B. Von Dreele, D. E. Cox, D. Louër and P. Scardi, *J Appl Crystallogr*, 1999, **32**, 36–50.

164   B. H. Toby, *Powder Diffr*, 2008, **21**, 67–70.

165   T. J. Rivlin, *Chebyschev Polynomials: From Approximation Theory to Algebra and Number Theory*, John Wiley and Sons, 1990.

166   L. W. Finger, D. E. Cox and A. P. Jephcoat, *J Appl Crystallogr*, 1994, **27**, 892–900.

167   G. Caglioti, A. Paoletti and F. P. Ricci, *Nuclear Instruments*, 1958, **3**, 223–228.

168   R. B. Von Dreele, J. D. Jorgensen and C. G. Windsor, *J Appl Crystallogr*, 1982, **15**, 581–589.

169   J. Rodríguez-Carvajal, *Physica B Condens Matter*, 1993, **192**, 55–69.

170   B. Hunter, *AINSE Symposium on Neutron Scattering Powder Diffraction; Australian Neutron Beam users group meeting*, 2000, **31**, 20.

171   B. H. Toby, *J Appl Crystallogr*, 2001, **34**, 210–213.

172   B. D. Josephson, *Physics Letters*, 1962, **1**, 251–253.

173   B. D. Josephson, *Rev Mod Phys*, 1964, **36**, 216–220.

174   C. E. Gough, in *Physics of High-Temperature Superconductors*, Springer, Berlin, Heidelberg, 1992, pp. 423–436.

175   P. Debye, *Ann Phys*, 1912, **344**, 789–839.

176   M. Henini, *III-Vs Review*, 2000, **13**, 40–44.

177   J. E. Chalmers, A. K. Srivastava, R. J. C. Dixey, K. Sivakumaran and P. J. Saines, *CrystEngComm*, 2019, **21**, 894–901.

178   S. Romero, A. Mosset and J. C. Trombe, *J. Solid State Chem.*, 1996, **127**, 256–266.

179   J. C. Tan, J. D. Furman and A. K. Cheetham, *J Am Chem Soc*, 2009, **131**, 14252–14254.

180   A. K. Cheetham, C. N. R. Rao and R. K. Feller, *Chemical Communications*, 2006, 4780–4795.

181   L. G. Burley, J. H. Beecham-Lonsdale, A. K. Srivastava, I. E. Collings and P. J. Saines, *Dalton Transactions*, 2021, **50**, 5437–5441.

182   A. Pabst, *J Chem Phys*, 1943, **11**, 145–149.

183   B. C. Melot, J. E. Drewes, R. Seshadri, E. M. Stoudenmire and A. P. Ramirez, *Journal of Physics: Condensed Matter*, 2009, **21**, 216007.

184   P. Mukherjee and S. E. Dutton, *Adv Funct Mater*, 2017, **27**, 1–7.

185   N. D. Kelly and S. E. Dutton, *Inorg Chem*, 2020, **59**, 9188–9195.

186   S.-D. Han, X.-H. Miao, S.-J. Liu and X.-H. Bu, *Chem Asian J*, 2014, **9**, 3116–3120.

187   P. J. von Ranke, V. K. Pecharsky, K. A. Gschneidner and B. J. Korte, *Phys Rev B*, 1998, **58**, 14436–14441.

188   J. A. Barclay and W. A. Steyert, *Cryogenics (Guildf)*, 1982, **22**, 73–80.

189   T. Krenke, E. Duman, M. Acet, E. F. Wassermann, X. Moya, L. Mañosa and A. Planes, *Nat Mater*, 2005, **4**, 450–454.

190   N. D. Kelly, C. Liu and S. E. Dutton, *J Solid State Chem*, 2020, **292**, 121640.

191   Q.-F. Xu, B.-L. Liu, M.-Y. Ye, L.-S. Long and L.-S. Zheng, *Inorg Chem*, 2021, **60**, 9259–9262.

192   R. D. Shannon, *Acta Crystallographica Section A*, 1976, **A32**, 751–767.

193   G. B. Martins, M. Laukamp, J. Riera, E. Dagotto, G. Balster Martins, M. Laukamp, J. Riera and E. Dagotto, *Phys Rev Lett*, 1997, **78**, 3563–3566.

194   A. Zorko, D. Arčon, A. Lappas and Z. Jagličić, *New J Phys*, 2006, **8**, 60–60.

195   J. Das, A. V. Mahajan, J. Bobroff, H. Alloul, F. Alet and E. S. Sørensen, *Phys Rev B*, 2004, **69**, 144404.

196   T. I. Arbuzova, I. B. Smolyak, S. V. Naumov and A. A. Samokhvalov, *Physics of the Solid State*, 1998, **40**, 1702–1705.

197   I. Kruk, J. E. L. Waldron and M. A. Green, *Inorganics (Basel)*, 2019, **7**, 66–77.

198   E. C. Heltemes and C. A. Swenson, *J Chem Phys*, 1961, **35**, 1264–1265.

199   D. Neogy and A. Chatterji, *J Chem Phys*, 1978, **68**, 5647–5652.

200   D. Neogy, P. Paul and K. N. Chattopadhyay, *J Magn Magn Mater*, 2004, **283**, 164–170.

201   R. Tlili, A. Omri, M. Bekri, M. Bejar, E. Dhahri and E. K. Hlil, *J Magn Magn Mater*, 2016, **399**, 143–148.

202   R. Bellouz, M. Oumezzine, E. K. Hlil and E. Dhahri, *J Magn Magn Mater*, 2015, **375**, 136–142.

203   Mat. Orendáč, P. Farkašovský, L. Regeciová, S. Gabáni, G. Pristáš, E. Gažo, J. Bačkai, P. Diko, A. Dukhnenko, N. Shitsevalova, K. Siemensmeyer and K. Flachbart, *Phys Rev B*, 2020, **102**, 174422.

204   K. Wang, J. Wan, Y. Xiang, J. Zhu, Q. Leng, M. Wang, L. Xu and Y. Yang, *J Power Sources*, 2020, **460**, 228062.

205   S. Manzetti and F. Mariasiu, *Renewable and Sustainable Energy Reviews*, 2015, **51**, 1004–1012.

206   C. Banza Lubaba Nkulu, L. Casas, V. Haufroid, T. De Putter, N. D. Saenen, T. Kayembe-Kitenge, P. Musa Obadia, D. Kyanika Wa Mukoma, J.-M. Lunda Ilunga, T. S. Nawrot, O. Luboya Numbi, E. Smolders and B. Nemery, *Nat Sustain*, 2018, **1**, 495–504.

207 E. Mossali, N. Picone, L. Gentilini, O. Rodrìguez, J. M. Pérez and M. Colledani, *J Environ Manage*, 2020, **264**, 110500.

208 Science Foundation Ireland, LiCoRICE, https://www.sfi.ie/challenges/zero-emissions/licorice/.

209 D.Z.T. Mulrooney, University College Dublin, 2021.

210 N. E. Brese and M. O'Keeffe, *Acta Crystallogr B*, 1991, **47**, 192–197.

211 X. H. Liu, W. Liu, W. J. Hu, S. Guo, X. K. Lv, W. B. Cui, X. G. Zhao and Z. D. Zhang, *Appl Phys Lett*, 2008, **93**, 202502.

212 A. D. Fortes and I. G. Wood, *Powder Diffr*, 2012, **27**, 8–11.

213 Stokes, H.T., D. M. Hatch and B. J. Campbel, ISODISTORT, ISOTROPY Software Suite, iso.byu.edu.

214 B. J. Campbell, H. T. Stokes, D. E. Tanner and D. M. Hatch, *J Appl Crystallogr*, 2006, **39**, 607–614.

215 A. A. Coelho, *J Appl Crystallogr*, 2018, **51**, 210–218.

216 M. McElfresh, *Fundamentals of Magnetism and Magnetic Measurements*, Quantum Design Technical Document, 1994.

Appendix A

Discrepancy Terms in Refinements

The most used and straightforward of these discrepancy terms is the weighted profile R-factor, R_{wp}, with "R" standing for "reliability". It is obtained by simply considering the square root of the minimised quantity scaled by the weighted observed intensities, so that Eqn. 2.18 becomes:

$$R_{wp} = \sqrt{\frac{\sum w_i \big(y_i(calc) - y_i(obs)\big)^2}{\sum w_i [y_i(obs)]^2}}. \qquad (A.1)$$

A simpler profile R-factor, R_p, simply ignores the weights w_i:

$$R_p = \frac{\sum y_i(calc) - y_i(obs)}{\sum y_i(obs)}. \qquad (A.2)$$

If we assume an ideal model can be achieved, the calculated intensities $y_i(calc)$ represent the "true" values of the observed intensities $y_i(obs)$, therefore the quantity $(y_i(calc) - y_i(obs))^2$ will be equal to the estimated uncertainty $\sigma[y_i(obs)]$, and the numerator in Eqn. 2.19 becomes one. This leads to another important term, the expected R-factor, R_{exp}, which corresponds to the best R_{wp} that can be obtained while fitting the data in such an ideal situation, the only difference left being the intrinsic uncertainty from data collection. This term is expressed as:

$$R_{exp}^2 = \frac{N - P}{\sum w_i \big(y_i(obs)\big)^2}, \qquad (A.3)$$

with N being the number of data points in the diffraction pattern and P the number of parameters used in the refinement, the numerator then representing, statistically, the degrees of freedom. Essentially, R_{exp}, can be thought as an estimate of the quality of the data itself.

Another important discrepancy term used to estimate the quality of the fit is that of chi-squared, χ^2:

$$\chi^2 = \frac{1}{N} \sum \frac{y_i(calc) - y_i(obs)^2}{\sigma^2[y_i(obs)]}, \qquad\qquad (A.4)$$

which, for similar consideration as for R_{exp}, should ideally be unitary, *i.e.* $\chi^2 = 1$. In practice, however, this is not possible, and χ^2 can only approach unity the better the fit. At the beginning of the refinements, χ^2 tends to assume very large values due to the high discrepancy between the starting model and the data against which it is refined, and ideally χ^2 should never increase during a least-squares refinement. In practice, small increases can occur when the parameters being refined are correlated to one another. It must also be noted that under no circumstance should chi-squared drop to values below one, as $\chi^2 < 1$ would imply that the fit is better than the uncertainty $\sigma[y_i(obs)]$ itself. This in turn implies that either the $\sigma[y_i(obs)]$ are overestimated or the refinement algorithm is attempting to fit noise in the powder pattern.

Other discrepancy terms can be defined. These are the intensity and the structure factor R-factors, R_I and R_F, which are often used during the refinements of structure models against single-crystal diffraction data, but these won't be discussed further.

Components of the MPMS instrument

Along with the main components described for the MPMS system in Chapter 3, the following components are also present:[216]

- **Temperature control system**: controls the temperature of the sample and the cooling, guaranteeing

- **Magnetic field control system**: coordinates the current in the magnetic solenoid – responsible for the generation of the magnetic field and made of a superconducting NbTi alloy submerged in liquid helium – and the component known as the Quick Switch, which enables an electric current to be supplied to the solenoid according to its temperature. When the Quick Switch is at sufficiently low temperatures, it becomes superconducting and a short results, cutting the voltage supply to the solenoid. This makes the produced magnetic field very stable.

- **Motion control system**: allows for the movement of the sample within the sample chamber and through the detector without mechanical vibrations which may affect the measurement.

- **Chamber atmosphere control system**: ensures the sample chamber and the sample transport are held in a medium vacuum of ~10 Torr at room temperature. Reducing the gas pressure enables the sample and the sample chamber wall to achieve a uniform temperature. It is important that the chamber and the transport are cooled using liquid helium as the presence of oxygen, nitrogen, carbon dioxide, water and other atmospheric contaminants will freeze when cooling below room temperature in such a vacuum.

- **Cryogen monitoring system**: monitors the level of liquid helium.

Appendix B

Table B.1: Selected bond distances for Ho(HCO$_2$)(C$_2$O$_4$) collected at 120 K

	Distance (Å)
Ho1-O1	2.391(3)
Ho1-O1	2.451(3)
Ho1-O2	2.402(3)
Ho1-O3	2 × 2.390(2)
Ho1-O4	2 × 2.413(2)
Ho1-O4	2 × 2.437(2)
O1-C1	1.269(6)
O2-C1	1.228(6)
O3-C2	1.242(4)
O4-C2	1.261(4)

Table B.2: Selected bond distances for Er(HCO$_2$)(C$_2$O$_4$) collected at 120 K.

	Distance (Å)
Er1-O1	2.379(4)
Er1-O1	2.439(4)
Er1-O2	2.386(4)
Er1-O3	2 × 2.380(3)
Er1-O4	2 × 2.406(3)
Er1-O4	2 × 2.422(3)
O1-C1	1.279(7)
O2-C1	1.225(8)
O3-C2	1.239(5)
O4-C2	1.269(5)

Table B.3: Crystallographic details of Tb(HCO$_2$)(C$_2$O$_4$) obtained from neutron diffraction patterns collected at 20 K. Final total refinement statistics R$_p$ and R$_{wp}$ were 2.02 % and 2.79 %, respectively.

Space Group	a (Å)	b (Å)	c (Å)	Volume (Å^3)	
Pnma	7.02827(12)	10.56945(18)	6.59041(11)	489.57(2)	
Site	**x**	**y**	**z**	**U$_{iso}$(Å^2)**	**Fractional Occupancy**
Tb	0.20348	3/4	0.64422	-0.00154(14)	1
O1	0.53581(15)	3/4	0.53670(19)	-0.0013(2)	1
O2	0.5537(2)	3/4	0.19622(18)	0.0035(3)	1
O3	0.23952(13)	0.54446(8)	0.48093(12)	0.00219(16)	1
O4	0.08759(12)	0.37633(8)	0.34904(15)	0.00139(16)	1
C1	0.62361(15)	3/4	0.37314(18)	-0.00040(19)	1
C2	0.09602(12)	0.47884(6)	0.45179(11)	0.0079(14)	1
D	0.7793(2)	3/4	0.3794(2)	0.0193(5)	1

Table B.4: Crystallographic details of Tb(HCO$_2$)(C$_2$O$_4$) obtained from neutron diffraction patterns collected at 1.6 K. Final total refinement statistics R$_p$ and R$_{wp}$ were 1.78 % and 2.33 %, respectively.

Space Group	a (Å)	b (Å)	c (Å)	Volume (Å^3)	
Pnma	7.02786(7)	10.56956(9)	6.59095(6)	489.585(5)	
Site	**x**	**y**	**z**	**U$_{iso}$(Å^2)**	**Fractional Occupancy**
Tb	0.20348	3/4	0.63422	-0.00226(11)	1
O1	0.53412(13)	3/4	0.53750(16)	-0.00014(18)	1
O2	0.55451(17)	3/4	0.19809(15)	0.0027(2)	1
O3	0.23976(11)	0.54461(7)	0.48073(10)	0.00123(12)	1
O4	0.08744(10)	0.37650(6)	0.35105(12)	0.00055(12)	1
C1	0.62398(13)	3/4	0.37206(16)	0.00114(17)	1
C2	0.09633(10)	0.47893(5)	0.45247(9)	0.00007(11)	1
D	0.77909(17)	3/4	0.3773(2)	0.0220(3)	1

Table B.5: Crystallographic details of Ho(HCO$_2$)(C$_2$O$_4$) obtained from neutron diffraction patterns collected at 20 K. Final total refinement statistics R$_p$ and R$_{wp}$ were 2.00 % and 2.54 %, respectively.

Space Group	*a* (Å)	*b* (Å)	*c* (Å)	Volume (Å^3)	
Pnma	6.95296(11)	10.50898(17)	6.54600(10)	478.307(18)	
Site	**x**	**y**	**z**	**U$_{iso}$(Å^2)**	**Fractional Occupancy**
Ho	0.20113	¼	0. 36659	-0.00362(10)	1
O1	0.08872(12)	0.62483(7)	0.64957(14)	0.00059(10)	1
O2	0.24191(12)	0.45439(8)	0.52021(12)	0.00059(10)	1
O3	0.5531(2)	1/4	0.80342(17)	0.00097(14)	1
O4	0.53296(16)	1/4	0.46215(19)	0.00097(14)	1
C1	0.09695(11)	0.52101(6)	0.54860(10)	-0.00021(10)	1
C2	0.62232(16)	1/4	0.62810(18)	-0.00021(10)	1
D	0.7800(2)	1/4	0.6222(2)	0.0241(4)	1

Table B.6: Crystallographic details of Ho(HCO$_2$)(C$_2$O$_4$) obtained from neutron diffraction patterns collected at 1.6 K. Final total refinement statistics R$_p$ and R$_{wp}$ were 2.11 % and 2.93 %, respectively.

| Space Group	*a* (Å)	*b* (Å)	*c* (Å)	Volume (Å^3)	
Pnma	6.95346(9)	10.50704(12)	6.54620(7)	478.267(7)	
Site	**x**	**y**	**z**	**U$_{iso}$(Å^2)**	**Fractional Occupancy**
Ho	0.20113	1/4	0.36659	-0.00354(12)	1
O1	0.08872(13)	0.62480(8)	0.64964(16)	0.00052(11)	1
O2	0.24198(14)	0.45426(9)	0.52040(13)	0.00052(11)	1
O3	0.55321(23)	1/4	0.8034(2)	0.00102(16)	1
O4	0.53300(18)	1/4	0.4619(2)	0.00102(16)	1
C1	0.09696(13)	0.52098(7)	0.54850(12)	-0.000023(11)	1
C2	0.62227(18)	1/4	0.6279(2)	-0.000023(11)	1
D	0.7800(2)	1/4	0.6220(3)	0.0242(4)	1
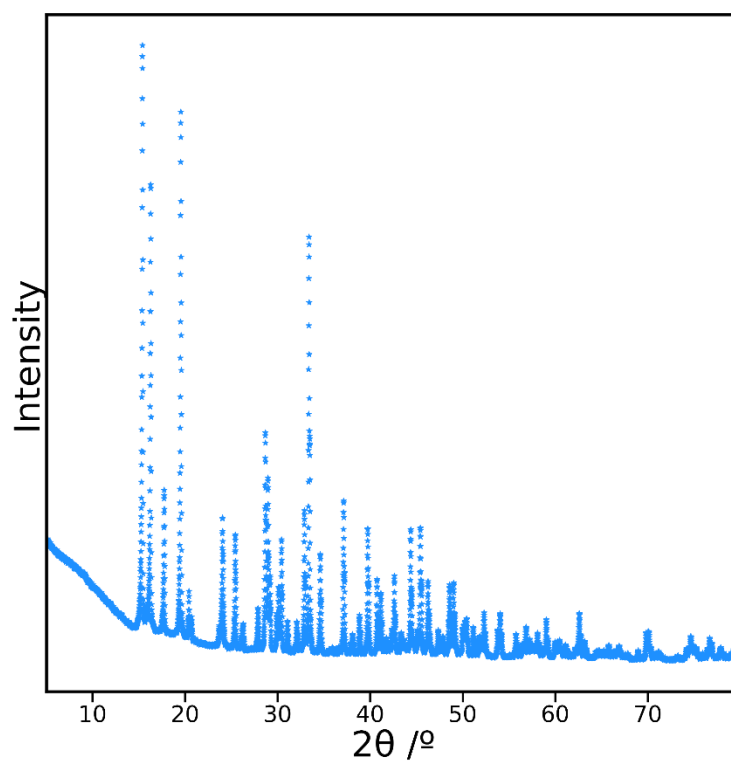
Figure B.1: Conventional powder X-ray diffraction pattern of a sample obtained from the unsuccessful synthesis of $La(HCO_2)(C_2O_4)$, measured using a Cu source ($\lambda = 1.54$ Å). The phase has not been identified.
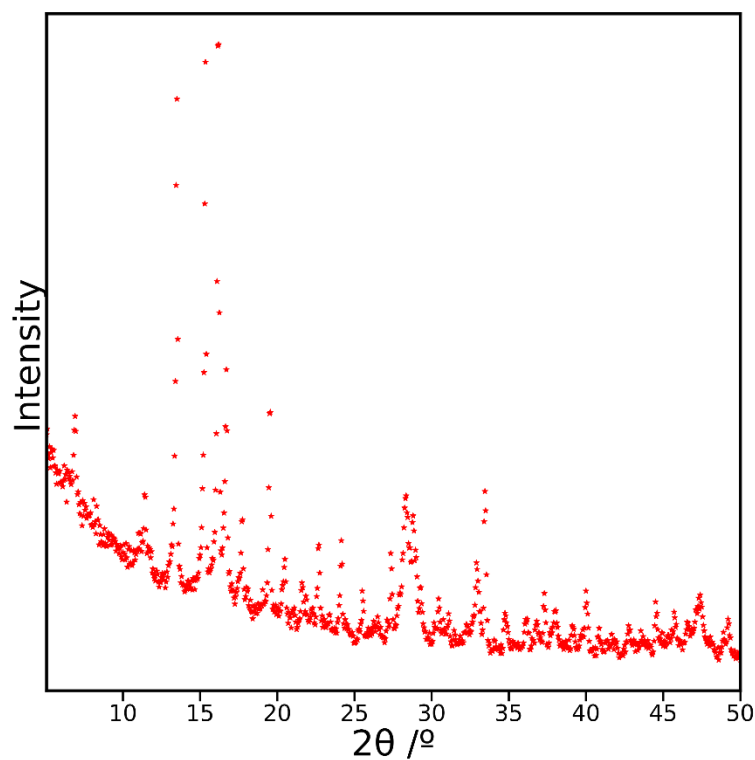
Figure B.2: Conventional powder X-ray diffraction pattern of a sample obtained from the unsuccessful synthesis of $Ce(HCO_2)(C_2O_4)$, measured using a Cu source ($\lambda = 1.54$ Å). The phase has not been identified.
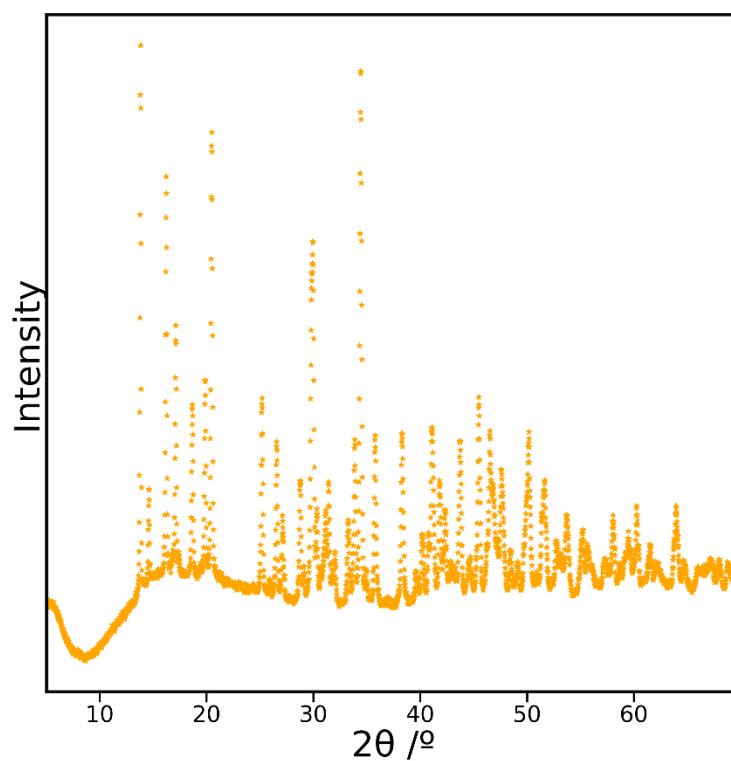
Figure B.3: Conventional powder X-ray diffraction pattern of a sample obtained from the unsuccessful synthesis of $Pr(HCO_2)(C_2O_4)$, measured using a Cu source ($\lambda = 1.54$ Å). The phase has not been identified.
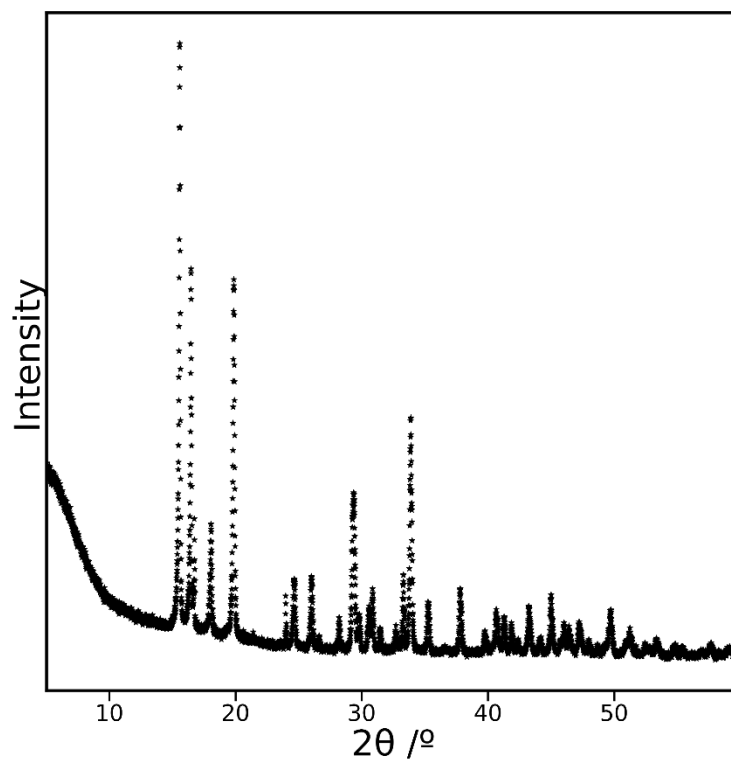
Figure B.4: Conventional powder X-ray diffraction pattern of a sample obtained from the unsuccessful synthesis of $Nd(HCO_2)(C_2O_4)$, measured using a Cu source ($\lambda = 1.54$ Å). The phase has not been identified.
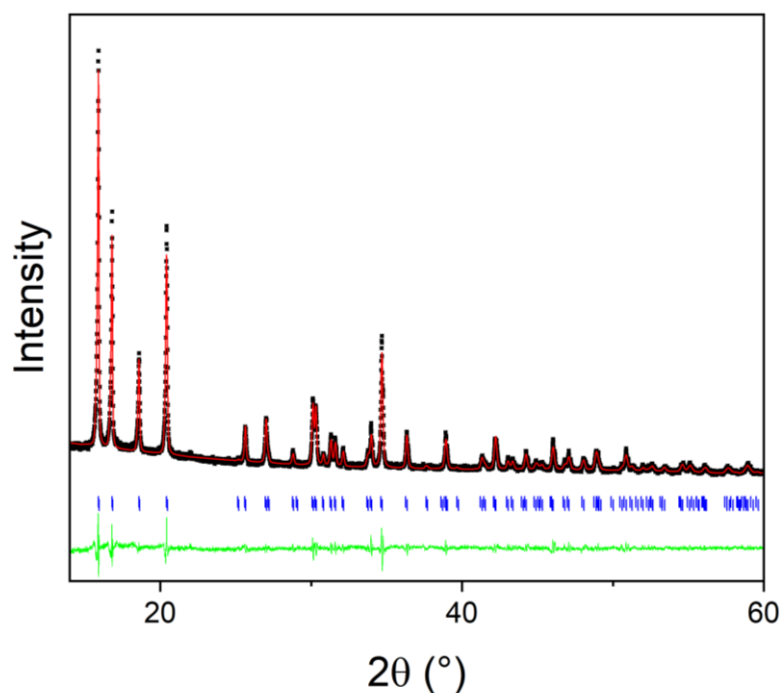
Figure B.5: Conventional powder X-ray diffraction pattern of Sm(HCO$_2$)(C$_2$O$_4$), measured using a Cu source (λ = 1.54 Å) and fitted using the Le Bail method to highlight phase purity. The crosses, red and green lines are experimental and calculated intensities and the difference curve. Vertical markers indicate the position of the Bragg reflections. R_p, R_{wp} and χ^2 of 2.88 %, 3.66 % and 3.33 are obtained respectively from the refinement with a = 7.13136(14) Å, b = 10.6840(2) Å and c = 6.65763(15) Å for the unit cell parameters.
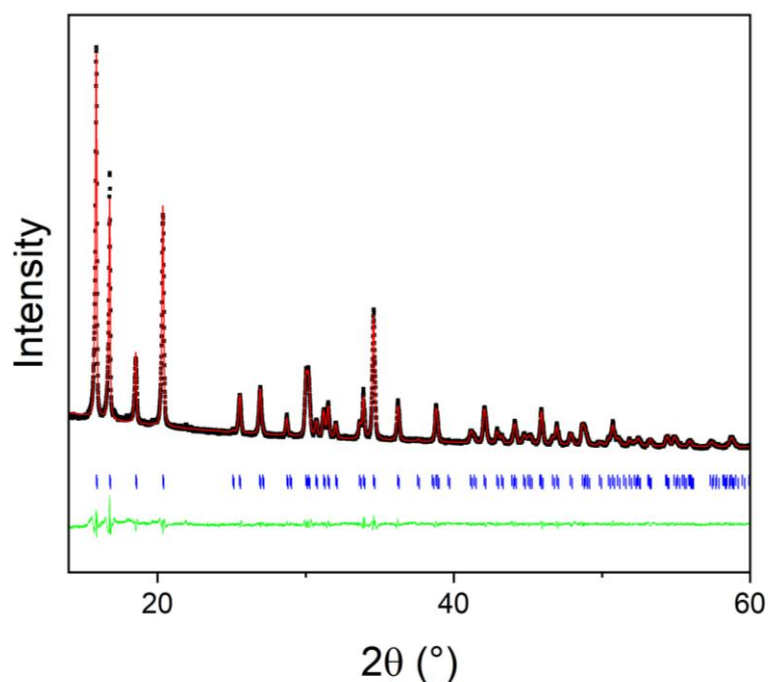
Figure B.6: Conventional powder X-ray diffraction pattern of Eu(HCO$_2$)(C$_2$O$_4$), measured using a Cu source (λ = 1.54 Å) and fitted using the Le Bail method to highlight phase purity. The crosses, red and green lines are experimental and calculated intensities and the difference curve. Vertical markers indicate the position of the Bragg reflections. R_p, R_{wp} and χ^2 of 2.66 %, 3.47 % and 3.62 are obtained respectively from the refinement with a = 7.08694(14) Å, b = 10.6524(2) Å and c = 6.6324(2) Å for the unit cell parameters.
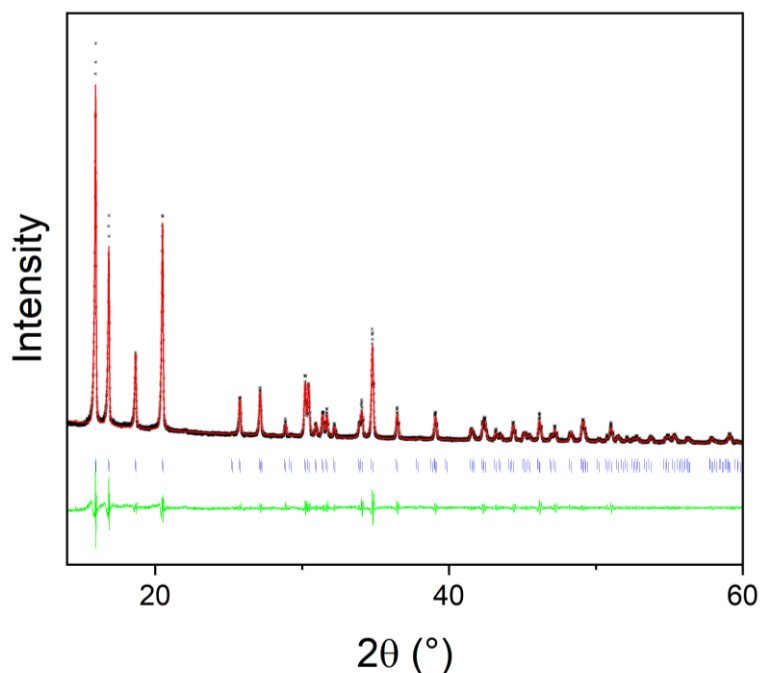
Figure B.7: Conventional powder X-ray diffraction pattern of Gd(HCO$_2$)(C$_2$O$_4$), measured using a Cu source (λ = 1.54 Å) and fitted using the Le Bail method to highlight phase purity. The crosses, red and green lines are experimental and calculated intensities and the difference curve. Vertical markers indicate the position of the Bragg reflections. R_p, R_{wp} and χ^2 of 3.03 %, 3.82 % and 1.81 are obtained respectively from the refinement with a = 7.0431(3) Å, b = 10.6194(4) Å and c = 6.6070(3) Å for the unit cell parameters.
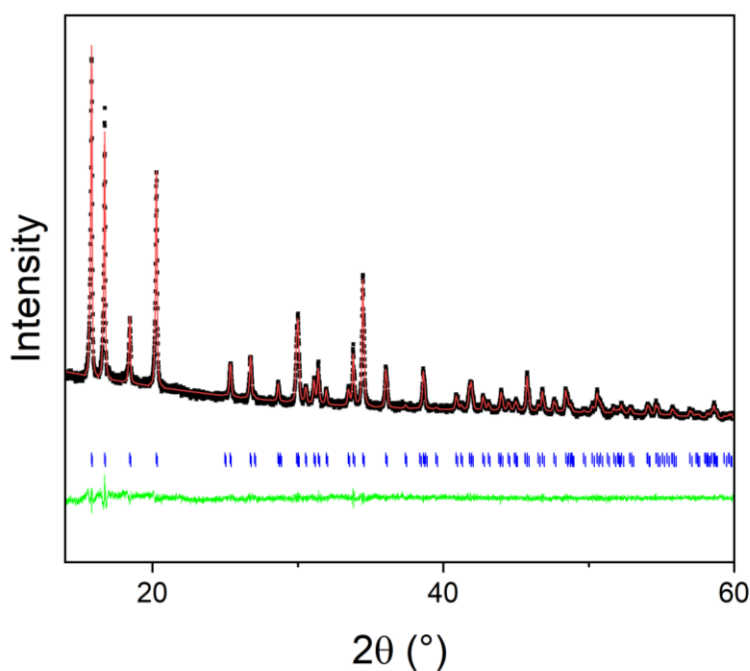
Figure B.8: Conventional powder X-ray diffraction pattern of Tb(HCO$_2$)(C$_2$O$_4$), measured using a Cu source (λ = 1.54 Å) and fitted using the Le Bail method to highlight phase purity. The crosses, red and green lines are experimental and calculated intensities and the difference curve. Vertical markers indicate the position of the Bragg reflections. R_p, R_{wp} and χ^2 of 2.30 %, 3.65 % and 1.72 are obtained respectively from the refinement with a = 7.02274(18) Å, b = 10.5980(3) Å and c = 6.59748(18) Å for the unit cell parameters.
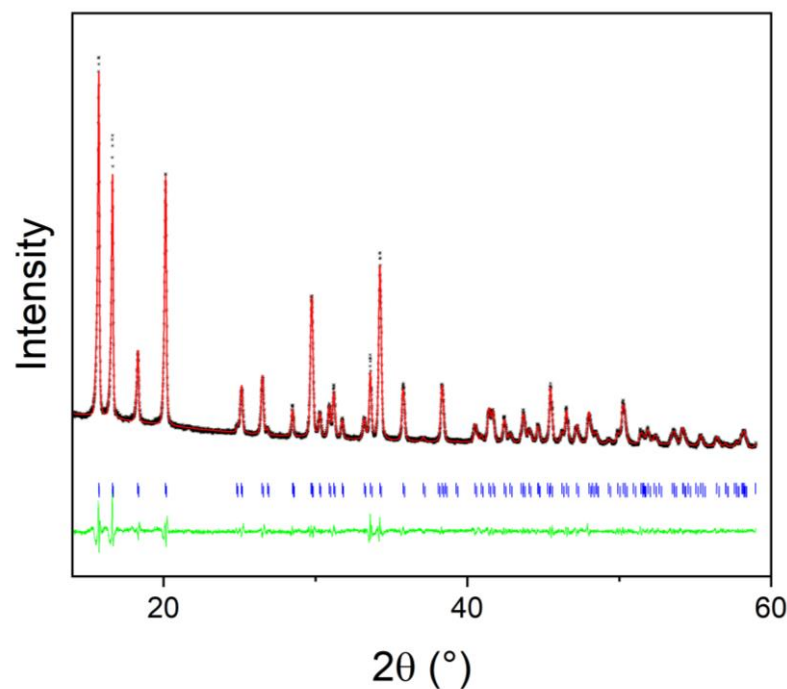
Figure B.9: Conventional powder X-ray diffraction pattern of $Dy(HCO_2)(C_2O_4)$, measured using a Cu source ($\lambda = 1.54$ Å) and fitted using the Le Bail method to highlight phase purity. The crosses, red and green lines are experimental and calculated intensities and the difference curve. Vertical markers indicate the position of the Bragg reflections. R_p, R_{wp} and χ^2 of 2.56 %, 3.23 % and 3.52 are obtained respectively from the refinement with $a = 6.98194(13)$ Å, $b = 10.5752(2)$ Å and $c = 6.58162(14)$ Å for the unit cell parameters.
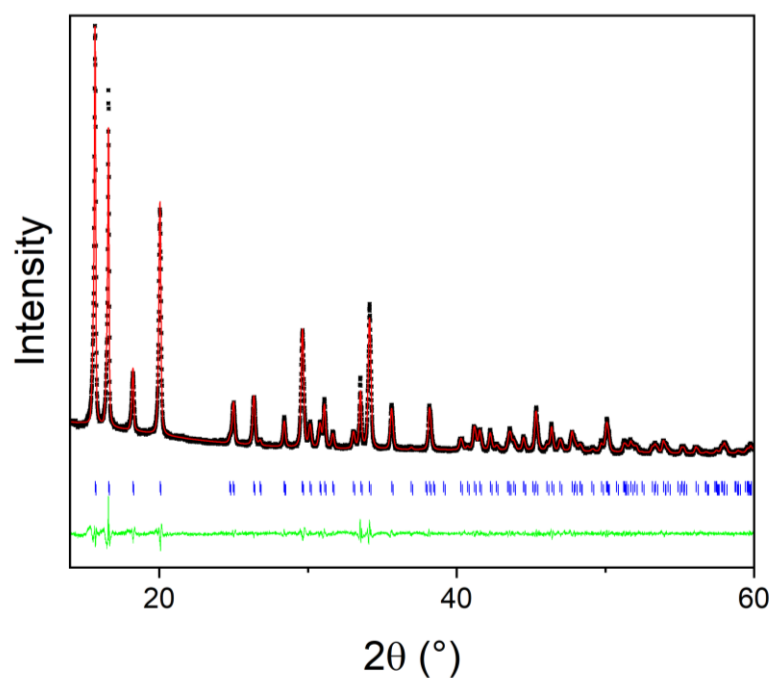
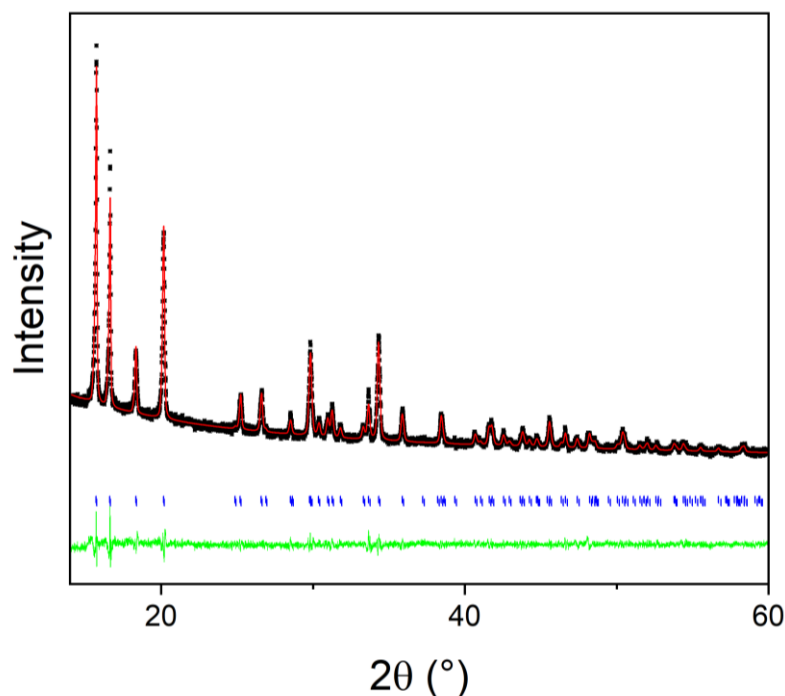**Figure B.10:** Conventional powder X-ray diffraction pattern of $Ho(HCO_2)(C_2O_4)$, measured using a Cu source ($\lambda = 1.54$ Å) and fitted using the Le Bail method to highlight phase purity. The crosses, red and green lines are experimental and calculated intensities and the difference curve. Vertical markers indicate the position of the Bragg reflections. R_p, R_{wp} and χ^2 of 4.09 %, 5.13 % and 2.84 are obtained respectively from the refinement with $a = 6.97292(19)$ Å, $b = 10.5811(4)$ Å and $c = 6.58207(20)$ Å for the unit cell parameters.

Figure B.11: Conventional powder X-ray diffraction pattern of $Er(HCO_2)(C_2O_4)$, measured using a Cu source ($\lambda = 1.54$ Å) and fitted using the Le Bail method to highlight phase purity The crosses, red and green lines are experimental and calculated intensities and the difference curve. Vertical markers indicate the position of the Bragg reflections. R_p, R_{wp} and χ^2 of 4.36 %, 5.58 % and 4.63 are obtained respectively from the refinement with $a = 6.92593(17)$ Å, $b = 10.5448(3)$ Å and $c = 6.55559(18)$ Å for the unit cell parameters.
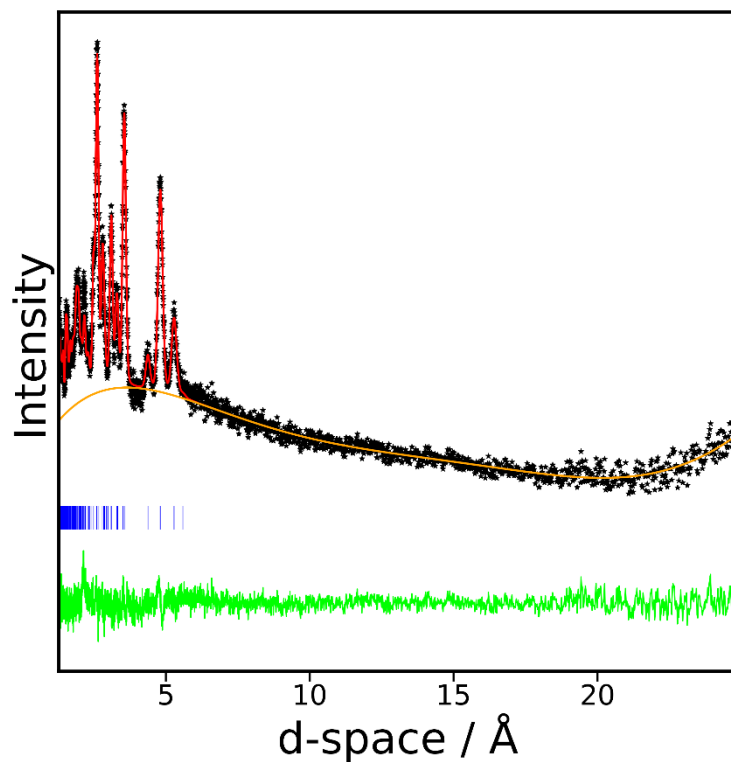
Figure B.12: Neutron diffraction pattern collected from $Tb(HCO_2)(C_2O_4)$ at 1.6 K using bank 1 of the GEM diffractometer fitted using the Rietveld method with R_p and R_{wp} of 1.48% and 1.88%, respectively. The crosses and the red, orange, and green lines indicate the observed and calculated intensities, the estimated background and difference curve, respectively. The markers indicate the reflection allowed by the structure.
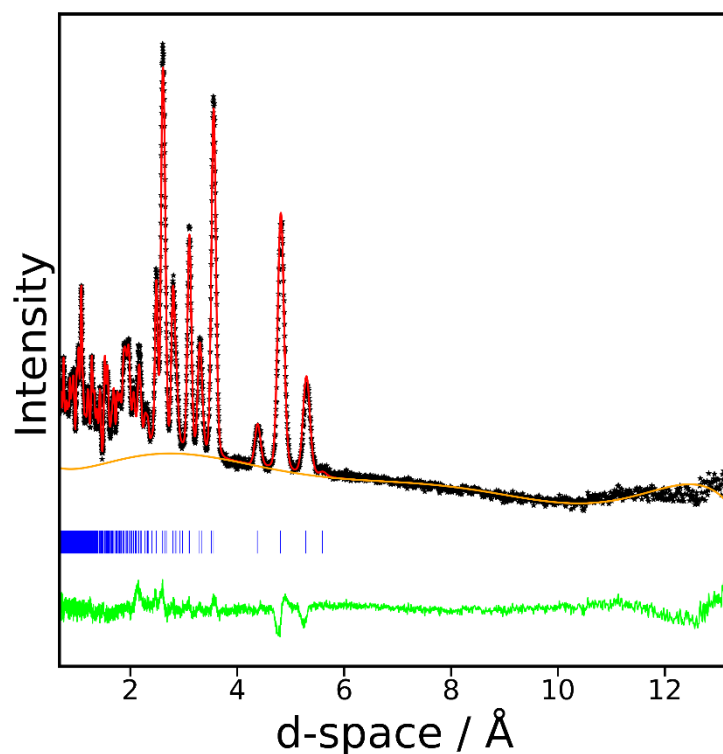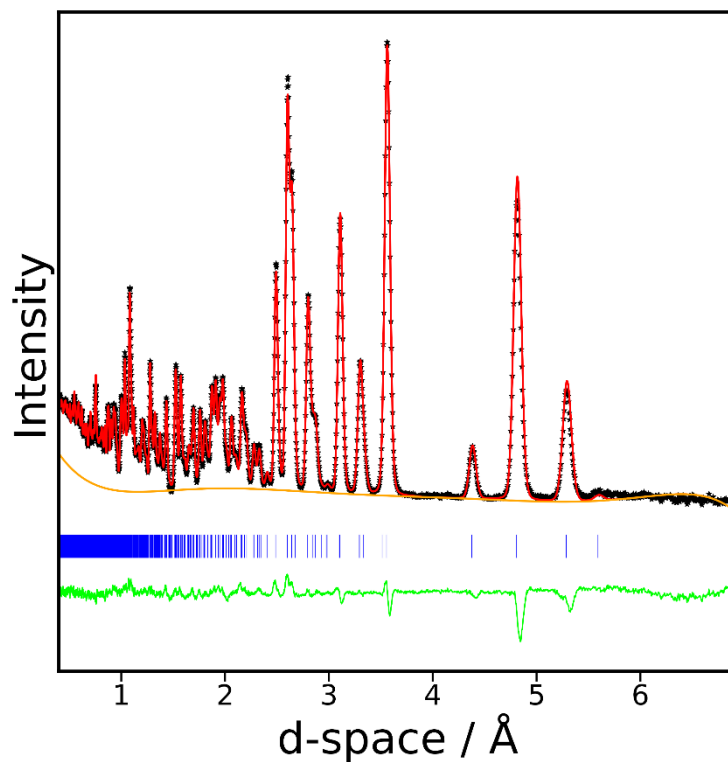
Figure B.13: Neutron diffraction pattern collected from Tb(HCO$_2$)(C$_2$O$_4$) at 1.6 K using bank 2 of the GEM diffractometer fitted using the Rietveld method with R_p and R_{wp} of 1.55% and 1.79%, respectively. The crosses and the red, orange, and green lines indicate the observed and calculated intensities, the estimated background and difference curve, respectively. The markers indicate the reflection allowed by the structure.

Figure B.14: Neutron diffraction pattern collected from Tb(HCO$_2$)(C$_2$O$_4$) at 1.6 K using bank 3 of the GEM diffractometer fitted using the Rietveld method with R_p and R_{wp} of 1.82% and 2.04%, respectively. The crosses and the red, orange, and green lines indicate the observed and calculated intensities, the estimated background and difference curve, respectively. The markers indicate the reflection allowed by the structure.
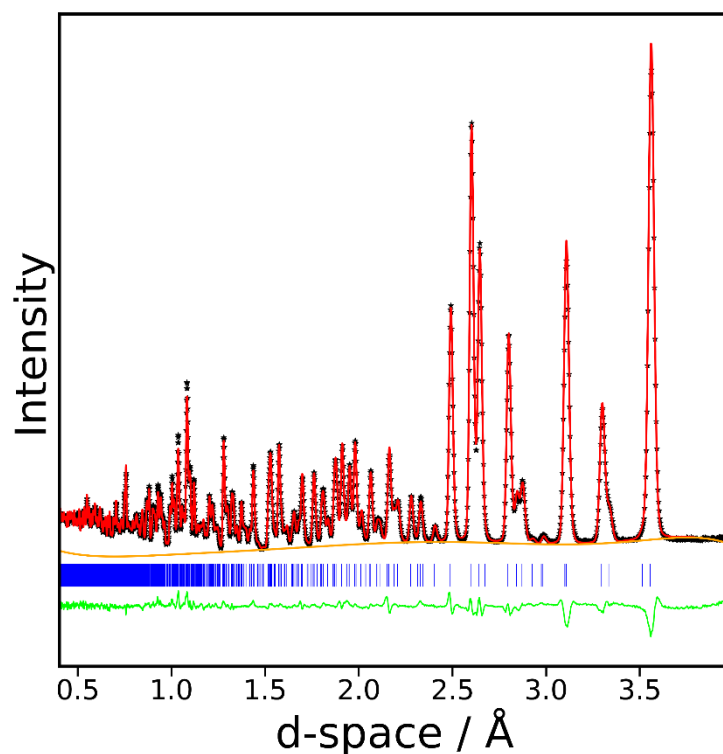
Figure B.15: Neutron diffraction pattern collected from Tb(HCO$_2$)(C$_2$O$_4$) at 1.6 K using bank 4 of the GEM diffractometer fitted using the Rietveld method with R_p and R_{wp} of 2.27% and 2.42%, respectively. The crosses and the red, orange, and green lines indicate the observed and calculated intensities, the estimated background and difference curve, respectively. The markers indicate the reflection allowed by the structure.
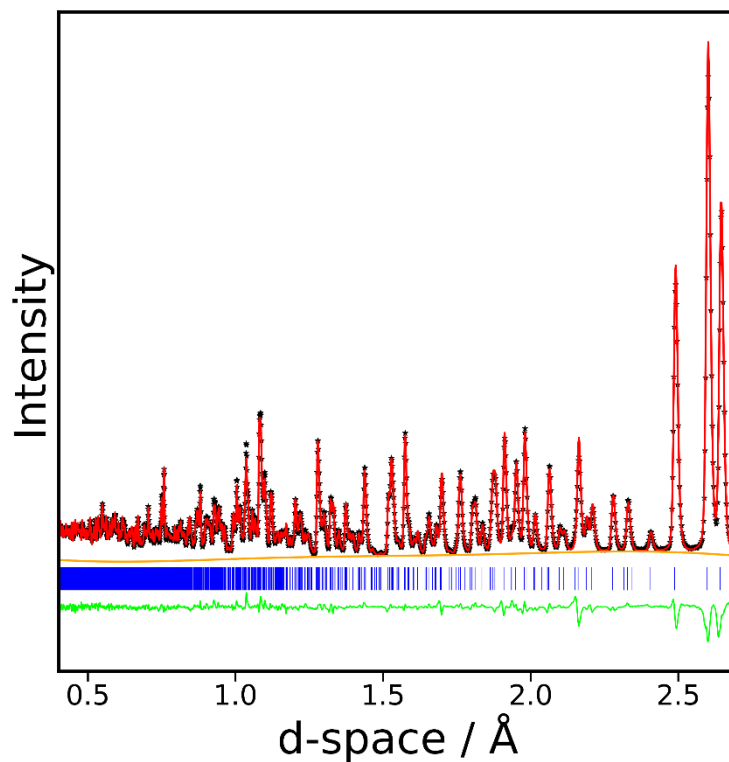

Figure B.16: Neutron diffraction pattern collected from Tb(HCO$_2$)(C$_2$O$_4$) at 1.6 K using bank 5 of the GEM diffractometer fitted using the Rietveld method with R_p and R_{wp} of 2.72% and 2.92%, respectively. The crosses and the red, orange, and green lines indicate the observed and calculated intensities, the estimated background and difference curve, respectively. The markers indicate the reflection allowed by the structure.
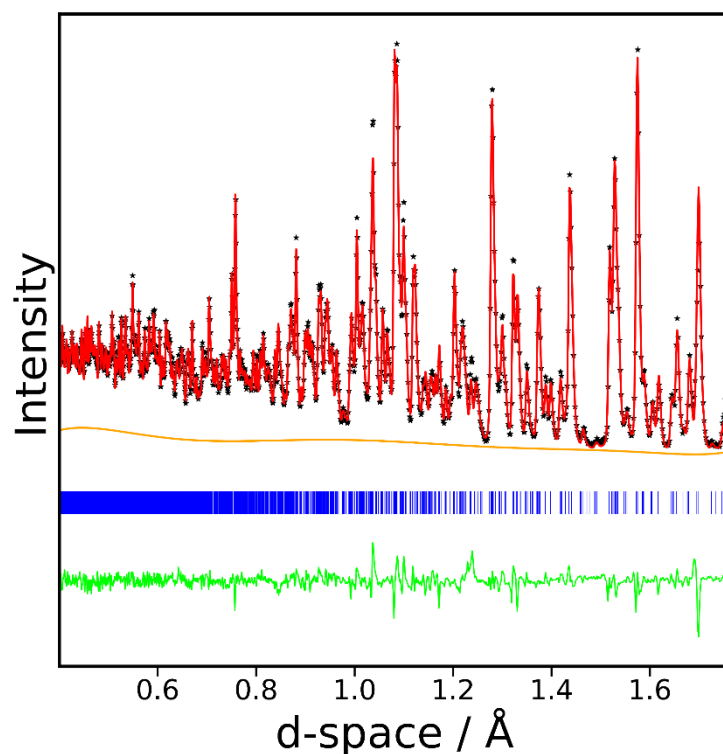
Figure B.17: Neutron diffraction pattern collected from Tb(HCO₂)(C₂O₄) at 1.6 K using bank 6 of the GEM diffractometer fitted using the Rietveld method with R_p and R_{wp} of 1.48% and 1.94%, respectively. The crosses and the red, orange, and green lines indicate the observed and calculated intensities, the estimated background and difference curve, respectively. The markers indicate the reflection allowed by the structure.
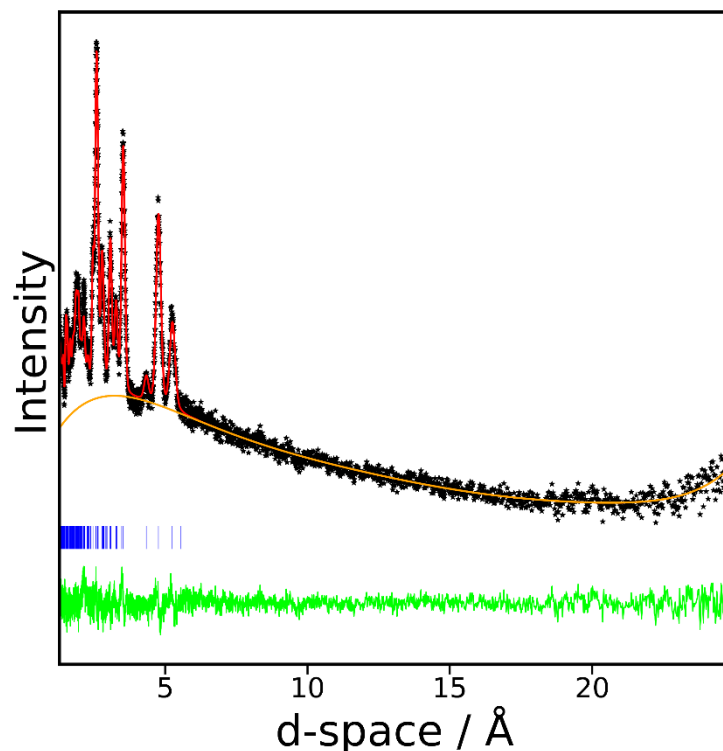

Figure B.18: Neutron diffraction pattern collected from Ho(HCO₂)(C₂O₄) at 1.6 K using bank 1 of the GEM diffractometer fitted using the Rietveld method with R_p and R_{wp} of 1.56% and 1.87%, respectively. The crosses and the red, orange, and green lines indicate the observed and calculated intensities, the estimated background and difference curve, respectively. The markers indicate the reflection allowed by the structure.

Figure B.19: Neutron diffraction pattern collected from $Ho(HCO_2)(C_2O_4)$ at 1.6 K using bank 2 of the GEM diffractometer fitted using the Rietveld method with R_p and R_{wp} of 1.56% and 1.85%, respectively. The crosses and the red, orange, and green lines indicate the observed and calculated intensities, the estimated background and difference curve, respectively. The markers indicate the reflection allowed by the structure.
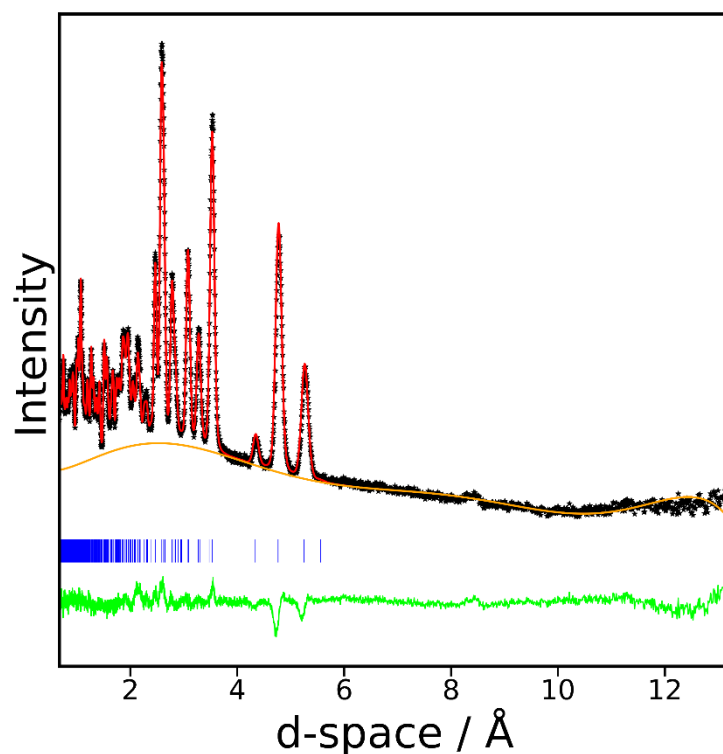

Figure B.20: Neutron diffraction pattern collected from $Ho(HCO_2)(C_2O_4)$ at 1.6 K using bank 3 of the GEM diffractometer fitted using the Rietveld method with R_p and R_{wp} of 2.24% and 2.29%, respectively. The crosses and the red, orange, and green lines indicate the observed and calculated intensities, the estimated background and difference curve, respectively. The markers indicate the reflection allowed by the structure.
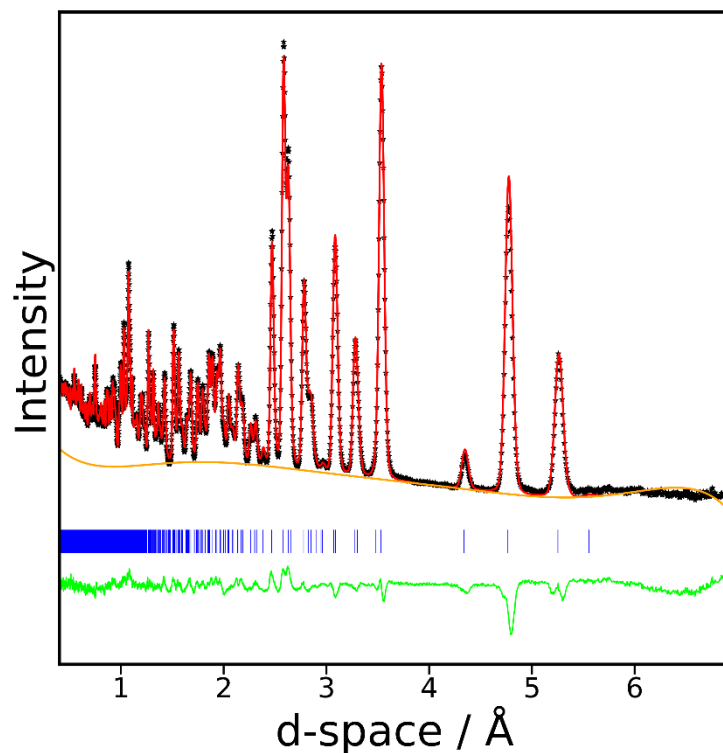
Figure B.21: Neutron diffraction pattern collected from $Ho(HCO_2)(C_2O_4)$ at 1.6 K using bank 4 of the GEM diffractometer fitted using the Rietveld method with R_p and R_{wp} of 2.88% and 3.27%, respectively. The crosses and the red, orange, and green lines indicate the observed and calculated intensities, the estimated background and difference curve, respectively. The markers indicate the reflection allowed by the structure.
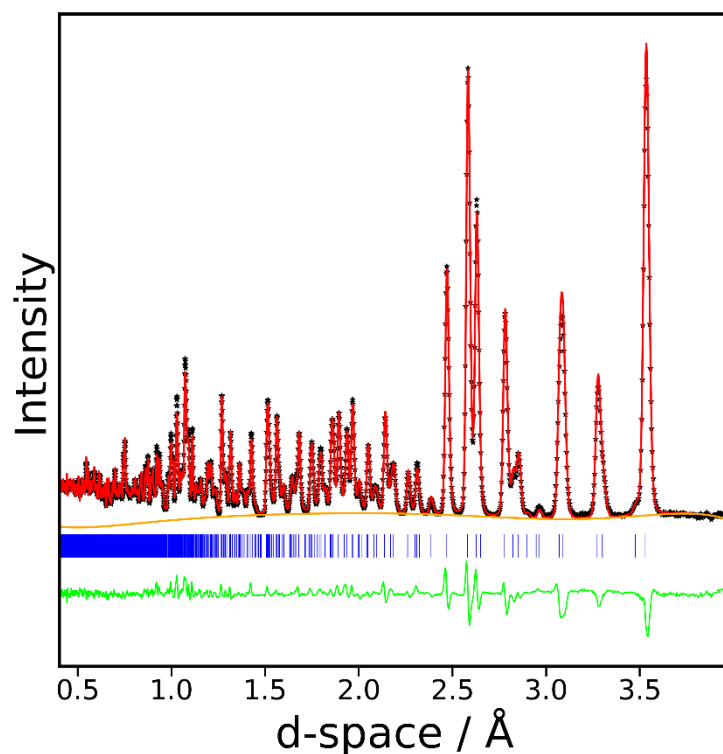

Figure B.22: Neutron diffraction pattern collected from $Ho(HCO_2)(C_2O_4)$ at 1.6 K using bank 5 of the GEM diffractometer fitted using the Rietveld method with R_p and R_{wp} of 2.90% and 3.11%, respectively. The crosses and the red, orange, and green lines indicate the observed and calculated intensities, the estimated background and difference curve, respectively. The markers indicate the reflection allowed by the structure.
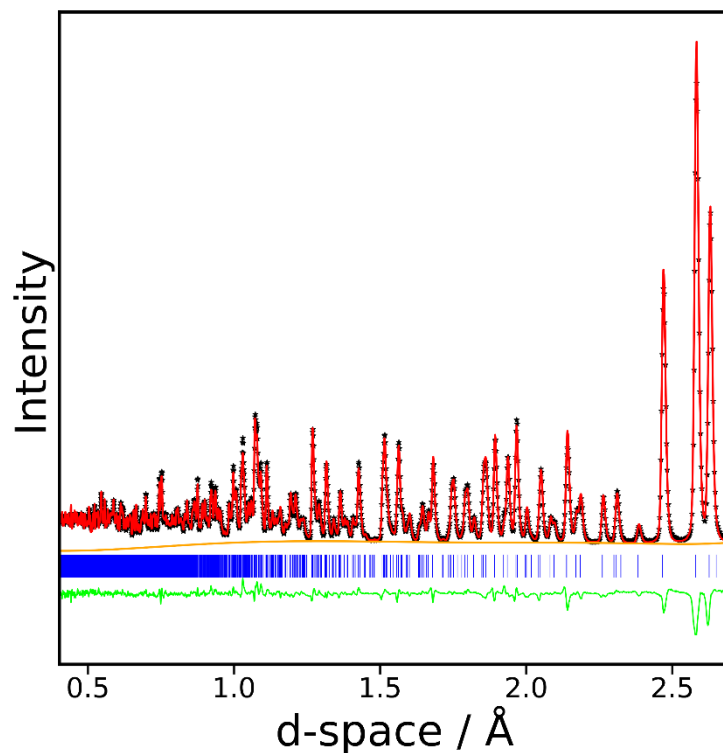
Figure B.23: Neutron diffraction pattern collected from Ho(HCO$_2$)(C$_2$O$_4$) at 1.6 K using bank 6 of the GEM diffractometer fitted using the Rietveld method with R_p and R_{wp} of 2.37% and 3.08%, respectively. The crosses and the red, orange, and green lines indicate the observed and calculated intensities, the estimated background and difference curve, respectively. The markers indicate the reflection allowed by the structure.
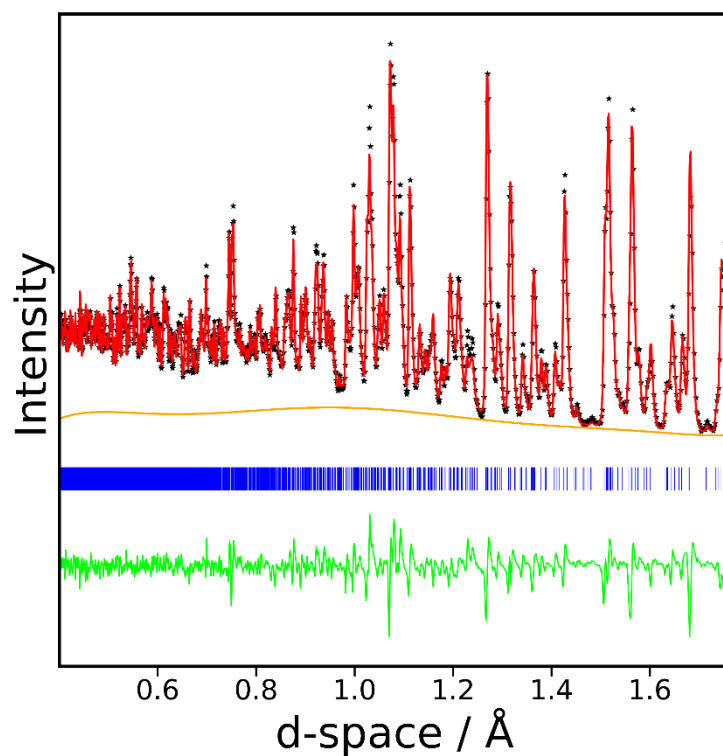
Appendix C

Figure C.1: SEM image of $Ho_{0.9}Er_{0.1}(HCO_2)_3$ acquired with a secondary electron (SE) detector.

Figure C.2: SEM image of $Ho_{0.8}Er_{0.2}(HCO_2)_3$ acquired with a secondary electron (SE) detector.

Figure C.3: SEM image of $Ho_{0.7}Er_{0.3}(HCO_2)_3$ acquired with a secondary electron (SE) detector.

Figure C.4: SEM image of $Ho_{0.6}Er_{0.4}(HCO_2)_3$ acquired with a secondary electron (SE) detector.
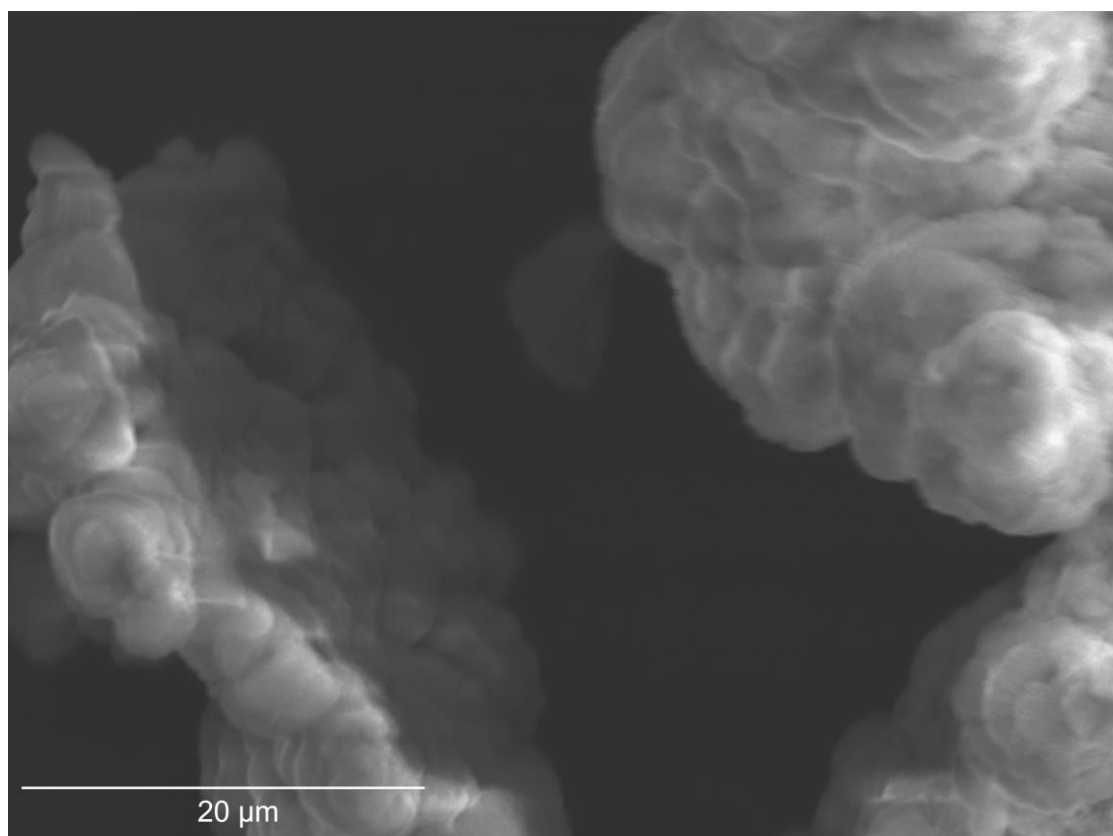
Figure C.5: SEM image of $Ho_{0.5}Er_{0.5}(HCO_2)_3$ acquired with a secondary electron (SE) detector.
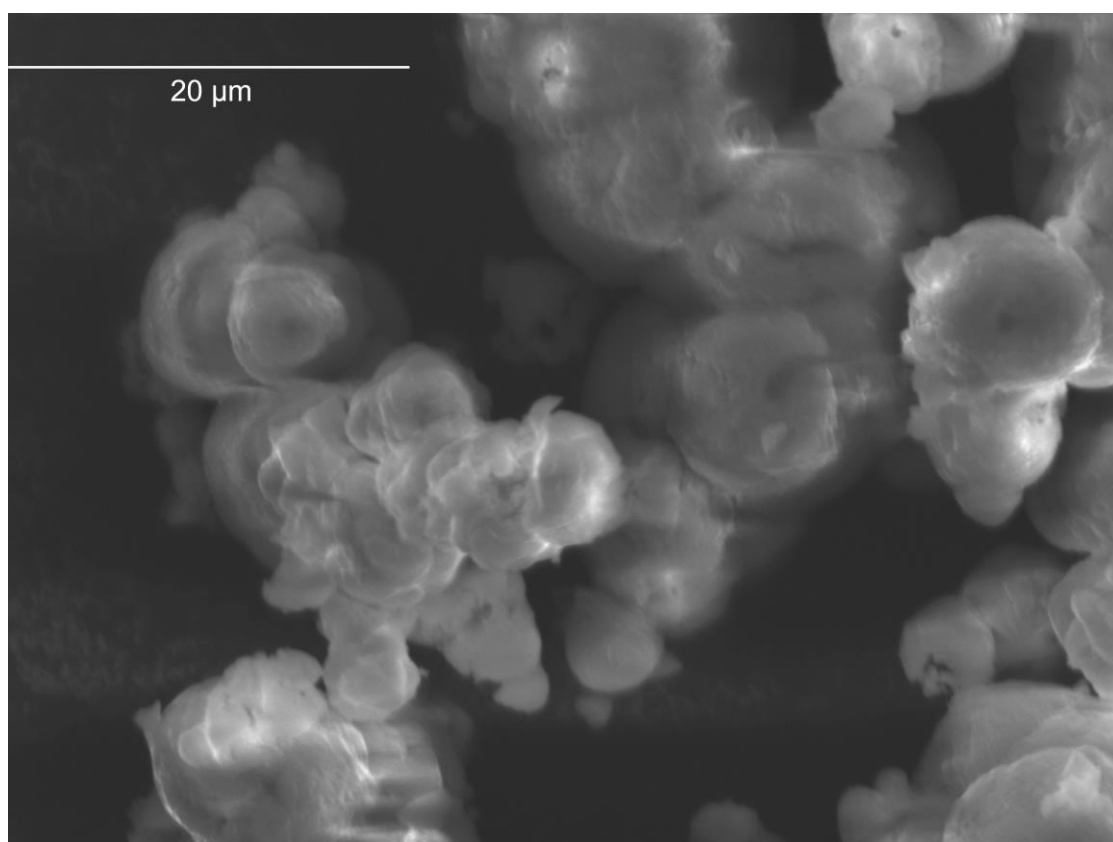
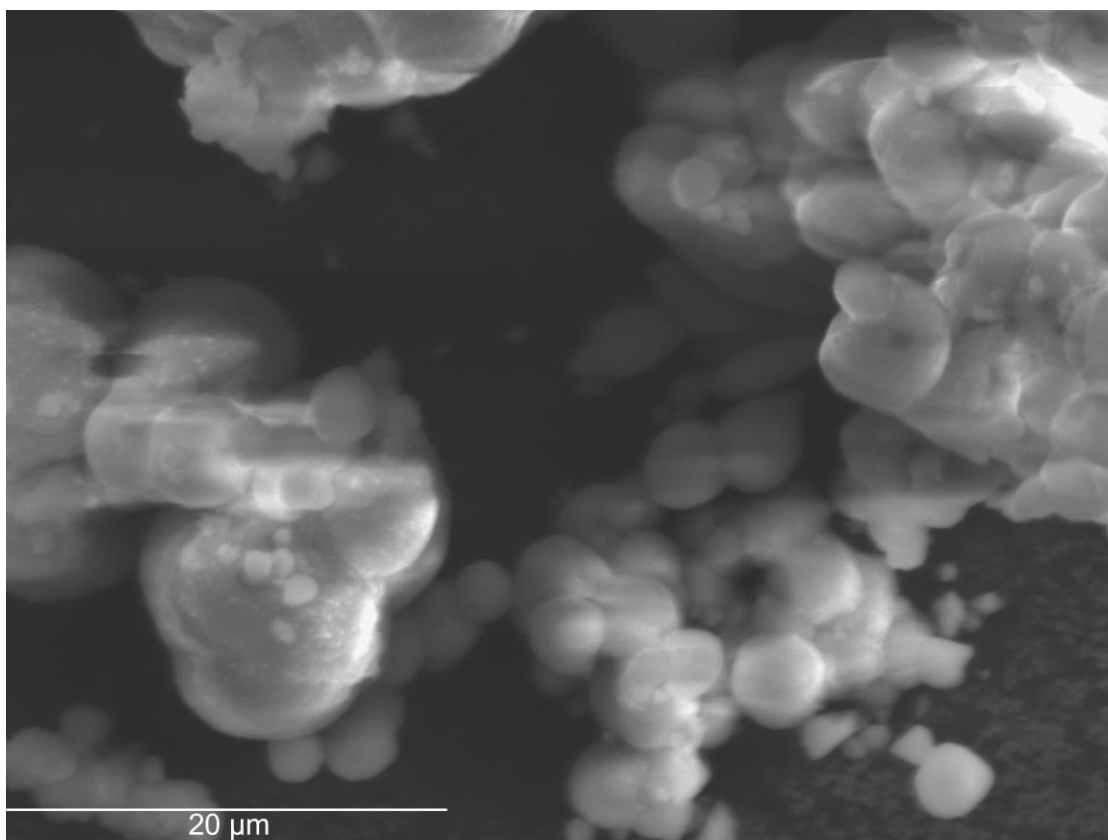**Figure C.6**: SEM image of $Ho_{0.4}Er_{0.6}(HCO_2)_3$ acquired with a secondary electron (SE) detector.
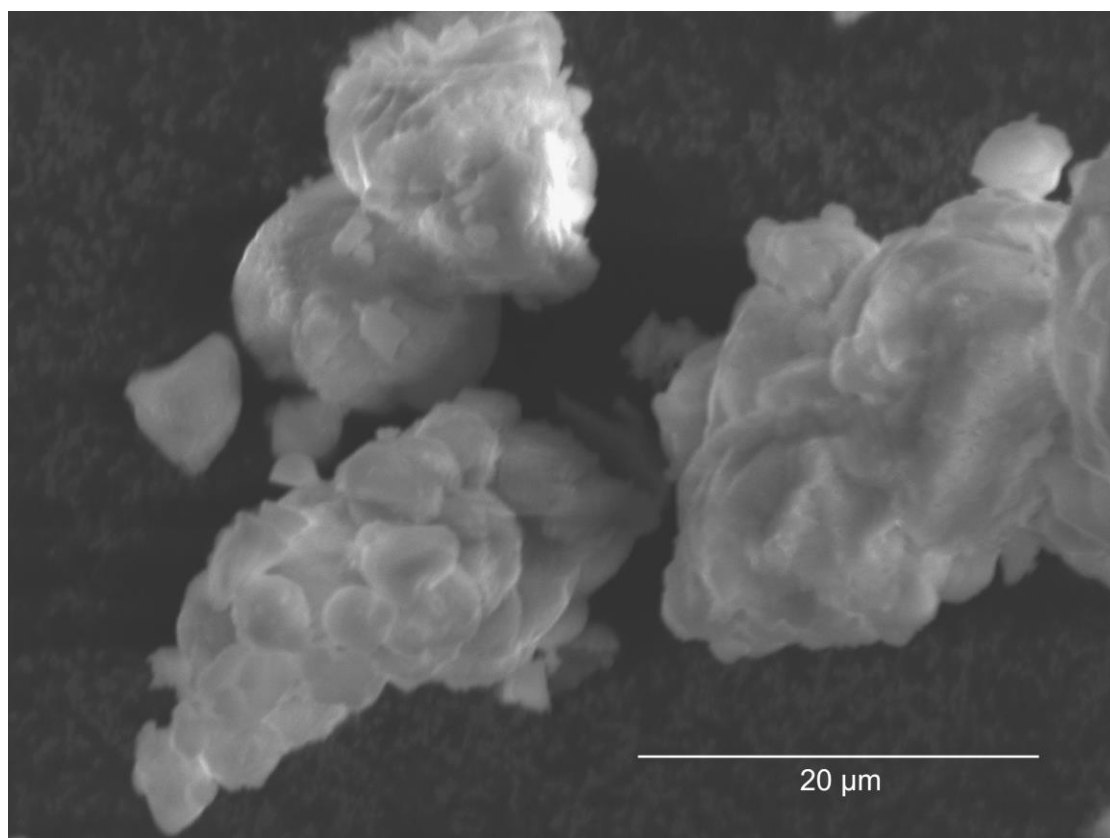
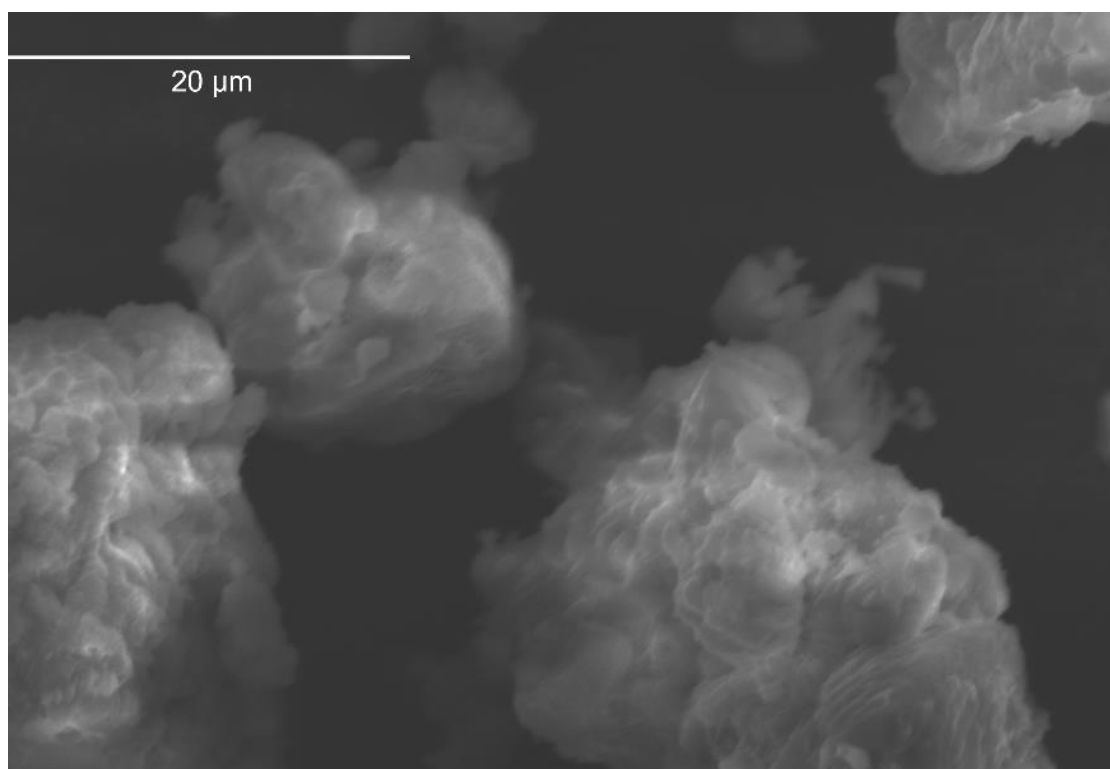**Figure C.7**: SEM image of $Ho_{0.3}Er_{0.7}(HCO_2)_3$ acquired with a secondary electron (SE) detector.
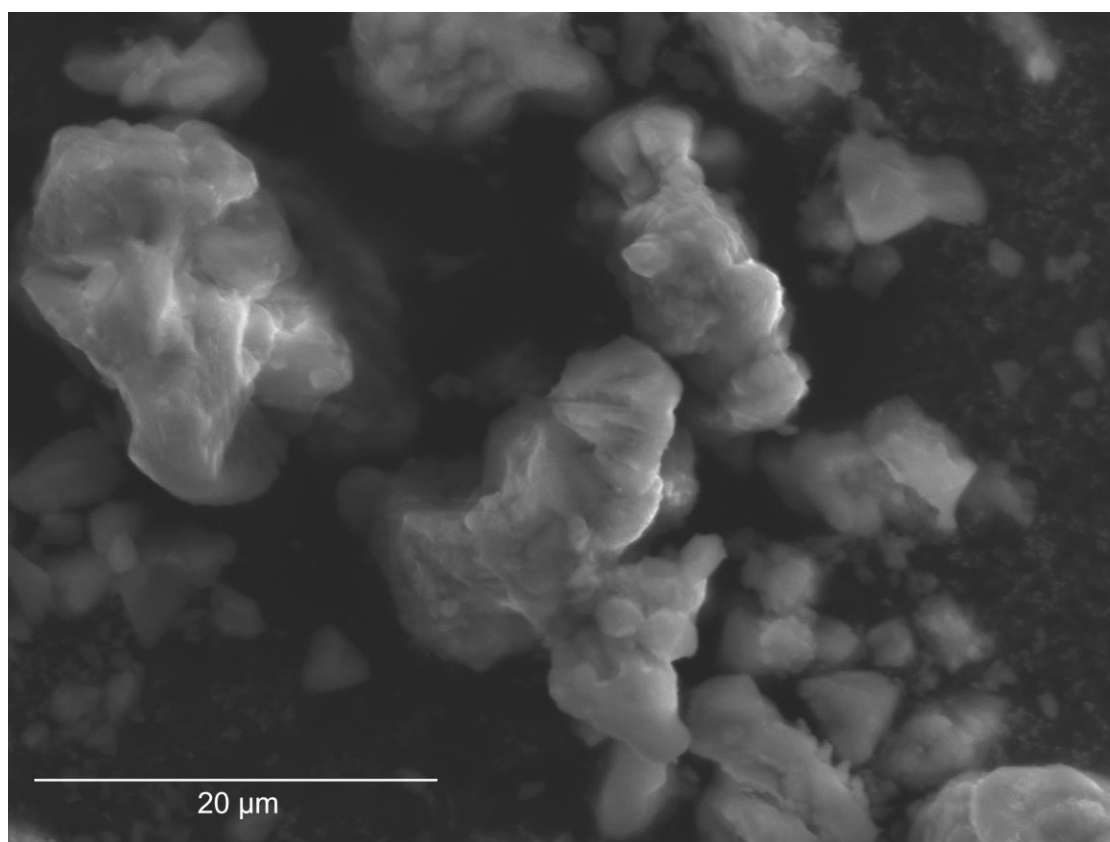
Figure C.8: SEM image of $Ho_{0.2}Er_{0.8}(HCO_2)_3$ acquired with a secondary electron (SE) detector.

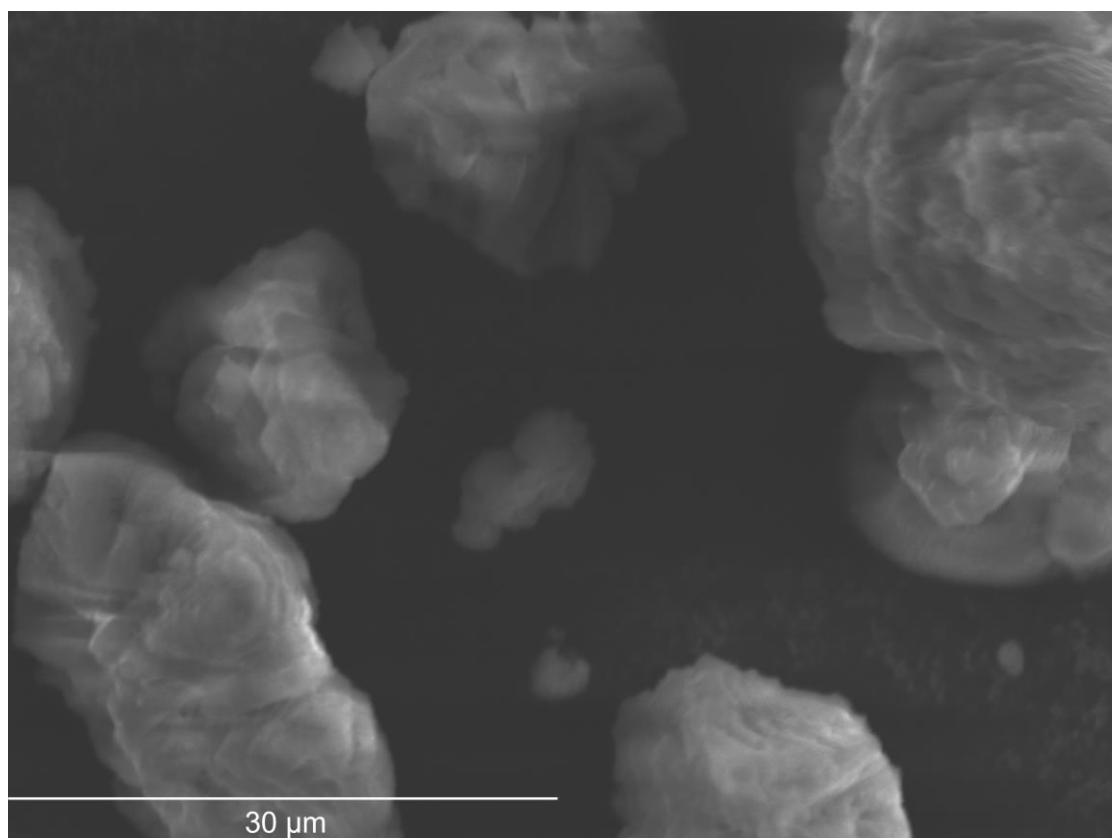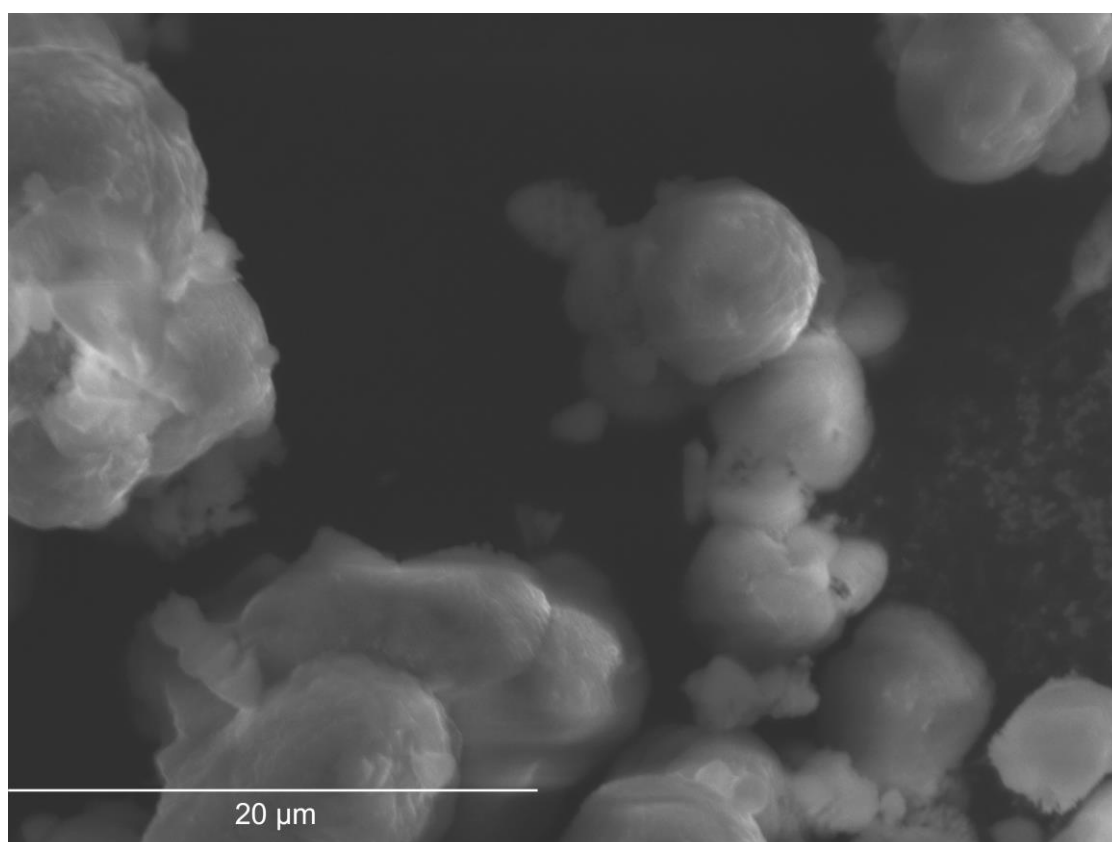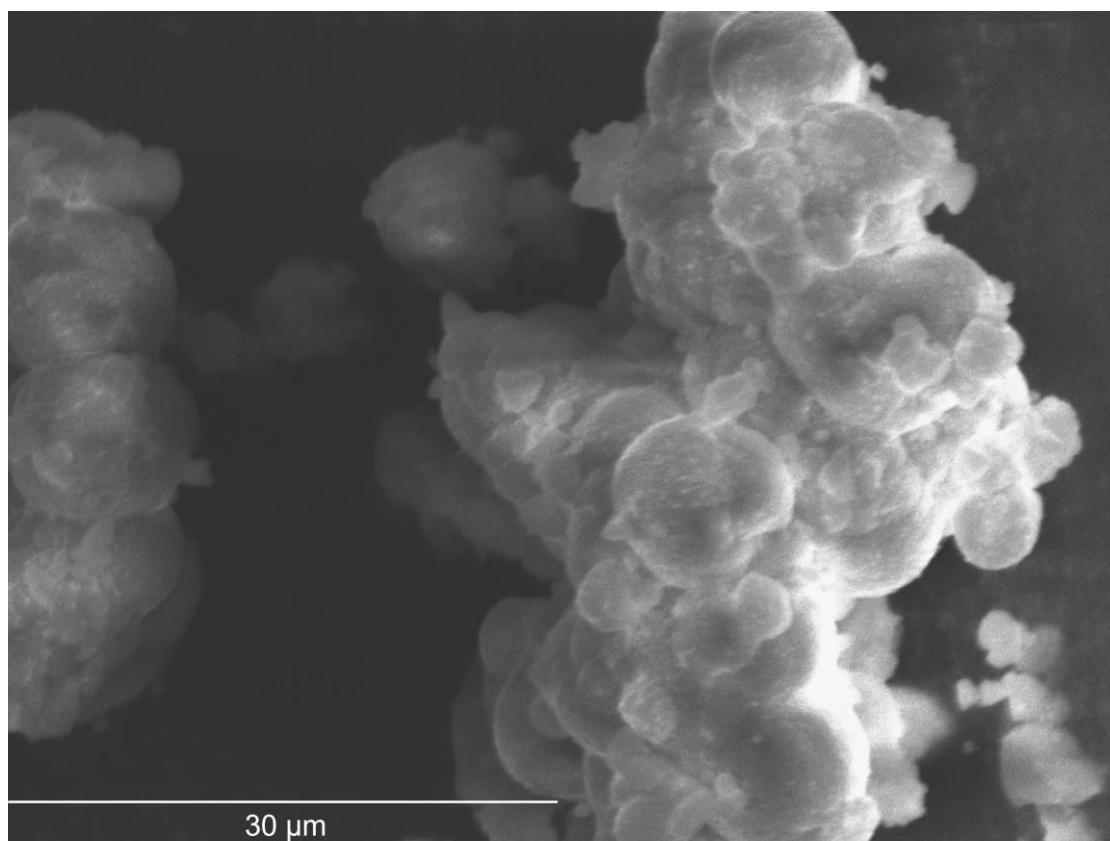**Figure C.9**: SEM image of $Ho_{0.1}Er_{0.9}(HCO_2)_3$ acquired with a secondary electron (SE) detector.

Table C.1: EDX atomic percentages of Holmium and Erbium for $Ho_{0.9}Er_{0.1}(HCO_2)_3$ determined on different points and areas of the observed region under SEM.

Element	Ho	Er
	91.79	
	90.96	8.21
	91.68	9.04
	91.06	8.32
	91.81	8.94
	91.19	8.19
	91.26	8.81
	92.01	8.74
	91.67	7.99
	92.49	8.33
Atomic %	91.15	7.51
	90.81	8.85
	92.22	9.19
	91.58	7.78
	91.60	8.42
	90.84	8.40
	91.59	9.16
	90.84	8.31
	91.69	8.37
	91.63	
Average	91.49	8.51
Standard Deviation	0.47	0.47

Table C.2: EDX atomic percentages of Holmium and Erbium for $Ho_{0.8}Er_{0.2}(HCO_2)_3$ determined on different points and areas of the observed region under SEM.

Element	Ho	Er
	79.74	20.26
	78.76	21.24
	78	22
	78.56	21.44
	79.48	20.52
	79.28	20.72
	78.58	21.42
	79.16	20.84
	80.36	19.64
	79.38	20.62
Atomic %	80.02	19.98
	78.98	21.02
	79.68	20.32
	80.22	19.78
	78.61	21.39
	79.03	20.97
	79.18	20.82
	80.55	19.45
	79.7	20.3
	79.5	20.5
	79.94	20.06
Average	79.37	20.63
Standard Deviation	0.66	0.66

Table C.3: EDX atomic percentages of Holmium and Erbium for $Ho_{0.7}Er_{0.3}(HCO_2)_3$ determined on different points and areas of the observed region under SEM.

Element	Ho	Er
	67.58	32.42
	68.55	31.45
	69.14	30.86
	69.29	30.71
	69.27	30.73
	69.23	30.77
	69.46	30.54
	68.21	31.79
	66.81	33.19
	69.21	30.79
Atomic %	67.62	32.38
	69.1	30.9
	68.84	31.16
	68.37	31.63
	69.19	30.81
	68.65	31.35
	67.55	32.45
	69.51	30.49
	69.62	30.38
	68.62	31.38
Average	68.69	31.31
Standard Deviation	0.78	0.78

Table C.4: EDX atomic percentages of Holmium and Erbium for $Ho_{0.6}Er_{041}(HCO_2)_3$ determined on different points and areas of the observed region under SEM.

Element	Ho	Er
	59.07	40.93
	59.71	40.29
	59.17	40.83
	59.78	40.22
	59.34	40.66
	59.86	40.14
	59.88	40.12
	59.6	40.4
	60.06	39.94
	59.98	40.02
Atomic %	59.5	40.5
	59.69	40.31
	59.41	40.59
	59.78	40.22
	59.65	40.35
	59.44	40.56
	59.09	40.91
	60.48	39.52
	60.63	39.37
	59.8	40.2
Average	59.70	40.30
Standard Deviation	0.41	0.41

Table C.5: EDX atomic percentages of Holmium and Erbium for $Ho_{0.5}Er_{0.5}(HCO_2)_3$ determined on different points and areas of the observed region under SEM.

Element	Ho	Er
	49.5	50.5
	47.34	52.66
	49.32	50.68
	46.94	53.06
	49.37	50.63
	48.71	51.29
	49.7	50.3
	49.69	50.31
	50.1	49.9
	50.86	49.14
Atomic %	50.45	49.55
	47.89	52.11
	50.66	49.34
	49.24	50.76
	48.29	51.71
	47.29	52.71
	48.61	51.39
	48	52
	51.38	48.62
	46.97	53.03
Average	49.02	50.98
Standard Deviation	1.33	1.33

Table C.6: EDX atomic percentages of Holmium and Erbium for $Ho_{0.4}Er_{0.6}(HCO_2)_3$ determined on different points and areas of the observed region under SEM.

Element	Ho	Er
	39.96	60.04
	39.47	60.53
	39.69	60.31
	40.51	59.49
	38.77	61.23
	39.16	60.84
	40.74	59.26
	39.53	60.47
	38.64	61.36
	39.22	60.78
Atomic %	38.69	61.31
	39.33	60.67
	38.46	61.54
	39.36	60.64
	39.19	60.81
	38.44	61.56
	39.57	60.43
	39.07	60.93
	38.57	61.43
	38.76	61.24
	39.19	60.81
Average	39.25	60.75
Standard Deviation	0.62	0.62

Table C.7: EDX atomic percentages of Holmium and Erbium for $Ho_{0.3}Er_{0.7}(HCO_2)_3$ determined on different points and areas of the observed region under SEM.

Element	Ho	Er
	29.76	70.24
	29.05	70.95
	29.26	70.74
	30.87	69.13
	28.93	71.07
	29.16	70.84
	28.85	71.15
	29.99	70.01
	29.03	70.97
Atomic %	29.19	70.81
	28.22	71.78
	29.52	70.48
	29.36	70.64
	28.68	71.32
	29.39	70.61
	29.07	70.93
	29.13	70.87
	29.57	70.43
	28.31	71.69
Average	29.23	70.77
Standard Deviation	0.59	0.59

Table C.8: EDX atomic percentages of Holmium and Erbium for $Ho_{0.2}Er_{0.8}(HCO_2)_3$ determined on different points and areas of the observed region under SEM.

Element	Ho	Er
	19.54	80.46
	20.63	79.37
	19.1	80.9
	20.72	79.28
	18.38	81.62
	19.46	80.54
	18.67	81.33
	20.67	79.33
	18.87	81.13
	18.69	81.31
Atomic %	18.71	81.29
	20.17	79.83
	19.04	80.96
	19.31	80.69
	18.67	81.33
	20.25	79.75
	18.89	81.11
	20.31	79.69
	19.52	80.48
	20.03	79.97
Average	19.48	80.59
Standard Deviation	0.77	0.77

Table C.9: EDX atomic percentages of Holmium and Erbium for $Ho_{0.1}Er_{0.9}(HCO_2)_3$ determined on different points and areas of the observed region under SEM.

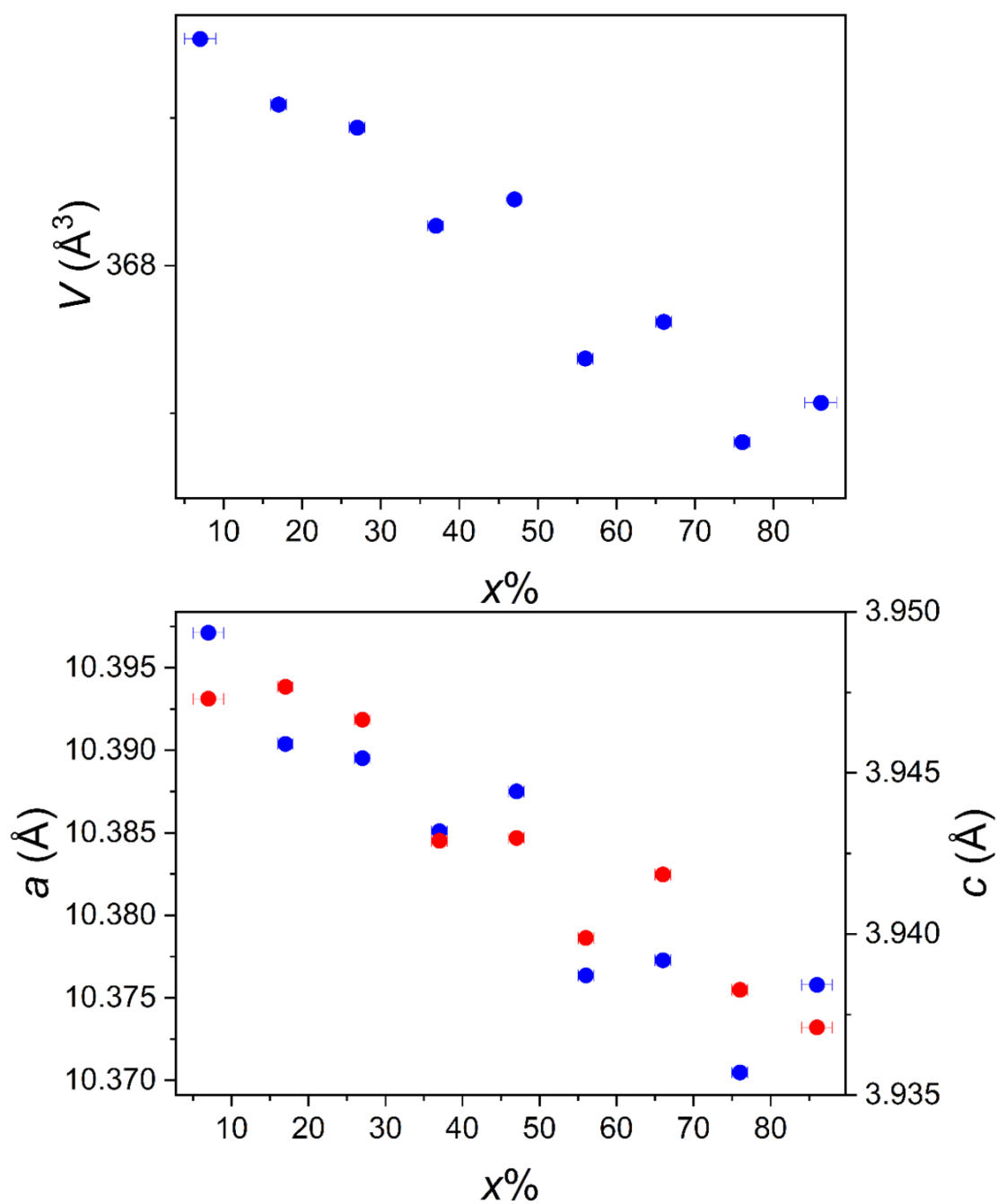| Element	Ho	Er
	8.59	91.41
	7.42	92.58
	8.8	91.2
	9.45	90.55
	6.3	93.7
	10.03	89.97
	9.25	90.75
	4.52	95.48
	7.03	92.97
Atomic %	9.24	90.76
	8.29	91.71
	9.34	90.66
	7.44	92.56
	8.15	91.85
	5.17	94.83
	10.84	89.16
	9.99	90.01
	6.19	93.81
	11.61	88.39
	5.06	94.94
Average	8.14	91.86
Standard Deviation	1.96	1.96

Figure C.10: Plots of the unit cell volume (top) and lattice parameters *a* and *c* (bottom), the latter shown in blue and red, respectively, for the orthorhombic unit cell of $Ho_{1-x}Er_x(HCO_2)_3$. Horizontal error bars show the uncertainty on the composition determined *via* X-ray fluorescence for the solid solutions.

Table C.10: Refinements statistic for the Le Bail refinements of powder X-ray diffraction patterns of $Ho_{1-x}Er_x(HCO_2)_3$.

Sample	R_p	R_{wp}	χ^2
$Ho_{0.90}Er_{0.10}(HCO_2)_3$	2.35	3.12	2.42
$Ho_{0.80}Er_{0.20}(HCO_2)_3$	2.69	3.72	2.86
$Ho_{0.70}Er_{0.30}(HCO_2)_3$	2.96	4.04	3.01
$Ho_{0.60}Er_{0.40}(HCO_2)_3$	2.48	3.34	2.85
$Ho_{0.50}Er_{0.50}(HCO_2)_3$	3.99	5.30	4.53
$Ho_{0.40}Er_{0.60}(HCO_2)_3$	3.10	4.00	3.05
$Ho_{0.30}Er_{0.70}(HCO_2)_3$	2.56	3.47	2.44
$Ho_{0.20}Er_{0.80}(HCO_2)_3$	3.16	4.07	3.05
$Ho_{0.10}Er_{0.90}(HCO_2)_3$	2.62	3.53	2.75
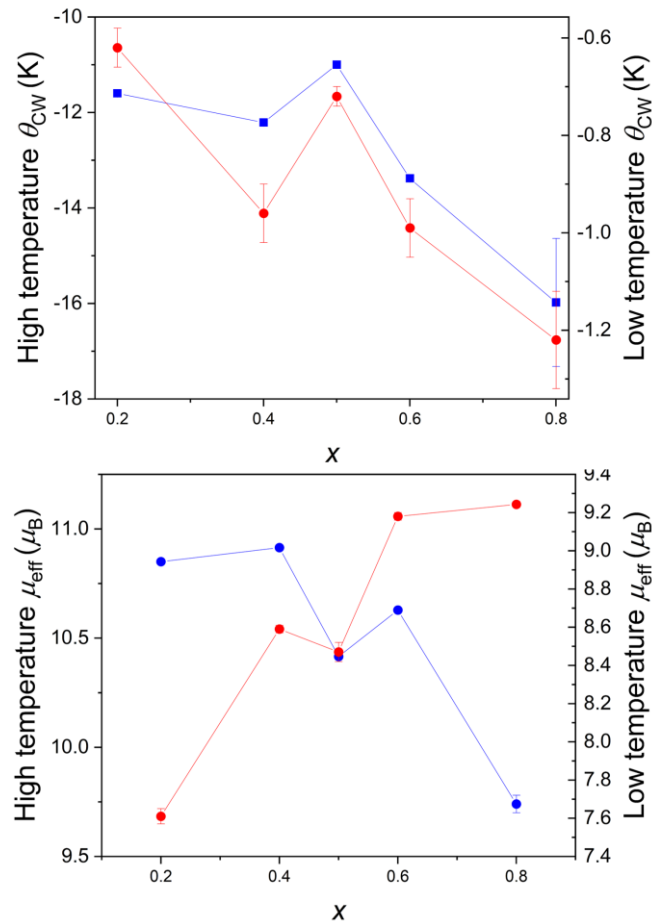
Figure C.11: High- (blue) and low-temperature (red) Weiss constant θ_{CW} (top) and effective magnetic moment μ_{eff} (bottom) *vs* concentration of Er, obtained from fits to the Curie-Weiss law of the SQUID data measured on $Ho_{1-x}Er_x(HCO_2)_3$.

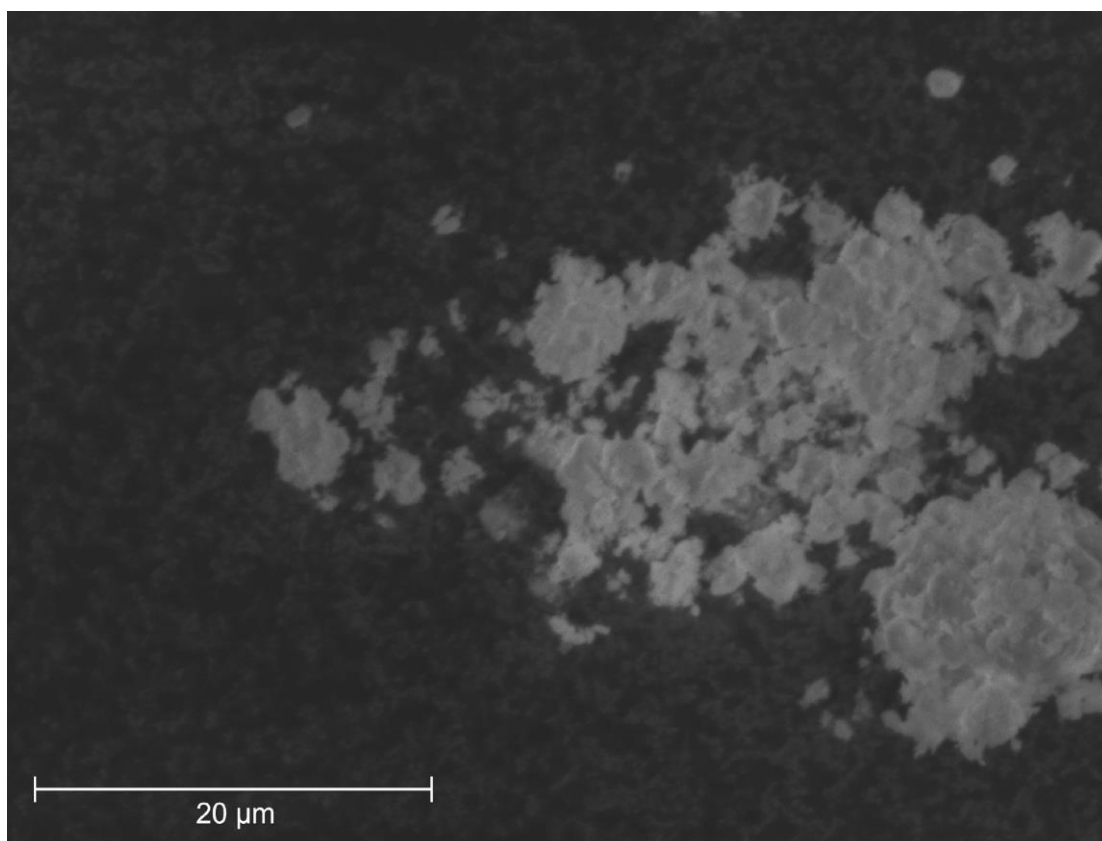**Figure C.12:** SEM image of Y0.025Tb0.975(HCO2)3 acquired with a secondary electron (SE) detector.

Figure C.13: SEM image of $Y_{0.05}Tb_{0.95}(HCO_2)_3$ acquired with a secondary electron (SE) detector.

Figure C.14: SEM image of $Y_{0.10}Tb_{0.90}(HCO_2)_3$ acquired with a secondary electron (SE) detector.

Figure C.15: SEM images of two different regions of $Y_{0.20}Tb_{0.80}(HCO_2)_3$, acquired with a secondary electron (SE) detector at the same magnification.

Figure C.16: SEM images of two different regions of $Y_{0.40}Tb_{0.60}(HCO_2)_3$, acquired with a secondary electron (SE) detector at different magnifications.

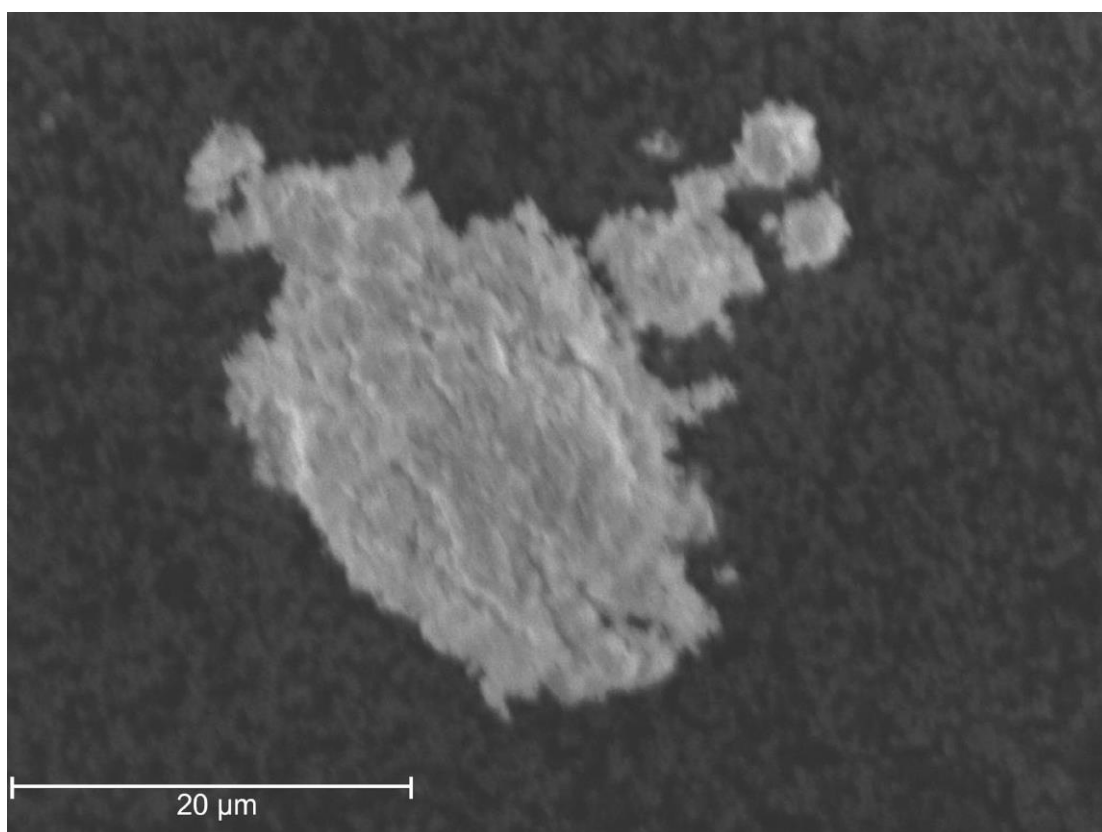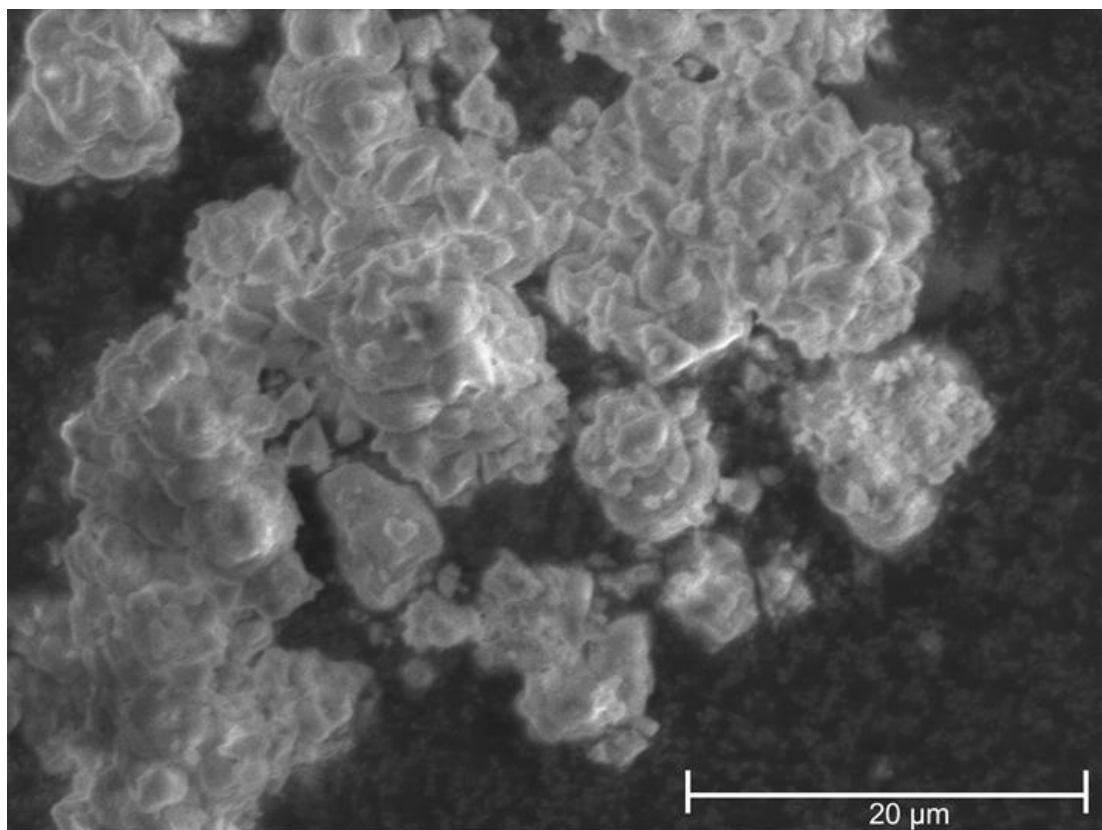**Figure C.17**: SEM image of $Y_{0.60}Tb_{0.80}(HCO_2)_3$, acquired with a secondary electron (SE) detector.

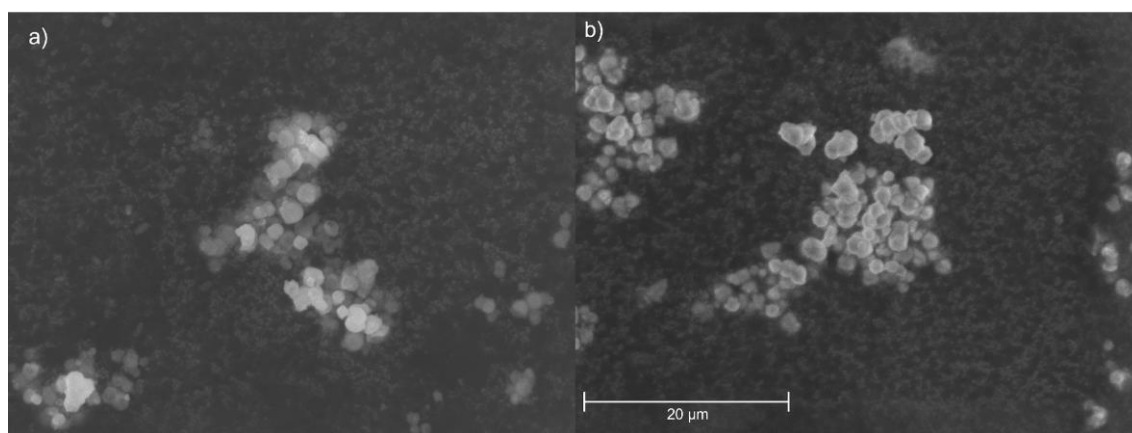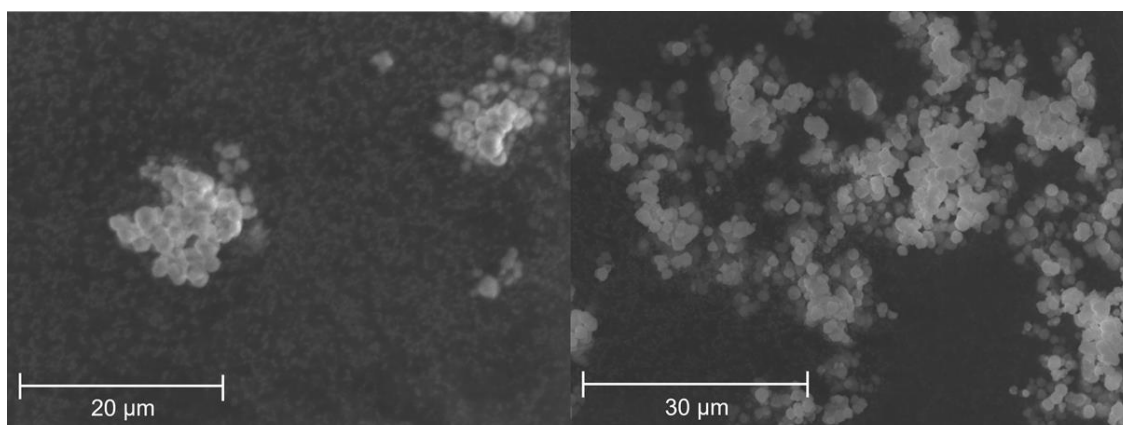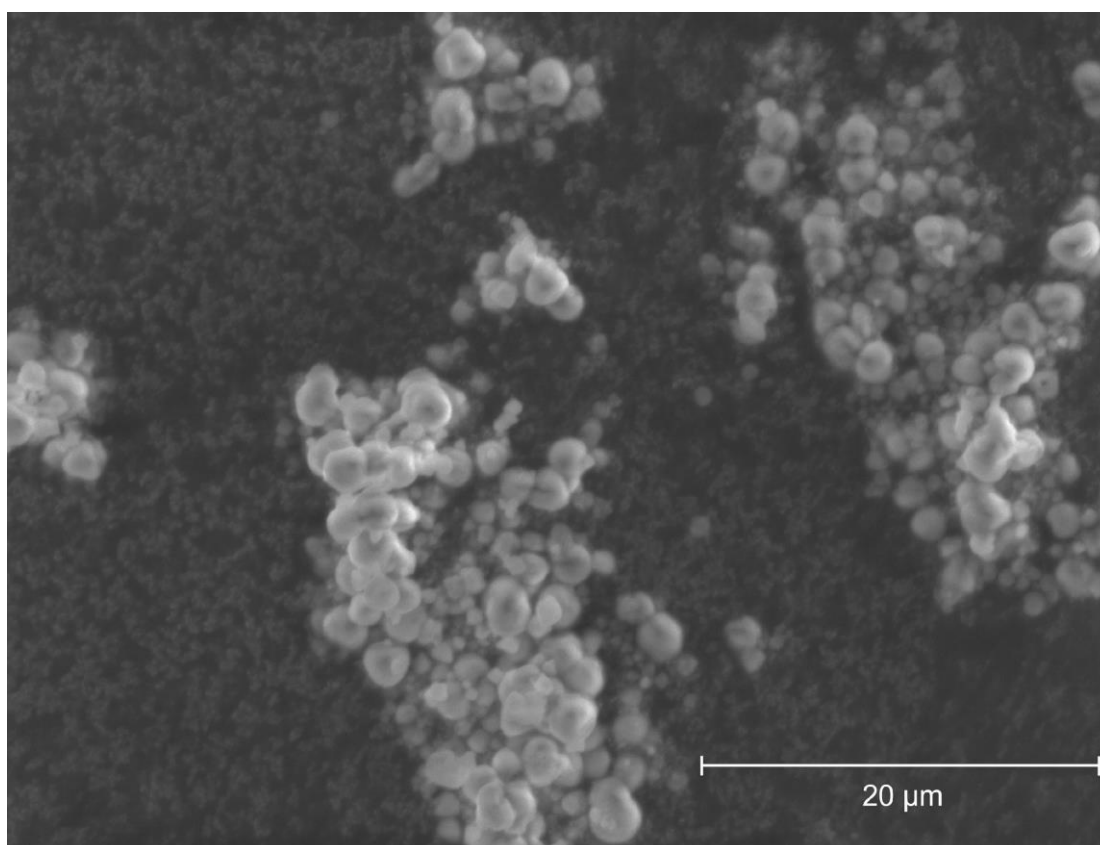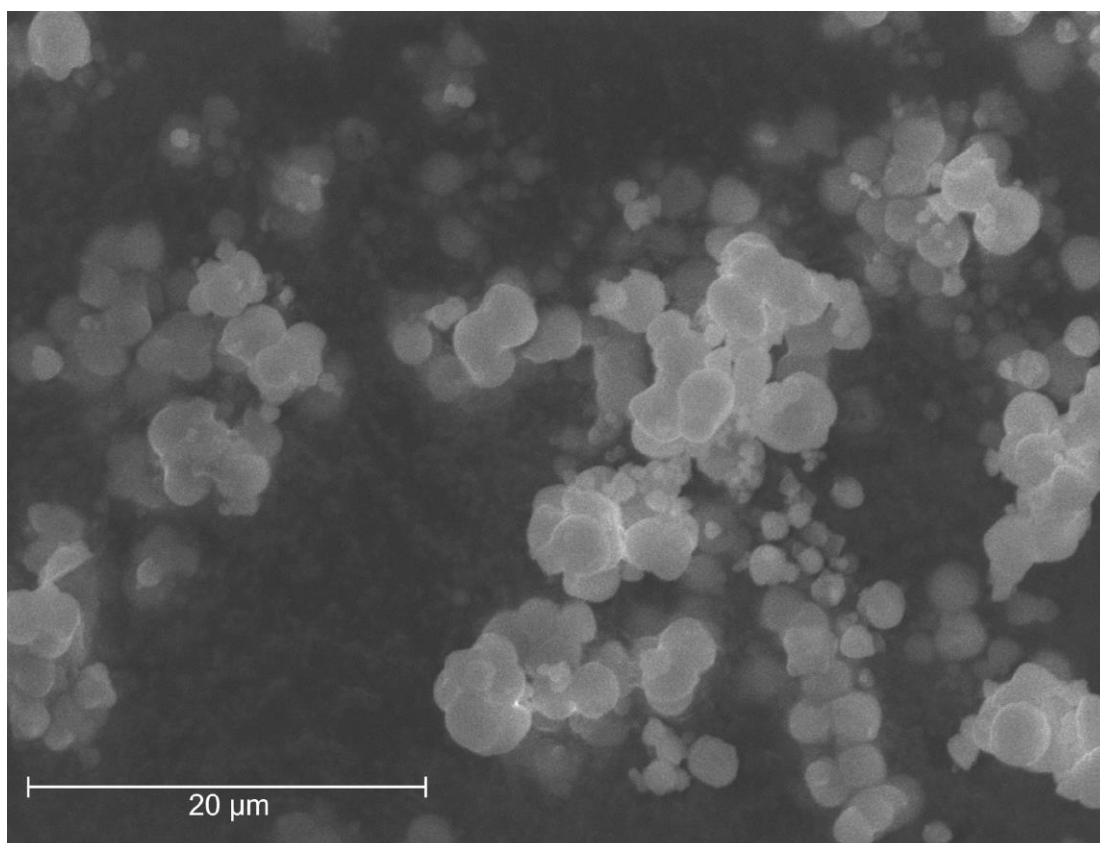**Figure C.18**: SEM image of $Y_{0.80}Tb_{0.40}(HCO_2)_3$, acquired with a secondary electron (SE) detector.

Table C.11: EDX atomic percentages of yttrium and terbium for $Y_{0.025}Tb_{0.975}(HCO_2)_3$ determined on different points and areas of the observed region under SEM.

Element	Y	Tb
	-1.36	101.36
	3.17	96.83
	4.86	95.14
	1.44	98.56
Atomic %	1.87	98.13
	-0.72	100.72
	5.64	94.36
	2.57	97.43
	2.92	97.08
Average	2.27	97.73
Standard Deviation	2.30	2.30

Table C.12: EDX atomic percentages of yttrium and terbium for $Y_{0.05}Tb_{0.95}(HCO_2)_3$ determined on different points and areas of the observed region under SEM.

Element	Y	Tb
	5.89	94.11
	1.58	98.42
	5.53	94.47
	3.54	96.46
	5.74	94.26
Atomic %	7.01	92.99
	3.21	96.79
	3.55	96.45
	4.42	95.58
	5.45	94.55
	7.5	92.50
Average	4.87	95.14
Standard Deviation	1.77	1.77

Table C.13: EDX atomic percentages of yttrium and terbium for $Y_{0.10}Tb_{0.90}(HCO_2)_3$ determined on different points and areas of the observed region under SEM.

Element	Y	Tb
	17.85	82.15
	15.23	84.77
	17.84	82.16
	8.51	91.49
	30.84	69.16
	8.15	91.85
Atomic %	9.78	90.22
	14.96	85.04
	17.17	82.83
	11.78	88.22
	10.87	89.13
	8.43	91.57

Average	14.28	85.72
Standard Deviation	6.41	6.41

Table C.14: EDX atomic percentages of yttrium and terbium for $Y_{0.20}Tb_{0.80}(HCO_2)_3$ determined on different points and areas of the two observed regions under SEM.

Element	Y	Tb
	28.86	71.14
	25.88	74.12
	25.79	74.21
	29.9	70.1
	26.35	73.65
	27.57	72.43
	28.93	71.07
	27.31	72.69
	27.24	72.76
	29.06	70.94
	28.05	71.95
Atomic %	24.12	75.88
	18.91	81.09
	23.11	76.89
	40.13	59.87
	24.88	75.12
	27.33	72.67
	23.31	76.69
	20.99	79.01
	31.25	68.75
	23.99	76.01
	33.7	66.3
	18.99	81.01
Average	26.77	73.23
Standard Deviation	4.65	4.65

Table C.15:. EDX atomic percentages of yttrium and terbium for $Y_{0.40}Tb_{0.60}(HCO_2)_3$ determined on different points and areas of the two observed regions under SEM.

Element	Y	Tb
	50.64	49.36
	54.16	45.84
	48.86	51.14
	55.9	44.1
	46.25	53.75
	25.28	74.72
	43.9	56.1
	53.45	46.55
	50.24	49.76
	43.09	56.91
	55.46	44.54
	56.43	43.57
	53.75	46.25
Atomic %	59.84	40.16
	43.95	56.05
	48.84	51.16
	41.87	58.13
	51.21	48.79
	46.15	53.85
	49.95	50.05
	45.07	54.93
	46.69	53.31
	49.19	50.81
	49.89	50.11
	50.69	49.31
	47.82	52.18
	49.44	50.56
Average	48.82	51.18
Standard Deviation	6.45	6.45

Table C.16: EDX atomic percentages of yttrium and terbium for $Y_{0.60}Tb_{0.80}(HCO_2)_3$ determined on different points and areas of the observed region under SEM.

Element	Y	Tb
Atomic %	75.56	24.44
	64.87	35.13
	67.52	32.48
	59.22	40.78
	60.42	39.58
	76.05	23.95
	73.71	26.29
	63.63	36.37
	65.06	34.94
	69.92	30.08
	66.24	33.76
	67.78	32.22
	62.63	37.37
	72.24	27.76
	70.25	29.75
	73.1	26.9
	64.3	35.7
	69.05	30.95
Average	67.86	32.14
Standard Deviation	5.01	5.01

Table C.17: EDX atomic percentages of yttrium and terbium for $Y_{0.80}Tb_{0.60}(HCO_2)_3$ determined on different points and areas of the observed region under SEM.

Element	Y	Tb
	82.49	17.51
	83.6	16.4
	82.56	17.44
	83.89	16.11
	83.08	16.92
	83.78	16.22
	83.69	16.31
	84.06	15.94
	83.64	16.36
	84.08	15.92
Atomic %	84.84	15.16
	82.73	17.27
	85.4	14.6
	83.36	16.64
	83.63	16.37
	83.25	16.75
	81.54	18.46
	80.9	19.1
	82.85	17.15
	83.22	16.78
Average	83.33	16.67
Standard Deviation	1.02	1.02

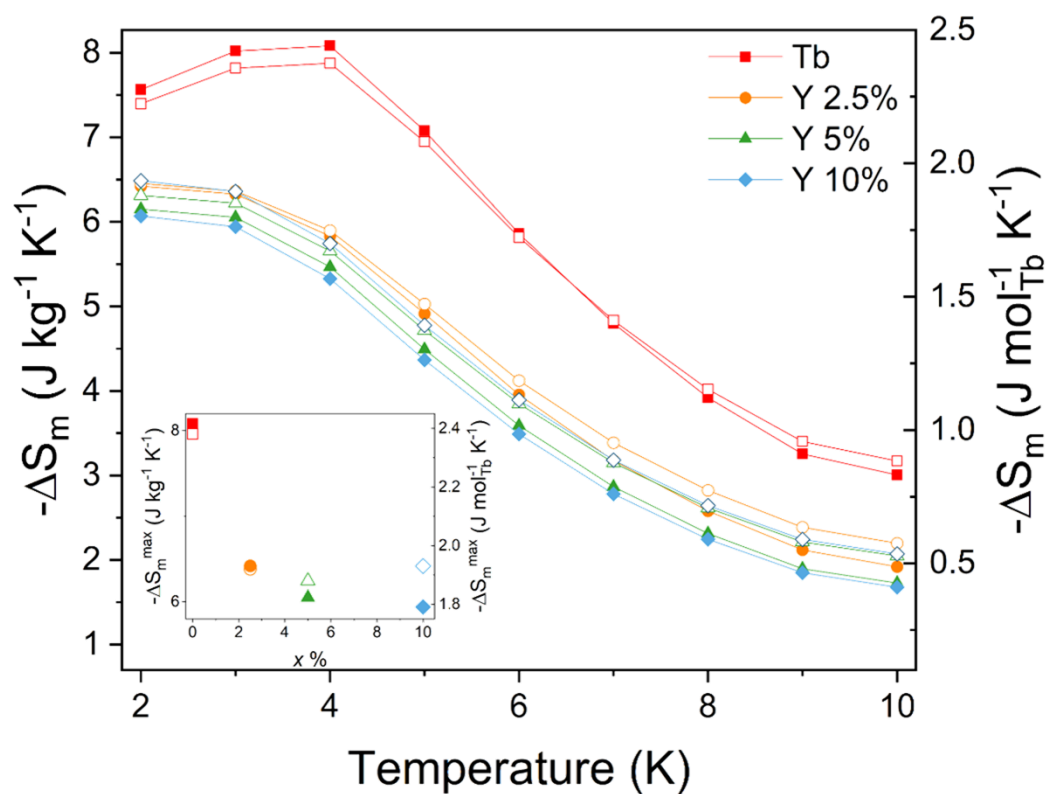**Figure. C.19**: Magnetic entropy changes extracted from the magnetisation data for $Tb(HCO_2)_3$ and the $Tb_{1-x}Y_x(HCO_2)_3$ (x = 0.025, 0.05, 0.10) solid solutions for ΔB = 1-0 T. Hollow symbols represent normalised molar values per amount of Tb. Inset shows the values of $-\Delta S_m^{max}$ for each sample.

Appendix D

Table D.1: Restraints set on interatomic distances for the refinements of $[Li(C_2O_4)]_2[Co_5(OD)_8]$ nuclear phase *via* the Rietveld method. The weight of the restraints was chosen to be 25%.

Atom 1	Atom 2	Restrained Distance (Å)
C20	C21	1.600
C20	O22	1.275
C20	O23	1.275
C21	C20	1.600
C21	O24	1.275
C21	O25	1.275
O10	D2	1.000
O11	D1	1.000
O12	D3	1.000
O13	D4	1.000

Constrained parameters

Hard constraints were chosen for some parameters that describe the $[Li(C_2O_4)]_2[Co_5(OD)_8]$ nuclear phase. Fractional occupancies for the atoms D1, D2, D3 and D4 were set to refine with the same starting value and were constrained to one another, while isotropic displacement parameters U_{iso} were grouped as follows:

- Li, C20, C21, O22, O23, O24 and O25, due to these atoms belonging to the $[Li(C_2O_4)]^-$ layers and being part of the Li^+ coordination environment.
- Co1, Co2, Co3, O10, O11, O12 and O13, due to these belonging to the $[Co_5(OD)_8]^{2+}$ layers and belonging to the Co^{2+} coordination environment.
- D1, D2, D3, D4, being part of the Li^+ coordination environment, while possessing a significantly lower mass than the other atoms.

Hard constraints were chosen for parameters describing the D2O phase as well. Specifically, the fractional occupancies for D1 and D2 were set to be equal and were constrained to one another in order to refine with the same shifts.

The lattice parameters of the nuclear phase and the magnetic phase – with the *c*-axis doubled for the latter – were constrained during the refinements to maintain the relationship as described by the *k*-vector = (0, 0, 0.5).

Equations Describing Simulated DFT Configurations

The following equations were determined by Dr N. Bristowe (Durham University) as explained in section 6.6 (see Eqn. 6.2). The energies reported on the right-hand side of each equation are those relative to the lowest-energy configuration determined *via* DFT, described by the first equation with *k*-vector = (0, 0, 0.5), and having energy ~ -330.822 meV.

Equations for *k*-vector = (0, 0, ½):

$$2.25 \left(-4J_1 + 8J_2 + 4J_3 - J_4 - J_5 + J_6\right) + K = 0 \; meV$$

$$2.25 \left(4J_1 + 8J_2 - 4J_3 - J_4 - J_5 + J_6\right) + K = 56.065 \; meV$$

$$2.25 \left(-4J_1 - 8J_2 - 4J_3 - J_4 - J_5 + J_6\right) + K = 175.115 \; meV$$

$$2.25 \left(4J_1 - 8J_2 + 4J_3 - J_4 - J_5 + J_6\right) + K = 110.3 \; meV$$

Equations for *k*-vector = (0, 0, 0):

$$2.25 \left(-4J_1 + 8J_2 + 4J_3 - J_4 - J_5 - J_6\right) + K = 0.82 \; meV$$

$$2.25 \left(4J_1 + 8J_2 - 4J_3 - J_4 - J_5 - J_6\right) + K = 56.89 \; meV$$

$$2.25 \left(J_4 + J_5 + J_6\right) + K = 67.83 \; meV$$

$$2.25 \left(J_4 + J_5 + J_6\right) + K = 72.01 \; meV$$

$$2.25 \left(-4J_1 - 8J_2 - 4J_3 - J_4 - J_5 - J_6\right) + K = 175.89 \; meV$$

$$2.25 \left(4J_1 - 8J_2 + 4J_3 - J_4 - J_5 - J_6\right) + K = 111.1 \; meV$$

$$2.25 \left(-4J_1 + J_4 - J_5 + J_6\right) + K = 67.13 \; meV$$

$$2.25 \left(4J_1 + J_4 - J_5 + J_6\right) + K = 62.67 \; meV$$

$$2.25 \left(-4J_3 - J_4 + J_5 - J_6\right) + K = 120.82 \; meV$$

$$2.25 \left(+4J_3 - J_4 + J_5 - J_6\right) + K = 60.93 \; meV$$

Other Rietveld Refinements of Diffraction Patterns of [Li(C₂O₄)]₂[Co₅(OD)₈] at 8 K
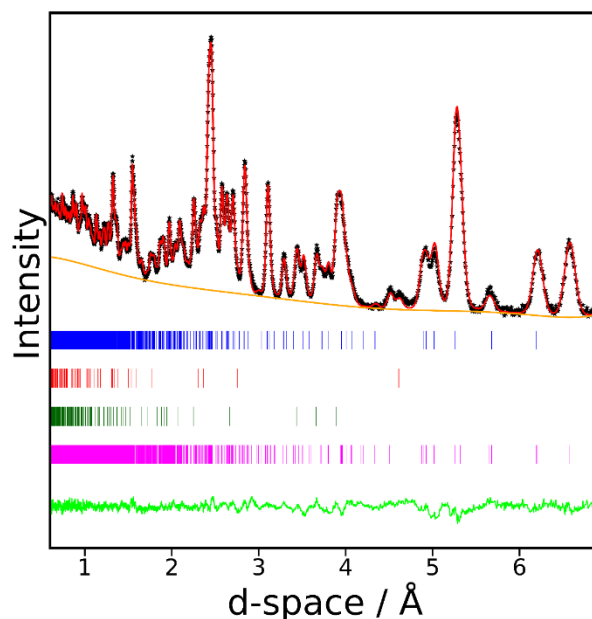
Figure. D.1: Neutron diffraction pattern collected from [Li(C₂O₄)]₂[Co₅(OD)₈] at 8 K using bank 3 of the GEM diffractometer fitted using the Rietveld method with R_p and R_{wp} of 2.01 % and 2.11 %, respectively. The crosses and the red, orange, and green lines indicate the observed and calculated intensities, the estimated background and difference curve, respectively. Blue, red, green and magenta markers represent reflections allowed by the [Li(C₂O₄)]₂[Co₅(OD)₈], Co(OD)₂ , D₂O and the magnetic phases, respectively.
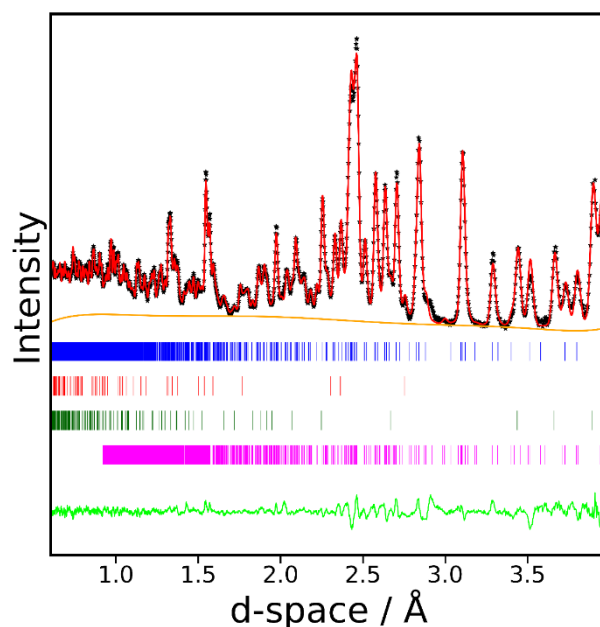
Figure. D.2: Neutron diffraction pattern collected from [Li(C₂O₄)]₂[Co₅(OD)₈] at 8 K using bank 4 of the GEM diffractometer fitted using the Rietveld method with R_p and R_{wp} of 2.39 % and 2.47 %, respectively. The crosses and the red, orange, and green lines indicate the observed and calculated intensities, the estimated background and difference curve, respectively. Blue, red, green and magenta markers represent reflections allowed by the [Li(C₂O₄)]₂[Co₅(OD)₈], Co(OD)₂ , D₂O and the magnetic phases, respectively.

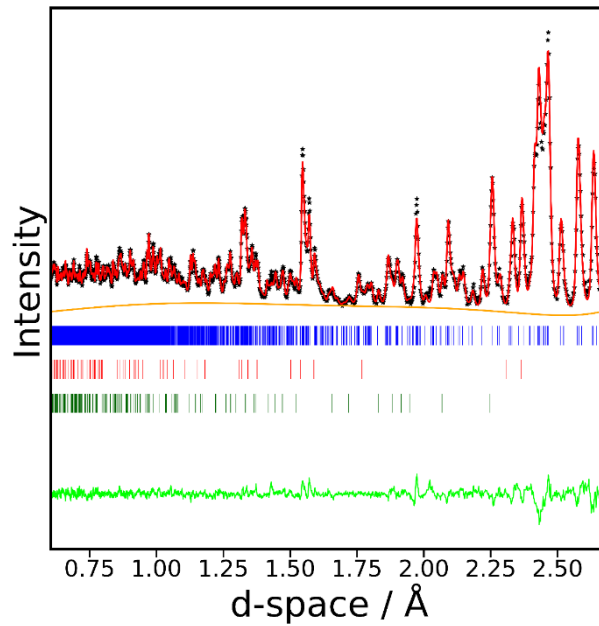**Figure. D.3:** Neutron diffraction pattern collected from $[Li(C_2O_4)]_2[Co_5(OD)_8]$ at 8 K using bank 5 of the GEM diffractometer fitted using the Rietveld method with R_p and R_{wp} of 2.52 % and 2.66 %, respectively. The crosses and the red, orange, and green lines indicate the observed and calculated intensities, the estimated background and difference curve, respectively. Blue, red, green and magenta markers represent reflections allowed by the $[Li(C_2O_4)]_2[Co_5(OD)_8]$, $Co(OD)_2$, D_2O and the magnetic phases, respectively.

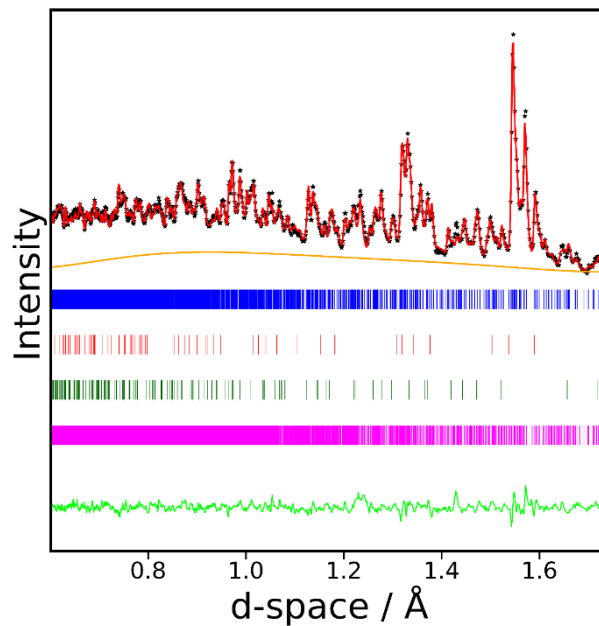**Figure. D.4:** Neutron diffraction pattern collected from $[Li(C_2O_4)]_2[Co_5(OD)_8]$ at 8 K using bank 6 of the GEM diffractometer fitted using the Rietveld method with R_p and R_{wp} of 1.51 % and 1.83 %, respectively. The crosses and the red, orange, and green lines indicate the observed and calculated intensities, the estimated background and difference curve, respectively. Blue, red, green and magenta markers represent reflections allowed by the $[Li(C_2O_4)]_2[Co_5(OD)_8]$, $Co(OD)_2$, D_2O and the magnetic phases, respectively.